ANALYSIS OF LOW-PRESSURE EVAPORATIVELY COOLED POLYMER ELECTROLYTE MEMBRANE FUEL CELLS

by

Paul Alan Benson

A Doctoral Thesis

Submitted in partial fulfilment of the requirements for the award of

Degree of Doctor of Philosophy of Loughborough University

April 2004

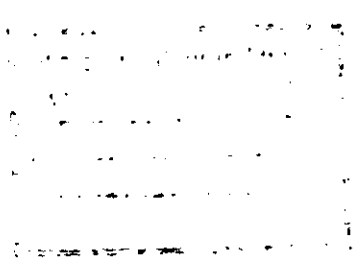

Dedicated to the loving memory of my Grandfather...

Abstract

The polymer electrolyte membrane fuel cell is being proposed for a number of power generation systems. With regard to replacing conventional technologies, they offer many advantages including quiet operation with low emissions. However, the key issue for the success of fuel cell system will be a superior operational efficiency. The associated sub-systems for controlling fuel cell stack thermal and water management contribute significantly to the reduction in stack weight and volume and increase the associated operational parasitic losses. In this thesis a novel fuel cell operational method has been proposed which utilises a combined humidification and cooling mechanism based on the direct injection of liquid water to the cathode flow-field. Several analyses were performed to investigate critical issues for the workable concept of such an EC, or evaporatively cooled, fuel cell system.

The EC mechanism was built into a single fuel cell rig and demonstrated an effective degree of thermal control and an electrochemical performance slightly lower to that obtained with the more 'conventional' method of pre-saturation of the reactant air. This difference was attributed to a lesser degree of humidification water reaching the membrane due to the hydrophobic nature of the diffuser material. Following this, two steady state system models were constructed, based on the polarisation characteristics obtained from the fuel cell, and illustrated the much improved parasitic loss characteristics of an EC system in comparison to an 'LC', liquid cooled, system.

A segmented current collector plate in a single fuel cell rig was used to illustrate differences in spatial performance over the EC fuel cell electrode with the utilisation of parallel and interdigitated flow field designs. Large elevations in current density, particularly at the end of the cathode gas tracks were observed when using the latter which, due to the forced flow mechanism, also produced a higher air pressure drop from cathode inlet to exit but was able to cope more ably with the presence of liquid water.

With a view to lowering cathode pressure drop, several diffuser materials were studied to establish an alternative to Carbel CL. Ex-situ testing illustrated the high cross-plane pressure drop of Carbel CL due to the deformable nature of the woven carbon cloth substrate. The properties of each diffuser tested are discussed in relation to their structure and post-treatments. Alternative diffusers which appeared to exhibit superior permeability properties were then tested in a single fuel cell set up with the interdigitated flow-field on the cathode. The cathode pressure drop of the loaded and unloaded fuel cell illustrated the accumulation of water in diffuser pores.

Acknowledgements

I would like to thank Paul Adcock for providing the opportunity for me to carry out this research and for his advice and support throughout the work. I am also grateful to Graham Wigley for his advice, particularly during the writing up of this thesis.

I would also like to express my gratitude towards the departments engineering technicians including Tony Newbold and Pete Hood for their assistance in the design and manufacture of equipment.

Thanks go to MIRA, in particular Geoff Callow, for their financial support.

Most importantly, this thesis would not have been in any way possible without the endless love and support from my wife Galiya and my Mum. An immeasurable amount of gratitude goes to my Aunt Margaret and Uncle Arthur who, in my frequent visits, have made me welcome in their home and ensured my diet during my student years at Loughborough University has been exceptional.

Table of Contents

List of Figures

List of Equations

Nomenclature

Symbols	Definition
α_x	Activity expression for component x
a	Stoichiometric reaction coefficient for hydrogen
A	Area
b	Stoichiometric reaction coefficient for oxygen
b_k	Tafel slope coefficient from Kim empirical equation
b_L	Tafel slope coefficient from Lee empirical equation
c	Stoichiometric reaction coefficient for water
C_p	Specific heat at constant pressure
C_v	Specific heat at constant volume
d	Diameter
d_m	Hydraulic mean diameter
ε_{ad}	Adiabatic efficiency
ε_{pump}	Efficiency of pump
ε_{rev}	Reversible efficiency
$\varepsilon_{rev}^{carnot}$	Reversible efficiency of Carnot device
η_{sum}	Sum of irreversible fuel cell operating losses
η_{act}	Activation overpotential
η_{IR}	Ohmic overpotential
η_{conc}	Concentration overpotential
η_{open}	Open-circuit overpotential
E_e	Potential for anode or cathode
$E_{o,K}$	Open circuit potential from Kim empirical equation
$E_{o,L}$	Open circuit potential from Lee empirical equation
E_{rev}	Reversible potential
E_{rev}^{O}	Reversible potential at STP
E_{op}	Fuel cell operating potential
F	Faradays constant
F_r	Friction losses
γ	Ratio of specific heats
g	Standard acceleration due to gravity
ΔG	Change in Gibbs free energy
ΔG_{react}	Gibbs free energy of reactants
ΔG_{prod}	Gibbs free energy of products
ΔG_{rev}	Change in Gibbs free energy for a reversible process
ΔG_{rev}^{O}	Change in Gibbs free energy for reversible process at STP
ΔH	Change in enthalpy of formation
H_2O_{prod}	Product water

H_2O_{diff}	Water back-diffusing from cathode to anode
$H_2O_{rem,a}$	Water removed from anode by hydrogen flow
$H_2O_{rem,c}$	Water removed from cathode by air flow
h	Head of fluid
h_f	Head loss due to friction
i	Fuel cell current density
$i_{L,e}$	Limiting current for anode or cathode
$i_{o,e}$	Exchange current density for anode or cathode
I	Current
κ_e	Electron transfer coefficient for anode or cathode
k	Darcy permeability
$k^{'}$	Intrinsic permeability
K_s	Conventional saturated permeability
λ_x	Stoichiometry of component x
L	Length
μ	Viscosity
m_L	Concentration loss coefficient from Lee empirical equation
m_K	Concentration loss coefficient from Kim empirical equation
$\dot{M}_{air}$	Mass flow rate of air
$\dot{M}_{cool}$	Mass flow rate of coolant
n	number of moles
$\dot{n}_x$	Molar flowrate of component x
n_{H_2O}	Electro-osmotic drag coefficient
n_K	Concentration loss coefficient from Kim empirical equation
n_L	Concentration loss coefficient from Lee empirical equation
$N_{H_2O}^{net}$	Net water osmotic drag across fuel cell membrane
$N_{H_2O}^{diff}$	Back diffusion of water from cathode to anode
ω	Correction factor for kinetic energy term
ψ	Friction factor
p	Pressure potential
P_x	Partial pressure of component x
P^O	Pressure at standard conditions
P_{pump}	Power requirement for pumping of fluid
P_{sat}	Saturation pressure of water
P_{tot}	Total pressure
PR	Pressure ratio
ϕ	Relative humidity
$\overline{Q}_{FC}$	Rate of heat generated by fuel cell
R	Universal gas constant
R	Resistance
$R_{cell,L}$	Ohmic resistance coefficient from Lee empirical equation

$R_{cell,K}$	Ohmic resistance coefficient from Kim empirical equation
Re	Reynolds number of fluid
ρ	Density
σ_{error}	Standard deviation for calculation of error values
ΔS	Change in entropy
T	Temperature
u	Velocity
v	Volume of unit mass of fluid
V	Volume
$\dot{V}_x$	Volumetric flow of component x
v^O	Molar volume at standard conditions
W_s	Net work on unit mass of fluid
W_{rev}^{carnot}	Reversible work performed by Carnot device
W_{el}	Electrical work performed/mol H2
x_{H_2O}	Gaseous mole fraction of water
Δz	Change in height
z	Thickness
ξ_L	Pressure ratio coefficient from Lee empirical equation

Abbreviations	Definition
ac	Alternating Current
AFC	Alkaline Fuel Cell
CHP	Combined Heat and Power
dc	Direct Current
DMFC	Direct Methanol Fuel Cell
EC	Evaporatively Cooled
GDE	Gas Diffusion Electrode
GDL	Gas Diffusion Layer
HPLC	high pressure liquid chromatography
ICE	Internal Combustion Engine
LC	Liquid Cooled
MCFC	Molten Carbonate Fuel Cell
MFC	Mass Flow Controller
ORR	Oxygen reduction reaction
PAFC	Phosphoric Acid Fuel Cell
PEM	Polymer Electrolyte Membrane/Proton Exchange Membrane
PEMFC	Polymer Electrolyte Membrane Fuel Cell
PFSA	Perfluorosulphonic Acid
PVDF	Polyvinylidene Fluoride
RH	Relative Humidity
sccm	Standard Cubic Centimeters per Minute
SLPM	Standard Liters Per Minute
SOFC	Solid Oxide Fuel Cell

Chapter 1

Fuel Cells as a Power Source

1.1 Overview

The fuel cell itself is an old innovation, first pioneered by Sir William Grove in 1838 with significant contributions in research later made by Mond and Langer. The technology has not warranted serious investigation in the field of energy generation until recent years where fundamental breakthroughs have been achieved, particularly in materials research and improving economics. Presently, fuel cells are approaching commercialisation for several applications, including road vehicles, decentralised power production, residential energy systems and portable electronics.

A fuel cell can be generally defined as an electrochemical device which produces electrical power directly from the oxidation of a fuel and the reduction of an oxidant. The operating principles - the direct conversion of chemical energy in the reactants to dc power - are identical to those of a primary battery. However, with a battery the reactants form the internal structure of the device and hence the operating efficiency, a function of the reactant concentration, is steadily reduced as electrochemical reactions proceed until finally the reactants are completely exhausted.

Therefore, fuel cells can theoretically operate at a fixed efficiency as long as the fuel and oxidant are continually supplied. In addition, with fuel cells producing power via an electrochemical reaction, the efficiency is not governed by the Carnot limitations experienced with all heat engines carrying out combustion processes, Equation 1.01[1].

$$\varepsilon_{rev}^{carnot} = \frac{W_{rev}^{carnot}}{(-\Delta H)} = 1 - \frac{T_2}{T_1} \qquad \textbf{Equation 1.01}$$

Another advantage is the ability to produce zero or near-zero quantities of emissions when pure fuel and oxidant are used with the only by-products being heat and water. It is these characteristics, along with reliable and quiet operation, that have made fuel cells particularly attractive for a large variety of power generation applications.

The accelerating rate of research and development undertaken in fuel cell technology is representative of the steady change in the perspective of the global energy supply. Most developed industrial nations are presently attempting to reduce their dependency on non-sustainable fossil fuels, with increased environmental awareness being a significant factor in the trend towards the large-scale adoption of renewable energy.

---

[1] Where $\varepsilon_{rev}^{carnot}$ is the maximum thermal efficiency, W_{rev}^{carnot} is the reversible electrical work performed, ΔH is the change in enthalpy between the produces and reactants, T_2 and T_1 are the two absolute temperatures for operation of the heat engine.

1.1.1 Operating principles

A single fuel cell consists of two electrodes, the anode and cathode, separated by a solid or liquid electrolyte. The anode is the negatively charged electrode where the fuel source dissociates into electrons and cations. The cathode is the positively charged electrode where anions are formed when the oxidant accepts electrons via the external circuit. In all fuel cells water is a product of the electrochemical reactions.

Fuel cells use either acid or alkali electrolytes, which allow good ionic conduction (cations in the case of acid, anions in the case of alkali) but act as good electrical insulators. The chemical processes and ionic charge transfers are as shown in Fig 1.01

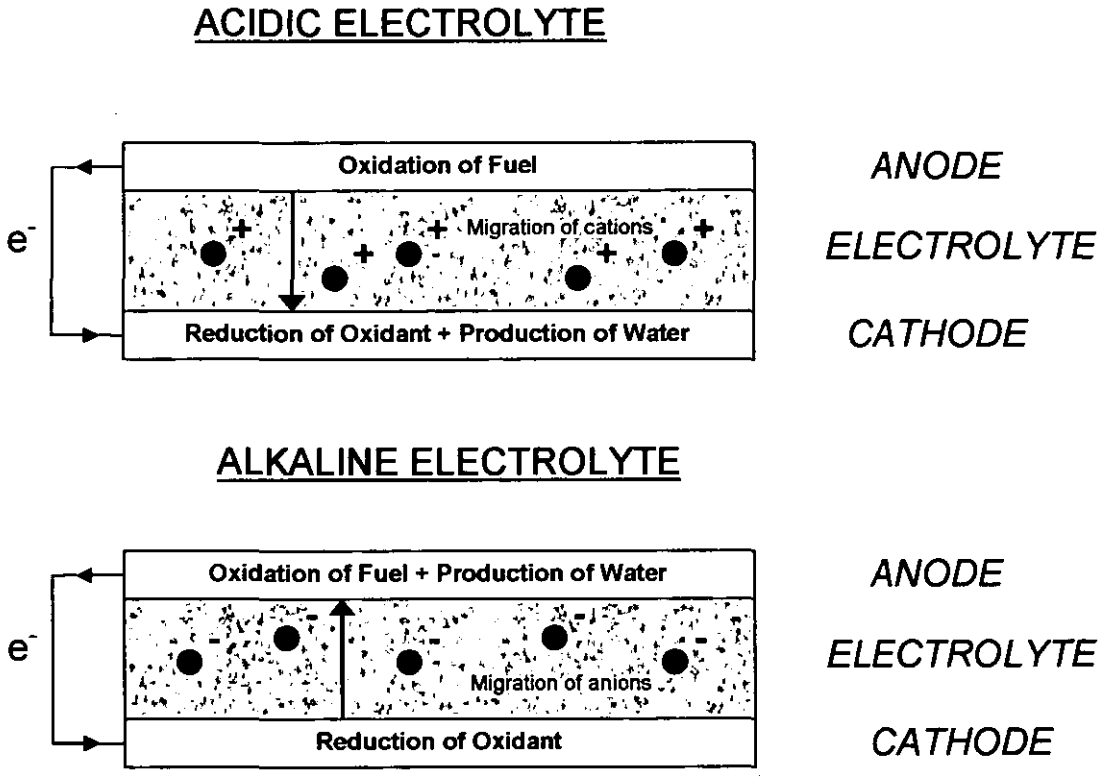

Fig 1.01 Fuel cell operating principles for acidic and alkaline electrolytes

To produce useful levels of power, many fuel cells are electrically connected to form a fuel cell 'stack'.

1.1.2 Fuel Cell Types

There are several categories of fuel cell, with the electrolyte utilised dictating the classification and characteristics such as the operating conditions (temperature, pressure etc), electrochemical reactions, source of fuel and component materials. These parameters is illustrated in Fig 1.02 below:

Fuel Cell Type	Anode Reaction	Cathode Reaction	Electrolyte	Ionic Charge Carrier	Operating Temperature
Polymer Electrolyte Fuel Cell (PEMFC)	$H_2 \rightarrow 2H^+ + 2e^-$	$^1/_2O_2 + 2H^+ + 2e^- \rightarrow 2H_2O$	Perfluorinated sulphonic acid membrane	H^+	50-100°C
Alkaline Fuel Cell (AFC)	$H_2 + 2OH^- \rightarrow 2H_2O + 2e^-$	$^1/_2O_2 + H_2O + 2e^- \rightarrow 2OH^-$	30-50 wt % aqueous Potassium Hydroxide	OH^-	<100°C
Phosphoric Acid Fuel Cell (PAFC)	$H_2 \rightarrow 2H^+ + 2e^-$	$^1/_2O_2 + 2H^+ + 2e^- \rightarrow 2H_2O$	100 wt % Phosphoric Acid	H^+	160-220°C
Molten Carbonate Fuel Cell (MCFC)	$H_2 + CO_3^{2-} \rightarrow H_2O + CO_2 + 2e^-$	$^1/_2O_2 + CO_2 + 2e^- \rightarrow CO_3^{2-}$	Lithium and Potassium Carbonates	CO_3^{2-}	600-800°C
Solid Oxide Fuel Cell (SOFC)	$H_2 + O^{2-} \rightarrow 2H_2O + 2e^-$	$^1/_2O_2 + 2e^- \rightarrow O^{2-}$	Zirconium and yttrium oxides	O^{2-}	800-1000°C
Direct Methanol Fuel Cell (DMFC)	$CH_3OH + H_2O \rightarrow CO_2 + 6H^+ + 6e^-$	$^3/_2O_2 + 6H^+ + 6e^- \rightarrow 3H_2O$	Perfluorinated sulphonic acid membrane	H^+	60-120°C

Fig 1.02 Table of fuel cell types and operational characteristics

In the proceeding sections there follows a brief overview of each type of fuel cell along with some examples of their applications.

1.1.2.1 Alkaline fuel cell – technology and history overview

Francis Thomas Bacon (1904-1992) first experimented with alkaline fuel cells as an alternative to the acid electrolytes used in Groves's early research – these produced equivalent performance and were not as corrosive to the electrodes. In the early 1960's aircraft engineer Pratt and Whitney, licensed Bacons technology to develop AFC's for NASA space programs and this has since been used in Apollo and Shuttle missions.

The alkaline nature of the electrolyte means that the oxygen reduction kinetics are much faster than with an acidic electrolyte which enables less expensive non-noble electro-catalysts to be used, e.g. Raney Nickel on anode, Raney Silver on cathode as used by Siemens. The major drawback of with AFC's is the requirement of very pure reactant supplies particularly the complete absence of carbon dioxide which destroys the electrolyte, producing carbonate by-products.

$$CO_2 + 2OH^- \rightarrow (CO_3)^{2-} + H_2O \qquad \textbf{Equation 1.02}$$

The space application AFC's used potassium hydroxide in a stabilised matrix as a liquid electrolyte was unsuitable for such applications. However, research has shown that a much longer operating lifetime is obtained with a circulating solution of KOH where by continually refreshing the electrolyte the build-up of carbonates is avoided. The pure liquid electrolyte also provides a better barrier against gas leakage and can function as a cooling mechanism. However even using a circulating alkaline electrolyte, a large and complex carbon dioxide 'scrubbing' subsystem is needed when operating on non-pure fuel, e.g. from a hydrocarbon reformer, or oxidant, e.g. air. This has severely restricted the number of suitable applications for AFC's.

1.1.2.2 Phosphoric Acid fuel cell – technology and history overview

In very early research, phosphoric acid as a fuel cell electrolyte was largely discounted due to the lower ionic conductivity obtained compared to sulphonic acid based electrolytes. However, research in the 1960's by Elmore and Tanner discovered that phosphoric acid was not electrochemically reduced under the fuel cell operating conditions – unlike sulphonic acid. Major advances in materials research allowed a 100% concentration of phosphoric acid to be used within a stabilised silicon carbide matrix – leading to improvements in performance and better endurance of electrodes. The electrodes used in the PAFC are generally platinum-based catalysts dispersed on a carbon-based support. The higher temperature of the PAFC over other acid electrolyte based fuel cells allows tolerance of impurities which poison the catalysts at lower temperatures.

The PAFC has become the most commercially advanced fuel cell system for the provision of residential power and units have been installed worldwide by several companies. Examples of this include UTC Fuel Cells PC25 'Fuel Cell Power Plant', the 200kW footprint version having been supplied to several key locations in the United States, Cropper (2002). In Japan, Fuji Electric has been heavily involved in PAFC system development with 50kW and 100kW units being commercially available since the late 1990's. However, there are indications that many of the residential fuel cell developers are starting to turn away from the PAFC in favour of alternatives such as PEMFC.

1.1.2.3 Molten Carbonate fuel cell – technology and history overview

In the late 1950's the Dutch scientists Broers and Ketelaar shifted research on high temperature fuel cells away from the then, unsuccessful attempts at development in SOFC's to used fused (molten) carbonate salts. Initially, a mixture of lithium and potassium carbonate (Li_2CO_3 / K_2CO_3) materials immobilised in a porous sintered disk of magnesium oxide were used as the electrolytes. However, the molten electrolyte was slowly lost and the electrodes were also gradually degraded. Further research has resulted in a much more stable porous lithium aluminate matrix being used as the electrolyte support.

The MCFC fuel cell demands such high operating temperatures, e.g. 800°C, that most applications are restricted to large stationary power plants. However, this allows internal reforming of reactants, the recovery of waste heat and cheaper non-noble catalysts can be used - usually Nickel based materials. A downside of the MCFC is that due to these high operating temperatures it requires a much more rigorous procedure for materials selection and maintenance due to the degradation, sealing and thermal expansion properties.

Fuel Cell Energy, previously Energy Research Corp., has been developing MCFC technology since the 1970's and is currently developing and commercialising a 250kW incarnation which features internal reforming. In Japan research into MCFC technology has been funded by the government since 1981, with development work now mainly done by Ishikawajima Heavy Industries.

1.1.2.4 Solid Oxide fuel cell – technology and history overview

The first work into SOFC's can be traced back to the research undertaken by the Swiss scientist Baur who experimented with solid oxide electrolytes in the 1930's, using such materials as zirconium, yttrium, cerium, lanthanum and tungsten. There were problems with high internal resistance, melting, and semi-conductive short circuiting. However, since then major advances in materials have been made and the SOFC now represents a straightforward two-phase gas-solid system with less associated problems than the MCFC.

Similar to the MCFC, the high temperature allows internal reforming of hydrocarbon reactants but has restricted the applications to residential power generation. The solid nature of the electrolyte has allowed several different designs implementing both the fuel cell and reformers into the stack – with the tubular design (developed by Siemens Westinghouse) being the best known example of this.

Many companies are now involved in developing SOFC's including MHI, NTT and J-Power in Japan, Rolls Royce in the UK and Siemens-Westinghouse in the US. The latter has successfully operated a 100kW cogeneration SOFC in the Netherlands and a 220kW proof-of-concept hybrid SOFC/gas turbine power plant in California.

1.1.2.5 Polymer Electrolyte fuel cell – technology and history overview

This type of fuel cell is also be referred to as the 'proton exchange membrane' fuel cell or 'solid polymer' fuel cell. The first practical PEM fuel cells were developed by the General Electric Company for the Gemini space missions and used polystyrene based membranes. However, these materials suffered from a debilitating short lifetime (around 500 hours) due to chemical attack from the harsh fuel cell oxidative/reductive environment - this was one of the major reasons for NASA adopting AFC technology for the Apollo missions. Perfluorinated sulphonic acid (PFSA) membranes were developed in the 1970's, which gave enhanced performance and increased the lifetime of a PEM fuel cell to several thousands of hours - the Nafion® series of polymers, developed by DuPont are the most established PFSA materials.

The PEM fuel cell has by far the largest development effort current going on with around 80 companies working on the technology at the time of writing. Two of the most prestigious developers are Ballard Power Systems in Canada and UTC fuel cells in the U.S. A full overview of the current developments in PEMFC technology is given in Chapter 2.

1.1.2.6 Direct Methanol fuel cells– technology and history overview

Of all fuel cell types, this technology most resembles the PEMFC, as it utilises a similar polymer electrolyte. Here, methanol is reduced directly on the anode with power produced at temperatures similar to the PEMFC, typically 100°C. The high energy density of methanol and its liquid state make this a particularly attractive technology. However a major detriment to performance is the movement of methanol fuel across the electrolyte from anode to cathode during operation, effectively 'shorting' the fuel cell and greatly reducing the efficiency. Hence, most of the research currently being undertaken with this technology is focused on developing new membrane materials which reduce this crossover effect.

This technology is most suited for micro-power applications such as portable electronics, and to this end, NEC, Sony and Toshiba are involved in the integration of DMFC technology into laptops for long-life operation, scheduled for release in 2004 and 2005, Cropper (2002). The most prestigious DMFC developers are Smart Fuel Cell and Manhattan Scientifics, the former demonstrating a 40W stand alone unit at the 2002 Hannover fair which powered a laptop, reportedly for 3-5 times longer than traditional batteries.

1.2 References

Cropper, M., "Fuel Cell Market Survey: Stationary Applications", Fuel Cell Today Website, 22nd May 2002

Cropper, M., "Fuel Cell Market survey: Portable Applications", Fuel Cell Today Website, 18th September, 2002

Chapter 2

The Polymer Electrolyte Membrane Fuel Cell

2.1 The PEM Fuel Cell

2.1.1 Chapter Overview

In this Chapter the operating mechanisms of the PEM fuel cell are discussed, including details on the thermodynamics of operation. Following this, the components used in the build of a PEM fuel cell are individually described. Finally, some of the key developments in PEM fuel cells are discussed which, at the time of writing, has almost brought the technology to the stage of commercialisation for selected applications.

2.1.2 Basic principles of PEMFC operation

A general overview of the operating mechanisms of all fuel cells was provided in Chapter 1 - here the specific aspects of PEM fuel cell operation are detailed.

A single PEM fuel cell produces power as shown in Fig 2.01.

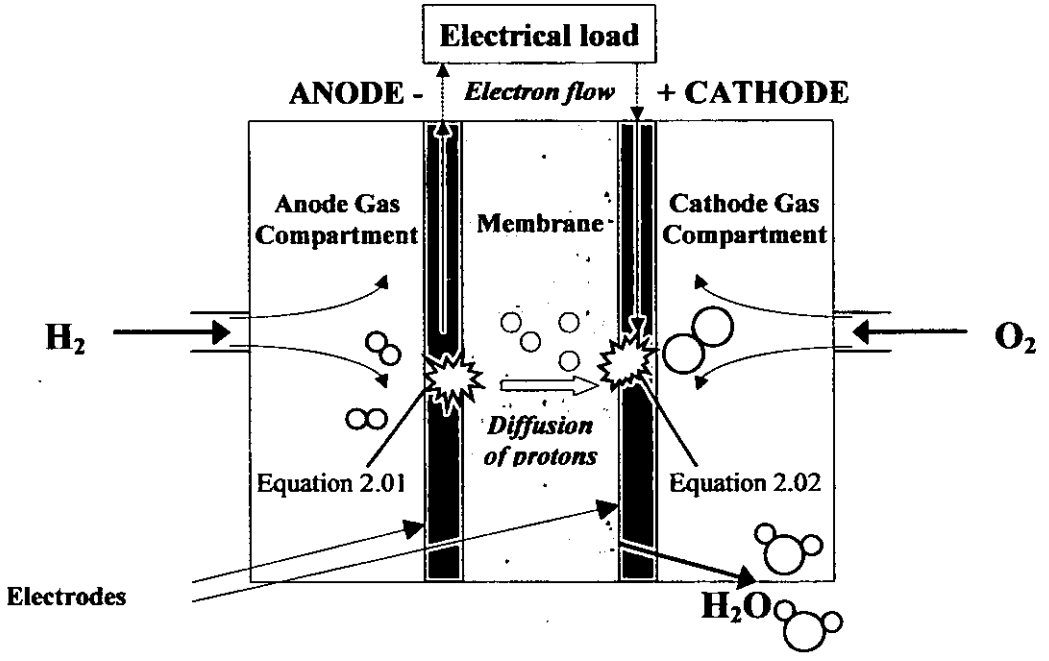

Fig 2.01: Operating principle of the polymer electrolyte fuel cell

Hydrogen gas is delivered to the anode and oxygen (usually in the form of air) is delivered to the cathode. The anode catalyst facilitates the oxidation of hydrogen gas:

$$H_2 \rightarrow 2H^+ + 2e^- \qquad \textbf{Equation 2.01}$$

The protons then migrate through the solid polymer membrane to the cathode side, creating a difference in voltage potential. This initiates a flow of electrons, i.e. movement of charge, from anode to cathode, directed round the external circuit providing useful electrical work. On re-entering the cell at the cathode, the electrons facilitate the reduction of oxygen, which takes place over the platinum catalyst:

$$\frac{1}{2}O_2 + 2H^+ + 2e^- \rightarrow H_2O \qquad \textbf{Equation 2.02}$$

The products of the overall fuel cell reaction are water and some heat.

$$H_2 + \frac{1}{2}O_2 \rightarrow H_2O \qquad \textbf{Equation 2.03}$$

2.1.2.1 Thermodynamics of PEM fuel cell operation

The theory of PEM fuel cell efficiency and irreversible losses of operation are now discussed.

Definition of reversible potential

Considering again Equation 2.03 - as stated earlier, this reaction releases an overall level of energy defined as ΔH[1], which in the fuel cell is distributed between electrical energy and heat. The maximum amount of electrical work available from a fuel cell can be described as the change in *Gibbs free energy* of the reaction (sometimes defined as Gibbs free energy of formation of reaction) and is denoted by the expression ΔG. This is the difference between the Gibbs free energy of products and reactants.

$$\Delta G = G_{prod} - G_{react} \qquad \textbf{Equation 2.04}$$

The value of Gibbs free energy is not constant and changes with temperature and state. If there are no losses in the fuel cell then the reaction is defined as a reversible (or ideal) process, that is, ΔG is completely converted to electrical energy. A reversible process is defined as occurring at such an infinitesimally slow rate that there is no change in operating conditions - constant temperature and pressure etc.

The potential of a fuel cell is defined as the electrical work, W_{el} done in moving charge through the fuel cell circuit divided by the number of electrons transferred. For a reversible process is related to the change in Gibbs free energy by the expression[2]:

$$W_{el} = \Delta G_{rev} = -nFE_{rev} \qquad \textbf{Equation 2.05}$$

For reactants and products in the defined 'standard state' (298°K, 1atm. pressure with liquid water as product) then the equation includes the superscript ^{O} to denote this:

$$\Delta G^{O}_{rev} = -nFE^{O}_{rev} \qquad \textbf{Equation 2.06}$$

[1] Here representing the difference in the enthalpy of formation of the products and reactants of equation 2.03. This can be based on the lower heating value (LHV) where all product water is vapour or higher heating value where all product water is liquid (HHV)

[2] Where n = number of electrons transferred in reaction, F is faraday's constant, 96485 Coulombs/ mol and E is the ideal reversible potential of the cell. The negative sign is due to the Gibbs free energy that is released.

In this case, as ΔG^{o} is -237.2 kJ/mole H_2, the reversible potential is calculated as 1.229 V. However on drawing power there are always irreversible losses of fuel cell operation which are detailed in later sections.

Definition of efficiency

The efficiency of a fuel cell – indeed any energy conversion device - is defined as the *amount of useful energy produced relative to the change in stored chemical energy when the fuel is burned.* For a fuel cell operating reversibly this is:

$$\varepsilon_{rev}^{fc} = \frac{\Delta G_{rev}}{\Delta H} \qquad \textbf{Equation 2.07}$$

The enthalpy of formation of reaction ΔH has a value of -285.8 kJ/mole -based on the higher heating value which here gives a theoretical efficiency value of:

$$\varepsilon_{rev} = \frac{237.2}{285.8} = 83\% \qquad \textbf{Equation 2.08}$$

The relationship between enthalpy of formation of reaction and Gibbs free energy in a fuel cell operating reversibly is expressed as:

$$\Delta G = \Delta H - T\Delta S \qquad \textbf{Equation 2.09}$$

The difference between ΔG and ΔH is defined as the operating temperature in Kelvin, T, multiplied by the change in entropy, ΔS. This is the amount of energy lost by changes in thermodynamic degrees of freedom.

Nernst equations-Open circuit outside standard operating conditions

Outside standard conditions (1 atmosphere of pressure and 25°C) the theoretical reversible potential (and hence change in Gibbs free energy) for a fuel cell has to be calculated by using the *Nernst* equation. This provides a relationship between the standard reversible potential for the cell reaction and the reversible potential at other temperatures and partial pressures of reactants and products. This is defined from first principles as follows:

Re-writing the fuel cell reaction as:

$$aH_2 + bO_2 \rightarrow cH_2O \qquad \textbf{Equation 2.10}$$

where a = 1, b = ½ and c = 1

Allows an expression of the free energy change of the FC reaction under non standard conditions, Fuel Cell Handbook (2000)[3]:

$$\Delta G = \Delta G^O - RT \ln \frac{[\alpha_{H_2O}]^c}{[\alpha_{H_2}]^a [\alpha_{O_2}]^b} \qquad \textbf{Equation 2.11}$$

α refers to "activity" which, in the case of gases behaving ideally, is defined as[4]:

$$\alpha_x = \frac{P_x}{P^O} \qquad \textbf{Equation 2.12}$$

Substituting Equations 2.05 and 2.06 into 2.11 gives the Nernst equation:

$$E = E^O - \frac{RT}{nF} \ln \frac{[\alpha_{H_2O}]^1}{[\alpha_{H_2}]^1 \cdot [\alpha_{O_2}]^{\frac{1}{2}}} \qquad \textbf{Equation 2.13}$$

This illustrates that the reversible potential for the fuel cell reaction falls with increasing operating temperature but can be increased with higher reactant partial pressures.

A working example using the Nernst equation is illustrated to calculate the standard reversible potential for a fuel cell using air where oxygen makes up 21% of the gas molar composition. Using Equations 2.12 and 2.13 and assuming the activity of the liquid water product is unity, at standard temperature and pressure the theoretical potential of the fuel cell is:

[3] Where R is the universal gas constant – 8.3145 J/ mol K

[4] Where P_x is the partial pressure of the gas and P^o is the standard pressure 101325 Pa

$$E = E^{O} - \frac{RT}{nF}\ln\frac{\left[P^{O}\right]^{\frac{3}{2}}}{P_{H_2}[0.21P_{air}]^{1/2}} \qquad \textbf{Equation 2.14}$$

$$E = 1.229 - \frac{8.314 Jmol^{-1}K^{-1}\cdot 298.15K}{2\cdot 96485 cmol^{-1}}\ln\frac{1}{(0.21)^{\frac{1}{2}}} = 1.219V \qquad \textbf{Equation 2.15}$$

Therefore, there is a drop of 10 mV in the theoretical reversible fuel cell potential when using air instead of a pure oxygen source.

Irreversible losses of operation - overpotentials

Useful power is obtained from a fuel cell only when current is drawn and here the actual cell potential deviates from the calculated reversible potential due to a number of irreversible losses, η_{sum}. This is expressed as[5]:

$$\eta_{sum} = E_{rev} - E_{op} \qquad \textbf{Equation 2.16}$$

The effect of these losses (referred to individually as overpotentials) is illustrated in a typical polarisation plot, shown in Fig 2.02. All polarisation plots conform to this basic shape.

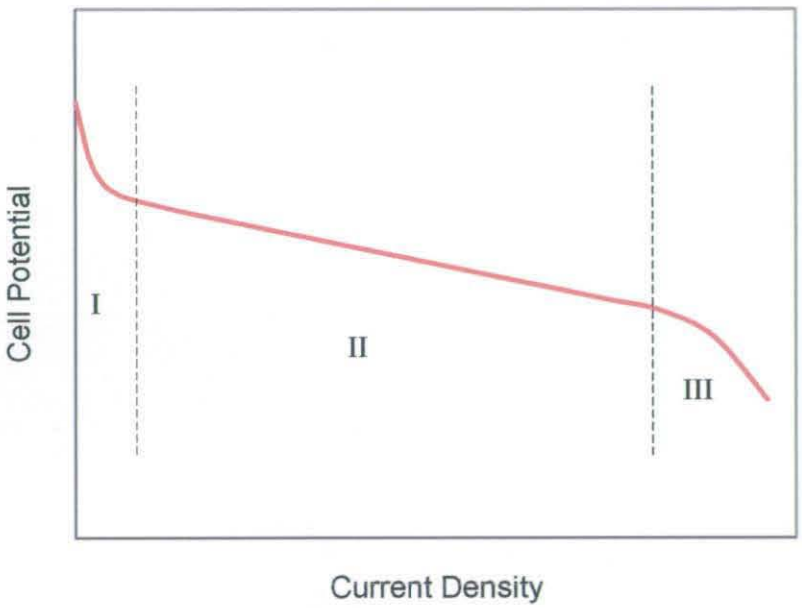

Fig. 2.02 Generalised polarisation plot

The polarisation curve is separated into three distinct regions each of which is dominated by a specific overpotential that is caused by a certain physical phenomena occurring in the fuel cell. There are four types of overpotential -activation overpotential η_{act}, ohmic overpotential η_{IR}, mass transport (or concentration) overpotential η_{conc} and also a fourth, η_{open} resulting from gas crossover and a small magnitude of current flow through the membrane. The latter is sometimes not classed as an overpotential in the literature as it does not alter in magnitude with current drawn and hence does not dominate any particular region of the polarisation curve. The effect of η_{open} is to lower the potential of

[5] where E_{rev} is reversible cell potential and E_{op} is operating voltage

the fuel cell at zero Amps, referred to as 'open circuit potential', away from the reversible potential.

Activation overpotential represents the energy barriers that have to be overcome to drive the electrochemical reactions on the anode and cathode catalytic surface. This dominates the low current section of the polarisation curve - region I. Ohmic overpotential results from the electrical resistance of all components of the cell and on Fig. 2.02 dominates the linear middle section of the plot - region II. Concentration overpotential becomes increasingly prominent at high limiting current densities where it becomes difficult to provide a sufficient flow of reactants to the catalyst sites - region III.

Thermodynamics of overpotentials

The contributions of *individual* overpotentials to a fuel cell polarisation plot are illustrated in Fig. 2.03. The effect of η_{open} is seen as the difference between the light blue plot representing reversible potential, E_{rev} and the dark blue plot which is open circuit voltage, typically 0.2 Volts. This explains why in a single PEM fuel cell the maximum open circuit potential is approximately 1V.

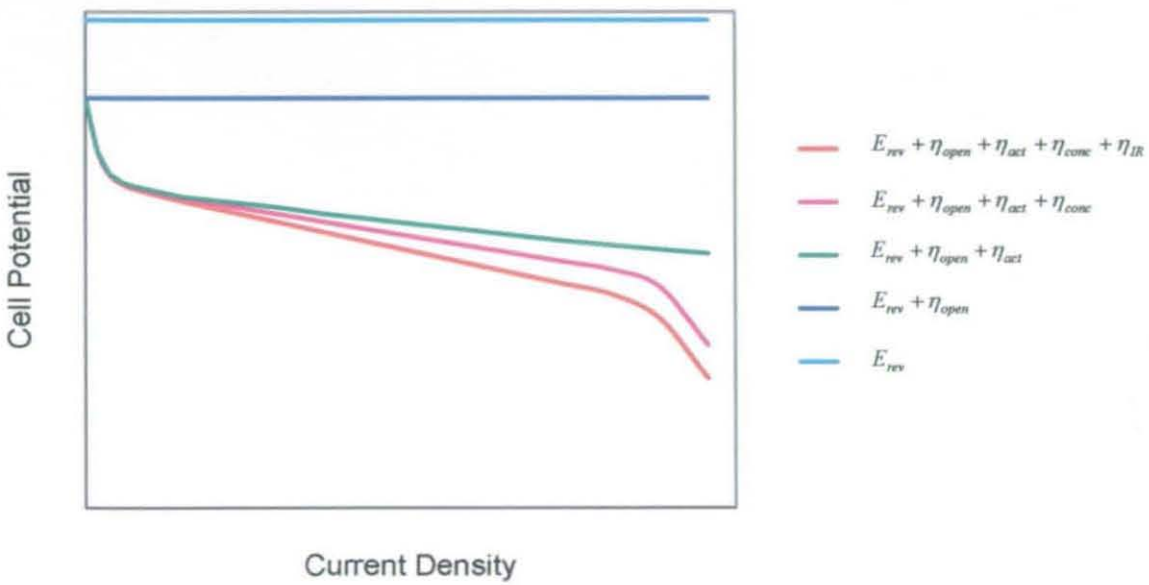

Fig. 2.03 Polarisation plot illustrating individual overpotentials

The remaining three plots show the effect of activation, resistance and concentration overpotentials. The green plot shows how the activation overpotential lowers the operating potential dramatically at low currents. The magenta plot includes concentration overpotential which shows a 'bending down' of the polarisation plot at high currents. The

red plot includes the resistance overpotential showing the inclusion of a linear ohmic loss.

Calculation of overpotentials of operation

An expression for fuel cell operating voltage can be obtained by deriving an equation that accounts for all three overpotentials, excluding η_{open}.

$$\eta_{sum} = \eta_{act} + \eta_{conc} + \eta_{IR} \qquad \textbf{Equation 2.17}$$

These are now examined individually.

Activation overpotential

Activation overpotential represents the energy lost driving the transfer of electrons for completion of the half-reactions at the electrodes. In the PEM fuel cell the contribution of anode activation overpotential is usually regarded as negligible as the reaction kinetics of oxygen reduction at the cathode is a significantly slower and more complex process. This essentially means that activation overpotential of the fuel cell is directly related to the rate of the cathode reaction.

An equation representing cathode activation polarisation is shown below (Fuel cell handbook) – which is referred to as the "Tafel equation"

$$\eta_{act} = \frac{RT}{\kappa n F} \ln \frac{i}{i_{o,cat}} = \frac{RT}{\kappa n F} \ln i - \frac{RT}{\kappa n F} \ln i_{o,cat} \qquad \textbf{Equation 2.18}$$

Here κ is the "electron transfer coefficient" of the cathode reaction representing the proportion of the electrical energy applied that is utilised to change the rate of the electrochemical reaction. The value of κ is in the range zero to unity but for a PEM fuel cell cathode is typically 0.1 to 0.5, Dicks et al (2000). The expression $i_{o,cat}$ represents the cathode exchange current density, describing the rate of the equilibrated cathode half-reactions, and i is the current density from the fuel cell.

A visual representation of activation overpotential is obtained by expressing Equation 2.18 in the following form, Fuel Cell Handbook (2000):

$$\eta_{act} = x + y \ln i \qquad \textbf{Equation 2.19}$$

Such an illustration is referred to as a Tafel plot and this is used to measure the exchange current density and provide a visual understanding of the activation polarisation of the fuel cell. The term x, of Equation 2.19 has the value $-\frac{RT}{\kappa nF}\ln i_{o,cat}$ and y has the value $\frac{RT}{\kappa nF}$ and is called the *Tafel slope*. This can be obtained from a slope of a plot of activation overpotential as a function of $\ln i$, refer to Fig 2.04, Fuel Cell Handbook (2000).

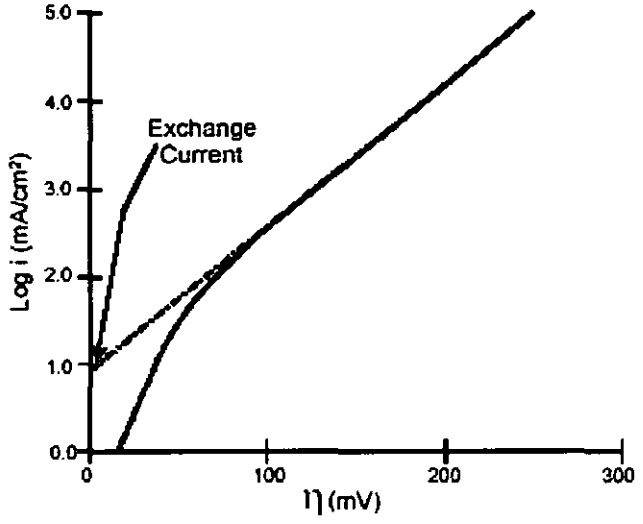

Fig. 2.04 Generalised Tafel plot

Therefore the cathode exchange current density is the crucial factor in reducing activation overpotential. Increasing cathode exchange current density can be achieved by raising the cell temperature, increasing pressure and concentration and improving the catalyst surface area.

Ohmic overpotential

Ohmic losses occur due to the electrical resistance in all fuel cell components: ionic and electronic resistance in the electrodes, electronic resistances in the gas diffusers, bipolar plates and even in the stack connections. However, the dominant contribution to the ohmic overpotential losses usually arises from the ionic resistances in the PFSA membrane. Ohmic overpotential is proportional to current in a similar manner to Ohm's law and can be modelled thus: [6]

$$\eta_{IR} = I \cdot R_{cell} \qquad \textbf{Equation 2.20}$$

[6] where I is the current flowing through the cell and R_{cell} is the sum total of the fuel cell resistances

The dominant ionic-resistive losses of the membrane can be reduced by decreasing the electrode separation, i.e. using a thinner membrane such as the Gore reinforced type. The linear nature of this equation is reflected in the middle region of the polarisation curve where ohmic overpotential dominates.

Concentration polarisation

When gas diffusion limitations reduce the reactant availability to catalyst sites, part of the available reaction energy is used to drive the mass transfer, creating a corresponding loss in output voltage defined as concentration overpotential – or mass transfer overpotential. Several processes may contribute to concentration polarisation: slow diffusion of the gas phase through electrode pores to reactant sites or slow diffusion of products through from the reaction sites.

To model concentration overpotential it is necessary to envisage the formation of a concentration gradient as gaseous reactants are consumed at both electrodes by the half reactions. The extent of this concentration gradient will be dependant on the level of current being drawn. Assuming a linear concentration gradient and using Fick's first law of diffusion, the mass transport overpotential can be expressed as, Dicks et al (2000)[7]:

$$\eta_{conc} = \frac{RT}{nF} \ln\left(1 - \frac{i}{i_{L,e}}\right) \qquad \textbf{Equation 2.21}$$

The main source for diffusion overpotential in a fuel cell will be the diffusion of oxygen through the gas diffusion backing on the cathode side, where there will be a high presence of liquid product water. Using air as the oxygen source 'dilutes' the cathode reactant, resulting in a much higher rate of concentration overpotential; in the literature this is referred to as the 'blanketing effect' of nitrogen. Diffusion overpotential is much smaller on the anode than on the cathode due to the high permeation rates of hydrogen gas.

Final expression

The potential of an electrochemical cell is defines as the difference in potential of the cathode E_c and the anode E_a. The effect of individual electrode overpotentials is to

[7] Where $i_{l,e}$ is the limiting current at the specific electrode

increase the anode potential and decrease the cathode potential thereby reducing overall cell potential.

An expression for anode potentials can be obtained by adding the activation and mass transfer overpotentials:

$$E_a = E_{rev,a} + \eta_{act,a} + \eta_{conc,a} = 0 + \frac{RT}{\kappa_a n_a F}\ln\frac{i}{i_{o,a}} + \frac{RT}{n_a F}\ln\left(1 - \frac{i}{i_{L,a}}\right) \qquad \textbf{Equation 2.22}$$

Similarly, an expression can be obtained for cathode overpotential by subtracting the activation and mass transfer overpotentials from the theoretical potential for the cell conditions.

$$E_c = E_{rev,c} - \eta_{act,c} - \eta_{conc,c} = E_{t,c} - \frac{RT}{\kappa_c n_c F}\ln\frac{i}{i_{o,c}} - \frac{RT}{n_c F}\ln\left(1 - \frac{i}{i_{L,c}}\right) \qquad \textbf{Equation 2.23}$$

Using Equations 2.22 and 2.23 and accounting for the ohmic overpotential (Equation 2.20) the fuel cell voltage can be expressed as a function of current density:

$$E = E_c - \frac{RT}{n_c F}\left[\frac{\ln\left(\frac{i}{i_{o,c}}\right)}{\kappa_c} + \ln\left(1 - \frac{i}{i_{L,c}}\right)\right] - \frac{RT}{n_a F}\left[\frac{\ln\left(\frac{i}{i_{o,a}}\right)}{\kappa_a} + \ln\left(1 - \frac{i}{i_{L,c}}\right)\right] - IR$$

Equation 2.24

2.2 Components of the PEM fuel cell

Brief Overview

The individual components of a single PEM fuel cell are illustrated below in Fig. 2.05:

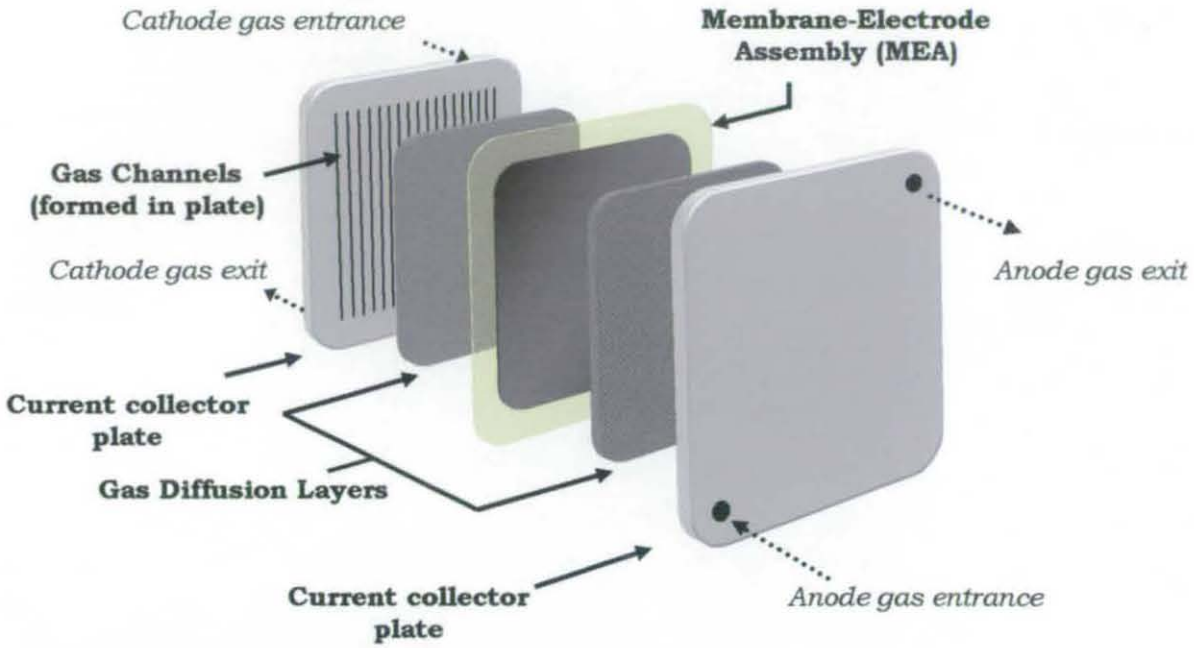

Fig 2.05: Exploded diagram of a single polymer electrolyte fuel cell

At the centre of the PEMFC is a membrane-electrode assembly, referred to as the MEA, comprising a proton conducting polymer electrolyte sheet with platinum-containing electrodes bonded to either side. Porous, carbon-based gas diffusion layers surround the MEA followed by gas flow/current collector plates. In a fuel cell stack where several single cells are positioned adjacently, a single plate supplies hydrogen and oxygen to two adjacent cells and is referred to as a 'bipolar plate'.

The role of each component in the PEM fuel cell arrangement is now discussed in detail.

2.2.1 Membrane electrode assembly

2.2.1.1 PFSA membrane

The proton conduction mechanism of the fuel cell operation is made possible by the chemical structure of the perfluorinated polymer membrane at the heart of the MEA - a PTFE (Teflon) base with 'side-chains' terminated by sulphonic acid groups HSO_3. The ionic bonding of these acid groups results in the presence of SO_3^- and H^+ ions which are mutually attractive thus forming side chain clusters within the material. The hydrophilic regions around the sulphonated side chains can lead to the absorption of large quantities of water, increasing the weight and volume of the membrane structure. Within these hydrated regions, the H^+ ions (protons) are relatively weakly attracted to the SO_3^- groups and are able to move. With sufficient structure hydration it is possible for the protons to move through the length of the structure and be transferred to another phase as long as another proton is substituted for the one leaving the polymer. This is the basis of the proton exchange mechanism and hence the operation of a PEM fuel cell, i.e. when protons are created by the oxidation of hydrogen at the anode there is a net ion exchange across the polymer, driven by the difference in chemical potential with the electrons moving round the external circuit to produce dc power.

As detailed in Chapter 1, a major advancement was made in PEMFC technology when fluorinated polymers were developed as the proton conducting membrane material. The most common fluorinated polymer used in PEM fuel cells is Nafion, manufactured by Dupont. The chemical structure of Nafion is as illustrated below

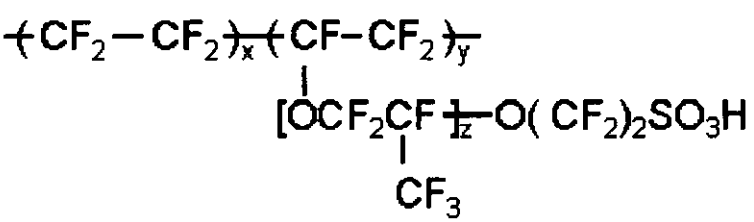

Fig 2.06: Chemical structure of Nafion® (x = 6-10, y = z = 1)

The high electro-negativity of fluorine means that the structure has a high ionic conductivity and the CF_2 groups prior to the acid group provide chemical stability. The Dow Chemical Company and Asahi Chemical Company also synthesise advanced perfluorosulphonic acid side chains and a higher ratio of sulphonic acid to CF_2 groups, Yoshida et al (1998), Wakizoe et al (1995).

However, all of these materials have thick polymer structures resulting in a high degree of ohmic resistance within the fuel cell. Attempting to produce thinner structures resulted in higher rates of gas crossover and poorer mechanical stability. These problems were

overcome by W.L Gore who produced composite membranes, where solubised Nafion is incorporated in a fine mesh Teflon support, Bahar et al (1999). To date, this type of membrane exhibits the best performance in PEM fuel cells although cheaper alternatives continue to be developed, Vargas et al (1999).

One of the major problems with all perfluorinated sulphonic acid membranes is their high cost, which is due to the expensive fluorination step in the manufacturing process. However, there is now a substantial ongoing effort to develop less expensive, alternative partially fluorinated or hydrocarbon based polymer materials with comparable stability and proton conduction to the PFSA structure.

2.2.1.2 Electrodes

On either side of the membrane, the half-cell reactions occur in the electrodes which are usually porous structures interspersed with a loading of catalyst. Despite the large degree of work into finding alternatives, Toda et al (1999), Ross et al (2000), platinum-based catalysts remain the optimum material for generating the anode and cathode half-reactions, Equations 2.01 and 2.02.

In the earliest examples of PEM fuel cell technology, the platinum loading on the electrodes was reported to be as high as 28 mg cm^{-2}, however following several technological advances the required loading can currently be as low as 0.2 mg cm^{-2}, varying between anode and cathode.

The reduction of oxygen on the catalyst represents a significantly more complex process than the oxidation of hydrogen due to:

- The strong O-O bond
- The formation of highly stable Pt-O or Pt-OH species
- The four electron transfer reaction
- The possible formation of a partially oxidised species (e.g H_2O_2 – hydrogen peroxide)

In a typical PEM fuel cell using pure platinum catalyst, at a current density of 1 Amp cm^{-2}, the combined overpotential losses of the anode are 20 mV and the cathode is around 400 mV, as illustrated in Fig. 2.07, Costamagna et al (2001).

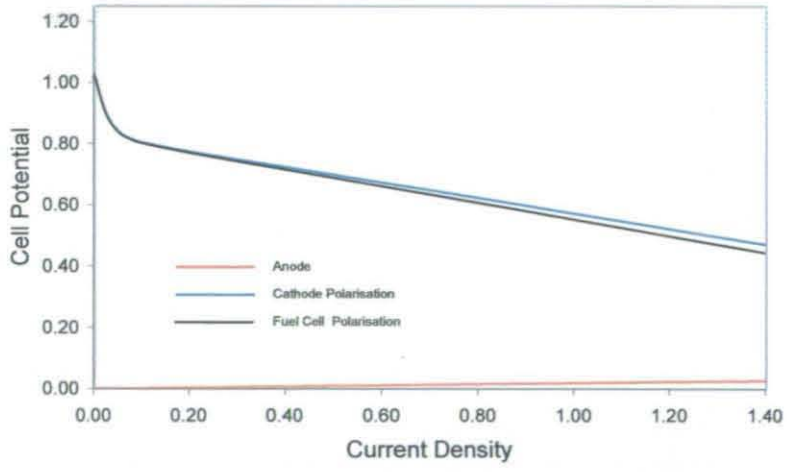

Fig 2.07: Half cell polarisation curves for PEM fuel cell

Hence, the oxidation of hydrogen does not present any limitation to PEM fuel cell performance if a pure source is used. However, in many fuel cell systems the hydrogen contains traces of impurities such as carbon monoxide, sulphur and ammonia as a result of a reforming process where hydrogen has been extracted from a hydrocarbon feedstock. All of these substances can poison the anode catalyst, i.e. the blocking of catalyst sites. Carbon monoxide in particular is the major poison in all low temperature fuel cells and will always be present in the feed from a hydrocarbon fuel reformer. The CO is preferentially adsorbed by the platinum – the strength of the Pt-CO bond being higher than the Pt-H bond.

Methods of reducing the CO content in the anode have included using a gas clean-up unit between the reformer and the fuel cell stack or mixing a small amount of air into the fuel feed which stimulates the oxidation of CO over the catalyst (Ralph et al, 1998). However, catalysts have been developed that are tolerant to CO content in the hydrogen supply – one of the best examples of this is a $Pt_{0.5}Ru_{0.5}$ composition (Ralph, 1997) (Acres et al 1997).

The major developments in reducing the required loadings of catalyst are discussed in the next section as it comes under the category of the method of manufacture for the membrane-electrode-assembly.

2.2.1.3 Gas diffuser materials

These are included in this section as with particular PEM fuel cell manufacturing methods, they form an integral part of the MEA arrangement.

The gas diffusion layers ensure an even distribution of the gaseous reactants to the catalyst sites as well as providing the electrical connection to the conducting bipolar plates. The fine porous structure of the gas diffusion layers allows the gas to spread out as it diffuses so that when the gas penetrates the layer, it will be in contact with the entire surface of the electrode. They are typically manufactured from carbon cloth or carbon paper, and can be made significantly hydrophobic by the incorporation of PTFE into their structure which prevents the accumulation of water, which would otherwise severely hinder the rate of gas diffusion to the electrodes.

2.2.1.4 MEA assembly method

Three phase boundary

For the successful operation of the PEM fuel cell, the PFSA membrane electrolyte, platinum catalyst and gaseous reactants must all be in contact, in addition to the provision of an electrical pathway to and from the external load circuit - this interface is referred to as the *three-phase boundary* or three-phase zone.

In fuel cells with liquid electrolytes such as alkaline (AFC) or phosphoric acid (PAFC), this is easily achieved as the electrolyte readily penetrates into the porous electrode structure, which enables almost complete utilisation of the catalyst – refer to diagram A in Fig. 2.08 (Scherer, 1997). However, the solid gas-impermeable nature of the polymer electrolyte means the three-phase boundary is a much more distinctly defined region in a PEM fuel cell – diagram B in Fig. 2.08.

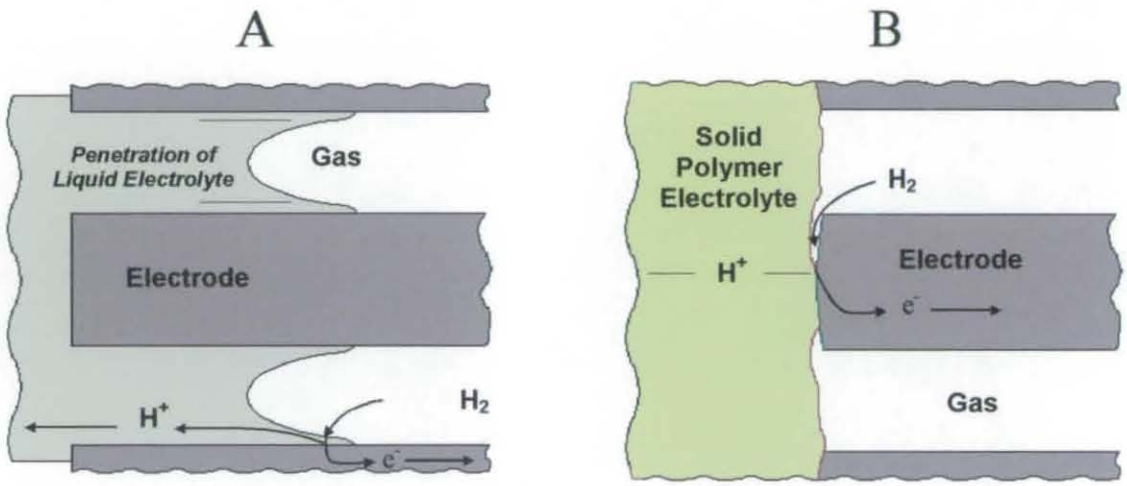

Fig 2.08: Illustration of the three-phase boundary for A – alkaline fuel cell B – PEM fuel cell

However, using a solid electrolyte means gases can adsorb directly onto the catalyst from the bulk gaseous phase as opposed to first having to dissolve into a liquid electrolyte.

Significant developments have been made since the beginning of the 1990's in developing membrane electrode assemblies for PEM fuel cells which exhibit a much more intimate form of the three phase zone – these are described in the next section.

MEA manufacturing routes

There are two primary routes for the manufacture of a solid polymer membrane electrode assembly. The first involves the application of the catalyst to layers of diffusion material to form gas diffusion electrodes which are then applied to the membrane by a hot-pressing process. The second involves the direct deposition of catalyst to the membrane to form an MEA arrangement, minus the gas diffusion layers which are introduced separately in the construction of the fuel cell. These developments have been made in conjunction with efforts to reduce platinum catalyst loadings and are now explained in further detail.

Three methods of developing membrane electrode assemblies, the former two utilising gas diffusion electrodes and the third utilises the direct application of catalyst to membrane, Kim et al, (1999) are shown in Fig. 2.09.

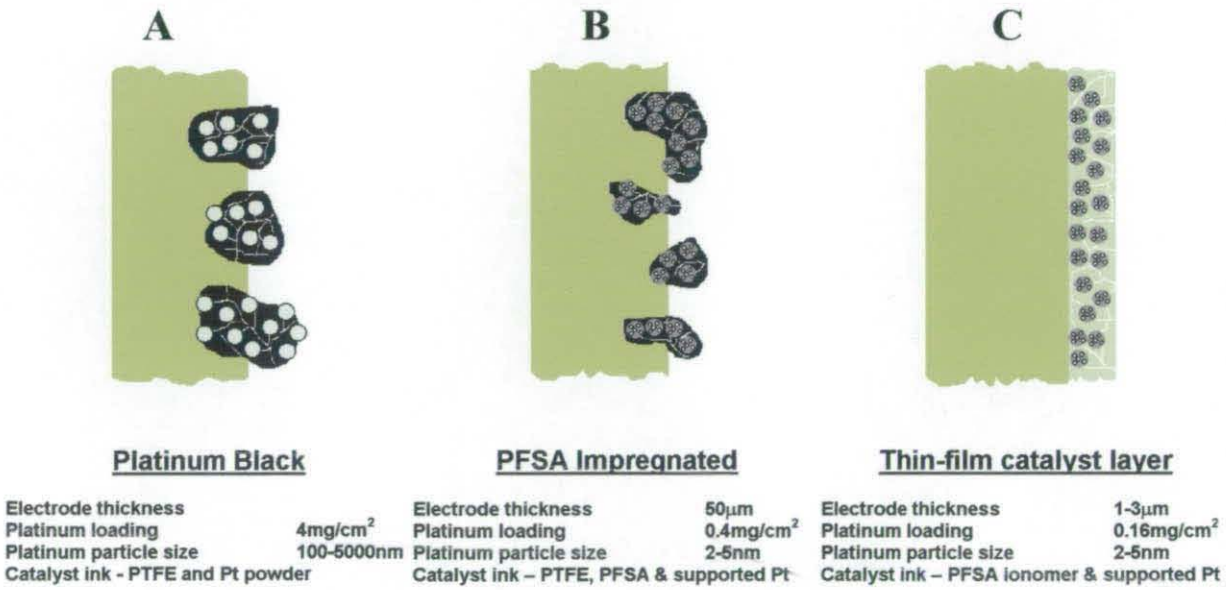

Fig. 2.09 : Development of low platinum loading MEA's

Early PEM fuel cells used the 'platinum black' electrode structure (A), comprising PTFE and platinum powder, 100-5000 nm particle size. The MEA was prepared by mixing the catalyst components to form a viscous ink which was then applied to gas diffusion layers to form gas diffusion electrodes and these were subsequently hot-pressed to the polymer membrane, Chun et al (1998). The major drawback with this structure was the poor utilisation of catalyst, with many platinum particles not in contact with the polymer membrane and hence unable to transfer protons into the electrolyte with others embedded into the membrane with no access to gaseous reactants. Additionally, the large nominal size of the platinum particles used resulted in a high loading requirement

(~4 mg/cm^2) in order to obtain a satisfactory fuel cell performance. However, in specialist applications where the economic factor is not the main concern, such as military and space applications, this electrode structure will still be acceptable.

The next generation of MEA (B) used small particles of platinum supported on large carbon particles are used to yield a large platinum surface area with a smaller platinum loading. Secondly, a solubised form of the PFSA electrolyte is included in the catalyst ink, where on manufacture of the gas diffusion electrodes the three-phase boundary is extended further into the third dimension, Passalacqua et al (1998).

Researchers at Los Alamos National Laboratory first demonstrated the construction of an MEA by applying PTFE free thin film catalyst layers to each side of a polymer membrane, Zawodzinski et al, (1995). The catalyst ink is either directly applied to the membrane surface by a process such as spraying, painting or rolling or initially cast onto PTFE blanks, which are then hot-pressed to the membrane and peeled away after cooling - transfer printing method. The thin film catalyst layer structure produces good fuel cell performance with a small platinum loading (0.12 – 0.16 mg/cm^2) by allowing a more intimate contact between catalyst and membrane - similar to the three-phase boundary in liquid electrolyte based fuel cells and hence higher platinum utilisation. In addition, various mass transfer resistances at the three-phase boundary are reduced due to the very thin electrode structure.

However, the thin-film structure has been shown to suffer from poor mechanical strength, resulting in steadily decaying fuel cell performance in long-term operation, Wilson et al (1995). The structural durability of the PFSA electrolyte in the thin-film catalyst layer can be improved by preparing the catalyst ink using an initial ion-exchanged form of the solubilised PFSA electrolyte, where the protons are substituted by other cations such as sodium (Na^+), Moore et al (1986), or tetrabutylammonium (TBA^+), Moore et al (1992).

2.2.2 Bipolar plates

The flow plates house the gas channels that distribute hydrogen and oxygen to the fuel cell electrodes and complete the electrical circuit of a single fuel cell. The electrons produced from the oxidation of hydrogen are conducted through the catalyst and diffusion layers of the anode to the raised area of the plate. They then pass through the plate to the external circuit where useful electrical work is done before re-entering the fuel cell via the cathode plate, completing the electrochemical reaction.

In a fuel cell stack, these plates are referred to as 'bipolar' plates as they have gas channels on both sides so that one plate supplies hydrogen and oxygen to two adjacent cells. The particular arrangement of gas transport channels in the plate is known as the 'flow-field'. The width and depth of the channels as well as the flow-field geometry has a significant influence on the distribution of the reactant gases across the active electrode area of the MEA.

The bipolar plate must satisfy several requirements:

- Impermeability to gaseous reactants
- Chemical stability in oxidising and reducing environments
- High electrical conductivity
- Adequate strength
- Low cost and light weight.

Many different materials have been used for bipolar plates, including:

- Machining of graphite sheet
- Injection or compression moulding of graphite filled polymer resins
- Machining or chemical etching of metal plates such as stainless steel

Graphite exhibits excellent electrical conductivity properties but is brittle and thus requires thick structures. Metals exhibit excellent strength; conductivity and machining ability however have high density and are prone to corrosion, Makkus et al, (2000). Future mass production bipolar plates are likely to utilise a moulding process of polymer doped with a conducting phase.

2.2.3 Seals, manifolding and compression

For safe operation of the PEM fuel cell the hydrogen and oxidant supplies must be completely separated from each other – due to the potential hazard of an explosive gas mixture in the presence of a catalyst. This is achieved by using a gasket, usually made from a grade of silicone based rubber to surround the non-active regions of the anode and cathode of the fuel cell. The size of the non active region is defined by a ratio of the electrode area utilisation, i.e. active electrode area / total fuel cell area, which is typically 80% in modern PEM fuel cells.

The effectiveness of the sealing gasket depends on the clamping pressure exerted to the fuel cell by bolts or tie bars which are usually incorporated through the peripheral non-active areas of the fuel cells. The clamping, or compaction, pressure serves to reduce the contact resistance between individual fuel cell components.

2.3 PEM fuel cell systems and applications

2.3.1 Overview

The proposed applications for PEM fuel cell systems at the time of writing are split between three main target markets:

- Stationary applications
- Automotive applications
- Portable Applications

2.3.2 Stationary

In the present age of nuclear and coal power station decommissioning there is genuine worry about the capacity for meeting future consumer and industry power consumption, with electricity demand set to increase 45% in the UK by the year 2020. This view is also reflected in other highly developed industrialised nations such as the United States, where in 2003 there were several high-profile consumer power shortages.

Some examples of SOFC and MCFC stationary systems were detailed in Chapter 1, however PEM fuel cell systems have also been proposed for small off-grid, distributed CHP applications, to supply single or multiple households with electricity. The heat generated by the fuel cell system can be recovered as hot water. The advantages of such a fuel cell application are the avoidance of mains power losses and the fluctuating market price of electricity, in addition to the option to sell excess power to the national grid.

The demands on the fuel cell stack are lowest with stationary power applications, with the volumetric and gravimetric system densities not as crucial as operating efficiency and reliability. Examples of small PEMFC power generation units include the 4 kW Avanti system by Nuvera, the 5 kW GenSys system by Plug Power and the 1 kW Ebara system by Ballard Power Generation Systems.

2.3.3 Automotive

According to a study, Chalk et al (2000), the transportation sector comprises 28% of worldwide energy consumption, with the number of vehicles on the road continuing to rise rapidly, particularly in Asian markets. This economy is almost completely reliant on dwindling oil reserves and there is also increasing concern regarding poor air quality and hazards to human health, particularly in metropolitan areas, as a result of the compounds from vehicle exhausts. To address the latter issue, a number of initiatives have been set-up by governing bodies attempting to force vehicle manufacturers to conform to tight emission standards, the most notable examples being the Euro standards by the EU and the regulations in the US state of California. However, it is the increasing realisation of finite oil stocks that have been the main driving factor in the development of PEM fuel cell vehicles.

This application has the most stringent requirements for the fuel cell stack volumetric and gravimetric power densities. In addition, the calculated cost figure projected by the US government required to make automotive PEM fuel cells competitive with the internal combustion engine is 50 US$/kW, (Appleby, 1999). The automotive application also produces the largest challenge in terms of hydrogen storage and supply; see section 2.3.5.

Several prototype fuel cell vehicles have been demonstrated in the last five years with the most notable being the NECAR series from DaimlerChrysler, using fuel cell technology from Ballard. In 2003, many of the world's major car manufacturers began field trials of fuel cell vehicles in small fleets, whereas previous to this, demonstrations were confined to in-house testing under controlled conditions. At the time of writing, the largest of these are being undertaken by DaimlerChrysler and Ford; both testing around 60 vehicles each in a variety of locations including Germany, Japan, Singapore, Canada and the US, Cropper et al (2004).

2.3.4 Portable

Advanced power sources are required to power the present, and particularly, the next generation of multifunctional hand-held electronic devices, due to the clear operational lifetime limitations of secondary Lithium-ion battery technology. PEMFC technology has been proposed for these applications however presently the DMFC is more suited to these applications due to the issue of hydrogen storage. One exception is Casio, Japan who have been involved in the development of PEM fuel cells to power notebook computers and PDA's (Personal Digital Assistants), with commercialisation scheduled for 2004

Commercially available PEM portable systems are currently more common in the 10-1000 W range. Ball Aerospace has developed small 50 W and 100 W systems which are fuelled by high pressure storage of hydrogen. Ballard Power Systems are currently marketing their 1.2 kW Nexa Power Module, Cropper (2002).

2.3.5 Developments in hydrogen fuel storage

For all proposed PEM fuel cell applications, with the possible exception of stationary applications, a major issue will the storage of hydrogen for the fuel cell stack. The hydrogen can be stored in a pure form or extracted from a hydrocarbon fuel although the latter introduces significantly complexity to the FC system – these methods are discussed now.

There are three principle pure source storage technologies available:

- High pressure storage
- Cryogenic storage
- Hydride storage.

The storage of hydrogen in metallic pressure vessels results in low gravimetric efficiency, however, higher pressure (34 MPa) light-weight polycarbonate tanks are becoming available. Here, a thin plastic or metallic liner guarantees the leak rate, reinforced by a shell consisting of a high performance fibre material embedded in a matrix material. This method has the drawbacks of difficult market acceptance, safety, and a low energy storage density of 31 g/L at 34 MPa

.Liquefied hydrogen has a higher storage density of 71 g/L and has been the storage and delivery method of choice for large industrial-scale quantities. The conditions necessary to store liquid hydrogen are fairly severe requiring a temperature of 20°K at 200kPa. In order to maintain these conditions, liquid hydrogen is typically stored in a bulky double walled super-insulated storage vessel leading to low volumetric energy densities. In addition, the liquefaction process is highly energy intensive (30-40% of stored energy value), handling of a cryogenic fluid raises consumer health issues and fuel evaporation rates can be as high as 2% per day.

There are two main categories of hydride storage; *metal hydride storage* which is the storage of H-atoms within certain metals, that will reversibly hydride and dehydride by the simple gas-solid chemical reaction and *chemical hydride storage* where previously synthesised compounds can be destructively reacted with water to liberate hydrogen gas.

Although the conversion to a "hydrogen economy" is now nearly universally accepted, the process will be extremely costly and will take decades to complete. The issues surrounding the development route to a hydrogen infrastructure are complex and well

beyond the scope of this thesis. The short term solution for supplying hydrogen for fuel cell systems is the use of a hydrocarbon fuel processing system, Hart et al (2000), Ogden et al (1999). Perhaps the largest challenge is the integration of these small reforming systems into fuel cell vehicles where the two main processes that have been proposed is steam reforming of methanol or partial oxidation of petrol. The latter process requires much more stringent gas-clean up steps to avoid poisoning the fuel cell with impurities such as sulphur compounds, nitrous oxides and carbon monoxide.

2.4 References

Acres, G.J.K.; Frost, J.C.; Hards, G.A.; Potter, R.J.; Ralph, T.R.; Thompsett, D.; Burstein, G.T.; Hutchings, G.J., "**Electrocatalysts for fuel cells**", Catalysis Today, Vol. 38, pp393-400, 1997

Appleby, J.A., "**The Electrochemical Engine for Vehicles**", Scientific American, pp58-63, July 1999

Bahar, B.; Cavalca, C.; Cleghorn, S.; Kolde, J.; Lane, D.; Murthy, M.; Rusch, G. "**Effective selection and use of advanced membrane electrode power assemblies**", Journal of new Materials for Electrochemical Systems 2, pp179-182, 1999

Chalk, S.G., Miller, J.F., Wagner, F.W., "**Challenges for fuel cells in transport applications**", Journal of Power Sources, Vol. 86, pp40-51, 2000

Chun Y.; Kim, C.; Peck, D.; Shin, D., "**Performance of a polymer electrolyte membrane fuel cell with thin film catalyst electrodes**", Journal of power Sources, Vol. 71, pp 174-178, 1998

Costamagna, P.; Srinivasan, S., "**Quantum jumps in the PEMFC science and technology from the 1960's to the year 2000 – Part 1 Fundamental scientific aspects**", Journal of Power Sources, 102, pp242-252, 2001

Cropper, M., "**Fuel Cell Market survey: Portable Applications**", Fuel Cell Today Website, 18th September, 2002

Cropper, M.; Jollie, D., "**Fuel Cell Vehicles: The First Fleet Trials**", Fuel Cell Today Website, 9th February, 2004

Dicks, A.; Larmanie, J.E., "**Fuel Cell Systems Explained**" , John Wiley and Sons, Chichester, England, 2000

Fuel Cell Handbook, Fifth Edition, EG & G Services Parsons, Inc. Science Applications International Corporation, US Department of Energy, Office of Fossil Energy, West Virginia, October 2000

Hart, D.M.; Leach, M.A.; Fouquet, R.; Pearson, P.J.; Bauen, A; "**Methanol Infrastructure – will it affect the introduction of SPFC vehicles**", Journal of Power Sources, Vol. 86, pp542-547, 2000

Kim, K.J.; Shahinpoor, M.; Razani, A., "**Electro-active polymer materials for solid polymer fuel cells**", Proceedings from the SPIE conference on Electroactive Polymer Actuators and Devices, SPIE Vol. 3669, March 1999

Makkus, R.C.; Janssen, A.H.H.; de Bruijn, F.A.; Mallant, R.K.A.M.; "**Use of stainless steel for cost competitive bipolar plates in the SPFC**", Journal of Power Sources, Vol. 86, pp274-282, 2000

Marianowski, L.G.; Ho, D.L.; Blair, L.; Podolski, W.; "**Development of a $10/kW Bipolar separator plate**", FY 2000, Progress Report for Fuel Cell Power Systems, US Department of Energy, pp119-122

Moore, R.B.; Martin, C.R.," **Procedure for preparing solution-cast perfluorosulfonate ionomer films and membranes**", Analytical Chemistry, Vol 58 (12), pp2569-2570, 1986

Moore, R.B.; Cable, K.M.; Croley J. , "**Barriers to flow in semicrystalline ionomers – A procedure for preparing melt-processed perfluorosulfonate ionomer films and membranes**", Journal of Membrane Science, Vol. 75 (1-2), pp 7-14, 1992

Ogden, J.M.; Steinbugler, M.M.; Kreutz, T.G., "**A comparison of hydrogen, methanol and gasoline for fuel cell vehicles: implications for vehicle design and infrastructure development**", Journal of Power Sources, Vol. 79, pp143-168, 1999

Passalacqua, E.; Lufrano, F.; Squadrito, G.; Patti, A.; Giorgi, L. "**Influence of the structure in low-Pt loading electrodes for polymer electrolyte fuel cells**", Electrochimica Acta, Vol.43, No. 24, pp3665-3673, 1998

Ralph, T.M.; Hards, G.A., "**Fuel Cells: clean energy production for the new millennium**", Chemistry & Industry, pp334-342, 4th May, 1998

Ralph, T.R., "**Proton Exchange Membrane Fuel Cells: Progress in Cost Reduction of the key components**", Platinum metals review, Vol. 41(3), 102-113, 1997

Ross, P.N.; Markovic, N.M.; Schmidti, T.J.; Stamenkovic, V. "**New Electrocatalysts for Fuel Cells**", FY 2000, Progress Report for Fuel Cell Power Systems, US Department of Energy, pp115-118

Scherer, G.G., "**Interfacial aspects in the development of polymer electrolyte fuel cells**", Solid State Ionics 94, pp249-257, 1997

Toda, T.; Igarashi, H.; Watanabe, M., "**Enhancement of the electrocatalytic O_2 reduction on Pt-Fe alloys**", Journal of Electroanalystical Chemistry, 460, pp 258-262, 1999

Vargas, M.A.; Vargas, R.A.; Mellander, B-E. "**New proton conducting membranes based on PVAL/H_3PO_2/H_2O**", Electrochimica Acta, Vol. 44, pp 4227-4232, 1999

Wakizoe, M.; Velev, O.A.; Srinivasen, S. "**Analysis of proton exchange membrane fuel cell performance with alternative membranes** ", Electrochimica Acta, Vol. 40 (3), pp335-344, 1995

Wilson, M.S.; Valerio, J.A.; Gottesfeld, S., "**Low Platinum Loading Electrodes for polymer electrolyte fuel cells fabricated using thermoplastic ionomers**", Electrochimica Acta, Vol. 40, No 3, pp 355-363, 1995

Yoshida, N.; Ishisaki, T.; Watakabe A.; Yoshitake M. "**Characterisation of Flemion membranes for PEMFC**", Electrochimica Acta, Vol. 43 (24), pp3749-3754, 1998

Zawodzinski, C; Wilson, M.H.; Gottesfeld, S., "**PEM Fuel Cell Stack Development based on Membrane Electrode Assemblies of Ultra-Low Platinum Loadings**", Proceedings of the First International symposium on proton conducting membrane fuel cells, Electrochemical Society Proceedings Volume 95-23, 1995

Chapter 3

Primary analysis of cathode evaporative cooling for a PEM fuel cell

3.1 Chapter Overview

To obtain a steady and continuous supply of power from a PEM fuel cell stack over a full range of electrical load demands, adequate thermal control and water management are critical considerations.

In this Chapter the disadvantages of conventional fuel cell stack humidification and temperature control subsystems are discussed. A novel method of combining humidification and cooling is introduced, involving the direct injection of liquid water to the cathode flow-field which has the potential to eliminate these penalties. This technique is integrated into a single PEM fuel cell test assembly and the following experimental analyses performed.

- The effects of operating conditions on fuel cell performance with humidified air supply - presented in the form of 'polarisation plots'
- A study of how the polymer membrane water content is affected by operating conditions with no source of external humidification
- A performance comparison of direct cathode water injection and the pre-saturation of air as humidification methods

An analysis of direct cathode water injection, functioning as both fuel cell humidification and cooling, is outlined separately in Chapter 4.

3.1.1 Fuel cell humidification

3.1.1.1 Introduction

As electrical current is drawn from a PEM fuel cell, a level of water is produced on the catalyst sites of the cathode as a result of the electrochemical reduction of oxygen – refer to Equation 2.02. Ideally, this should keep the PFSA membrane structure sufficiently hydrated for any fuel cell operating conditions and/or duration, as shown in Fig. 3.01.

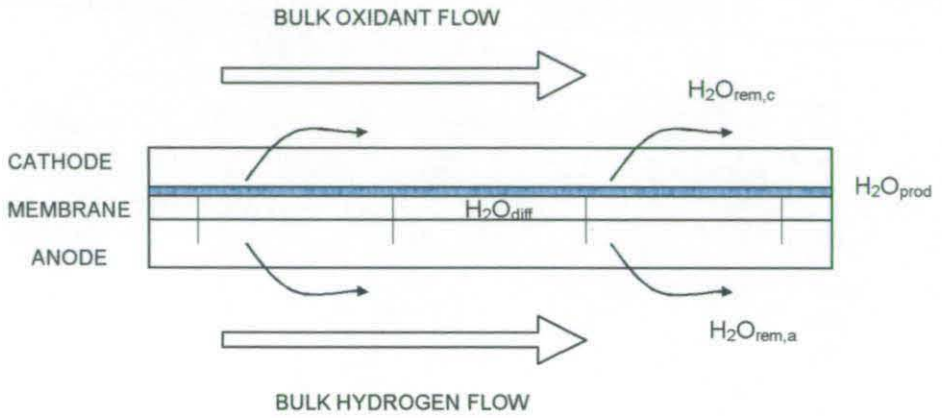

Fig 3.01 – Simplified illustration of water distribution in a cell

Here, the product water is represented by the expression H_2O_{prod} and the proportion of water diffusing from cathode to anode, keeping the entire thickness of the membrane structure hydrated, is represented by the expression H_2O_{diff}. Hydrogen and air passing through and/or over the anode and cathode removes a proportion of excess water, $H_2O_{rem,a}$ and $H_2O_{rem,c}$ respectively, by evaporation, preventing accumulation. This water balance is expressed as:

$$H_2O_{prod} = H_2O_{rem,a} + H_2O_{rem,c} \qquad \textbf{Equation 3.01}$$

Unfortunately, this scenario is almost impossible to achieve for the majority of PEM fuel cell operating conditions. Maintaining a fully humidified membrane while feeding dry reactant gases requires low-temperature operation and/or a counterflow gas configuration – see section 3.1.1.4. This is due to reactant gases evaporating associated water from the membrane structure, as they flow across flow-field channels and through the porous diffuser material, at a faster rate than product water can be generated at the cathode. This water imbalance can be expressed as:

$$H_2O_{prod} < H_2O_{rem,an} + H_2O_{rem,cat} \qquad \textbf{Equation 3.02}$$

If dehydration of the PFSA membrane structure occurs, the performance of the fuel cell deteriorates due to a large increase in ionic resistance as the rate of proton conduction is

a direct function of membrane water content. If allowed to become too dry, the membrane is susceptible to crossover of gaseous hydrogen and oxygen which, as well as further lowering fuel cell efficiency, can result in the formation of hotspots and subsequent irreversible damage to the polymer structure.

Hence, for the duration of fuel cell operation it is critical to ensure the membrane retains sufficient water content. In order to achieve this, the two main factors that have to be considered are:

1. The rate of water evaporation caused by the reactant gases
2. Water transport within the cell membrane structure.

These are discussed in further detail in the following sections.

3.1.1.2 Evaporation effect of reactant gases

The rate of water evaporation from any point on a PEM fuel cell membrane surface is dependant on the moisture content of the gas flowing adjacent. The expression, *relative humidity* - ϕ, describes the water content of a gas and is defined as[1]:

$$\text{Relative humidity, } \phi = \frac{P_{H_2O}}{P_{sat}} \qquad \textbf{Equation 3.03}$$

The ϕ value of a gas flow has an *inversely proportional relationship to the rate it will remove water from a fuel cell membrane by evaporation*. For a gas with a ϕ value of 100% RH, the partial pressure of entrained water vapour is equal to the saturation pressure; thus no more water can be evaporated, and the gas is defined as *fully saturated*.

The rapid rate of water evaporation from a PFSA membrane that is experienced when dry reactant gases are fed to the fuel cell is due to the non-linear nature of the relationship between temperature and saturation pressure of water. A graph with selected P_{sat} points and an approximation equation as a function of temperature between 0°C and 100°C is shown in Fig.3.02, Rogers and Mayhew (1988):

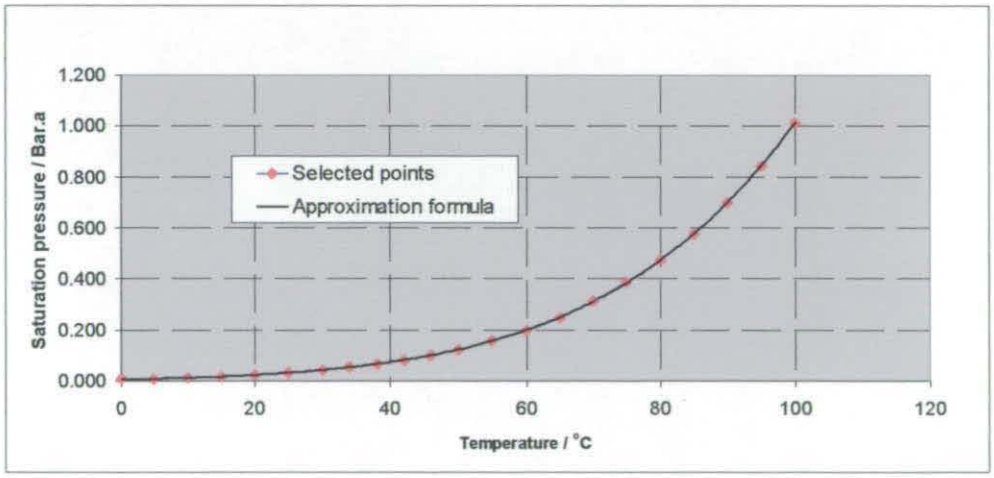

P_{sat} = 2.692723E-11T^5 + 2.947761E-09T^4 + 2.504888E-07T^3 + 1.489752E-05T^2 + 4.364382E-04T + 6.122185E-03 (T is expressed in degrees K) **Equation 3.04**

Fig 3.02 – Water saturation pressure graph and formula

[1] Where P_{H_2O} is the partial pressure of water vapour and P_{sat} is the saturation pressure for the water at the specific temperature, ϕ is expressed as %RH

Hence feed air, at ambient temperature and a high value of ϕ, is heated on passing through the fuel cell thus obtaining a much lower ϕ value. The dehydration effect of dry reactant gases is compounded by the fact that they are usually delivered to the fuel cell at a higher 'stoichiometric' rate than the value calculated to be required, refer to definition of stoichiometry - Appendix A1. This is particularly the case when using air as the oxidant due to the 'blanketing' effect of inert nitrogen on the diffusion of oxygen to catalyst sites, therefore necessitating increased supply rates to reduce mass transport overpotential, see section 2.2.1. A point of note is that small fuel cells may be able to utilise dry reactant gases and produce reasonable performance if they are not significantly heated on passing through the cells, i.e. less than 50°C at the exhaust.

3.1.1.3 Water transport

Maintaining a sufficient water content, or hydration state, in a PFSA membrane will promote a steady performance from the fuel cell and increase the operational lifetime. This can be referred to as attempting to achieve a zero *net water drag*, $N_{H_2O}^{net}$. This expression is defined as the product of different water movements across the membrane occurring during fuel cell operation, as illustrated in Fig 3.03.

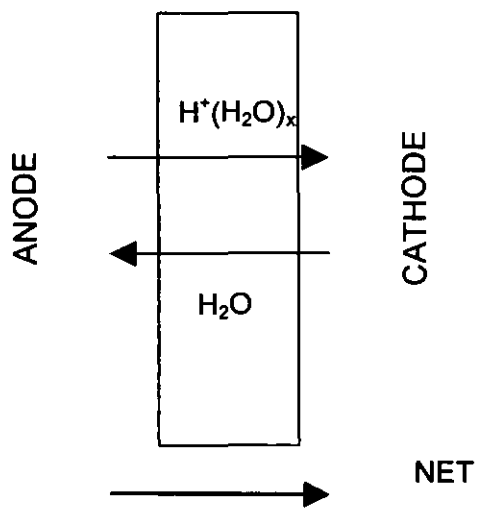

Fig. 3.03 – Simplified illustration of water transport in a cell

Protons migrating from anode to cathode force water molecules with them - this mechanism is referred to as *electro-osmotic drag*. This flux can be described as the chemical species $H^+(H2O)_x$, where x represents the mean number of water molecules transported with each proton - also known as the *electro-osmotic drag coefficient*. The degree of water transport via electro-osmotic drag is proportional to current density.

The electro-osmotic drag in addition to the electrochemical production of water produces an accumulation of water at the membrane/cathode interface. Consequently, water will diffuse back through the membrane to the anode, driven by the concentration difference. This water flux from cathode to anode is referred to as *back-diffusion* $N_{H_2O}^{diff}$ and compensates, to a certain extent, for the electro-osmotic drag. A major influence on the degree of back-diffusion observed is the membrane thickness, with a thin structure allowing a much a larger degree of water transport.

Therefore, the expression net water drag, or sometimes *net* electro-osmotic drag, accounts for both the electro-osmotic drag and back-diffusion mechanisms - this is expressed by Weisbrod et al (1995) as[2]:

$$N_{H_2O}^{net} = N_{H_2O}^{diff} + \frac{I \cdot n_{H_2O}}{F} \qquad \textbf{Equation 3.05}$$

However, in practice achieving a zero net water drag, particularly for a full range of fuel cell operating conditions and associated gas flows, is very difficult. At a low current density, the lower level of generated product water may not compensate for the water evaporated by reactant gas flows. At high current densities, the electro-osmotic drag of water associated with the high proton transport may dry out the anode side of the membrane or the cathode may flood. In addition, dynamic operation of a fuel cell, with constantly changing power demands, means achieving fixed water content in the membrane is even more challenging.

There are several studies in the literature detailing both in-situ and ex-situ measurements on the prediction of values for net electro-osmotic drag coefficient, Fuller et al (1992), Zawodzinski et al (1995), Zawodzinski et al (1993), Janssen et al (2001). Some of these were carried out by operating the fuel cell, condensing the exhaust gases and calculating the water content of both anode and cathode. Most of these studies have been based on Nafion PFSA membranes, which have typical thicknesses of 50 micron - 175 micron.

[2] Where I is total current density through the cell, F is the faraday constant and n_{H_2O} represents the electro-osmotic drag coefficient

3.1.1.4 Dry Operation

In small, low-temperature FC stacks, a slight reduction in electrochemical performance as a result of operating with dry reactant gases i.e. lower membrane water content, may be more desirable than the increased cost and complexity of introducing a humidification process. However, the key to running 'dry' in medium-large stacks is to achieve an even water balance over the entire membrane area. Buchi et al (1997), Dicks et al (2000) and Wynne et al (2001) described a method of doing this by using a counterflow arrangement of gases and maintaining precise stoichiometric flow rates of reactants – refer to Fig. 3.04.

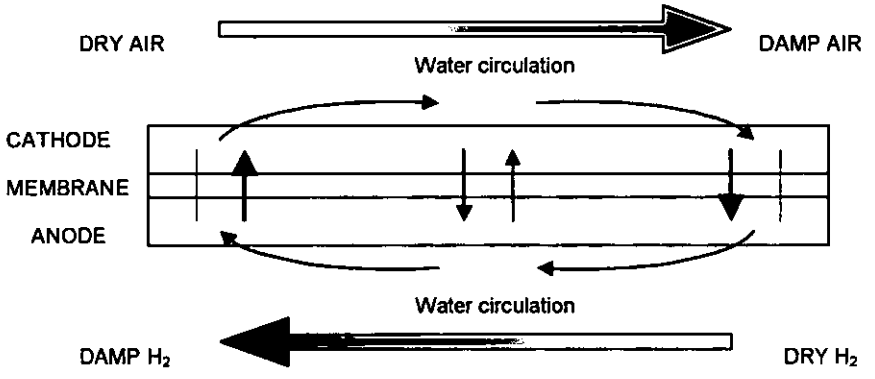

Fig 3.04 – Circulation of product water by counterflow gas configuration

Here, assuming an even distribution of current over the electrode area, the net electro-osmotic drag would be equivalent at all points in the fuel cell but the rate of back diffusion varies as water is circulated between the gases due to differing concentration gradients. Using this technique, Buchi et al (1995 and 1997) detailed a fuel cell performance, i.e. potential, some 20 - 40 percent lower than when an external humidification source was used. There will also be practical issues with such an arrangement, particularly the restrictions in flow field design in order to maintain a pure gas counterflow configuration.

The work by Buchi has shown that, for medium-large fuel cells, an additional supply of water is needed to keep the membrane structure adequately hydrated and thus allow the cell to operate most effectively - this is discussed in the next section.

3.1.1.5 Methods of external humidification for a fuel cell

Providing an additional supply of water to a fuel cell increases the risk of *electrode flooding*, when the rate of diffusion of gaseous reactants to catalyst sites is significantly retarded due to the presence of a surrounding liquid water film, thus lowering performance. Therefore, the level of water introduced has to be carefully controlled and is usually delivered in specific proportions, relative to reactant gas flow rates. Flooding of the anode does not usually present any significant detriment to fuel cell performance due to the high permeation rate of hydrogen gas, hence the problem is typically confined to the cathode.

The most common method of supplying additional water to a fuel cell is the pre-saturation of one or both reactant gases, typically at an elevated temperature. The basic premise being to induce a high ϕ value to the gases so that, on passing through the electrode, they are unable to remove significant quantities of water from the membrane by evaporation.

For small-scale laboratory fuel cell tests, gas saturation can be achieved simply by bubbling the hydrogen and air/oxygen through sparger bottles containing heated water, Rajalakshmi et al (2002). In medium to large scale fuel cell stacks, i.e. greater than 1 kW power output, the large flowrates needed would require impractical large columns of water to allow sufficient contact time for complete humidification. Therefore gas saturation is achieved using integrated *humidification sub-systems* which consist of areas, electrically isolated from the rest of the stack, where water and reactant gases flow on either side of a water-permeable membrane, refer to Fig 3.05. The diffusion of water through this membrane humidifies the gas, which then passes to electrochemically active fuel cells in the stack, Sdridhar et al (2001).

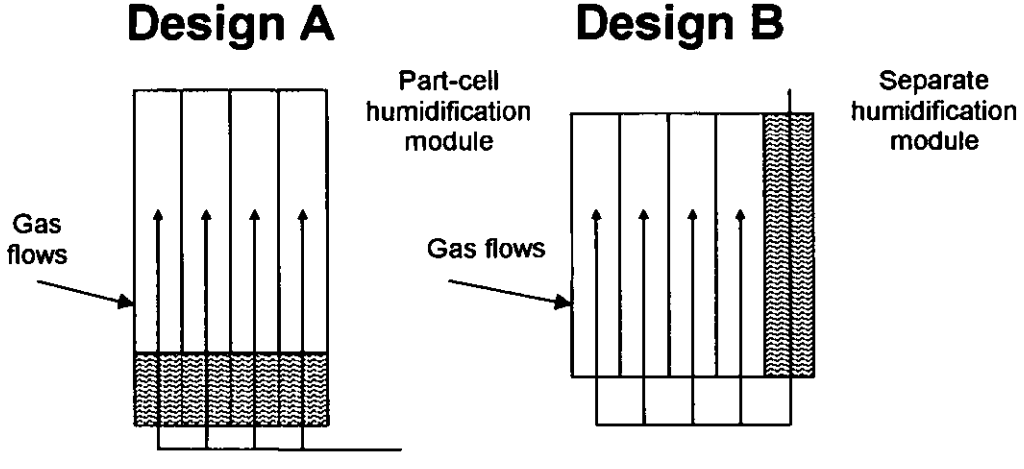

Fig 3.05 – Part/full cell humidification modules

The humidification areas can be designed as a designated section of each cell, utilising membranes with 'partial electrodes' (design A) but, more commonly, as a group of full-size cells grouped together, to form a 'humidification module' at one end of the stack (design B).

Delivering humidification water via reactant gases irreversibly links the two supplies, resulting in difficulty if attempting to change the supply of one without adversely affecting the other. For example, attempting to increase gas flow to reduce cathode flooding will result in even more water entering the stack. However, by far the biggest disadvantage of a humidification sub-system is the significant reduction in volumetric and gravimetric fuel cell stack power densities.

In the literature, there are examples of alternative fuel cell humidification techniques which do not introduce these penalties to the stack. These fall into one of two categories:

- Directly supplying water to individual cells, thereby de-coupling the water and gas supplies
- Making modifications to fuel cell components that attempt to promote a more even balance of water across cells.

Methods of the former include:

- Susai et al (2001) who detailed a method for the direct introduction of liquid water to flow-field channels. Wood et al (1998) carried out a study of direct liquid water injection using a cell equipped with the interdigitated flow field – see Chapter 6. The work detailed by Wilson et al (2000) utilises a hydrophilic polyester thread sown into the anode gas diffuser material of each cell to wick water across the entire electrode area. A patent filed by Carlstrom et al (2000) details a feature in the flow field plate to add/remove liquid water droplets to the gas tracks where necessary.

Methods of the latter are more numerous and include:

- Porous flow-field plates as detailed by Staschewski et al (1999) and extensively used by UTC fuel cells, Beal et al (1993), Bett at al (1998), Wheeler et al (2001), Reiser et al (1988), Kunz (1989). During operation these plates become saturated with liquid water collected from the electrochemical reaction and cross-cell diffusion of gaseous hydrogen and oxygen. This technique allows the diffusion of water from a cathode to adjacent anode of a neighbouring cell in the stack

effectively meaning that the risks of anode dehydration and/or cathode flooding are reduced.

- Other techniques use a pre-treated polymer membrane structure in the manufacture of the MEA to promote higher water content during operation. An example of this is the work of Watanabe et al (1996 and 1998) who detailed the use of embedded platinum and metal oxide particles which encouraged the formation of water from crossover oxygen and hydrogen. Watanabe et al (1993), Gonzalez-Martin et al (2000) and Cisar et al (1995) developed fuel cell membranes with micro-tubing embedded in the polymer structure to assist the back diffusion of water. In the former case, a liquid water supply was introduced to the membrane from a humidification area peripheral to the electrode.

The latter techniques would introduce excesses of cost, complexity and time to the membrane manufacture that would be impractical to scale up to high-volume processes.

3.1.2 Fuel cell cooling

3.1.2.1 Introduction

Temperature monitoring and control of a PEM fuel cell stack is always required as the irreversible operational inefficiencies result in the generation of waste heat, proportionally increasing with the level of power generated. Additionally, the need for a presence of liquid water in the cell membrane structure dictates that the operating temperature is limited to 90 - 100°C. Inadequate cooling combined with a high power output inevitably results in cell overheating and membrane dehydration.

The total energy generated by the hydrogen oxidation reaction (Equation 2.03) in the PEM fuel cell is calculated from the change in *enthalpy of formation* of products and reactants, symbolised by ΔH .

$$H_2 + \frac{1}{2}O_2 \rightarrow H_2O \qquad \textbf{Equation 2.03}$$

$\Delta H_{(LHV)}$ = -241.83 kJ/mole H_2

$\Delta H_{(HHV)}$ = -285.84 kJ/mole H_2

The subscripts represent *lower heating value* and *higher heating value,* with the former based on the assumption that all product water is in the vapour state and the latter assuming all product water is in the liquid state - the difference between the two representing the latent heat for water.

A formula for calculating the rate of heat generated by a fuel cell and thus the required cooling is[3]:

$$\overline{Q}_{fc} = \dot{n}_{H_2} \cdot \Delta H - I \cdot V \qquad \textbf{Equation 3.06}$$

For small fuel cell stacks with an 'open' cathode configuration a single fan can be used to supply air as the oxidant for the electrochemical reaction, with such a high stoichiometry that enough heat transfer occurs to keep the stack cool - with further cooling occurring by natural convection and radiation around the end plates and sides of the stack. For closed cathode stacks with a few active cells natural ambient cooling may be sufficient, however, as the stack power and size increases, the level of heat able to be removed from external surfaces decreases and temperature control has to be accomplished using

[3] Where $\overline{Q}_{fc}$ is the rate of heat generated by the fuel cell, n_{H2O} is the molar rate of hydrogen being utilised and I and V are the fuel cell current and voltage.

a separate cooling medium. Heat transfer with such a cooling medium occurs in specific areas, either incorporated as a part of each bipolar plate or more commonly, a number of full-size *cooling plates* equidistantly spaced in the stack and positioned between two single-sided, or uni-polar, flow plates.

De-ionised water is more likely to be employed as the cooling medium than air due to its larger specific volumetric heat capacity, allowing lower flow rates for adequate temperature control. Hence there will also be lower associated parasitics and smaller cross sectional area of cooling channels allowing higher stack packing density. In addition, ex-situ recovery and distribution of stack waste heat is much easier with a water coolant, making systems design more flexible.

There are, however, issues which arise from the integration of cooling plates into a FC stack.

- There is an increase in overall stack weight and volume.
- The performance of any individual cell is affected by its proximity to a cooling plate.
- The cooling medium is usually cooled by another coolant in a two-stage arrangement that necessitates the use of a multitude of extra devices such as pumps and heat exchangers. This makes the fuel cell system arrangement more complex and expensive and further lowers system power densities.

3.1.2.2 Evaporative cooling concept

During fuel cell operation the evaporation of water, either from the electrochemical reaction or a liquid humidification source, into the reactant gas flows will occur, as described in 3.1.1.2. On this change of state from liquid to vapour, a proportional amount of thermal energy, equivalent to the proportional amount of latent heat, is 'absorbed' by the gas and effectively removed as the gas flow leaves the fuel cell - this cooling mechanism is referred to as *evaporative cooling.*

The degree of evaporative cooling possible during fuel cell operation is dictated by the interrelationship between the saturation pressure of water and its partial pressure in a gas flow, illustrated as[4]:

$$x_{H_2O} \cdot P_{tot} = P_{H_2O} \qquad \textbf{Equation 3.07}$$

Referring back to Equation 3.03 which states that when the value of ϕ is 100%, the gas is saturated and no more water can be evaporated, hence no more thermal energy can be absorbed[5].

To increase the degree of heat removal from a fuel cell using the evaporative cooling method there must be one of the following changes in the characteristic operation:

- An increase in saturation pressure by increasing operating temperature, or
- A lowering of water partial pressure either by an increase in stoichiometric gas flow, or lowering of total system pressure.

Any of these must be in conjunction with a sufficient presence of liquid water to obtain 100% RH to obtain the maximum increase in heat removal.

---

[4] Where P_{tot} is the total pressure of the gas stream, x_{H_2O} is the gaseous species mole fraction of water and P_{H_2O} is the partial pressure of water vapour

[5] Occasionally in the literature figures for ϕ higher than 100% are reported. These have been calculated on a basis such that at all water is evaporated and 150RH% the water partial pressure is $1.5 \cdot P_{sat}$ Actually this represents two-phase flow.

3.1.2.3 Complete Evaporative Cooling

Typical operating conditions for a PEM fuel cell stack, i.e. high pressure, low reactant gas stoichiometry, do not favour a high degree of evaporative cooling. However, by operating at a low pressure, with a sufficient reactant gas flowrate and the appropriate injection of liquid water, it is theoretically possible to completely remove all waste heat Vanderborgh et al (1989)

Of the limited examples in the literature detailing the evaporative cooling concept, these are split between evaporative cooling external to the active cell, similar to the concept of a cooling plate, Cohen et al (1991), Katz et al (1993), or internal to the cell with the cooling actually occurring in the flow channels and diffuser, McElroy (1989), Brambilla et al (2000), Wilson et al (2000). The former method carries the associated weight and volume penalties of regular cooling plates and will be investigated no further here.

The concept of complete internal evaporative cooling is illustrated in Fig 3.06, using a basic energy balance model that represents the distribution of thermal energy in a single fuel cell using water injection to the *cathode* with variable operating pressure. The main assumptions are:

- Equivalent cell performance at each operating pressure
- All water leaving in the cathode exhaust.
- Air stoichiometry held at 2 (see definition in appendix A1)
- Fuel cell current held at 140 Amps
- Where applicable, water is injected to the cathode to fully saturate the air
- Fuel cell temperature held at 80°C

The required fuel cell cooling, $\overline{Q}_{fc}$ is represented by the magenta dashed line and has been calculated using Equation 3.06. The thermal energy leaving in the cathode exhaust is shown by the red line. It is seen that at operating pressures over 2.5 bar.a, not all of the product water can be evaporated by the air, that is to say that 100% RH is reached and the required cooling increases further.

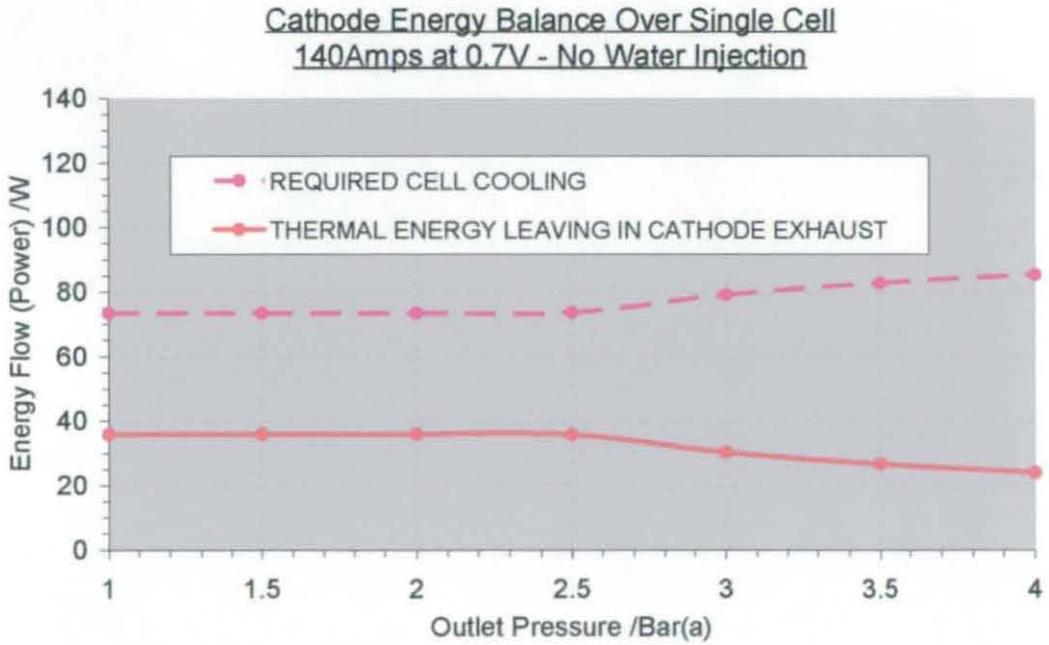

Fig 3.06 – Energy balance over fuel cell cathode – no water injection

The same model is now illustrated with the introduction of liquid water into the cathode stream to produce 100% RH exhaust air where appropriate – Fig 3.07.

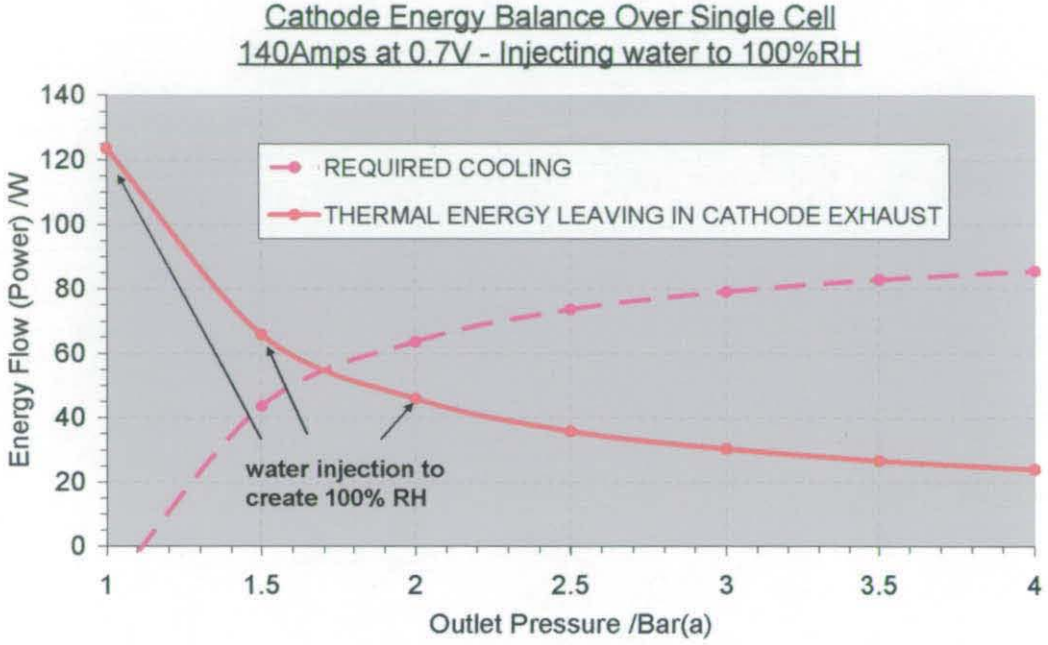

Fig 3.07 – Energy balance over fuel cell cathode – water injection

It is observed how, at approximately 1.1 bar.a, the required cooling is zero as here, enough water can be 'absorbed' by the air to yield complete evaporative cooling. The acronym EC will be used henceforth to represent fuel cell operation with complete internal evaporative cooling.

If proved experimentally, the EC operational method potentially could replace conventional plate-based stack cooling and humidification systems resulting in a simpler arrangement with much lower associated parasitic losses but, crucially, a much higher stack packing density. By operating at the lower pressure conditions necessary for complete evaporative cooling, the fuel cell stack will not provide optimum electrochemical performance, but this could be counterbalanced by the elimination of the high parasitic losses of air compression.

However, the direct supply of liquid water to fuel cells may introduce other issues such as the large presence of a two-phase flow in gas tracks and the even distribution of humidity and cooling over the entire electrode area.

3.2 Experimental Fuel Cell Rig Design

3.2.1 Overview

It was decided to investigate the feasibility of 'complete' evaporative cooling by constructing a fuel cell rig capable of simulating the thermal environment of a single cell in an EC stack - i.e. no cooling plates and an integrated liquid water injection mechanism. The primary goal was to achieve acceptable electrochemical performance from the fuel cell and maintain thermally stable operation. Other tests were to be undertaken (1) to establish relationships between membrane hydration and fuel cell performance and (2) to prove the feasibility of direct water injection as an effective fuel cell humidification technique.

The research is structured into three sections as follows:

Section A Fuel Cell Polarisation with variable Operating Conditions

The following areas were studied:

- The effect of operating conditions on the fuel cell performance with a fully hydrated membrane structure (section 3.3.2.)
- Repeating these tests with no external humidification – the only source of water is the fuel cell reaction at the cathode (section 3.3.3)

These experiments were to be carried out using MEA's manufactured by W.L. Gore which have a reinforced membrane structure and are thinner than the Nafion based materials – as detailed in Chapter 2. Thus, these should give a better water balance, i.e. closer to zero net water drag, as they promote greater rates of back diffusion and lower electro-osmotic drag due to the thinner structure, and would possibly allow the fuel cell to operate effectively with no humidification source.

Section B Direct Water Injection and Air Saturation

This consists of:

- A comparison of the electrochemical performance obtained from the fuel cell using direct liquid water injection and the 'conventional' humidification method of gas saturation by water vapour.

Section C EC operation

The following areas were studied:

- The effectiveness of evaporative cooling illustrated as a temperature profile along a gas track of the cathode flow-field
- The electrochemical performance obtained from the fuel cell operating in EC mode
- Temperature and potential responses of the thermally isolated cell to changes in water and gas flowrates

Section C is outlined separately in Chapter 4.

3.2.2 Single cell design

3.2.2.1 Component selection

A critical factor in the design of the rig was the specification of a sufficiently large active electrode area, as a small fuel cell would have difficulty generating enough heat to effectively demonstrate evaporative cooling. At Loughborough University, the established cell design used in stack construction employed a square 200 cm^2 active area - which was considered adequate for these purposes. Choosing this size meant that cell components such as MEA's, flow plates etc. were more likely to be readily available and the need for specially manufactured items would be minimised.

A single fuel cell test stand was available, comprising a mounted pair of 30 mm thick stainless steel end plates containing peripheral recesses for 12 compaction bolts and retaining nuts – refer to Fig. 3.08 below. The rear plate also contained a centrally positioned internal oil diaphragm, which, when pressurised by nitrogen (up to 10 bar.g), compensated for deflection induced by the compaction bolts on the edges of the end-plates thus ensuring a more even distribution of compaction pressure.

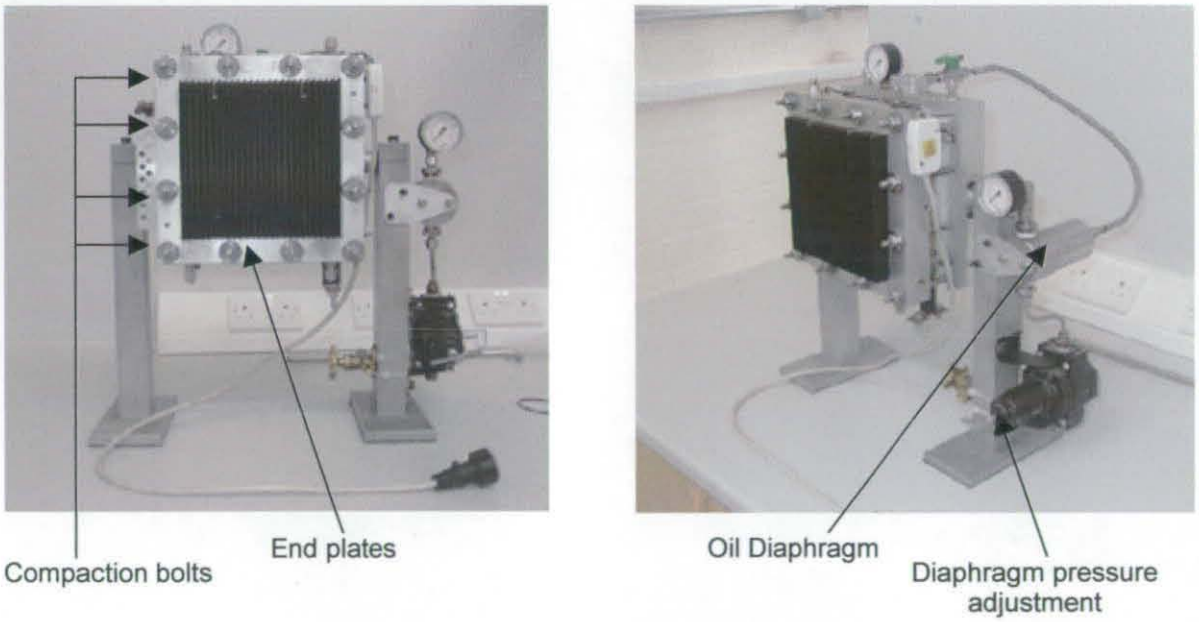

Fig 3.08 – Photographs of fuel cell end plates

The single sided flow field plates selected for use had been previously chemi-etched from a proprietary grade of stainless steel, and contained Advanced Power Sources flow field designs - interdigitated on the cathode and a parallel serpentine design on the anode - see Chapter 6 for detailed explanation of the flow-field concept and examples. As the plates were originally designed for stack use, the gas manifolding leading to, and from, the flow fields consisted of an array of ports instead of a rear "single-entry-manifold

single-exit manifold" design which these end-plates had originally been designed to be used with - this meant some form of adaptation would be required. The flow plates had not been in use for some considerable time, so a 0.2 micron layer of gold was sputtered onto the flow-field face[6] to reduce any surface resistance from passive oxide layers that would have accumulated, Davies et al (2000).

As mentioned previously, thin reinforced MEA's were used - Gore series 5510 MEA's - 35 micron membrane with 0.4 mg/Pt cm^2 catalyst loading both sides. As these were originally designed for LC stacks, they had hydrogen, air and water manifolding ports cut into the peripheral sub-gasket area - corresponding to the port design in the flow plates. To prevent gas crossover, the sealing gaskets were cut so as to only contain the hydrogen or air ports for the anode and cathode flow fields respectively. Carbel CL, a carbon cloth based diffuser material had been used in fuel cells at Loughborough University for some time so this was chosen, refer to Chapter 7 for more on fuel cell diffuser materials.

[6] This work was undertaken by TEER Coatings, Hartlebury, UK

3.2.2.2 Thermal Insulation

There were to be two operating modes for the fuel cell rig:

- The thermal simulation of a single cell in a evaporatively cooled (EC) stack - this effectively meant operating 'adiabatically' - no heat transfer to or from the cell
- The thermal simulation of a single cell in a liquid cooled (LC) stack which necessitates accurate cell temperature control

To obtain the adiabatic conditions in the cell necessary for the EC analysis, 30 mm thick PVDF blocks were positioned immediately behind the flow-field plates to minimise heat transfer with the large steel end plates - PVDF being chosen due to the good thermal insulation properties of the material. These blocks were also designed to supply the reactant gases to the supply ports of the anode and cathode flow plates, therefore by-passing the end-plate manifolding completely. This is shown in Fig. 3.09; with dashed lines illustrating the side feed plenum chambers and an array of small circular features representing small tappings which supplied the gas to the flow plate ports via the manifold features.

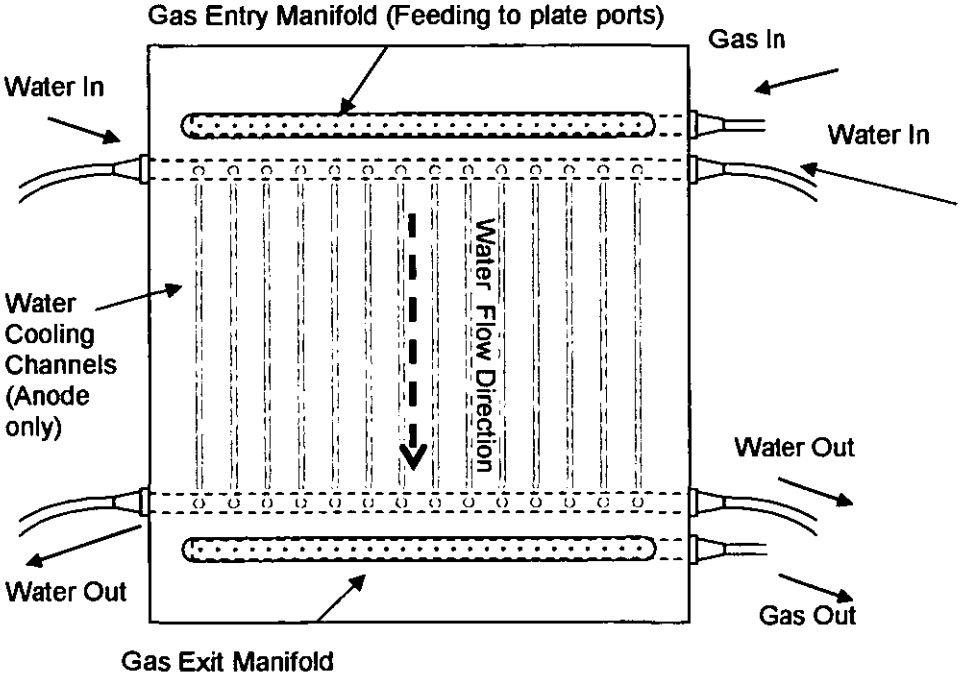

Fig. 3.09 Machined PVDF insulating plate for anode side of fuel cell

It was desirable to eliminate the requirement of continual rig disassembly to insert/remove the insulating PVDF blocks when switching between EC and LC operation. This would necessitate MEA and diffuser replacement on each occasion, introducing unacceptable time and cost to the testing. Therefore, cooling medium channels were

machined into the anode PVDF block to allow the fuel cell to be operated in both thermal configurations with no need for physical adjustment or test interruption, shown as dashed lines in Fig. 3.09.

3.2.2.3 Temperature and pressure control

To control the fuel cell temperature in LC mode a simple coolant loop was established with water continually supplied to the cooling channels of the anode PVDF block via a small diaphragm pump drawing from a water bath. If desired, the fuel cell temperature could be increased by heating the bath water using a submerged heating coil. Power to the coil was controlled by a 230 V ac power supply unit with an in-built switching mechanism which compared a temperature set-point, input via a digital LED interface, with a reading from a K type thermocouple in the fuel cell. To decrease the fuel cell temperature the water returning to the bath from the anode PVDF block was cooled in a small plate heat exchanger using mains tap water.

To maintain fixed anode and cathode pressures, adjustable regulators were fitted on the fuel cell exhaust lines. Immediately upstream of these were simple analogue pressure gauges which were used to establish the anode and cathode pressures for each test.

3.2.2.4 Reactant gas and water supply

An accurate and consistent supply of gas and water flowrates was essential, particularly for the EC analysis where this was critical for control of the fuel cell temperature. Therefore, new equipment was purchased, consisting of two air mass flow controllers (ranges 0-5 SLPM and 5-50 SLPM) and one hydrogen mass flow controller (range 0-5 SLPM) along with a 4 channel MFC controller box with LED digital interface[7]. With this apparatus anode and cathode reactant gas flowrates could be delivered to an accuracy of 5 sccm and adjusted with a short time response if necessary.

It was decided that for all tests, if operating with humidification, either by gas saturation or water injection, only the cathode would be supplied with water. An HPLC water delivery pump was available with a supply resolution of 0.1 cc/min to a maximum flowrate of 9.9 cc/min. An HPLC-pure grade of bottled water[8] was used at all times to minimise the risk of introducing impurities to the MEA and consequently causing degradation of performance in subsequent tests. A two-way valve immediately downstream of the pump could switch the water delivery between direct injection to the cathode flow-field or to a steam generation unit which saturated the air.

The steam generation unit consisted of a thermally insulated aluminium block with a machined flow channel and fittings for gas entry and exit. It contained two 0.5 kW (230 V ac) cartridge heaters located in machined holes. The temperature of the unit was maintained at 300°C using a similar method to the cell temperature control for LC operation, i.e. a 230 V ac power supply compared a measurement from a reference thermocouple in the block to a preset temperature set-point of 300°C and switched accordingly.

Prior to the steam generation unit was a small pipe heater, which increased the temperature of the air supply to the fuel cell operating temperature. This consisted of a heating coil wrapped around a small length of pipe with a reference thermocouple. The temperature of the coil was controlled in the same manner with a temperature set-point comparison switching power supply. This step was necessary to minimise any possible condensation of water vapour from the air before reaching the cathode inlet.

[7] Purchased from Aera, UK
[8] Obtained from Fisher Chemicals, Loughborough, UK

3.2.2.5 Direct liquid water injection technique

As stated previously, liquid water was to be injected only to the fuel cell cathode. Injecting to the anode with the aim of complete EC operation would require a large flow of hydrogen, possibly necessitating a recirculation pump and water 'drop-out' stages. There would also be a much larger degree of electro-osmotic drag and this may cause an increased rate of degradation in the membrane structure, i.e. increased 'flushing out" of fluoride ions. This would be especially risky when using a thin membrane structure such as that of the Gore MEA's.

Water injection features were machined into the rear of the stainless steel cathode flow plate as shown in Fig. 3.10.

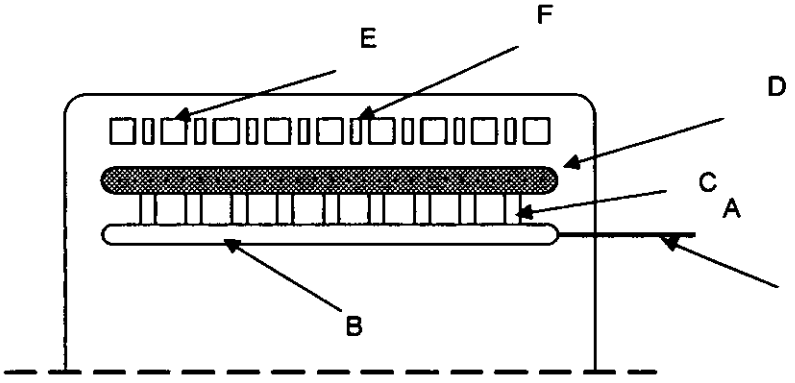

Fig. 3.10 Cathode water injection feature

Water was injected via a stainless steel tube (A) to a primary gallery (B) which is connected by individual channels (C) to the secondary gallery (D). The secondary gallery contained an array of holes, each aligned with the start of a gas track on the opposite flow-field face. The air was delivered to the flow field from the array of wider air ports (E). The hydrogen ports (F) were redundant here in this case.

It was critical that the water was delivered evenly through each hole to the gas tracks, as an uneven distribution would result in regions of the cell flooding and others overheating with the membrane drying out. However, from the tube delivery the water would follow paths of least resistance to flow - in this particular case the holes adjacent to the injection port. By packing the secondary gallery (D) with layers of filter paper and a layer of wet-proofed Toray carbon paper[9] a substantial pressure drop feature was created. The result was that, on cell assembly and compaction this 'piled-up' arrangement was sufficiently compressed by the adjacent gasket and PVDF block such that the resistance

[9] A carbon paper diffuser material – see Chapter 7 for information on diffuser grades

to water flow from the entry tube to each hole was approximately equivalent. This was checked ex-situ by compressing the gallery areas with press plates, injecting water with the HPLC pump and visually confirming an even flow between tracks.

3.2.2.6 Data monitoring and acquisition

For the polarisation and humidification method tests the fuel cell potential was displayed by a digital multimeter, using voltage probes connected to tabs on the top of the flow plates. The current was established by using a resistance shunt, fixed in position between the anode current lead and the load unit. The shunt was calibrated for 400 Amps, equivalent to a potential difference of 75 mV, thus producing an EMF of 187.5 μV for each amp of current flow – this was displayed by a second digital multimeter.

Current and potential data from the fuel cell were both logged manually, the pressure readings, corresponding to anode and cathode back-pressures, were noted from the analogue gauges. The temperature reading from the reference thermocouple in the fuel cell was displayed on the power supply LED display, and also manually noted.

For the EC tests, which necessitated continual logging of the fuel cell potential, the digital multimeter measuring potential was connected via an RS232 lead to a PC running basic logging and display software. The thermal profile of the cell for the EC tests was established by setting up a 'thermal mapping array' of 8 'K' type thermocouples positioned behind a single channel of the cathode flow plate. The thermocouples were positioned in pre-cut channels formed in the 1mm thick Grafoil sealing gasket, located between the rear of the cathode flow plate and the PVDF insulating block, and were spaced evenly over a distance of 120 mm as shown in Fig. 3.11.

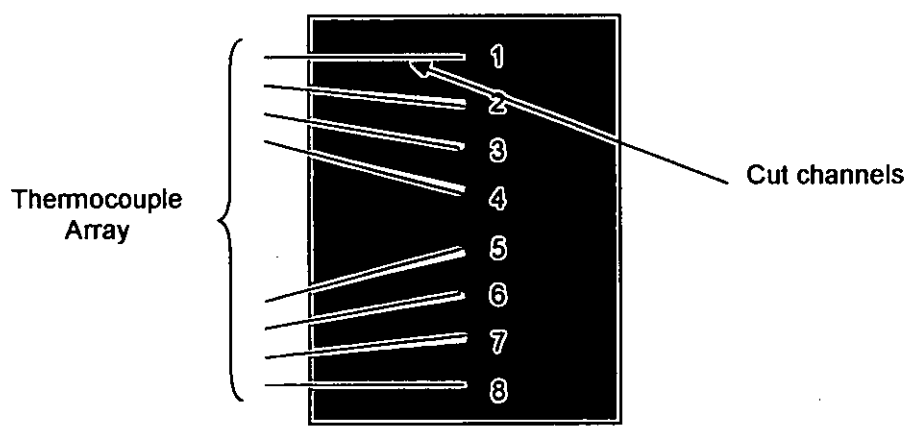

Cathode Grafoil gasket (manifolding not shown)

Fig. 3.11 Thermocouple array in Grafoil gasket

The thermocouples were wired to a DAQ board, connected to a laptop computer running DAQVIEW software via an IOTech DAQbook. This allowed the monitoring of all temperatures in real-time and also logging to data files.

Before testing commenced it was necessary to calibrate each thermocouple reading. The DAQVIEW software included an adjustable gradient and offset for each channel. A reference temperature of zero degrees centigrade was established by obtaining a container of crushed ice, inserting the thermocouple tips and adjusting the offsets accordingly. Next, the tips were inserted into boiling water and the gradient values were calibrated to obtain a displayed reading of 100°C.

3.2.2.7 Load cycling

To obtain useful polarisation data power has to be drawn from the fuel cell at points of regulated current or voltage. This is usually done by using a 'load unit' device to simulate various levels of power demand, operating potentiostatically, at a fixed voltage, or galvanostatically, at a fixed current. The power can be dispersed as heat, using a high rating resistor or FET (field effect transistor) cooled by a fan but alternative methods of dissipating fuel cell load include 'recycling' power to the mains supply, via an inverter step. or using alternative cooling methods such as water heat exchangers – particularly for very high currents.

The load unit used for these tests operated as a galvanostatic device and used a high rating FET and fan to dissipate the cell power. It was connected to the fuel cell via high current rated thick copper cables to copper bars which were welded to the sides of the stainless steel flow plates.

3.2.2.8 Fuel cell rig assembly

The fuel cell was assembled as follows:

An adjustment was made on the support leg (see Fig. 3.14) of the test stand which allowed the rear end plate to pivot upward through 90 degrees, and then be fixed in a horizontal position. The single cell was then built on top of the end plate (refer to Fig 3.12) beginning with the cathode PVDF block, then the cathode flow plate, cathode diffuser, MEA, anode diffuser, anode flow plate and anode PVDF block and completed by positioning the front end plate on top with each compaction bolt passing through the holes in the end plate (refer to Fig. 3.13). Each compaction nut was tightened gradually to a torque force of 10 Nm and the diaphragm pressurised to 10 bar.g with nitrogen. The assembly was then swung back to the vertical orientation and fixed in position.

The current leads were attached to the copper bars on the flow plates and the connections on the load unit via brass bolts and nuts. The potential probes were attached to tabs on the top of the flow plates and the thermocouples inserted into the channels in the Grafoil gasket. The thermocouples were sleeved with heatshrink insulating tubing to prevent possible electrical shorts, with the pots inserted into recesses in a positioning bracket bolted to the front end plate. The gas and water tubing were then attached either via push-fittings or Swagelock connections.

The photographs of the assembled rig shown below are minus all gas and electrical connections:

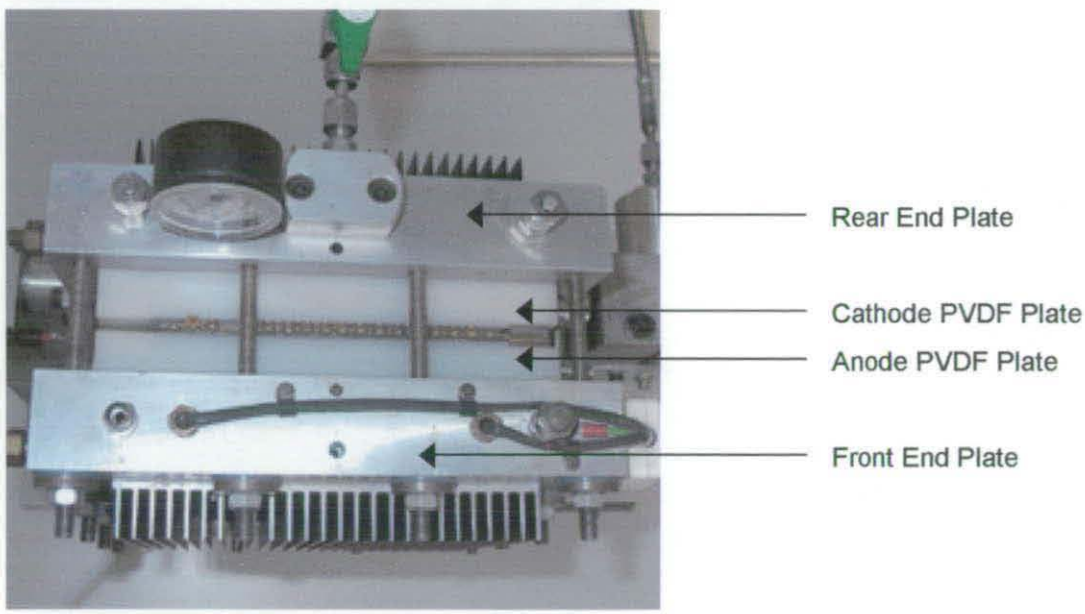

Fig. 3.12 Top View of FC rig

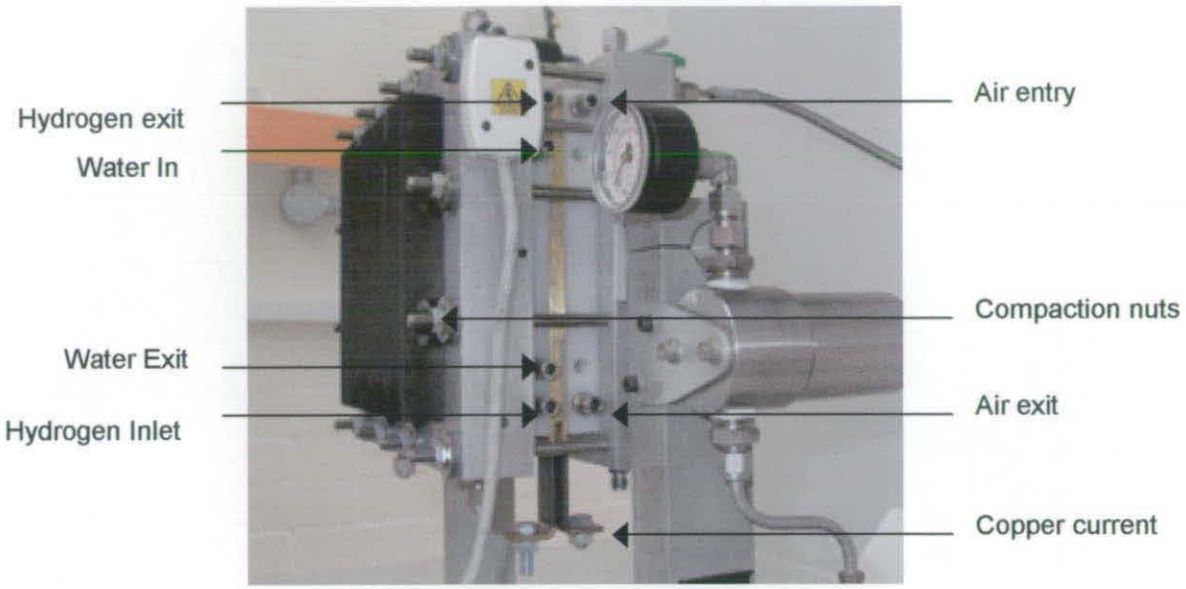

Fig. 3.13 Right hand view of FC rig

Fig. 3.14 Left-hand view of FC rig

The equipment was then set-up as shown below in Fig. 3.15:

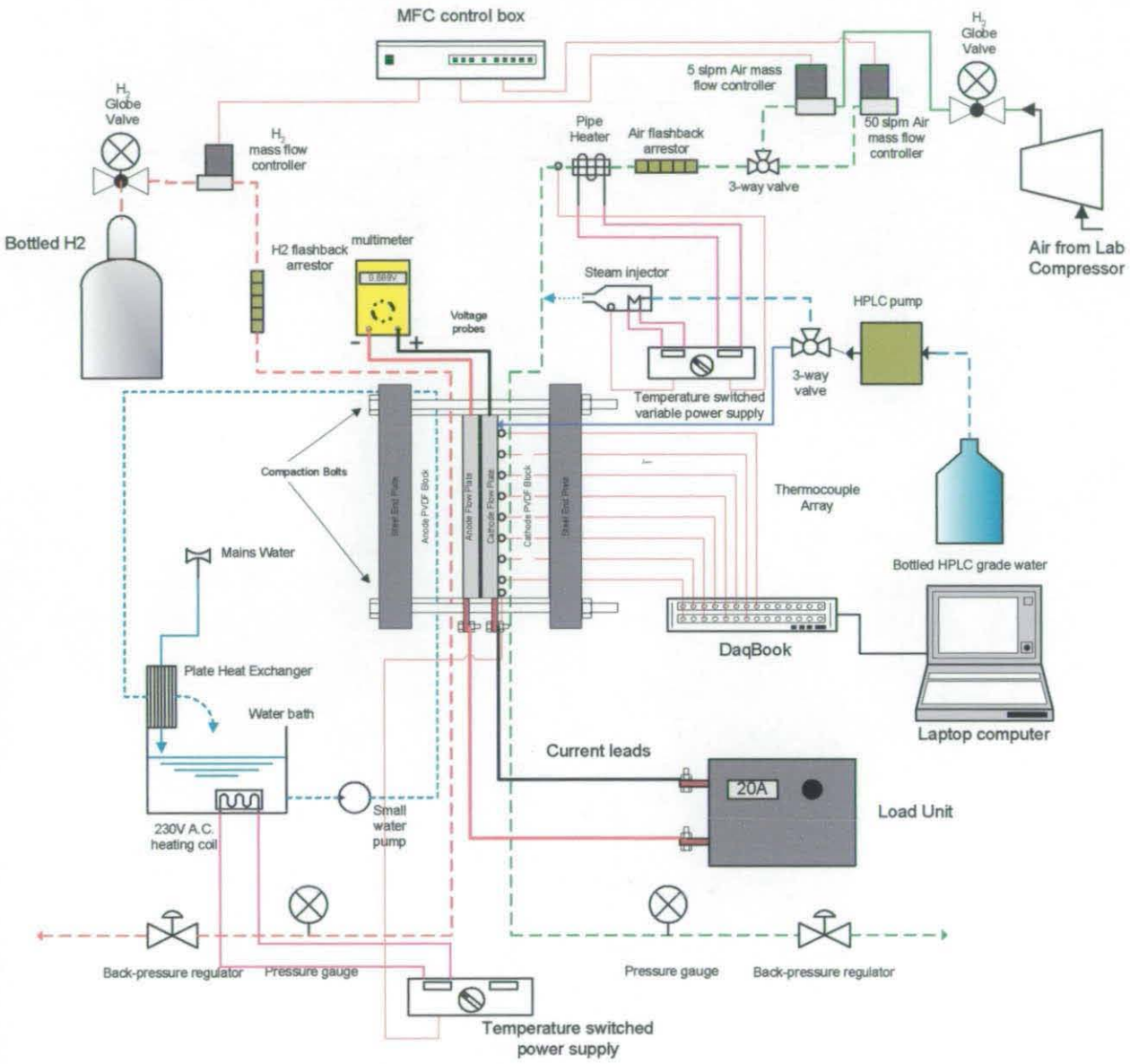

Fig. 3.15 Schematic of equipment set-up

3.3 Experimental Analysis

3.3.1 Pre-test procedures

The calculations for gas and water supply rates used for the tests detailed in this thesis are described in appendices A and B. The pre-test checks and shut-down procedures for the fuel cell operation are described in appendix C.

3.3.2 Section A: Fuel cell polarisation plots

3.3.2.1 Background

These initial tests carried out on the fuel cell rig would show the effects of variable operating conditions on the fuel cell performance. From this, relationships between operating conditions and the membrane hydration state could be established and also an illustration of the need for an external water source.

This was done by obtaining polarisation plots - sometimes referred to as 'polarisation curves' in the literature -which illustrate a current-voltage response from the fuel cell. As explained in Chapter 2, this is a standard and well established method for characterising the performance of fuel cells and can provide information on the physical phenomena occurring therein.

3.3.2.2 General test procedures

The polarisation curves were taken on an increasing current basis, starting at open circuit conditions with each point held for 120 seconds. This time period allowed partially equilibrated conditions, between the hydration state of the membrane and the water content of the electrodes, to be established. The gas stoichiometric ratios and water flowrates were altered immediately prior to stepping to the next current. The fuel cell potential was not allowed to drop below 0.45 V so the polarisation test was stopped if this point was reached.

The stages of the current shifts were as follows: 0, 5, 10, 15, 20, 40, 60, 80, 100, 120, 140, and 160 Amps. The resolution of the shifts was 5 Amps from open circuit up to 20 Amps, due to the large changes in potential with current in this region as a result of activation overpotential which must be accounted for in the plot.

During the polarisation test, the hydrogen supply was maintained at a stoichiometry of 1.5 and was not humidified. The reactant gases were fed to the fuel cell in a counterflow configuration – refer to Fig. 3.04.

3.3.2.3 Polarisation - Humidified membrane and variable operating conditions

Polarisation plots obtained from the fuel cell rig at a range of operating pressures (both anode and cathode) are shown below in Fig. 3.16. Power density plots are also illustrated on the same chart - these represent cell potential multiplied by the current density.

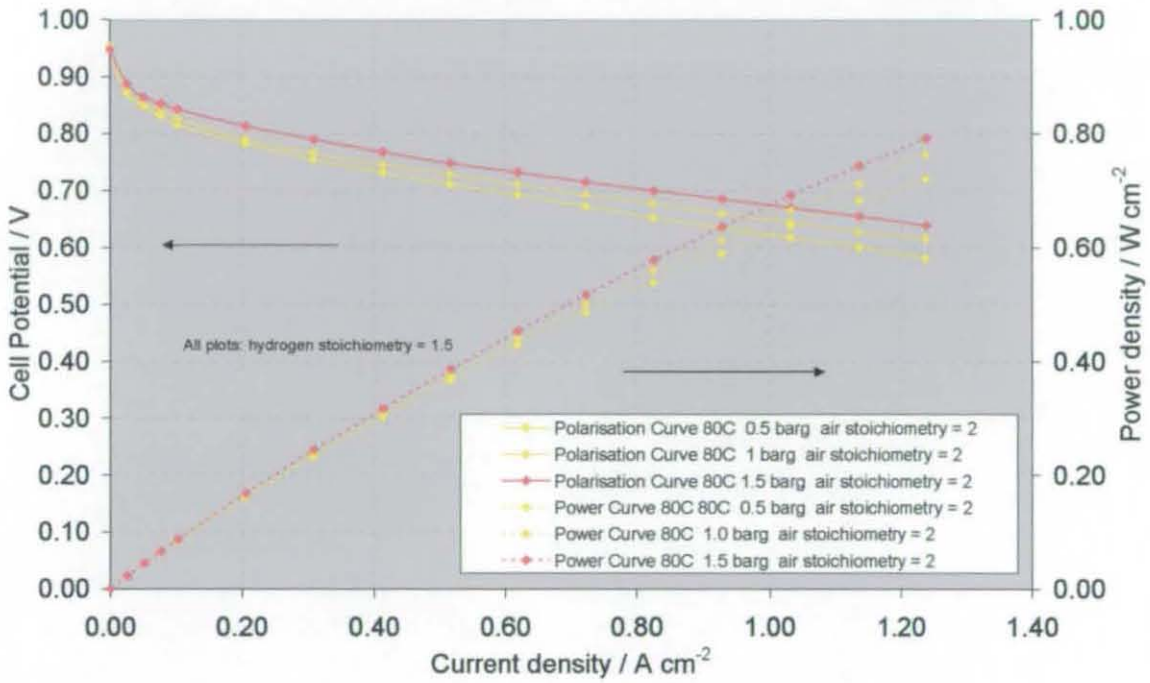

Fig. 3.16 Polarisation and power plots at variable operating pressures, air at 100% RH

The best cell performance was obtained at 1.5 bar.g operating pressure and the poorest at 0.5 bar.g. The linear slope of each plot is similar as there is equal ohmic overpotential and there is also little evidence of mass transport overpotential – possibly due to the nature of the interdigitated flow-field. The difference between each polarisation plot occurs at low current densities due to a lowering of activation overpotential with higher pressure, which confirms the theory detailed in section 2.2.1. The power density curves assist in illustrating that with higher stack operating pressure the more power can be supplied for a fixed value of cell potential, or efficiency.

Polarisation plots and power curves from the fuel cell using variable air stoichiometries are shown in Fig, 3.17 below.

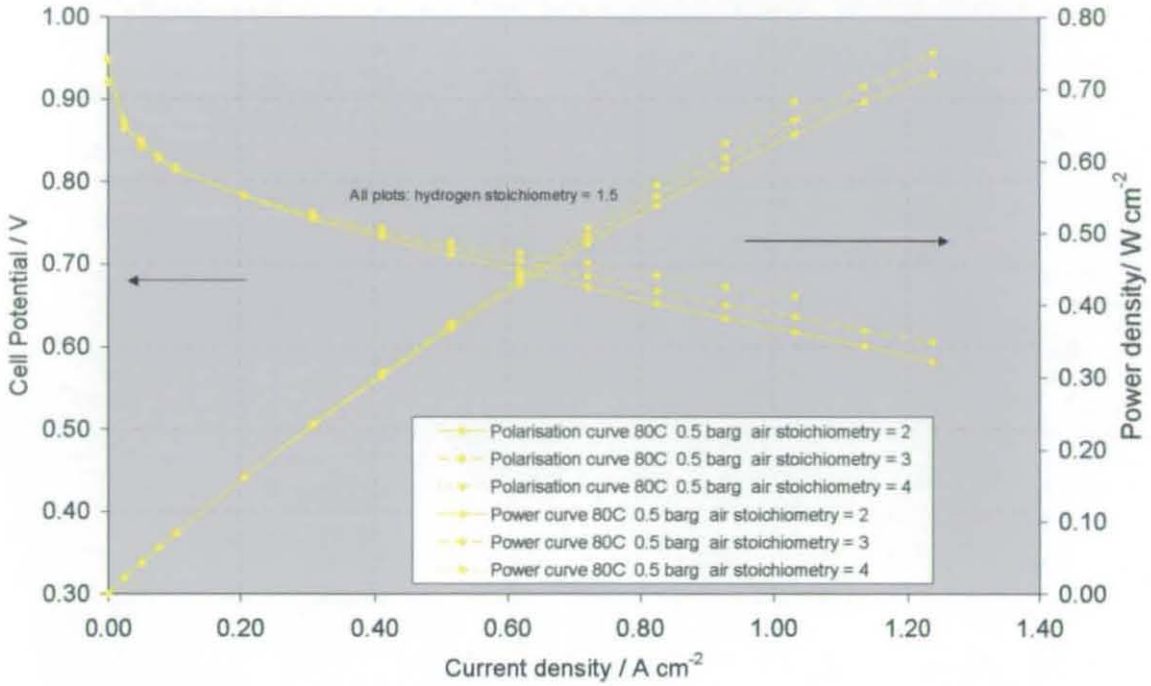

Fig. 3.17 Polarisation and power plots with variable air stoichiometries, air at 100%RH

It is observed the best performance is obtained with the highest air flowrate, in this case a stoichiometry of 4. Unlike Fig 3.16 the activation overpotential for each plot is identical but each plot has a different linear slope. The hydration level of the membrane is identical for each plot as the air supply is fully saturated; therefore, there is no difference in the ohmic overpotential. The difference in the slopes of the polarisations is due to increasing differences in mass transport overpotential between plots as the air stoichiometry is increased. Although insufficient current is drawn to cause the 'downward slope' feature that is usually observed at the top end of a polarisation plot, mass transport overpotential clearly exerts a greater influence with increasing current. However, as the air stoichiometry is increased, the oxygen concentration over the entire electrode area is increased and mass transport overpotential is lowered.

Completing this short series of tests, polarisation and power plots, obtained from the fuel cell at variable operating temperature, are shown in Fig 3.18.

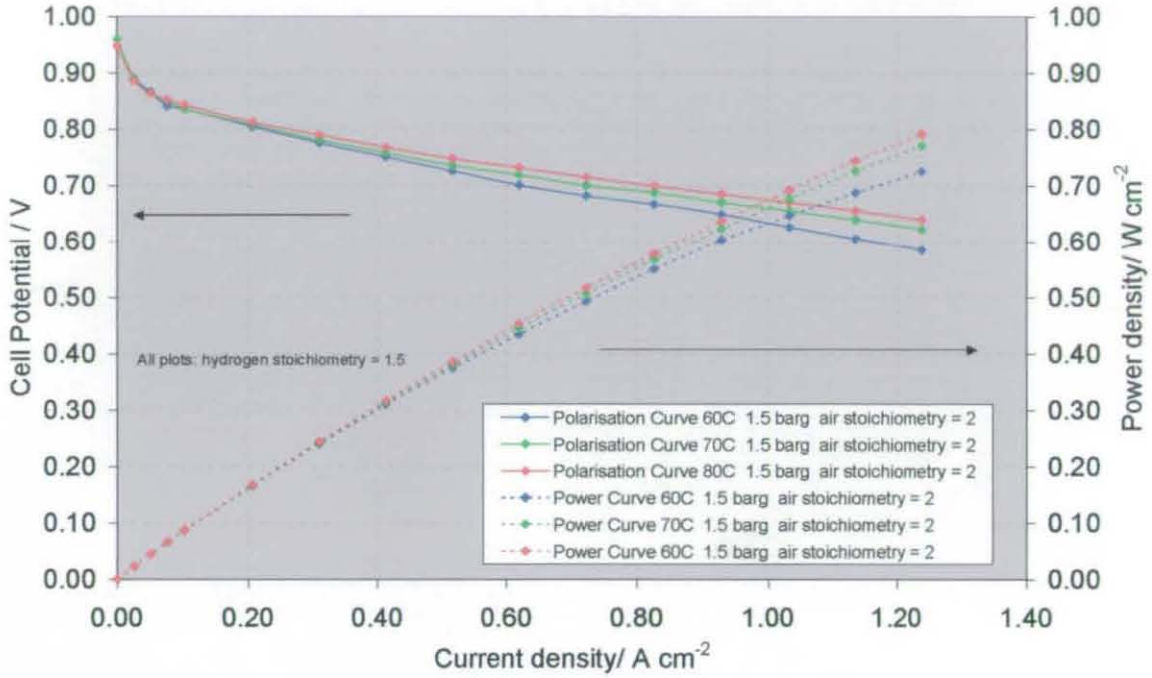

Fig. 3.18 Polarisation and power plots with variable fuel cell operating temperatures, air at 100%RH

The best performance occurs at the highest fuel cell operating temperature of 80°C and the poorest performance at the coolest temperature of 60°C. In a similar manner to Fig 3.17 the slopes of the plots vary, however, as identical air stoichiometry levels are being held, this cannot be attributed to differing levels of mass transport overpotential. The difference is due to a change in the ionic resistance of the cell membrane as the rate of proton conduction is proportional to temperature. There is also a slight difference in activation overpotential up to 0.20 A/cm^2 due to increases in reaction rates caused by temperature difference.

Conclusions

From Figs 3.16 - 3.18 it is observed how operating conditions influence the extent of the three main overpotentials of fuel cell performance. Changes in operating pressure are shown as differences at the beginning of the polarisation plot. Differences in temperature and stoichiometry affect the gradient of the linear section of the polarisation plot but this was due to different mechanisms.

It is clear why a higher power is obtained from an externally humidified fuel cell when operating with higher pressure, temperature and stoichiometry for a fixed efficiency point.

3.3.2.4 Unhumidified / Humidified polarisation plots

The next set of tests are polarisation plots at variable operating conditions carried out with 100% RH humidification by air saturation via the steam generation unit as in the previous section, then repeated with no humidification, i.e. operating 'dry'. This would allow a direct performance comparison between using a (1) humidified and (2) unhumidified air supply, in particular showing the effect of increasing ohmic overpotential on a polarisation plot caused by a dehydrated membrane. It would also provide information on the influence of operating conditions on the rate of evaporation of associated water from the membrane structure. Finally, it would allow an assessment of the capability of ultra-thin membrane structures to operate in a fuel cell without external humidification.

The test matrix undertaken is shown below:

Plot Reference	Temperature / °C	Pressure / bar.g	H_2 stoichiometry	Air stoichiometry	Air humidication / %RH
A	60	0.5	1.5	2	100
B	60	0.5	1.5	4	100
C	60	1.5	1.5	2	100
D	60	1.5	1.5	4	100
E	80	0.5	1.5	2	100
F	80	0.5	1.5	4	100
G	80	1.5	1.5	2	100
H	80	1.5	1.5	4	100
I	60	0.5	1.5	2	0
J	60	0.5	1.5	4	0
K	60	1.5	1.5	2	0
L	60	1.5	1.5	4	0
M	80	0.5	1.5	2	0
N	80	0.5	1.5	4	0
O	80	1.5	1.5	2	0
P	80	1.5	1.5	4	0

Fig. 3.19 Test matrix for humidified/unhumidified polarisation plots

Results

The eight polarisation plots with cathode humidification (A-H) are shown in Fig 3.20. They confirm earlier observations that the optimum fuel cell performance occurs with the highest operating temperature and pressure.

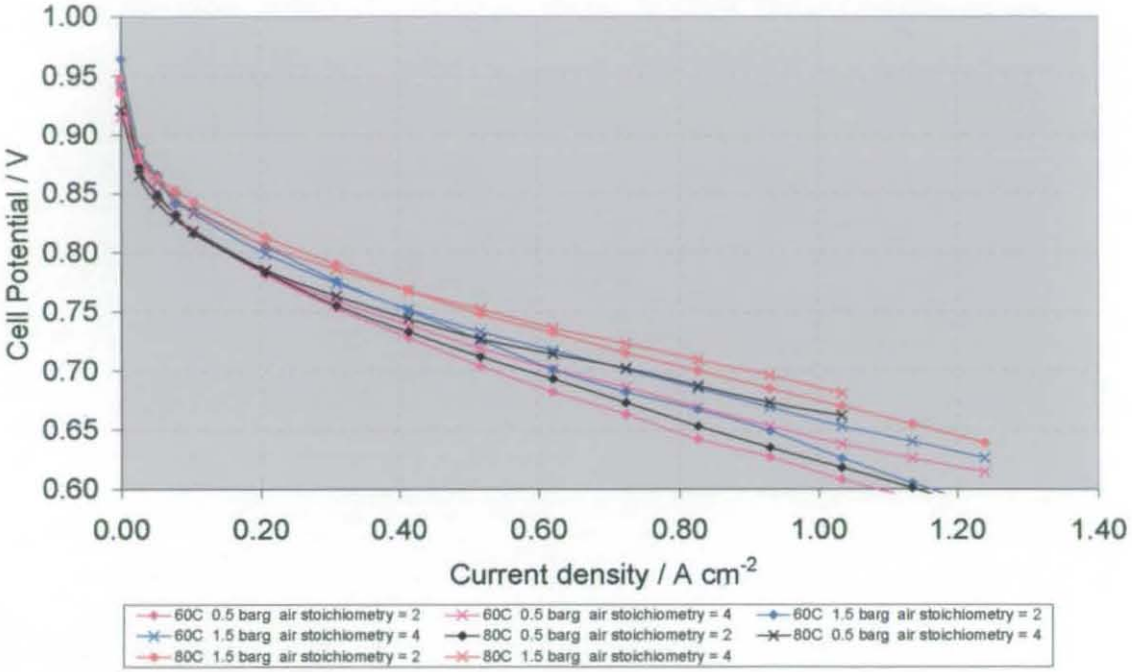

Fig. 3.20 Polarisation plots with 100% relative humidity of air

Polarisation plots for the same operating conditions as Fig. 3.20 with no external humidification (plots I-P) are illustrated in Fig. 3.21

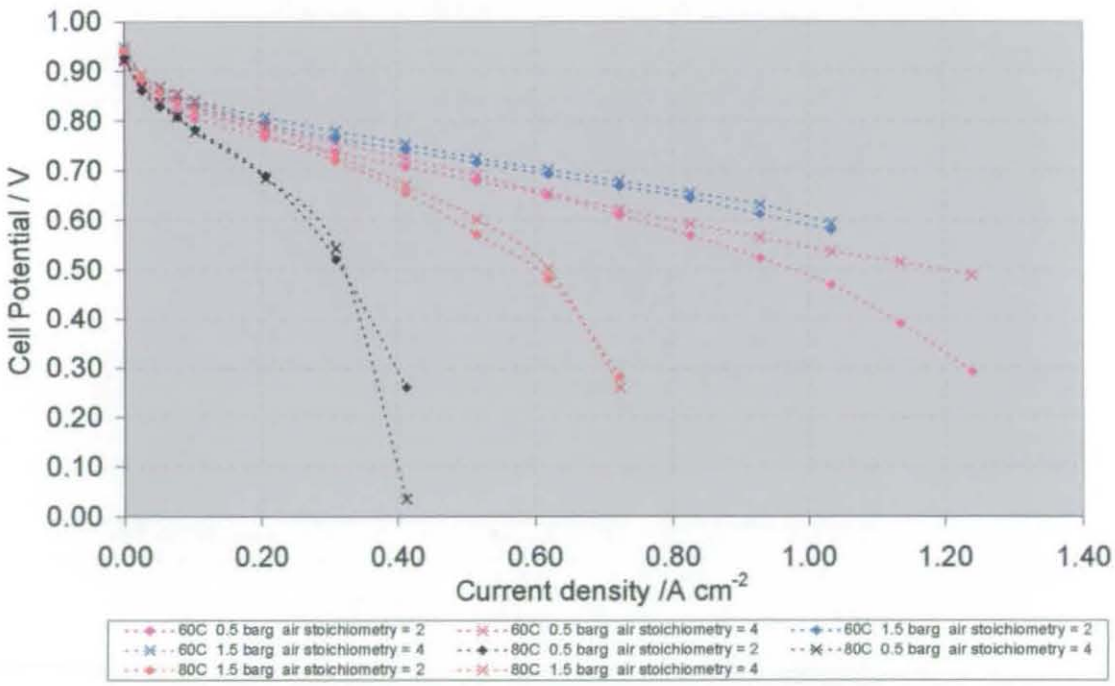

Fig. 3.21 Polarisation plots with no external humidification

The effect of increased membrane dehydration is clearly illustrated in Fig. 3.21. Operating at the lower temperature of 60°C, a superior fuel cell performance is obtained due to greater water content in the membrane. At the higher temperature of 80°C the hydrogen and air flows obtain a lower relative humidity value and evaporate water at a faster rate. Especially prominent in the 80°C plots is the excessive dehydration of the membrane at higher currents causing a non-linear polarisation slope. Although more water is produced with increasing current, this is more than offset by the extra evaporation by higher stoichiometric gas flowrates. This confirms that, *with a higher operating temperature a fuel cell requires a greater degree of humidification water to maintain adequate performance.*

Similarly from Fig. 3.16, operating at a higher pressure produces an increased performance from the fuel cell, however when operating 'dry' a lower operating pressure (0.5bar.g) further lowers the relative humidity value of the reactant gases. Hence the difference between low and high pressure plots is greater here, particularly at the higher operating temperature. This confirms that *with a higher operating pressure a fuel cell requires a lesser degree of humidification water to maintain adequate performance.*

At 60°C, the higher air stoichiometry operation gives superior performance over the full polarisation curve but at 80°C the high stoichiometry performance falls away at the top end of the polarisation curve due to excess dehydration by the greater gas flow with a low relative humidity value. This confirms that *using a higher reactant stoichiometry requires a greater degree of humidification water to maintain adequate fuel cell performance.*

All of these observations confirm the partial pressure law detailed earlier, Equation 3.07

The following graphs (Figs 3.22 - 3.25) illustrate direct comparisons between the humidified and the unhumidified polarisation plots as shown in Figs 3.20 and 3.21 at identical operating temperature and pressure.

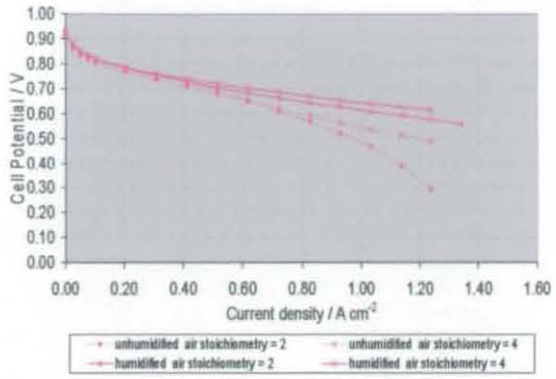

Fig. 3.22 Polarisation plots – unhumidified 60C & 0.5bar.g

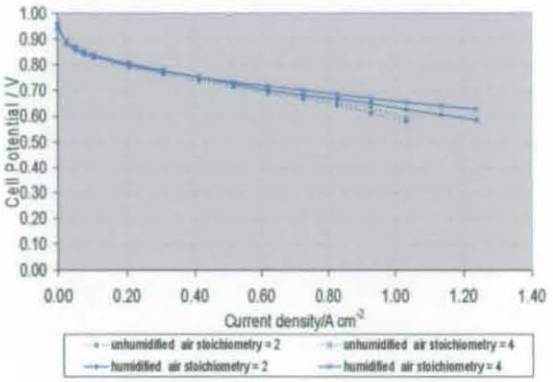

Fig. 3.23 Polarisation plots – unhumidified 60C & 1.5bar.g

The 60°C unhumidified plots show that at higher current densities, with the corresponding higher flow air rates, the hydration state of the membrane falls but at low current densities the level of water being produced is enough to keep the membrane sufficiently hydrated.

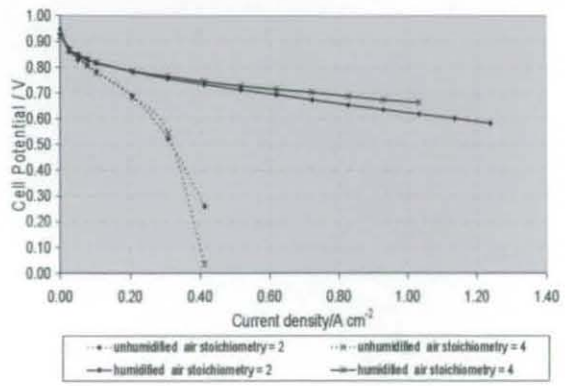

Fig. 3.24 Polarisation plots – unhumidified 80C & 0.5bar.g

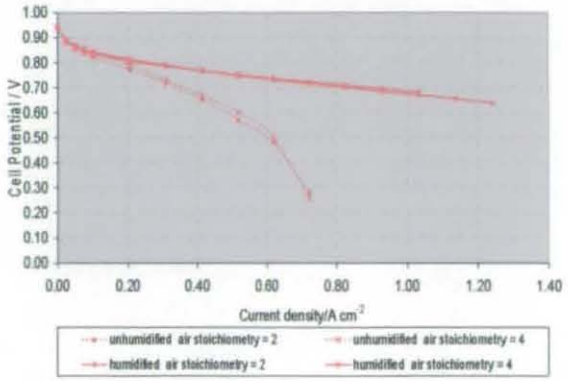

Fig. 3.25 Polarisation plots – unhumidified 80C & 1.5bar.g

At 80°C humidified operation produces better performance than unhumidified operation over the whole polarisation plot due to the lower relative humidity of air.

Conclusions

The general trend observed from this series of polarisation plots is that when operating the fuel cell with higher temperature and lower pressure, corresponding to a rise in water saturation pressure and lowering of partial pressure respectively, the performance obtained with unhumidified air falls below humidified air as the load current is increased. This is due to the dry stoichiometric gas flowrates removing water from the membrane structure.

The thin reinforced membrane structures of the Gore MEA's still require a method of external humidification, even at the lower operating temperature of 60°C, to obtain adequate performance. The extent of dehydration will be also be a function of the flow field and diffusers used in the fuel cell – this is discussed later in Chapters 6 and 7.

3.3.3 Section B: Comparison of humidification methods

3.3.3.1 Background

It is possible that during EC operation of a fuel cell, the presence of liquid water in the cathode gas tracks could severely restrict the diffusion rate of oxygen to catalyst sites, particularly at medium-high current densities (over 1 Amp/cm^2), and thus result in poor fuel cell performance. Therefore, to establish the feasibility of liquid water injection as a fuel cell humidification method a series of tests were designed and undertaken.

This was to be done by comparing fuel cell performance with the air pre-saturation technique and direct liquid water injection, which was intended to be utilised in later EC tests. It was desirable to see the effect of supplying water delivery rates well in excess of what is required for saturated air - 100% RH, to observe any performance enhancement or cathode flooding.

In these tests, a constant current is drawn from the fuel cell via the load unit, with the HPLC pump adjusted to deliver a range of water supply rates and the potential recorded at each point. The tests are undertaken for both humidification methods - air saturation via the steam generation unit and direct liquid water injection to the cathode flow-field with a variety of set pressures, air flows and temperatures.

3.3.3.2 General test procedures

These tests would involve periodically running the fuel cell with inadequate water supply rates. To prevent the membrane structure from drying out at low water injection rates and subsequently affecting all proceeding results, the injection rate was started high and gradually reduced. The hydrogen stoichiometry was kept at a constant 1.5 throughout and a counterflow configuration of gases was used, similar to the previous polarisation tests. The fuel cell current constantly drawn through the test was 140 Amps equivalent to a current density of 0.7 A/cm^2, representing a medium-range current density

The standard leak and crossover testing detailed in appendix C were carried out prior to testing and the hydrogen and air stoichiometric flow rates as detailed in appendix A are used.

3.3.3.3 Results

The first test is shown in Fig. 3.26 and illustrates potential readings from the fuel cell with three operating temperatures: 40°C, 60°C and 80°C with the pressure maintained at 0.5 bar.g and the air stoichiometry fixed at 2, equivalent to 4.65 SLPM.

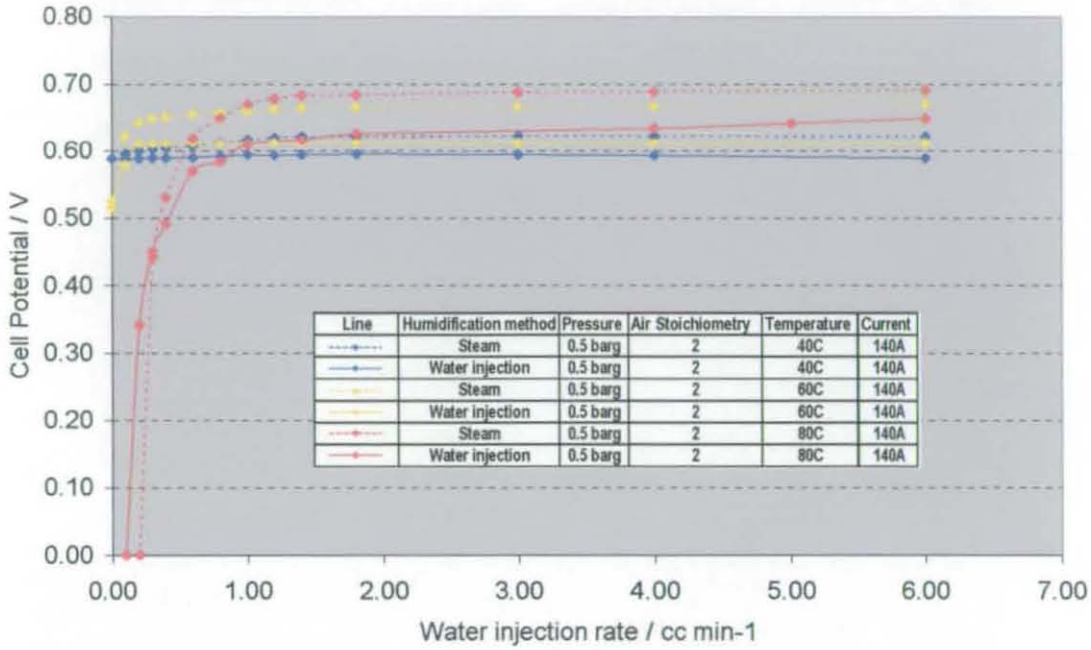

Fig. 3.26 Fuel cell performance – 0.7 Amp/cm^2 at variable rates of air saturation and cathode water injection – three operating temperatures

The main observation is that no significant electrode flooding is clear, even at high water delivery rates. The dehydration of the membrane structure is obvious at the lower water delivery rates, in a similar manner seen on the dry polarisation plots, Fig. 3.21.

Humidification of the reactant air by steam consistently produces a higher cell performance than by direct liquid injection to the cathode. The difference in the potential obtained using the two humidification methods increases with operating temperature. This suggests that as the fuel cell temperature is raised the difference in the membrane water content obtained in using the two humidification techniques is increased. It is possible that there could be lower water content in the membrane if the injected liquid water in the flow field does not penetrate the hydrophobic Carbel CL diffuser whereas the water vapour is able to reach the membrane more readily, being in the vapour state. If cathode flooding was responsible for the lower performance this would have been shown as decreasing potential as the rate of water injection increased. It is also noted that at 40°C the fuel cell is able to operate with negligible degradation in performance when there is no water input. This is due to the increased evaporation by higher temperature gas flows, as explained previously.

Results from the next series of tests, where the fuel cell was operating with variable pressure, and both humidification mechanisms are illustrated to Fig. 3.27.

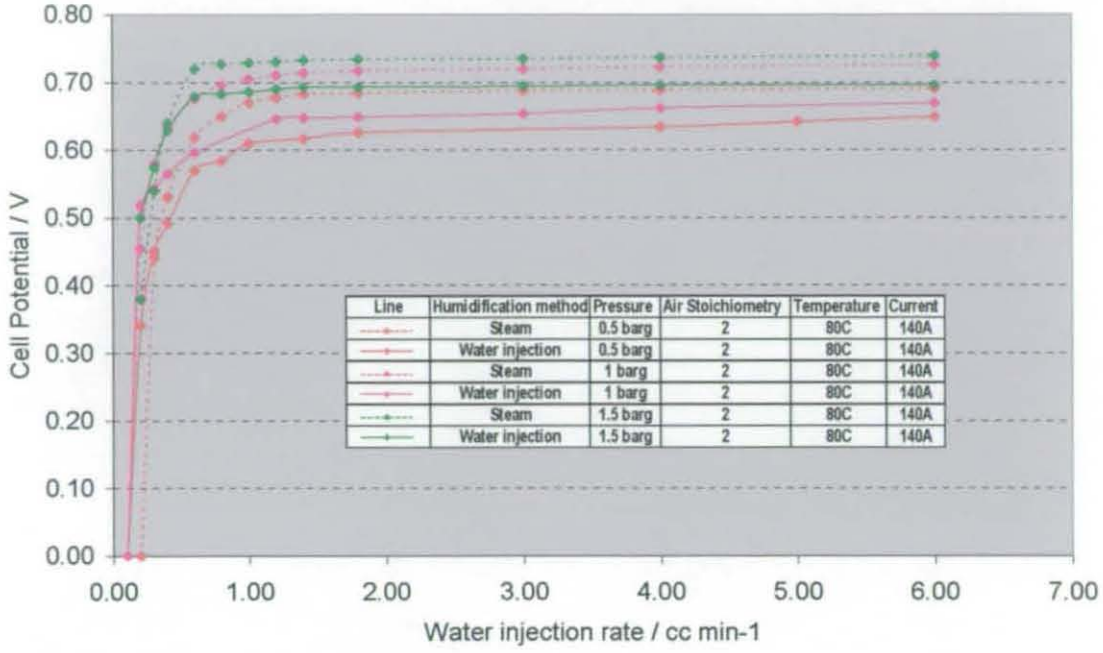

Fig. 3.27 Fuel cell performance – 0.7 Amp/cm^2 at variable rates of air saturation and cathode water injection – three operating pressures

In a similar manner to the profiles shown in Fig 3.26, humidification of the air by steam gives a superior performance over direct cathode water injection and there is no evidence of electrode flooding effects. The performance by water injection at 1.5 bar.g operating pressure is marginally better than by steam injection at 0.5 bar.g.

The final chart in this series, Fig 3.28, shows the fuel cell performance obtained for two air stoichiometric ratios with both humidification mechanisms.

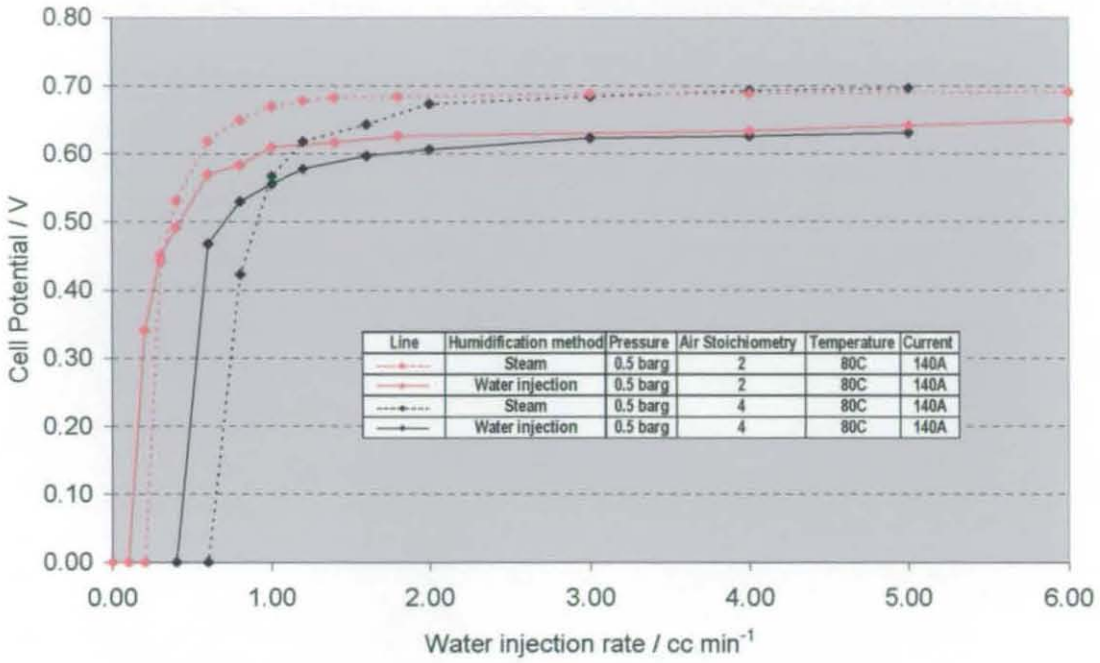

Fig. 3.28 Fuel cell performance – 0.7 Amp/cm^2 at variable rates of air saturation and cathode water injection – two air stoichiometries

Again steam saturation is shown to produce a superior fuel cell performance, though there seems to be very little difference between operating with high or low stoichiometry for both humidification methods. This is possibly due to the fact the current being drawn is 140 Amps (0.7 A/cm^2) and mass transport overpotential does not have the large influence on potential that would be more obvious at higher current densities. The same effect of membrane dehydration is seen with air flows with variable moisture content. It is noted that for very low water supply rates the water injection method gives a better performance.

3.3.3.4 Conclusions

The cathode water injection technique produced poorer performance than pre-saturation of the air by steam, possibly due to a certain degree of water not penetrating the diffuser backing and thus not compensating for the water being removed from the membrane by the air flow. This is possibly due to a large proportion of two-phase flow and thus partially dry air at the beginning of track – a direct result of using the water injection method for fuel cell humidification.

3.4 References

Beal, D.W.; Breault, R.D. "**Internally Cooled Proton Exchange Membrane Fuel Cell Device**", US Patent No. 5,262,249, 16th November 1993

Bett, J.A.S.; Wheeler, D.J.; Bushnell, C. "**Porous Carbon body with Increased Wettability by Water**", US Patent No. 5,840,414, 24th November 1998

Brambilla, M. "**Fuel Cell with Cooling System based on Direct Injection of Liquid Water**", International Patent Application Number WO 00/63992, 2000

Buchi, F.N.; Srinivasan, S. "**Operating Proton Exchange Membrane Fuel Cells Without External Humidification of the Reactant Gases: Fundamental Aspects**", Journal of the Electrochemical Society, Vol. 144, No.8, August 1997

Buchi, F.N.; Srinivasan, S.; Tran, D. "**Performance of PEM Fuel Cells Without External Humidification of the Reactant Gases**", Proceedings of the 1st International Symposium on Proton Conducting Membrane Fuel Cells, Electrochemical Society Proceedings Volume 95-23, pp226-240, 1995

Carlstrom, C.M.; Acker, W.P. "**Fluid flow plate for water management, Method for fabricating same, and fuel cell employing same**", US Patent No. 6,015,633, 18th January 2000

Cisar, A.J.; Gonzalez-Martin, A.; Murphy, O.J.; Simpson, S.F.; Salinas, S, "**Internally humidified membranes for use in fuel cells**", Proceedings of the Intersociety Energy Engineering Conference, v3, pp205-210, 1995

Cohen, R. "**Fuel Cell Evaporative Cooling using Fuel as Carrier Gas**", US Patent No. 4,994,331, 1991

Davies D.P.; Adcock P.L.; Turpin M.; Rowen S.J. "**Stainless steel as a bipolar plate material for solid polymer fuel cells**", Journal of Power Sources, Vol. 86 (1-2), pp237-242, 2000

Davies D.P.; Adcock P.L.; Turpin M.; Rowen S.J. "**Bipolar plate material for solid polymer fuel cells**", Journal of Applied Electrochemistry, Vol. 30 (1), pp101-105, 2000

Dicks, A.; Larmanie, J.E., "**Fuel Cell Systems Explained**" , John Wiley and Sons, Chichester, England, 2000

EG & G Services Parsons, Inc. Science Applications International Corporation, "**Fuel Cell Handbook**", Fifth Edition, US Department of Energy, Office of Fossil Energy, West Virginia, October 2000

Fuller, T.F.; Newman, J., "**Experimental Determination of the Transport Number of Water in Nafion 117 Membrane**", Journal of the Electrochemical Society, 139 (1992) 1332-1336

Gonzalez-Martin et al, "**Membrane with supported internal passages**", US Patent No. 6,149,810, 2000

Janssen, G.L.M.; Overvelde, M.L.J, "**Water transport in the proton-exchange-membrane fuel cell: measurements of the effective drag coefficient**", Journal of Power Sources 101, pp 117-125, 2001

Katz, M. "**Fuel Cell Evaporative Cooler**", US Patent No. 5,206,094, 1993

Kunz H.R. "**Solid Polymer Electrolyte Fuel Cell System with Porous Plate Evaporative Cooling**", US Patent No. 4,824,741, 25th April 1989

McElroy, J.F. "**High Power Density Evaporatively Cooled Ion Exchange Membrane Fuel Cell**", US Patent No. 4,795,683, 1989

Rajalakshmi, N.; Sridhar, P.; Dhathathreyan, K.S. "**Identification and characterization of parameters for external humidification used in polymer electrolyte membrane fuel cells**", Journal of Power Sources, Vol. 109 (2), pp452-457, 2002

Reiser, C.A.; Sawyer, R.D. "**Solid Polymer Fuel Cell Stack Water management System**", US Patent No. 4,769,297, 6th September 1988

Rogers, G.F.C.; Mayhew, Y.R., "**Thermodynamic and Transport Properties of Fluids**", Fourth Edition, Blackwell Publishers, 1988

Sridhar, P.; Perumal, R.; Rajalakshmi, N.; Raja, M.; Dhathathreyan, K.S. "**Humidification Studies on polymer Electrolyte membrane fuel cell**", Journal of Power Sources, Vol. 101, pp72-78, 2001

Staschewski, D.; Mao, Z.Q. "**Hydrogen-air PEMFC operation with extraordinarily low gas pressures and internal humidification-conception and experimental prototype stack**", International Journal of Hydrogen Energy, Vol. 24, pp543-548, 1999

Susai, T.; Kaneko, M.; Nakato, K.; Isono, T.; Hamada, A.; Miyake, Y. "**Optimization of proton exchange membranes and the humidifying conditions to improve cell performance for polymer electrolyte fuel cells**", International Journal of hydrogen Energy, Vol. 26, pp631-637, 2001

Vanderborgh, N.E.; Hedstrom, J.;Huff,J. "**Advanced space Power PEM fuel cell systems**", Proceedings of European space power conference, 2-6 October , 1999, Vol. 294 (1), pp211, 1989

Watanabe, M; Uchida, H.; Seki, Y.; Emori, M; Stonehart, P. , "**Self-Humidifying Polymer Electrolyte Membranes for Fuel Cells**", Journal of the Electrochemical Society, Vol. 143, pp 3847, 1996

Watanabe, M. "**Solid Polymer Electrolyte Fuel Cell**", U.S. Patent 5,472,799, 1995

Watanabe, M.; Uchida, H.; Emori, M. " **Polymer Electrolyte Membranes Incorporated with nanometer-Size Particles of Pt and/or metal Oxides: Experimental Analysis of the Self-Humidification and Suppression of Gas Crossover in fuel Cells**", Journal of Physical Chemistry B, 102, pp 3129-3137, 1998

Watanabe, M.; Uchida, H.; Emori, M. "**Analyses of self-humidification and suppression of gas crossover in Pt-dispersed polymer electrolyte membranes for fuel cells**", Journal of the Electrochemical Society 145, pp 1137, 1998

Watanabe, M.; Satoh, Y;, Shimura, C. "**Management of the Water content in Polymer Electrolyte Membranes with Porous Fiber Wicks**", Journal of the Electrochemical Society 140, No.11 pp. 3190-3193, 1993

Weisbrod, K.R.; Grot, S.A.; Vanderborgh, N.E. "**Through-The-Electrode Model of a Proton Exchange Membrane Fuel Cell**" Proceedings of the 1st International

Symposium on Proton Conducting Membrane Fuel Cells, Electrochemical Society Proceedings Volume 95-23, pp152-166, 1995

Wheeler D.J.; Yi, J.S.; Fredley R.; Patterson, T.; VanDine, L. "**Advancements in Fuel Cell Stack Technology at International Fuel Cells**", Journal of New Materials for Electrical Systems 4, pp233-238, 2001

Wilson, M.S.; Moeller-Holst, S.; Zawodzinski, C. "**Efficient Fuel Cell Systems**", FY 2000, Progress Report for Fuel Cell Power Systems, US Department of Energy, pp88-90, 2000

Wilson, M.S. "**Ambient Pressure Fuel Cell System**", US Patent No. 6,117,577, 12th September 2000

Wilson, M. "**Fuel Cell Membrane Humidification**", U.S. Patent No. 5,952,119, 14th September 2000

Wood, D.L.; Nguyen, T.V. "**Effect of direct liquid water injection and interdigitated flow field on the performance of proton exchange membrane fuel cells**", Electrochimica Acta, Vol. 43, No. 24, pp3795-3809, 1998

Wynne, R.K.; Neutzler, J.K., Barbir, F.; Garau, V.; Pierce, W.E. "**Self Humidifiying Fuel Cell**", US Patent 6,207,312 27th March 2001

Zawodzinski, T.A.; Davey, J.; Valerio, J.A.; Gottesfeld, S., "**The water content dependence of electroosmotic drag in proton-conducting polymer electrolytes**" Electrochimica Acta, Vol. 40, No.3, pp297-302, 1995

Zawodzinski, T.A.; Derouin, C.; Radzinski, S.; Sherman, R.J., Smith, V.T., Springer, T.E.; Gottesfeld, S., "**Water Uptake by and Transport through Nafion 117 Membranes**", Journal of the Electrochemical Society, Vol. 140, no 4, pp 1041-1047, April 1993

Chapter 4

Evaporatively Cooled Fuel Cell Testing

4.1 Chapter Overview

This Chapter details section C of the work programme initially outlined in section 3.2.1 – operation of the FC rig with the cathode water injection mechanism used for humidification AND cooling – i.e. true EC operation.

From section B in Chapter 3, it was shown that humidification of the fuel cell by water injection directly to the cathode flow field resulted in a slightly lower performance than by pre-saturation of the air, for an equivalent amount of drawn current (Figs 3.28 - 3.30). However, in this test the cell temperature was externally controlled by the closed loop cooling water circuit internal to the anode PVDF block.

The primary objective of this Chapter was to determine whether water injection to the cathode flow field is an effective cooling mechanism and hence prove the concept of the EC fuel cell. Another secondary aim was to characterise the performance of the EC fuel cell by varying selected operational parameters.

4.1.1 Temperature gradient across fuel cell

In 'conventional' LC fuel cell operation, it is usually desirable for the plate based cooling mechanism to maintain an even distribution of temperature across the electrode area. A large thermal gradient will result in a non-uniform current density and the possibility of undetected local overheating, depending on the location of temperature sensors. Methods of promoting uniform temperature distribution in LC stacks have included varying the coolant channel surface area or frequently reversing the direction of the coolant flow, Kothmann (1986).

The absence of an external cooling circuit, i.e. no bulk heat transfer, in EC operation means there is likely to be a pronounced temperature gradient across the fuel cell electrode in the direction of the cathode gas tracks. This will be measured by the thermocouples located behind a single track of the cathode flow plate – see section 3.2.2.6. During operation the temperature at any point along the gas track will be dependent on many factors and any model attempting to predict the thermal gradient would have to account for, but not be limited to, the following:

- Local current density
- Rate of water evaporation
- Heat transfer across cell
- Temperature of liquid and gaseous species

In addition, as the PVDF gas manifolding blocks can not be perfect insulators there will be also be heat transfer from the cell to the surroundings and any model will also have to account for this. The assumption could be made that the highest current density would be obtained from electrode areas adjacent to the start of the cathode gas tracks due to the highest concentration of oxygen at this point– the oxygen reduction reaction being the primary rate limiting process – refer to section 2.2.1. However this area should also yield the fastest rate of evaporative cooling as here water is injected at the beginning of each track to individual dry air flows. Conversely, at the end of the cathode gas tracks the current density of the cell may be expected to be lowest due to the depleted oxygen but the bulk air flow will have been heated on passing through the cell and also contain a high ϕ value due to evaporation.

Hence, there are no straightforward assumptions that can be made about the shape of the thermal gradient in a fuel cell formed during EC operation, and there are too many unknown parameters to attempt to construct an effective model.

4.2 Section C –Evaporative Cooling

4.2.1 Experimental design

The main priority of these tests was proving the electrochemical and thermal stability of the fuel cell during EC operation, which meant obtaining steady-state operational data, i.e. equilibrated points of potential and temperatures, collected over considerable time periods. These 'endurance' tests will yield more crucial information on fuel cell behaviour relative to operating conditions than polarisation plots, where each potential point is only recorded a short period following a shift in the load current, thus providing no information on performance stability.

Other considerations in the design of the tests:

- It was desirable to observe the changes in cell potential and gas track temperatures when 'shifting' from LC operation (using the cooling circuit in the anode PVDF block) to EC operation. This step would show the formation of a thermal gradient which was unique to the specific operating conditions.

- It was important to observe the effect of differing water and air flowrates on temperatures and potential, as these will be crucial factors in an EC fuel cell system.

- The need to observe dynamic changes in potential and temperature meant it was necessary to set a data logging rate of every second or few seconds for the duration of each test.

The first tests encapsulate all of the above factors including a switch from LC to EC operation followed by progressive shifts in the air and water flow rates. This was to be done firstly with a cell operating pressure of 0.5 bar.g and then repeated at 1.0 bar.g. The difference in the obtained thermal gradient between the two tests would illustrate the effect of operating pressure on EC fuel cell behaviour. In addition comparisons could be made with later LC tests, at the same *average* temperature, to specifically show the effect of a temperature gradient across the cell.

Other tests were designed to show dynamic responses of cell potential and temperature to increases in load current and the rate of liquid water injection. Altogether, this series of tests would prove the EC concept and provide a basic understanding of cell performance and the influence of operating conditions.

4.2.2 General test procedures

The equipment set-up for these tests was as shown previously in Fig. 3.15. The pre-testing procedures as detailed in appendix C were carried out prior to each test with the calculations used for determining the gas and water supply flowrates as detailed in appendix A1. The rate of current drawn from the fuel cell was controlled manually with the load unit. For all of these tests the stoichiometry of hydrogen was kept constant at 1.5 and not humidified. In a similar manner to the tests detailed in Chapter 3, a counterflow configuration of reactant gases was used.

To synchronise the collection of data it was essential to start the multimeter software, measuring fuel cell potential, and DaqView software, measuring thermocouple readings, both logging simultaneously. When switching from LC to EC operation it was imperative that when the cooling circuit was switched off, the water injection to the cell cathode from the HPLC pump immediately started. Any delay in this process would result in extremely rapid overheating of the fuel cell and possible damage to the MEA. In addition, the test was stopped if any temperature reading became in excess of 85°C

4.2.3 Shift in water and air flowrates

In these tests a constant current of 100 Amps was delivered by the fuel cell throughout, with a step increase in the air flowrate followed by reductions in the water injection rate from the HPLC pump. This was done firstly, maintaining anode and cathode back-pressures of 0.5 bar.g and then, secondly, with back-pressures of 1.0 bar.g. Steady state conditions were allowed to establish before a change was made in the water or air flows.

4.2.3.1 Operation at 0.5 bar.g

The fuel cell potential and temperature readings for the first two-and-a-half hours of the test are illustrated in Fig. 4.01a. The x-axis represents time, t in hrs:mins:secs format, the left hand y-axis, fuel cell potential in Volts and the right hand y-axis, thermocouple readings in °C. The black plot corresponds to cell potential and the coloured plots correspond to thermocouple temperature readings at positions along the cathode gas track, as shown on the key. Significant points during the test are labelled with letters and the embedded table defines the most crucial operating conditions at these points. The ϕ value for air is calculated assuming all injected water changes state from liquid to vapour, using Equations 3.03 and 3.07. No product water or anode humidification by back diffusion was accounted for in these calculations as these two mechanisms were assumed to be equivalent.

The data logging commences with 100 Amps being drawn from the fuel cell, supplied with an air stoichiometry of 2, equivalent to 3.32 SLPM, pre-humidified to approximately 100% RH by steam, with the water cooling circuit operational.

At point **'A'** the fuel cell temperature was controlled to approximately 60°C. A point of note is that the end of the gas track is relatively cool compared to all other positions even though this is the opposite side to where the cooling circuit water enters the anode PVDF block. This possibly indicates increased external cooling at track extremities or low current density at the end of the tracks

At point **'B'** the small diaphragm pump supplying the cooling water was switched off and the two-way valve downstream of the HPLC pump adjusted so that the humidification method was switched from steam saturation of the reactant air to a direct injection of water to the cathode. The water injection rate was increased to 2.7 cc/min which corresponded to an air: water molar ratio of 1:1. This rate was chosen as it is well in excess of 100% RH for the air flowrate (at this temperature the water flowrate is calculated to correspond to an RH of 447%). The temperatures were seen to rise rapidly and a thermal gradient began to form. Over the proceeding 90 minutes, the potential

Fig 4.01a EC fuel cell analysis - Shifts in water and air flowrates 100 Amps drawn, 0.5 bar.g operating pressure

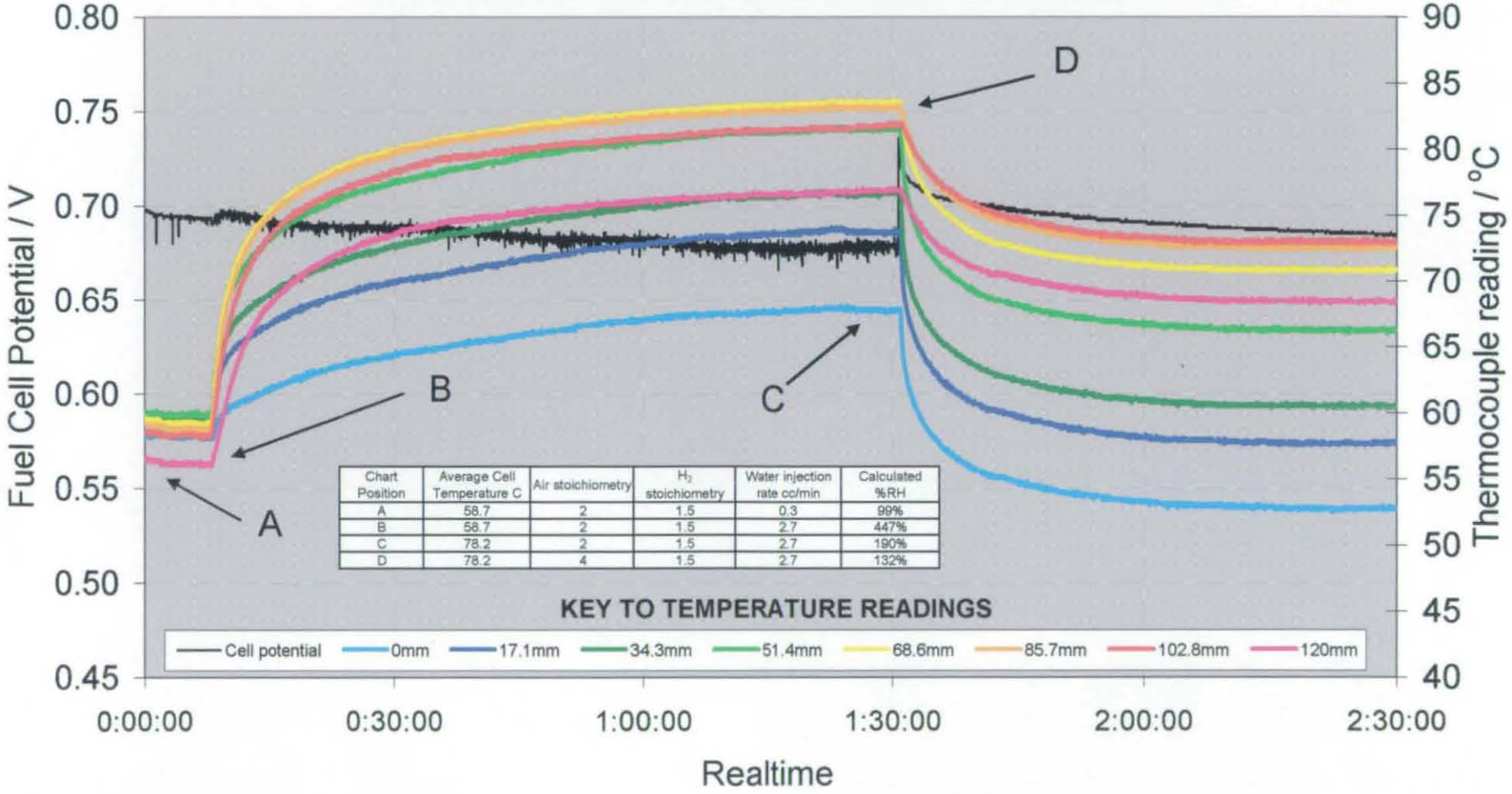

Chart Position	Average Cell Temperature C	Air stoichiometry	H_2 stoichiometry	Water injection rate cc/min	Calculated %RH
A	58.7	2	1.5	0.3	99%
B	58.7	2	1.5	2.7	447%
C	78.2	2	1.5	2.7	190%
D	78.2	4	1.5	2.7	132%

steadily decreased, becoming increasingly oscillatory in nature and the temperature readings which, initially sharply rose, levelled off asymptotically in a similar manner to a time constant response.

At point 'C' steady-state electrochemical and thermal conditions were established with the potential fluctuating with an average value of 0.675 V and an average gas track temperature reading of 78.2°C. The temperature at the start of the gas track, 0 mm, was the lowest at approximately 68°C and the highest temperature was approximately 84°C at a position 68.6mm down the gas track. As the start of the track was likely to be a position where the current density is high, due to high concentration of gaseous oxygen, it is clear the liquid water was evaporating rapidly immediately following injection into the cathode flow-field. The temperature at the end of the track, 120 mm was unusually low, in a similar manner seen at point A.

The oscillations in the cell potential value were primarily due to the constantly changing rates of oxygen diffusion to catalyst sites as water was continually flushed out and re-accumulated in the gas channels and diffuser pores. Clearly the presence of two phase flow had increased from point A and these oscillations may be a distinctive feature of a fuel cell utilising humidification via a water injection method.

At point 'D', the air stoichiometry was increased to 4, a shift in volumetric flow rate to 6.64 SLPM. All temperature readings dropped rapidly and the cell potential sharply increased by approximately 50 mV. The latter effect was caused by water droplets that had been previously entrained in the cathode diffuser pores and flow channels being 'blown out' by the sudden large shift in air flow allowing an increased rate of oxygen diffusion to catalyst sites. The 'levelling off' effect of potential value observed over the next hour was due to water being re-entrained in the diffuser until equilibrium between water accumulation and evaporation was re-established.

The decrease in temperatures immediately following point D, was due to an increased degree of evaporative cooling caused by the decrease in water vapour partial pressure. It is also observed how the change in individual thermocouple reading after the air volumetric flow increase is related to the position along the gas track. The thermocouple at the start of the track, 0 mm, registers a change of 68°C to 54°C in 20 minutes, a drop of 14°C, but at the end of the track this change is 76.5°C to 69.5°C - only 7°C. It is also observed that the oscillation of the cell potential value has reduced significantly due to a lower degree of two-phase flow, resulting in less restricted oxygen transport to catalyst sites.

An illustration of the fuel cell potential and temperature readings for the final two hours of this test is shown in Fig. 4.01b – the format of the chart is the same as that of Fig. 4.01a. Point **'E'** shows the steady state conditions reached after the shift in air flowrate at point D. The cell potential is 0.686 V and the average cell temperature is 65.3°C with the peak temperature of 73.0°C at a position 102.8 mm down the gas track.

For the remainder of the test, the rate of liquid water injection was periodically reduced. At point **'F'** the rate of water injection was approximately halved, from 2.7 cc/min to 1.3 cc/min. After approximately half-an-hour, the cell potential has fallen to around 0.675 V and the temperatures have risen 2-4 °C, depending on the position down the gas track. In a similar manner to Fig. 4.1a, a correlation is noticed where the temperature undergoes the largest change at the beginning of the gas track. At point **'G'** the water supply was then reduced to 1.0 cc/min with the same effect seen and the steady state cell potential dropping to 0.665 V, the average cell temperature rising to 69.3°C. At point **'H'** the water supply rate was halved to 0.5 cc/min, which corresponded to an air relative humidity of 53%. With this low moisture content the air flow was able to strip increased rates of water from the MEA, as reflected in the rapidly increasing thermocouple readings and the irregular, falling value of potential. The test was stopped before any permanent damage occurred to the MEA.

One major point of interest from this test was that after every reduction in the water injection rate (with the exception of point H) the potential dropped quickly and then levelled off. This illustrates changes in the membrane hydration state and, similar to section 3.3.3.3, shows that performance can be improved with air ϕ values greater than 100% RH. Therefore, although there may be two-phase flow along the track, if the gaseous air is not saturated at 100% RH, the MEA adjacent to the gas track at that point may be stripped of its water content as liquid water fails to penetrate the diffuser.

Fig 4.01b EC fuel cell analysis - Shifts in water and air flowrates
100 Amps Drawn, 0.5 bar.g operating pressure

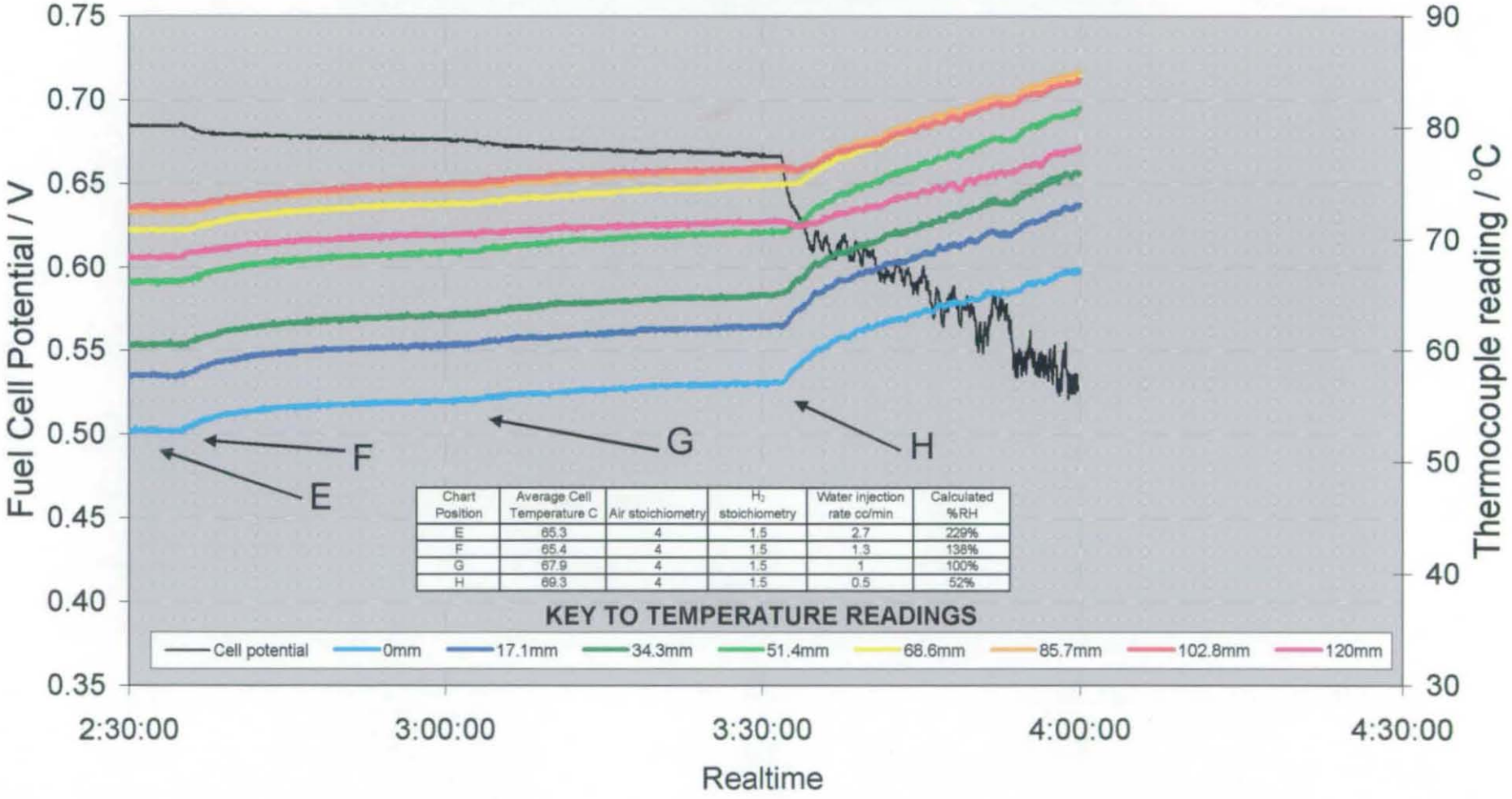

Chart Position	Average Cell Temperature C	Air stoichiometry	H_2 stoichiometry	Water injection rate cc/min	Calculated %RH
E	65.3	4	1.5	2.7	229%
F	65.4	4	1.5	1.3	138%
G	67.9	4	1.5	1	100%
H	69.3	4	1.5	0.5	52%

4.2.3.2 Operation at 1.0 bar.g

This was a repeat of the previous test except undertaken with anode and cathode operating pressures of 1.0 bar.g. Refer to Fig 4.02a which illustrates the fuel cell potential and thermocouple readings for the first two-and-a-half hours of the test - the chart has the same format as Figs. 4.01a and 4.01b.

The data logging commences with 100 Amps being drawn from the fuel cell with a supplied air stoichiometry of 2, equivalent to 3.32 SLPM, and approximately 100%RH humidification by steam with the water cooling circuit controlling the temperature to 60°C. The potential of the fuel cell at point **'A'** was 0.715 V. Again, the end of the gas track was observed to be relatively cool compared to all other positions.

At point **'B'**, the external water cooling circuit was turned off and the humidification method switched from, steam saturation of the air, to water injection with a delivery rate of 2.7 cc/min, i.e. corresponding to an even air/water molar ratio. The temperatures were seen to rise rapidly and a positive thermal gradient begins to form. For the following 85 minutes, a similar cell potential behaviour is observed as that of Fig 4.01a, i.e. increasing oscillation.

At point **'C'**, the fuel cell reached steady state thermal and electrochemical conditions with the potential oscillating at a value of 0.717 V. The average track temperature is 79.8°C, with the highest temperature of 84.9°C at a position 85.7 mm down the gas track. It is noticed that all of the temperature readings are higher than at point C in Fig. 4.01a which corresponds to the partial pressure law outlined in Chapter 3, with a lesser proportion of water able to be evaporated due to higher value of the total pressure.

At point **'D'** the air stoichiometry was increased to 4, corresponding to 6.64 SLPM, which produced a resultant jump in fuel cell potential by approximately 40 mV and rapid dip in temperatures, similar to that observed previously in Fig. 4.01a. Due to the decrease in water vapour partial pressure immediately following point D, an increased degree of evaporative cooling causes the decrease in temperatures. It was again observed how the level of oscillation in the cell potential value is reduced significantly after an increase in the air flow.

The final two hours of the test is illustrated in Fig. 4.02b. As steady state operational conditions were reached at point **'E'** the average cell temperature was 67.3°C with the highest temperature of 75.2°C at a position 102.8 mm down the gas track- i.e. the same position as in Fig. 4.01b. The cell potential settles to a value of 0.708V, actually below the value of 0.717 V obtained with an air stoichiometry of 2.

Fig 4.02a EC fuel cell analysis - Shifts in water and air flowrates
100 Amps drawn, 1.0 bar.g operating pressure

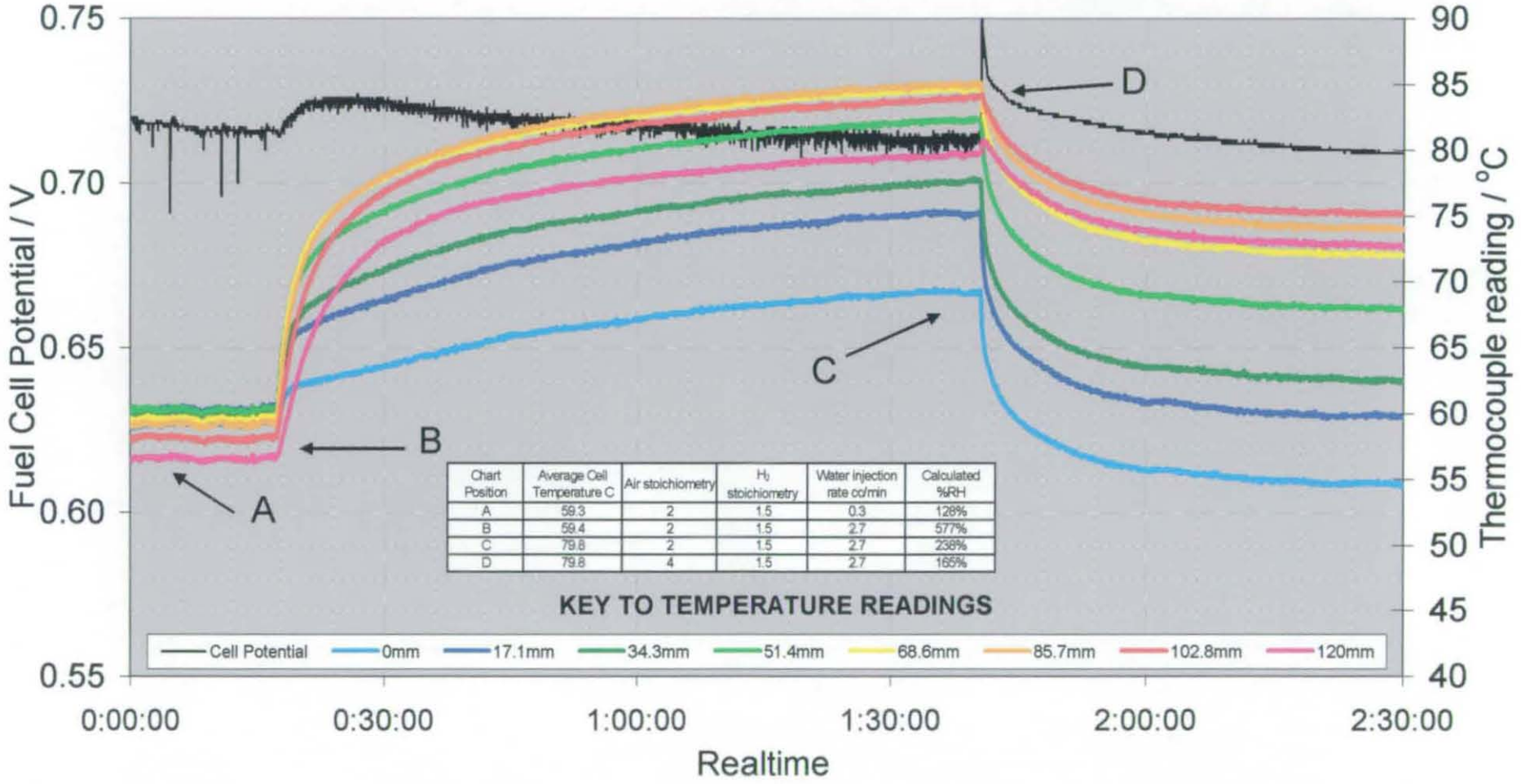

Chart Position	Average Cell Temperature C	Air stoichiometry	H_2 stoichiometry	Water injection rate cc/min	Calculated %RH
A	59.3	2	1.5	0.3	128%
B	59.4	2	1.5	2.7	577%
C	79.8	2	1.5	2.7	238%
D	79.8	4	1.5	2.7	165%

Fig 4.02b EC fuel cell analysis - Shifts in water and air flowrates
100 Amps drawn, 1.0 bar.g operating pressure

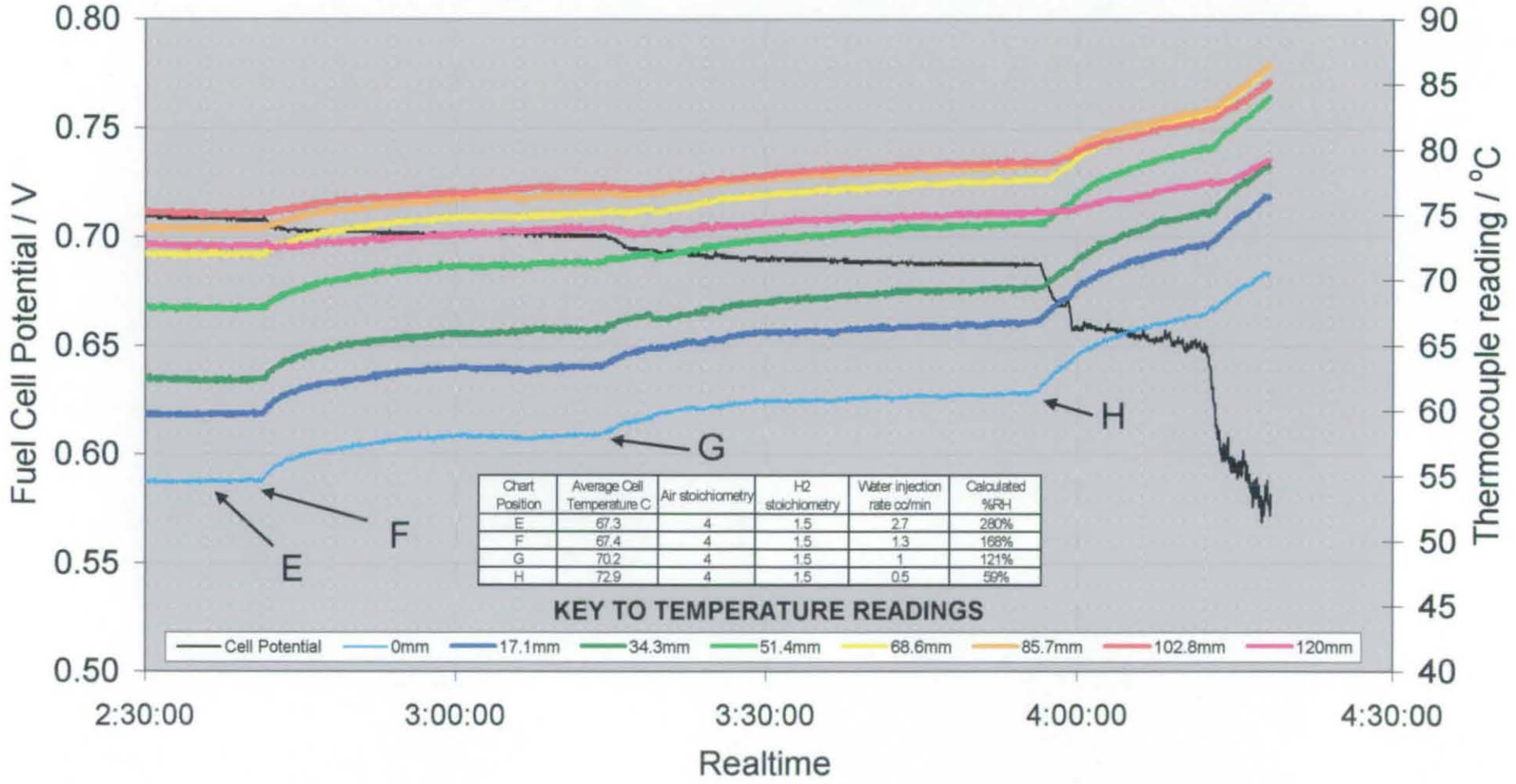

Chart Position	Average Cell Temperature C	Air stoichiometry	H2 stoichiometry	Water injection rate cc/min	Calculated %RH
E	67.3	4	1.5	2.7	280%
F	67.4	4	1.5	1.3	168%
G	70.2	4	1.5	1	121%
H	72.9	4	1.5	0.5	59%

Similar to the 0.5 bar.g test, the rate of liquid water injection from the HPLC pump was then periodically reduced, from 1.3 cc/min to 1.0 cc/min and finally to 0.5 cc/min - points F, G and H respectively on the chart. The behaviour of the fuel cell temperature rises and the potential drops were almost identical to those seen in Fig. 4.01b as the membrane hydration state is gradually lowered. At point **'F'** the rate of water injection was halved from 2.7 cc/min to 1.3 cc/min After around half-an-hour (point **'G'**) the temperatures increased around 2-4°C, depending on the position down the gas track with an average of 70.2°C and the steady-state potential reduced to 0.7 V. The water injection rate was then reduced to 1.0 cc/min and at point **'H'** the temperature reached 72.8°C and the potential dropped to 0.687 V. Following this, the water injection rate was halved to 0.5 cc/min, corresponding to a ϕ value for the air flow of 59% RH. As before, with an insufficient proportion of water in the air flow, water is stripped from the membrane structure, the temperatures rise rapidly, the potential becomes erratic and the test is stopped.

4.2.3.3 Comparison of temperature maps

Information on EC operation can be obtained from further examination of the steady-state potential and temperature data from the previous tests. The average gas track temperature readings from points C and E on Figs 4.01 and 4.02 is shown in Fig. 4.03.

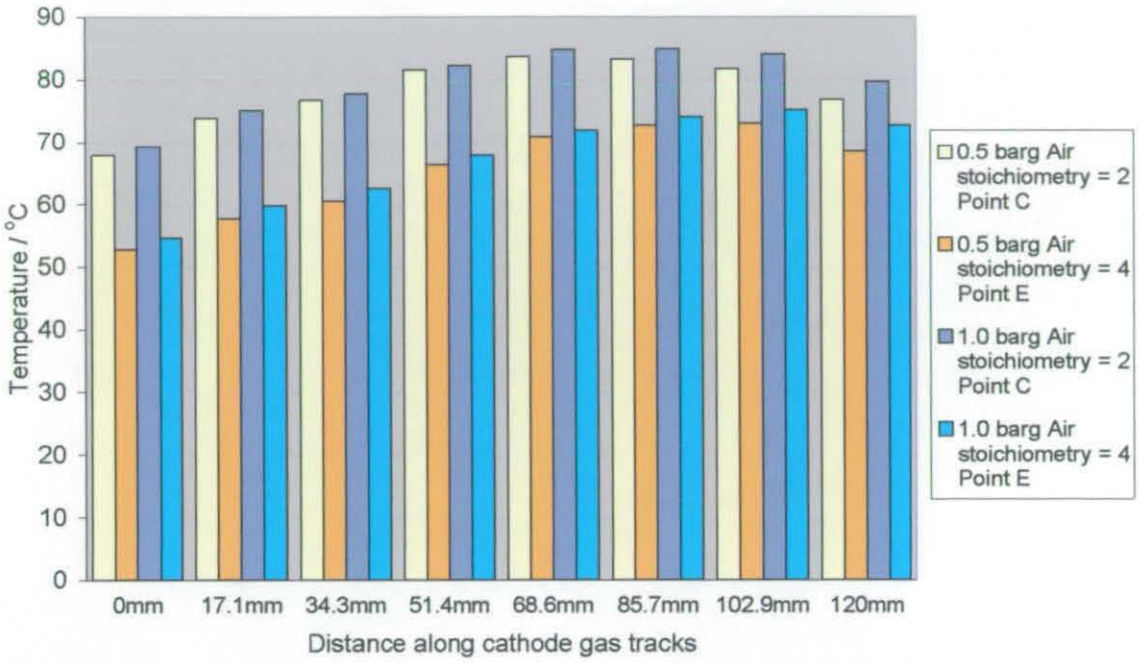

Fig. 4.03: Comparison of gas track temperatures from Figs. 4.01 and 4.02

It is observed that, with 100 Amps being drawn from the EC fuel cell, operating with an air stoichiometry of 4 produces an average temperature approximately 10°C lower than when operating with an air stoichiometry of 2. There is a slight elevation in all temperature readings for points C and E when operating at 1.0 bar.g.

For both fuel cell operating pressures, operating with an air stoichiometry of 4 results in the highest temperature being obtained at a position 102.9 mm along the cathode track whereas with an air stoichiometry of 2 the position of the highest temperature was 68.6 mm along the cathode track. This can be explained as, with the higher air flowrate, there is a higher current density over the last half of the electrode area due to increased concentration of oxygen.

4.2.3.4 Comparison of steady state fuel cell potentials

The fuel cell potentials at points A, C and E in Figs 4.01 and 4.02 are illustrated in Fig. 4.04.

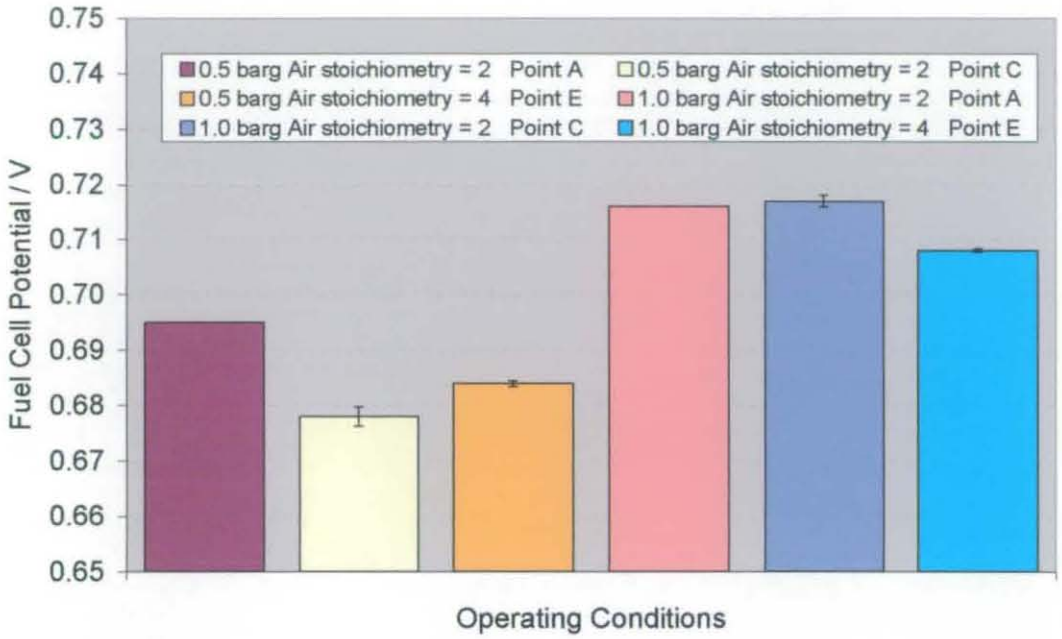

Fig. 4.04: Comparison of fuel cell potential values from Figs. 4.01 and 4.02

The key operating points obtained when using the cell in evaporative cooling mode (C and E) follow the trends seen in the polarisation plots as shown in Chapter 3 with the lowest potential, 0.678 V, obtained at low operating pressure and low air stoichiometry. However, it is observed that for an operating pressure of 1.0 bar.g the fuel cell potential with an air stoichiometry of 4, (0.708 V), was lower than that with 2, (0.717 V). In the polarisation curves of section 3.3.2.3, using a higher air stoichiometry produced a better performance even at the higher operating pressure. However the potential readings for the polarisation curve were taken after a short time period whereas on the endurance charts it is seen how the performance slowly reduces in value and oscillates as steady-state conditions are reached.

In the 0.5 bar.g test, on switching from operating points A to C, the fuel cell potential drops but at 1.0 bar.g the performance of points A and C is almost equivalent. This could be due, in part, to the difference in air ϕ values, where for 1.0 bar.g this is calculated to be 238% RH and for 0.5 bar.g is 190% RH. As illustrated earlier, calculated humidity values above theoretical full saturation can still influence the cell performance.

The potential values at points C and E in Fig. 4.04 are shown with error bars which reflect the size of the oscillations observed. The error values have been calculated using the standard deviation formula[1], Equation 4.01, and the potential values over the preceding 5 minutes before the point as the sample range.;

$$\sigma_{error} = \sqrt{\frac{n\sum x^2 - \left(\sum x\right)^2}{n(n-1)}} \qquad \textbf{Equation 4.01}$$

In the test using an operating pressure of 0.5bar.g the standard deviation of the oscillation was calculated to be 1.7 mV at point C and 0.7 mV at point E. In the second test at 1.0 bar.g the value of σ_{error} is 1.1 mV at point C and 0.3 mV at point E. As detailed in section 4.2.3.1, the size of the oscillation reflects the rate of oxygen diffusion to catalyst sites, and is less prominent for a higher air supply stoichiometry.

[1] Where x is a particular value and n is the number of values

4.2.4 Shift in drawn current

In the previous sections rapid changes in temperature were observed in response to changes in water and air flowrates when holding a fixed drawn current of 100 Amps from the fuel cell. The next test was performed to show the thermal response of the EC fuel cell to a large upward shift in the load current. Realistic conditions experienced by a fuel cell in a power generation application, such as an automotive propulsion system, will involve continual transient changes in power demand so this would be a useful test.

The cell potential and temperature readings for the approximate three hours duration of the test are illustrated in Fig. 4.05 - this chart has the same format as Figs 4.01 and 4.02. The data starts logging with the fuel cell delivering a nominal load of 20 Amps, running with an externally controlled temperature of 25°C, an operating pressure of 0.5barg and supplied with an air stoichiometry of 2. The measured potential at this point, **'A'**, is 0.766 V.

At point **'B'** the external cooling circuit was switched off and water directly injected at a rate of 0.2 cc/min, corresponding to an air : water molar ratio of 2 : 1. The temperature of the fuel cell rises and, to a small extent the potential follows this increase due to the reduction in ohmic membrane resistance at higher temperatures.

Steady state is reached at point **'C'** with the cell potential settling at 0.783 V with the average track temperature now 40.4°C with a slight thermal gradient having formed. At point **'D'**, the load current was raised to 80 Amps and the water injection rate increased to 1.1cc/min in order to maintain the air: water molar ratio of 2:1. The temperatures rise rapidly and the cell potential, which immediately dropped after the current shift, starts to slowly rise and then at approximately 1:30:00 hours, begins to fall slightly before levelling off at approximately 1:40:00 hours. This behaviour reflects a water balance being established between the hydration state of the membrane and the restrictions in oxygen transport. The initial rise can be attributed to the higher current producing an elevated membrane hydration level through the extra product water being generated adjacent to the membrane, and hence lowering internal cell ionic resistance. As this water starts to occupy more diffuser pores adjacent to the membrane and restricts oxygen transport, the performance starts to drop. Equilibrium is eventually reached with the increased oscillations of the potential value confirming the restrictions on oxygen transport.

At point **'E'** steady state is reached with the voltage potential settling at 0.685 V with an average track temperature of 76.8°C.

Fig 4.05 : EC fuel cell analysis
shift in current density 0.1 A/cm^2 to 0.4 A/cm^2

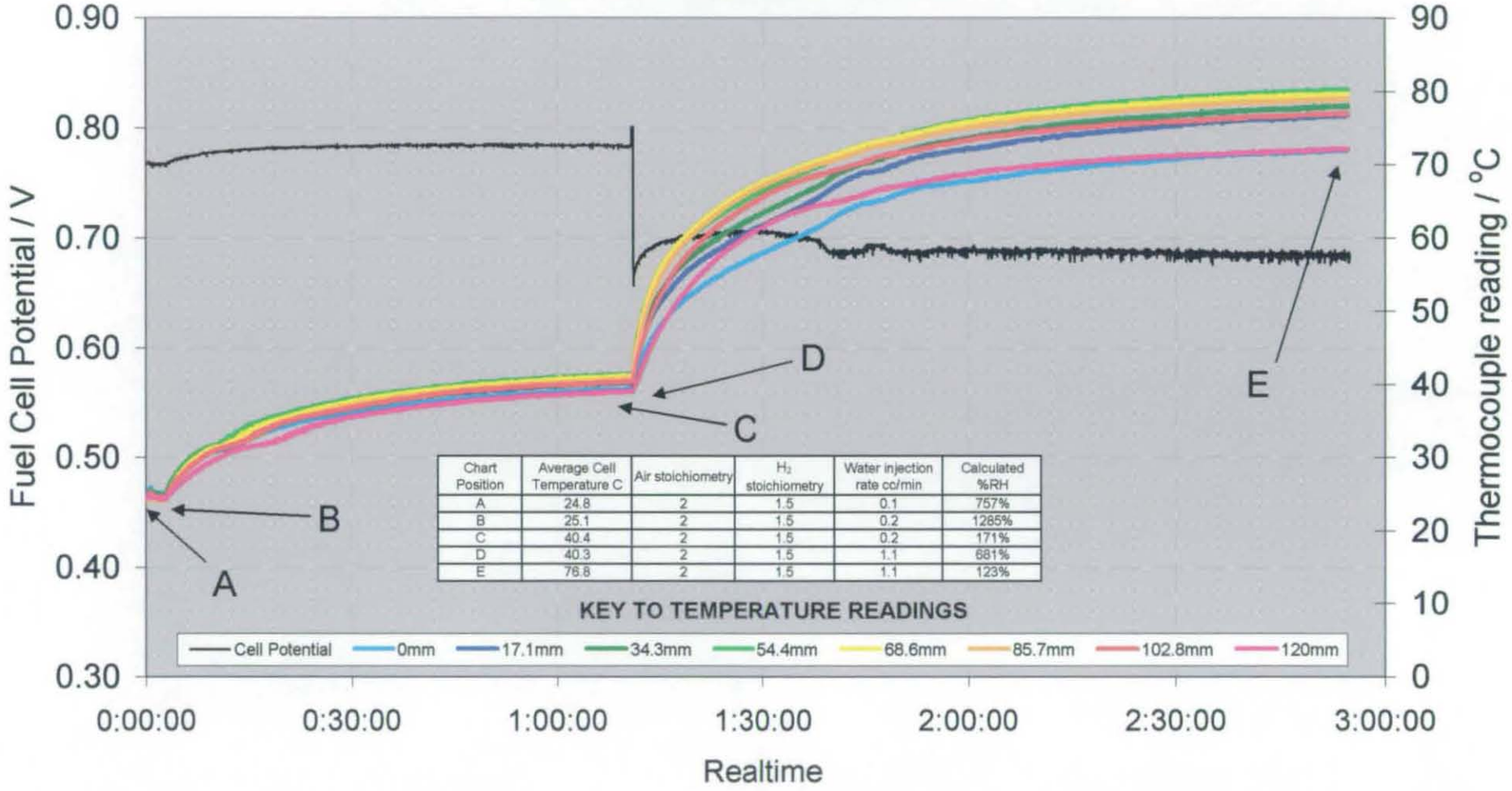

Chart Position	Average Cell Temperature C	Air stoichiometry	H_2 stoichiometry	Water injection rate cc/min	Calculated %RH
A	24.8	2	1.5	0.1	757%
B	25.1	2	1.5	0.2	1285%
C	40.4	2	1.5	0.2	171%
D	40.3	2	1.5	1.1	681%
E	76.8	2	1.5	1.1	123%

4.2.5 Shift in water injection rate

The final test was undertaken to determine the electrochemical and thermal fuel cell responses to a large upward shift in the rate of liquid water injection.

The fuel cell potential and temperature data for the approximate three hours of test duration are illustrated in Fig 4.06 - the chart has the same format as Figs 4.01, 4.02 and 4.05. The data logging starts with the cell initially drawing 80 Amps at an externally controlled temperature of 60°C, an operating pressure of 0.5 bar.g, air humidification to approximately 100% RH by steam and supplied with an air stoichiometry of 2. The fuel cell at point **'A'** has an average potential of 0.732 V.

At point **'B'** the external cooling circuit was switched off and water directly injected to the fuel cell at a rate of 1.1 cc/min (2:1 air water molar ratio). The fuel cell temperature rises and the potential drops, steady state conditions are reached after approximately 80 minutes. The increased oscillations in potential value and reduced performance as seen previously

At point **'C'** equilibrium has been established, the operating conditions here are identical to point E on Fig. 4.04. The potential and temperature are very similar showing the good repeatability of the tests.

At point **'D'**, the water injection rate was increased to 9.9 cc/min - the delivery limit of the HPLC pump. There is a very sharp drop in temperatures as an increased level evaporative cooling occurs. The sudden increase in potential corresponds to an increased level of membrane hydration and the fuel cell potential value begins to undergo a greater degree of oscillation.

After approximately 1 hour, steady-state conditions have been established, labelled as point **'E'** on the chart. The potential has settled at 0.70 V and the average gas track temperature is just below 60°C.

It was expected that with this very large water injection rate that degradation in potential value and performance stability would occur as the diffuser would be completely flooded, especially with an RH value approaching a calculated value of 623% RH towards point E, however the fuel cell copes ably. This may be due in part to the configuration of the interdigitated plate flow field which is studied in more detail in Chapter 6.

Fig 4.06 EC fuel cell analysis
shift in water supply - 1.1 cc/min to 9.9 cc/min, 80 Amps drawn

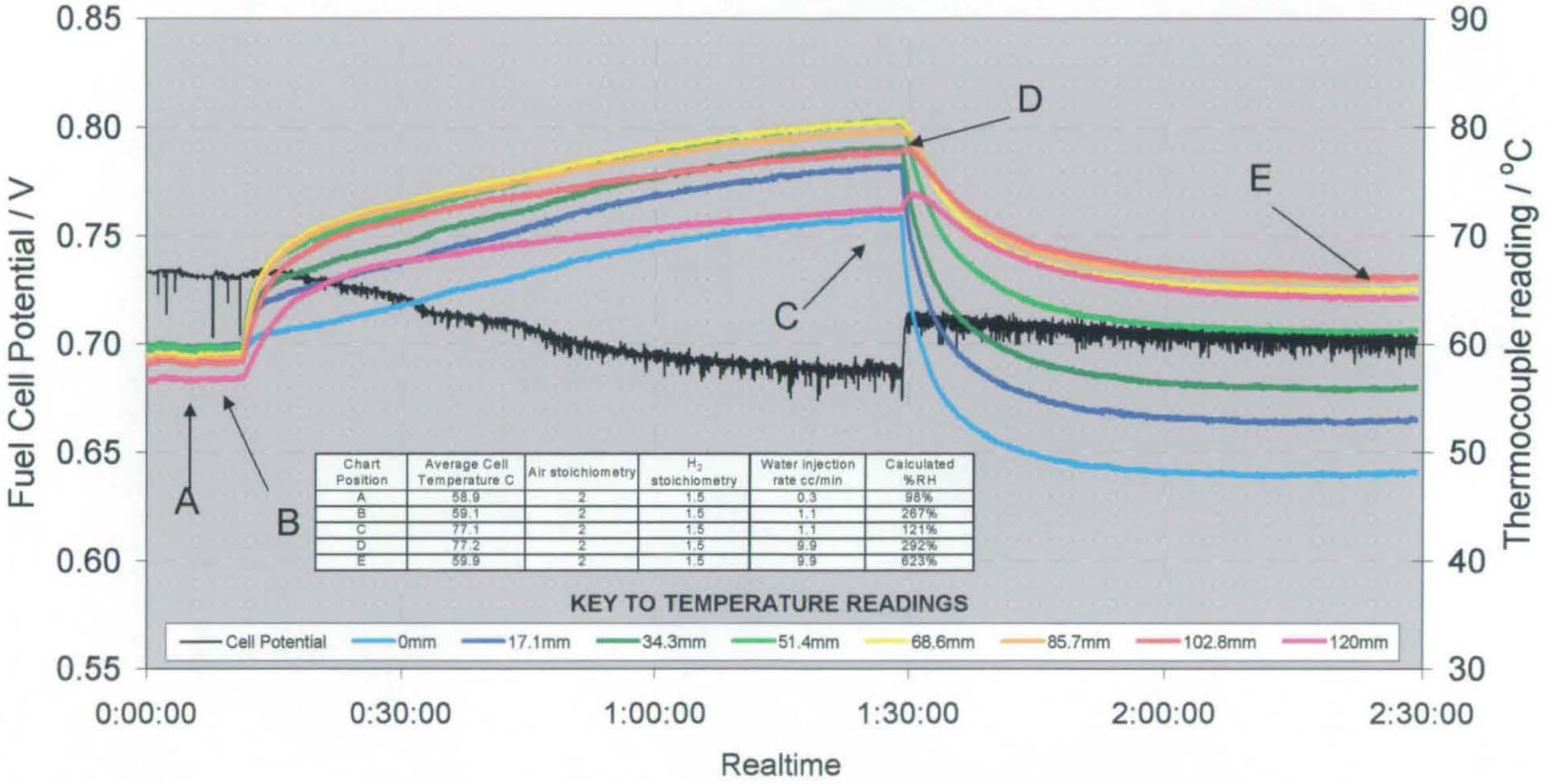

Chart Position	Average Cell Temperature C	Air stoichiometry	H_2 stoichiometry	Water injection rate cc/min	Calculated %RH
A	58.9	2	1.5	0.3	98%
B	59.1	2	1.5	1.1	267%
C	77.1	2	1.5	1.1	121%
D	77.2	2	1.5	9.9	292%
E	59.9	2	1.5	9.9	623%

It is also noticed that the track position with the highest temperature has shifted from 51.4 mm at point 'C' to 102.8 mm at point E. This change in the peak temperature position was noticed earlier when a higher air stoichiometric flow was introduced to the fuel cell – Fig. 4.03. This indicates that at point C, where the relative humidity of the air was 121% RH, the extent of evaporation was increased with extra water delivery. This was accompanied by an increase in performance due to an elevated water content in the membrane.

4.2.6 Evaporative cooling performance comparison

The steady-state EC performances illustrated in Figs 4.01 and 4.02 were then to be compared with performances obtained from the fuel cell, thermally controlled by using the water cooling circuit internal to the anode PVDF block, and utilising both air pre-saturation and liquid water injection humidification mechanisms while keeping all other operating conditions identical. Essentially, this was a comparison of EC operation and LC operation, similar to section B in Chapter 3.

The steady state potential values from Figs 4.01b and 4.02b, where the water injection rate was intermittently lowered from 2.7 cc/min down to 0.5 cc/min, were used as the EC performance data. For the LC comparisons, additional tests were carried out using the liquid injection and humidification of the air by steam, with the fuel cell controlled at the *average* temperature of the gas track for the equivalent point in the EC test. This was done for each of the water injection rates, at points F, G and H and also at the very end of the test when the potential became unstable, respectively corresponding to 2.7 cc/min, 1.3 cc/min, 1.0 cc/min and 0.5 cc/min. The steady state potential values were recorded after one hour operation at 100 Amps. To keep the tests consistent with the EC analysis, the gases were delivered to the fuel cell in a counterflow configuration with the dry hydrogen delivered at a stoichiometry of 1.5 and air delivered at a stoichiometry of 4.

The potential values from the fuel cell using the different operating modes at a pressure of 0.5 bar.g are shown in Fig. 4.07.

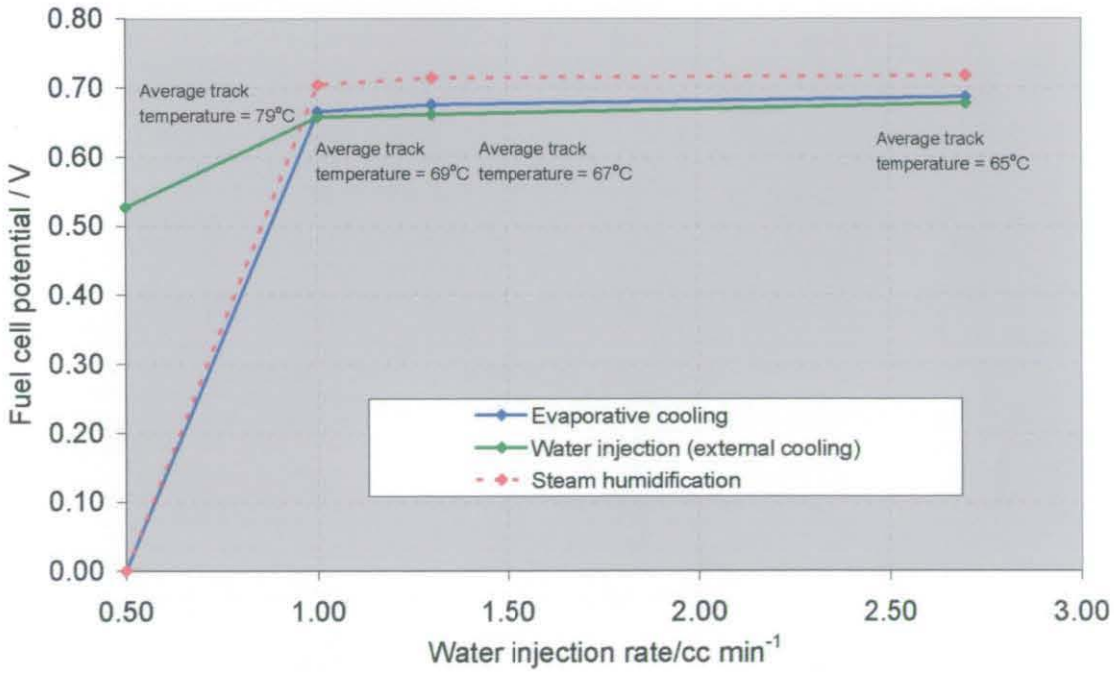

Fig. 4.07: Comparison of fuel cell performance obtained at 100 Amps using various cathode humidification methods – 0.5 bar.g

The potential in EC operation was taken as zero at the conditions where the cell performance became unstable, i.e. point H on Fig. 4.01b). A similar trend to Figs 3.26 - 3.28 is observed, with steam injection providing superior fuel cell performance - an exception being the lowest water injection rate. The EC operation, with the associated cell temperature gradient, produced a slightly elevated performance than LC operation with water injection.

The tests are repeated with an operating pressure of 1.0 bar.g – the results are shown in Fig. 4.08.

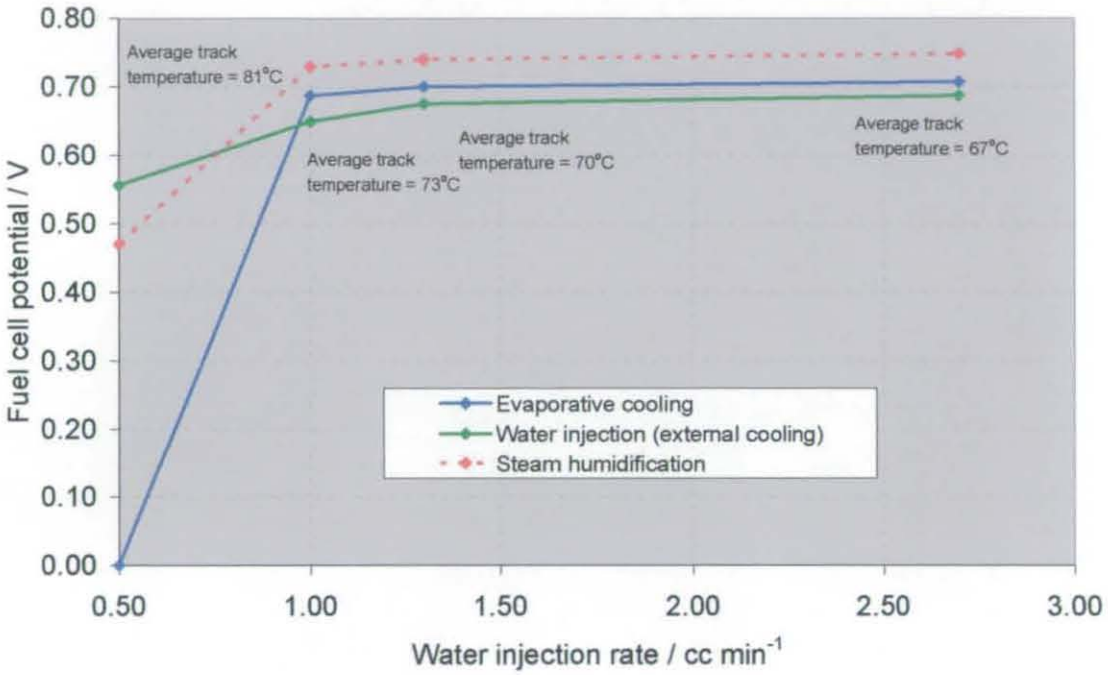

Fig. 4.08: Comparison of fuel cell performance obtained at 100 Amps using various cathode humidification methods – 1.0 bar.g

It is observed the steam humidification of the air again produces superior fuel cell performance and unlike Fig, 4.07 gives a stable performance with the lowest injection rate of 0.5 cc/min. EC operation gives a potential approximately 25 mV higher than LC mode water injection for input rates above 1.0 cc/min

From these results it can be stated that a higher temperature down the gas track improves local current density by reducing flooding and this is responsible for the elevated performance over water injection using the external cooling circuit.

4.3 Conclusions

The main conclusions drawn from the work on the evaporatively cooled fuel cell detailed in this Chapter are as follows:

- Evaporative cooling of a PEM fuel cell, via the mechanism of water injection to the cathode, has been demonstrated to be an effective combined humidification and cooling technique. The temperature profile data from the endurance tests illustrated that for this particular water delivery configuration, the cooling effect is rapid resulting in a lower temperature at the beginning of the cathode tracks.

- An increased air flow rate is shown to have a dramatic effect in reducing the EC fuel cell temperature. This effect could be considered for implementation in a control strategy for EC fuel cell systems where, during periods of high power, the air stoichiometry is increased for short periods, possibly a 'pulsing' effect.

- The fuel cell coped well with large and rapid shifts in current and water supply, although the latter may be partly due to the effectiveness of the forced diffusion cathode flow-field. An oscillating fuel cell potential value was observed and explained by the restrictions in oxygen transport to catalyst sites presented by two-phase flow in gas tracks. A higher air stoichiometry increased the stability of the potential value.

- The rate of water injection for optimum fuel cell performance was shown to be many times higher than the calculated amount for 100% RH, for this particular fuel cell configuration. The majority of the injected water content may take the form of droplets on the diffuser backside or outer layers. The actual rate of evaporation of the injected water by the air flow will be a function of gas track depth and width and possibly more crucially, the choice of diffuser material.

- The effect of an insufficient membrane water content was observed in Figs 4.01b and 4.02b when the injection rate was reduced to 0.5 cc/min.

- The development of an equilibrated membrane water content, balanced between evaporation and production, was observed after a shift in the current density drawn from the fuel cell.

Future work

It was considered advantageous to investigate some of the issues that would arise from scaling-up the evaporative cooling system to a complete stack – this is discussed in Chapter 5.

An in-depth analysis of humidification by direct cathode liquid water, studying the effects of flooding and choice of flow-field would be possible using a measurement of the distribution of current down the gas track. This could be related to some of the thermal mapping data obtained in this Chapter - this study is outlined in Chapter 6.

To promote a more even temperature distribution in an EC fuel cell stack it could be worth considering a design with alternate cathode flow directions in adjacent cells by using two sets of air manifolding across the stack and two feed points. The heat transfer between fuel cells would maintain a more even temperature using this 'staggered' configuration.

4.4 References

Kothmann, R.E. "Fuel Cell System with Coolant Flow Reversal", US Patent No. 4,582,765, 1986

Chapter 5:

EC Fuel Cell System Modelling

5.1 Chapter Overview

Modelling of individual fuel cells and systems provide effective diagnostic tools for performance optimisation, with the additional ability to reduce cost and time during the development of a finalised design. In effect, they move research and development away from the 'trial and error' type of experimental design and substantially increase the quality of work undertaken.

In this Chapter, using polarisation data obtained in earlier research, liquid cooled, LC, and evaporatively cooled, EC, steady state fuel cell system models are constructed. In addition, a brief overview is provided of the modelling of both single fuel cells and systems, with examples provided from the literature. These are used to illustrate the crucial role of system parasitic losses and the associated advantages of EC operation.

5.1.1 Single FC modelling

There are a number of published single PEM fuel cell models which are classified as either analytical models - based solely on theory, or empirical models - based on experimental results to a varying degree. These are further described as follows:

- Analytical models – These purely mathematical models deal with the fundamental physical phenomena occurring in PEM fuel cells, and attempt to relate the influence of operating parameters (temperature, pressure and humidity) to electrochemical performance. They describe one or more areas of a fuel cell i.e., gas channel and diffuser layers, catalyst layer or polymer membrane where the crucial phenomenon, respectively is: transport of gaseous species, electrochemical reaction kinetics and ionic and water transport. They usually take the form of large and complex systems of equations that encapsulate the mechanisms of electrochemical reaction kinetics and heat and mass transport in porous media with multi-component and multi-phase species.

- Empirical models – These reproduce fuel cell polarisation characteristics from experimental data using empirically derived equations. It is due to the complexity of the PEM fuel cell as a system to be modelled that empirical models were introduced. However, very little is learned about the physical phenomena affecting fuel cell performance when using these models.

There now follows a short overview of some of the most important analytical and empirical models in the literature.

5.1.1.1 Analytical models

A one dimensional analytical model was developed by Bernardi and Verbrugge (1992) who considered the PEMFC as consisting of two electrodes connected by a liquid like polymer membrane. Their results showed, that with a low cell current density, the cathode overpotential was large while at high current the resistance overpotential of the membrane began to dominate. The main drawback of this model was the assumption that the membrane was a completely humidified medium. This work was a continuation of an earlier model by Bernardi (1990)

Other examples detail water management in the fuel cell membrane such as that presented by Springer et al (1991) who considered the separate processes of electro-osmotic drag and back diffusion of water, explained earlier in Chapter 3, in a one-dimensional isothermal model of a complete cell. This produced water concentration profiles of the membrane from anode to cathode, also with figures for electro-osmotic drag and back diffusion at different temperatures, pressures and stoichiometry. These showed that severe dehydration can occur at the anode side at high current densities when back diffusion cannot compensate for water transport by electro-osmotic drag - these results were validated by experimental data. The limitations of the model were that the anode catalyst layer was neglected and the cathode catalyst layer was taken to be a thin reactive plane, i.e. no transport processes modelled inside the electrodes.

Later developments extended the models to a two-dimensional study, including a spatial resolution of current density in the direction of the gas tracks, e.g. Nguyen and White (1993). They presented a model describing the variation in current density, water transport stream temperatures and pressures along the channel. They modelled the effectiveness of various humidification levels of anode. However the gas transport processes in the gas diffusion layers and catalyst layers were not incorporated into the model.

Another example of a 2-D study is that by Fuller and Newman who performed an analysis of water and thermal management of a PEM fuel cell operated on reformate (a carbon dioxide and hydrogen mixture) using a two dimensional model. They treated the membrane as a concentrated ionic solution and used material and energy balances along the length of a gas track. Profiles were obtained of the water, gas and the current density distribution along the flow channel. Yi and Nguyen (1998) presented an advanced version of this model where the heat balance between solid and liquid phases and include coflow and counterflow gas configurations.

Work by Wilson and Springer (1993) fit a number of fuel cell performance curves using experimentally determined parameters. Here there is detailed modelling of the transport phenomena in the catalyst layers but nothing regarding the water transport in the cell. They validated these results with single cell experiments to obtain the effect of cathode gas composition and utilisation on the polarisation curves.

5.1.1.2 Empirical models

There have been two approaches to empirical modelling which differ in their consideration of the electrochemical phenomena in a fuel cell. Amphlett et al (1995) carried out a study using a model very similar to Equation 2.24, and went about solving for the constant values analytically.

A more simplified approach was undertaken by Kim et al (1995) who presented the following empirical equation[1]:

$$E_{op} = E_{o,K} - R_{cell,K} I - b_K \ln(I) - m_K \exp(n_K I) \qquad \textbf{Equation 5.01}$$

Although the terms of this equation do not individually represent physical phenomena, such as with Equation 2.24, it produces an accurate prediction of the polarisation curve if the correct values are used, as shown below in Fig. 5.01.

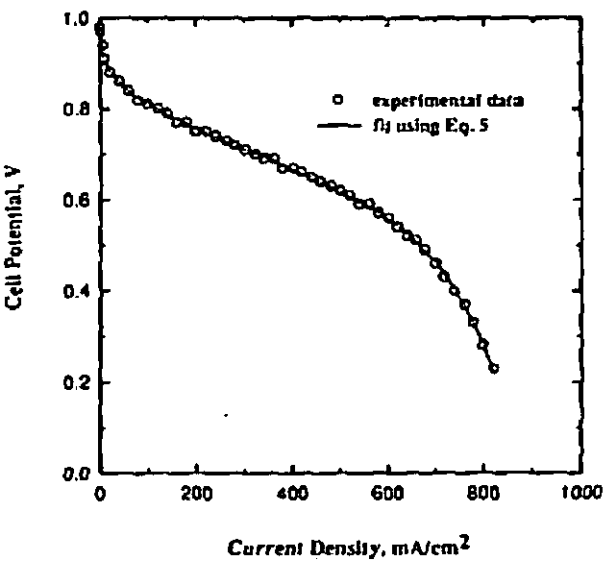

Fig. 5.01 Example of Kim empirical equation used for polarisation plot approximation (Kim, 1995)

This equation has also been shown by other authors to produce accurate representation of obtained fuel cell polarisation data, Hamelin et al (2001)

[1] E_{op} – cell voltage (mV), $E_{0,K}$ – open circuit potential (mV), I – current density (A/cm^2), $R_{cell,K}$ – ohmic resistance (ohm cm^2), $b_k \ln(I)$ – activation loss term, b_k – Tafel slope (mV/decade), $m_K \exp(n_k j)$ – concentration loss term, m_k – concentration loss coefficient (mV), n_K – concentration loss coefficient (cm^2/mA)

There have been several derivations of Equation 5.01, including those proposed by Sena et al (1999) Squadrito et al (1999) and also Lee et al (1998), the latter of whom proposed the following equation which introduced the effect of oxygen partial pressure.

$$E_{op} = E_{o,L} - R_{cell,L} I - b_L \ln(I) - m_L \exp(n_L I) - \xi_L \ln\left(\frac{P}{P_{O_2}}\right) \qquad \textbf{Equation 5.02}$$

Pisani et al, (2002) presented semi empirical equations where both mechanistic and empirical features were present in the fitting coefficients, by attempting to combine the works of Amphlett and Kim.

5.1.1.3 Limitations of fuel cell mathematical modelling

Analytical models

Although all analytical models are devoted to an accurate prediction of fuel cell performance it is very difficult to achieve perfect modelling of such complicated phenomena, especially in multi-component systems such as the PEM fuel cell. In addition, most models assume very specific and often unrealistic, idealised conditions which can include:

- A uniform supply of reactants
- Isothermal conditions across the electrode
- Constant pressure
- Known boundary concentrations

Furthermore, most models address specific aspects of PEMFC behaviour independently of other effects present. Any totally comprehensive analytical model would have to incorporate the combined effects of mass, momentum, energy and electrical current transport through plain (gas channel) and porous media (electrodes, membrane), and of electrochemical reactions (e.g. electro-kinetics, overpotential, entropy generation) at the three-phase boundary. This all must be done for multi-species and multi-component flows. By accurately incorporating all of these combined effects an analytical model could predict the polarisation characteristics of a fuel cell based on hydrogen and air flows, material parameters and design parameters. However, the development of such a comprehensive model remains a formidable challenge.

Empirical models

Although empirical models have some theoretical basis, many of the constituent terms are simply curve fitting tools. As these have little correspondence to theory or physical understanding they are accurate only over a small range of conditions. However the clear advantage of empirical models is the accurate representation of polarisation data although the reliance on pre-obtained experimental data is the major disadvantage. Another disadvantage is that a polarisation curve recalculation is required for any change in operating conditions that the empirical equation has omitted. A comprehensive empirical model would need to identify the correct dependence of the most important performance factors, e.g. temperature, pressure, stoichiometry, relative humidity and current of the fuel cell

5.1.2 System modelling

A system model simulates the performance of a partial or complete fuel cell system such that, by selecting input operating conditions, crucial parameters can be established such as power output, cooling, water demands and efficiency. Developing such a model allows many trade-offs to be analysed which will be especially desirable in fuel cell system development where there will be limitations in costs and timescales for producing the final design.

A useful feature of certain system models is the ability to individually predict the power demand of subsystems, such as a hydrocarbon-to-hydrogen fuel processor or air delivery, for a specified net system power output. This can even be done for small devices such as pumps which can greatly assist with in the size specification of these components. As it is the 'parasitic' power demands from these ancillary devices that are critical in the calculation of the overall system efficiency, especially those associated with the air delivery, the correct specification is crucial. System modelling also assists in the development of features such as control algorithms, specification of stack subsystems, i.e. thermal, water and air management, and system integration aspects.

System models can take the form of a simple steady-state flowsheet analysis for a pre-selected stack operating point, which uses simple mass and energy balances to calculate the individual power requirements and flows for each component of the system. Each physical component, such as the compressor, heat exchangers, pumps and fuel cell stack, is usually represented by a static performance or efficiency map.

More sophisticated system models introduce dynamic features which account for transient operational aspects such as, warm-up from cold or responses to frequent shifts in load demand which steady-state models could account for. Such a 'dynamic' model could be used to analyse system performance over a time period using power-cycles, which simulate the power demand of realistic operating conditions for the system application - an example is the modelling of a fuel cell vehicle system over a drive cycle such as the Federal Urban Drive Cycle. Dynamic system models can also be much more complex, accounting for aspects such as flow characteristics and inertia dynamics of the pumps and compressors.

5.1.2.1 System models

Virji et al (1998) presented a steady-state model, considering the effect of reformer pressure on the efficiency of a fuel cell system using a methane fuel source.

A large proportion of the system models detailed in the literature have been undertaken by organisations seeking to introduce fuel cell systems to the market - particularly automotive manufacturers[2]. Cownden et al (2001) studied an LC fuel cell system for transportation with a particular emphasis on individual subsystems and made several recommendations for performance enhancement. Fronk (2000), and colleagues at General Motors, addressed several issues relating to fuel cell engines, highlighting thermal management, stack and condenser water recovery and variation of radiator (stack) and condenser thermal loads.

Several models have been developed by the University of California including Friedman et al, (2001) and Badrinarayanan et al (2001), who studied stack thermal and water management in systems. Cunningham et al (2001) detailed a comparison of two simple direct hydrogen fuel cell systems using high and low pressure air delivery subsystems, i.e. compressor and blower.

True dynamic fuel cell system models are rarer and usually have been constructed to address a particular design problem. Turner et al (1999) and Boettner et al (2001) presented system models which accounted for temperature from cold on start-up. Other models, Guzzella (1999) Pukrushpan (2002), take into consideration the dynamics of the air compressor. Yerramalla et al (2003) included the effect of inverter load in a dynamic model of a fuel cell system

[2] At the time of writing, producing the first prototype PEM fuel cell vehicles

5.2 Development of EC and LC system models

Overview

Following on from the research detailed in Chapters 3 and 4 it was decided to model a simple FC system employing a stack with an integrated EC mechanism. This would be directly compared with a second model, of a more 'traditional' pressurised LC system containing integrated humidification and cooling plates and all associated sub-systems.

Crucial to the model was the ability to observe, over a range of net power demands, whether the reduced performance from the fuel cell stack in the EC system was comparable to the elevation in associated penalties of the LC system, i.e. large compressor parasitics and lower stack packing density. The critical parameters for this comparison were system efficiencies and stack weight and volume.

Model Development

Two steady-state fuel cell system models were developed, each in the form of a 'flow sheet analysis' for selected net power outputs. A 50 kW *design* power was chosen; this represented a "standard" requirement for a FC vehicle or a large residential FC power system, both of which are frequently quoted in the literature.

The performance of both FC stacks was based on polarisation data, obtained from the rig detailed in Chapter 3, and illustrated in Fig. 5.02, with power density curves also shown.

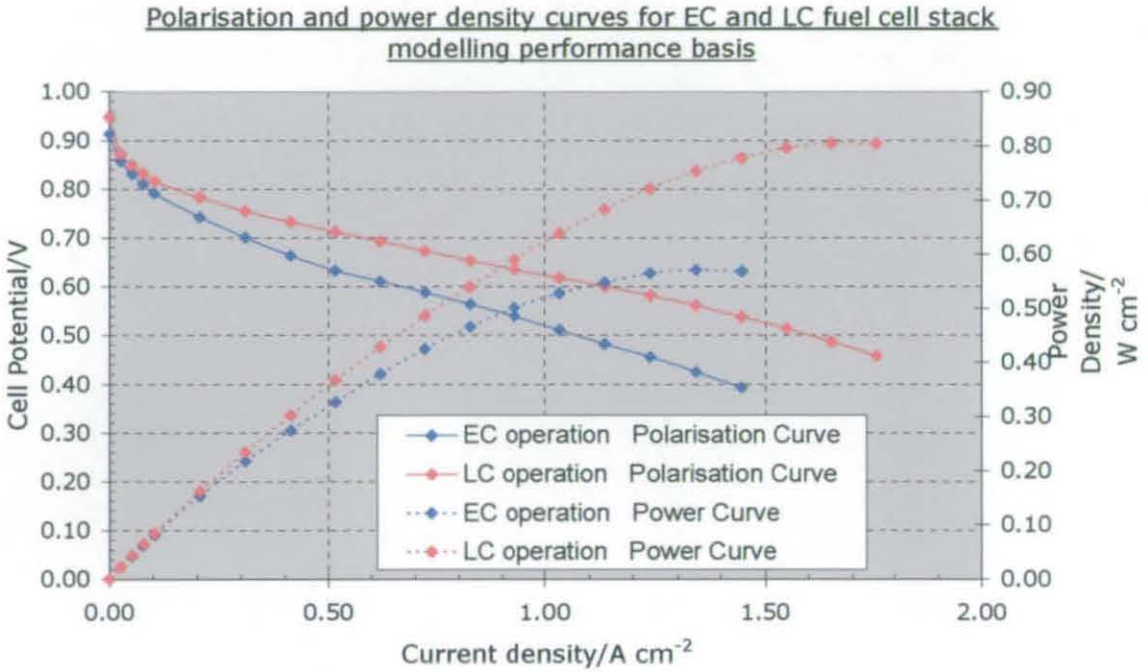

Fig. 5.02 Polarisation data to be utilised in both system models

The data to be used for the LC system are shown by the red plots – this was obtained at an operating pressure of 2 bar.g, using the steam injection unit to simulate saturation (100% RH) of the reactant air by water vapour. The data to be used for the EC low pressure system are shown by the blue plots – this was obtained when the cell was thermally insulated, with water injection to 100% RH into the cathode, at an operating pressure of 250 mbar.g.

Both plots were carried out at an operating temperature of 80°C with an air stoichiometry of 2, and dry hydrogen stoichiometry of 1.5.

To integrate these polarisation plots into the system models they were empirically approximated using Equation 5.01 described earlier, Kim et al (1995)

The two polarisation curves and their associated empirical approximations are shown in Figs 5.03 and 5.04 below. The constants of the equations were established by using the Solver function of Microsoft Excel and are illustrated on the charts:

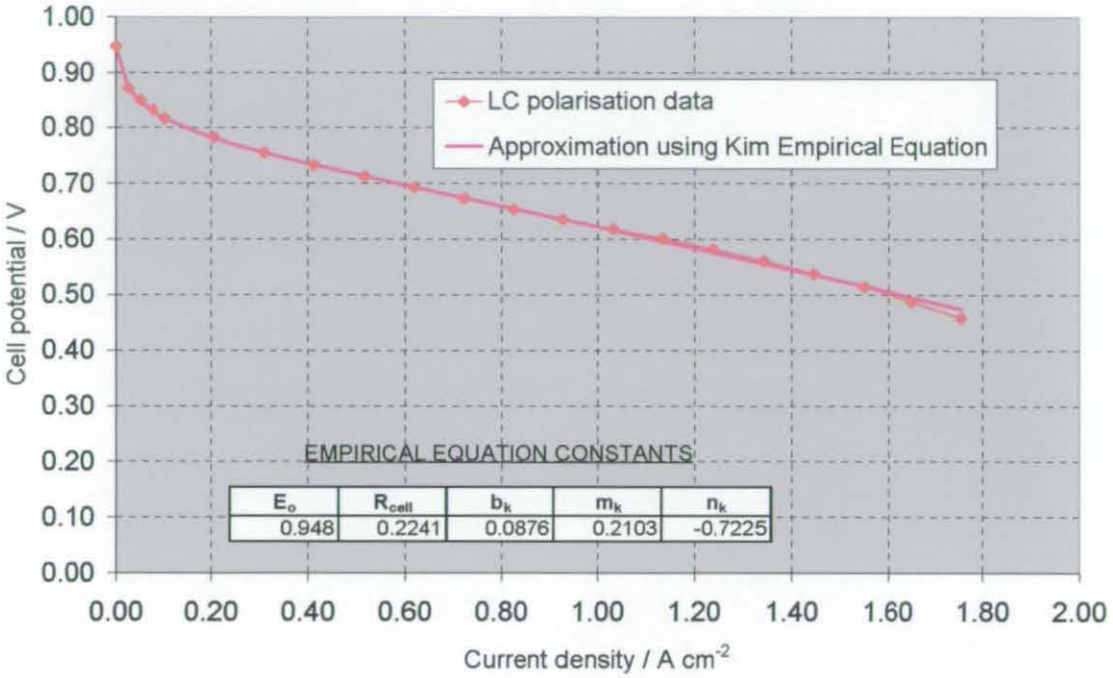

Fig. 5.03 Polarisation data to be utilised in LC system model with Kim empirical approximation

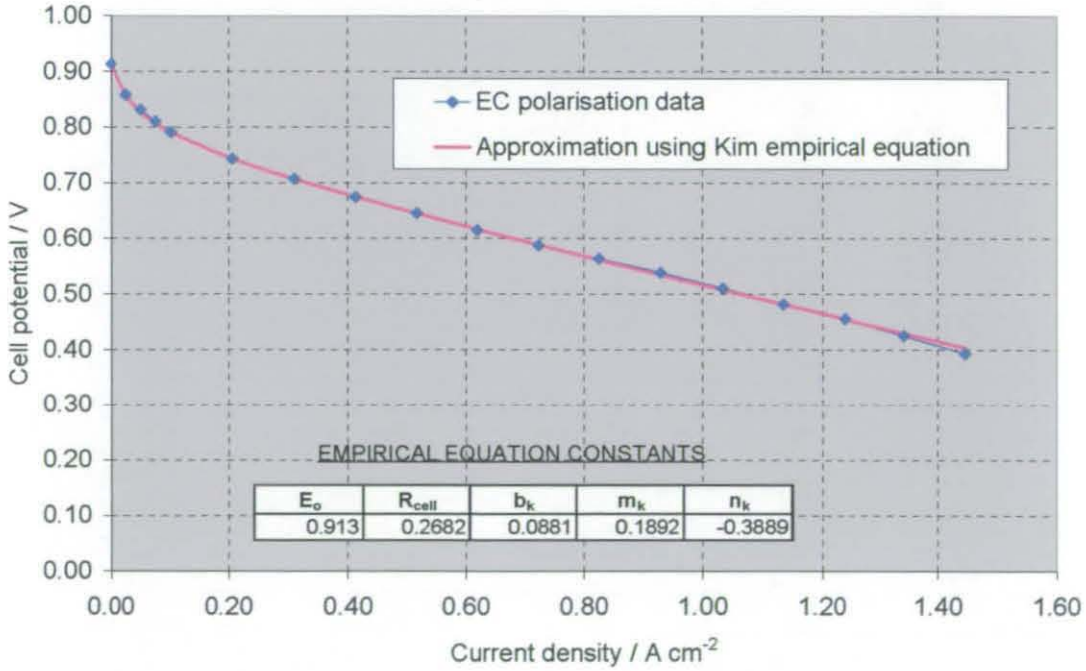

Fig. 5.04 Polarisation data to be utilised in EC system model with Kim empirical approximation

5.2.1 LC system overview

The flowchart for the pressurised stack system is illustrated below in Fig 5.05. The hydrogen was fed from a pressurised supply and regulated to the stack operating pressure of 2 bar.g. The air supply system was comprised of a compressor which sourced air from atmosphere and delivered to the stack at a pressure of 2 bar.g.. A turbine expander recovered energy from the pressurised cathode exhaust in order to maximise system efficiency.

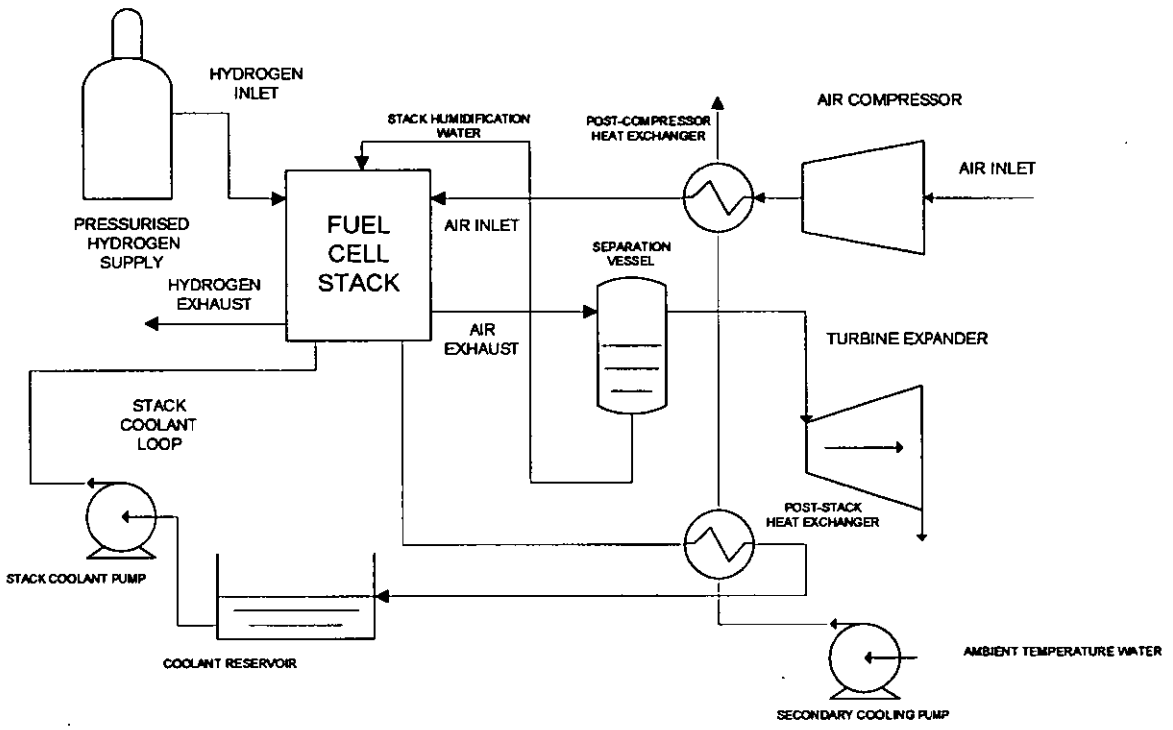

Fig. 5.05 Schematic representation of LC system

The stack was thermally controlled by a closed cooling loop, with a pump supplying deionised water coolant from a storage tank, to dedicated cooling plates spaced within the stack. On exiting the stack the heated coolant was cooled in a heat exchanger before returning to the tank reservoir.

The cell membranes in the stack were maintained fully hydrated using an integrated humidification module, where the air from the compressor was fully saturated to 100%RH prior to passing to the active cells. The humidification water was delivered under pressure to the module, from a separator, which removed excess water from the cathode exit stream. In this way the humidification water supply was constantly 'topped up' by the water generated by the hydrogen-oxygen reaction occurring in the stack.

The air delivered from the compressor was heated by thermodynamic irreversibilities of the pressurisation process so this was cooled in a pre-stack heat exchanger to 80°C before being fed to the stack. A small secondary coolant pump using an ambient temperature liquid water source supplied the cooling media for both heat exchangers, i.e. on stack air inlet and stack coolant exit.

5.2.2 EC system overview

The low pressure EC system flowchart, as shown in Fig. 5.06, has a simpler set up than the pressurised LC system. As before, the hydrogen was delivered from a pure, pressurised source and regulated to the stack operating pressure - in this case 250 mbar.g. - a low power centrifugal blower was used to supply the air to the stack.

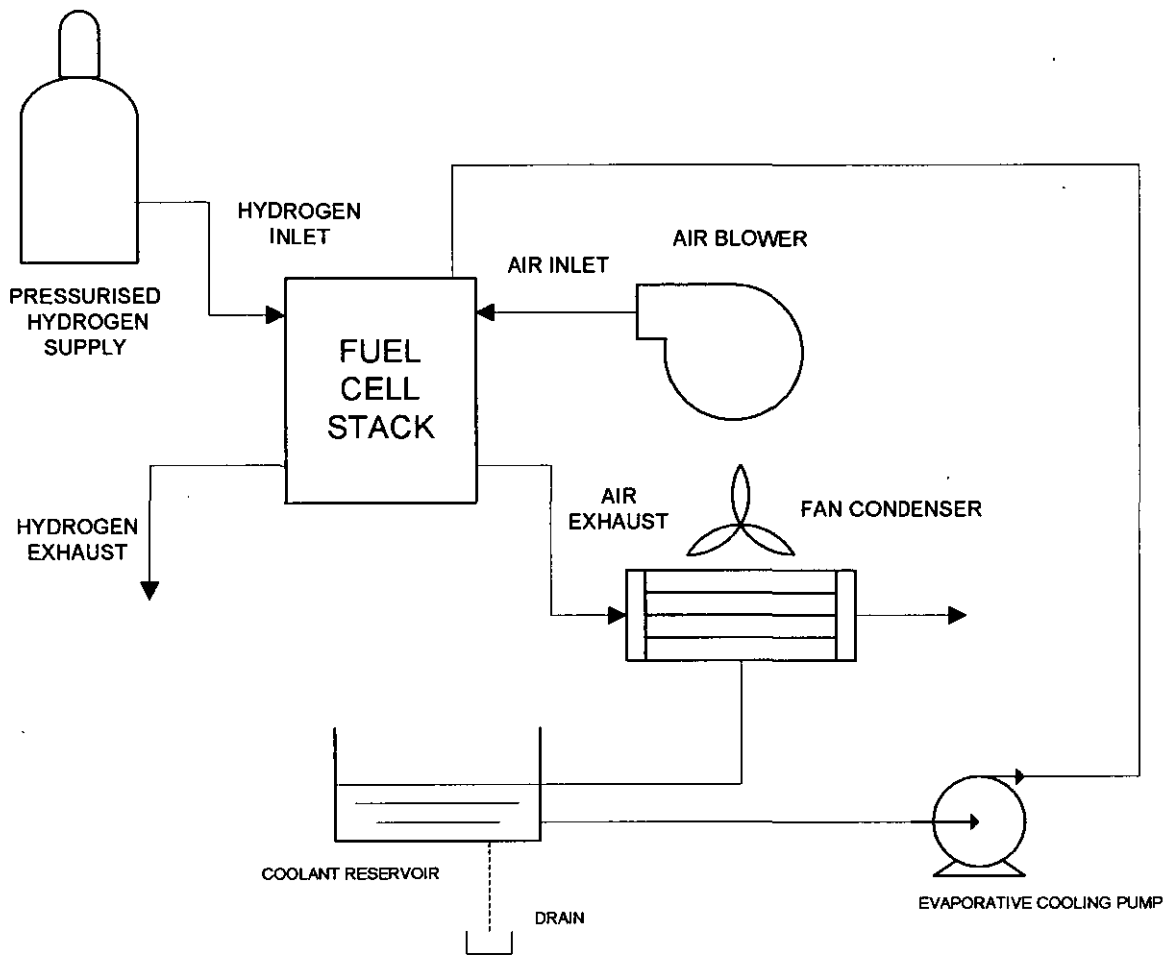

Fig. 5.06 Schematic representation of EC system

The stack was thermally controlled by the direct injection of liquid water to the cathode of each fuel cell using a small pump drawing from a reservoir. The reservoir was constantly supplied by water 'dropping-out' from the cathode exhaust air as it was cooled by a low power fan condenser. The water injection process to obtain 100% RH air also maintains the fuel cell membranes at an adequate hydration level so there was no requirement for any other humidification sub-system.

5.2.3 Model Calculations

Overview

Choosing the same design potential of 0.66 Volts for each fuel cell in the stacks meant that a clear efficiency comparison would be possible between both systems.

For a fuel cell, the operating efficiency is calculated as[3]:

$$\varepsilon_{op} = \frac{W_{el}}{\Delta H_{LHV}} \qquad \textbf{Equation 5.03}$$

W_{el} is calculated from the equation:

$$W_{el} = -nFE_{op} \qquad \textbf{Equation 5.04}$$

This is calculated as: $-2 \times 96500 \times 0.66$ = -127.38 kJ/mol H_2

The value of ΔH_{LHV} at 80°C is -242.38 kJ/mole H_2, therefore the efficiency of both fuel cell stacks is calculated as:

$$\varepsilon_{op}^{fc} = \frac{-127.38}{-242.38} = 52.55\%$$

In addition to the design load of 50 kW, the calculations were carried out for several partial system loads, 10%, 25%, 50% 75%, 100% and up to the calculated maximum theoretical power output of both stacks, and systems. The flowsheet analysis style of the model meant that all calculations were undertaken using Microsoft Excel

Using the fuel cell stack as the basis of each model, mass and energy balances - combined with calculations of power and heat requirements over all system components were performed, using standard heat transfer and chemical engineering equations. Taking into account all calculations enabled the system efficiencies to be calculated in addition to other factors, e.g. parasitic losses.

[3] Where W_{el} is the electrical work obtained and ΔH is the change in enthalpy for hydrogen based on the lower heating value

5.2.3.1 Assumptions

In these steady state models several assumptions were made regarding fuel cell stack operation in order to carry out the mass and heat transfer calculations. Firstly, it is was assumed that every cell in each stack had

- Perfect and equal distribution of reactants
- Equal performance (following the Kim approximations)
- Isothermal conditions, including the EC stack

In the EC system, the low-pressure blower was assumed to deliver the exact flowrate of air required to remove 100% of stack waste heat by the cathode evaporative cooling mechanism. All product and humidification water was assumed to leave with the cathode exhaust gases in each fuel cell (i.e. there was assumed to be no back diffusion). Common to both systems was a supply of hydrogen from a pure pressurised source and a supply of oxygen from atmospheric air (a composition of 79% nitrogen, 21% oxygen by volume).

5.2.3.2 System model variables

To construct both system models, several variables had to be assigned values that were representative of an actual EC or LC fuel cell system. A detailed list of the values chosen for both systems is shown in Fig. 5.07 overleaf. The choices of the most critical factors shown in this table are briefly explained here.

- The design potential of 0.66 V for each stack, represented an efficiency of 52.55%, based on LHV of the hydrogen fuel - a realistic 'design' stack operational point.
- The active area of both stacks was set at 1000 cm^2
- 80% of the MEA, and hence plate, area was specified to be electrochemically active, leaving the remaining 20% for manifolding and sealing
- For the calculation of cooling channel lengths the plates were assumed to be perfectly square
- Stainless steel was chosen as the bipolar plate material in both stacks therefore this is used for the bipolar plate weight calculations.
- Air was supplied to the pressurised stack at a stoichiometry of 2 to reduce the air compressor parasitic losses as much as possible.
- The mechanical efficiencies of the cooling and injection water pumps were set at 20% as this represented a realistic figure due to the relatively low flowrates required
- The dimensions chosen for the connecting pipework were selected as an accurate representation for the flowrates. In the calculation of the pressure drop through the pipework the pipes were assumed to be smooth walled.

FIG 5.07: CHOSEN VARIABLES FOR SYSTEM MODELS

LC Fuel Cell system

Fuel cell

Design potential (V)	0.66
Stack temperature (C)	80
Stack pressure (barg)	2
Hydrogen stoichiometry	1.5
Air stoichiometry	2
Active area size (cm^2)	1000
Material for bipolar plates	316 SS
Thickness of bipolar plates (mm)	2
Ratio of active area/total area	0.8
Ratio of fuel cells/cooling plates	4
Material for cooling plates	316 SS
Thickness of cooling plates (mm)	6
Temperature of entering coolant (C)	50
Temperature of leaving coolant (C)	60
Coolant used	Distilled Water
Ratio of fuel cells/humidification cells	10
Material for humidification plates	316 SS
Thickness of humidification cell plates (mm)	4

Cooling channels

Channel width (mm)	4
Channel depth (mm)	2
Ratio of channel area/total plate area	0.3

Coolant pump

Mechanical efficiency of pump	20%
Internal diameter of tubing (mm)	20
Length of tubing (m)	4
Total vertical height (m)	1

Compressor

Compressor isentropic efficiency	80%
Shaft transmission efficiency	97%

Turbine Expander

Expander isentropic efficiency	150%
Shaft transmission efficiency	97%

Secondary cooling pump

Mechanical efficiency of pump	20%
Internal diameter of tubing (mm)	20
Length of tubing (m)	4
Total vertical height (m)	1

EC Fuel Cell system

Fuel cell

Design potential (V)	0.66
Stack temperature- average (C)	80
Stack pressure (barg)	0.25
Hydrogen stoichiometry	1.5
Active area size (cm^2)	1000
Material for bipolar plates	316 SS
Thickness of bipolar plates (mm)	2
Ratio of active area/total area	0.8

Water pump

Temperature of water input, C	50
Pressure drop of injection feature (bar)	3
Internal diameter of tubing (mm)	8
Length of tubing (m)	2
Total vertical height (m)	1
Mechanical efficiency of pump	20%
Assume smooth pipework, roughness=0m	

Air Blower

Blower isentropic efficiency	80%
Shaft transmission efficiency	97%

Fan Condenser

Fan mechanical efficiency	50%
Pressure drop of air over HEX tubes, N/m^2	100
Temperature change of air, C	10

5.2.3.3 Mechanical equipment efficiencies at partial design throughputs

The mechanical operating efficiency of any flow equipment (pumps, compressors, motors etc) will be reduced as the flowrate deviates above or below the design point. Therefore a 'throughput efficiency' factor (expressed as a function of actual flowrate/design flow rate) is included in the power requirement calculation for all mechanical components, as illustrated in Fig. 5.08.

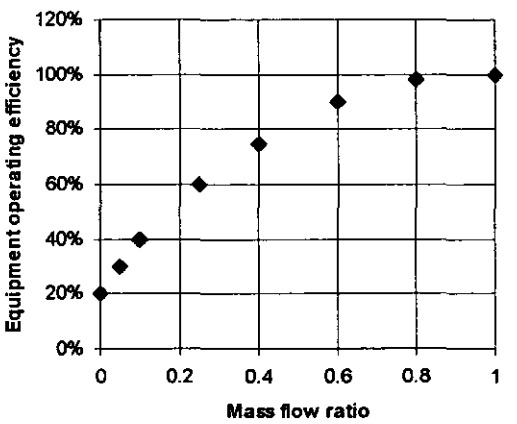

Fig 5.08: Equipment operating efficiency variation with mass flowrate

The equipment design flow rate, i.e. 100% throughput efficiency, for each piece of mechanical equipment is specified as the flowrate at maximum *stack power* instead of at the 50kW net *system design power*. Not doing this would result in much reduced system efficiencies when operating the system at maximum stack power due to the vastly reduced throughput efficiencies of the flow equipment.

5.2.3.4 Calculations

To begin each model, values were chosen for the characteristics of each fuel cell stack which allowed a calculation of waste heat, water and gas flowrates. All of the system component calculations stem from the required cooling and flows through the stack. As stated previously, many industry standard equations of Chemical Engineering were used for the component calculations in both systems - the most critical of these are explained in the following pages

After setting up all calculations, the minimum number of fuel cells required to produce 50 kW net system power at the 0.66 V design potential for each fuel cell is determined by utilising the multi-iteration function in Solver - an embedded application in Microsoft Excel. After setting the size of the stack, the necessary stack operating points needed to obtain the chosen partial system power loads were calculated by again using Solver.

Calculations of coolant pumping power

There are two coolant pumps in the LC system, one for the stack and one for the heat exchangers, and one in the EC system, for direct water injection to the fuel cell cathodes. Knowledge of the thermal conditions allowed a calculation of the required coolant mass flow rate in each case, which was then used in the calculation of pump power.

A power requirement for pumping a fluid through pipelines is described in Coulson and Richardson, (1993) stating the kinetic energy, potential energy, pressure energy, and friction is equal to the net work done by any pumped fluid on the surroundings (per unit mass)[4]:

$$\frac{\Delta u^2}{2\omega} + g\Delta z + \int_{P_1}^{P_2} vdP + W_s + F = 0 \qquad \textbf{Equation 5.05}$$

The total rate at which power, P_{pump}, must be transferred to the fluid is $\dot{M}_{cool} \cdot W_s$, where the mass flow rate of the coolant is $\dot{M}_{cool}$.

$$P_{pump} = -\dot{M}_{cool} W_s = \dot{M}_{cool}\left(\frac{\Delta u^2}{2\omega} + g\Delta z + \int_{P_1}^{P_2} vdP + F\right) \qquad \textbf{Equation 5.06}$$

In the LC and EC models, it can be assumed that for each pump none of the kinetic energy is recoverable as pressure energy as all the processes involve pumping a liquid from one open tank to another, i.e. the fluid pressure will be the same at the point of supply, delivery and return, therefore the term $\int_{P_1}^{P_2} vdP$ is zero. In addition, for a flow from reservoir to reservoir the velocity term can be taken as zero based on the fact the reservoir has a large surface area so no kinetic energy is recoverable as pressure energy and the power requirement becomes:

$$P_{pump} = M_{cool}(g\Delta z + F) \qquad \textbf{Equation 5.07}$$

Therefore the energy requirements are separated into only two components:

- The difference in vertical height at both ends of the pipework
- Friction losses of the cooling fluid through the length of the pipework.

[4] The net work done on unit mass of fluid is $-W_s$. with F as the energy lost to friction. The potential energy is represented by the $g\Delta z$ term , the change in fluid pressure is represented by $\int_{P_1}^{P_2} vdP$ and the kinetic energy is represented by $\frac{\Delta u^2}{2\omega}$

Equation 5.07 can be rewritten as the product of the coolant mass flowrate, the total *head* [5] and acceleration due to gravity and the addition of a term accounting for pump efficiency - ε_{pump}.

$$P_{pump} = \frac{1}{\varepsilon_{pump}} \dot{M}_{cool} hg \qquad \textbf{Equation 5.08}$$

The equivalent total head loss for the respective coolant was calculated for each system partial load and the corresponding required flowrate.

The head losses due to differences in known height of the pipework are relatively straightforward to include in the calculations. However, to calculate the head loss due to friction between the cooling fluid and pipework it was necessary to first obtain a dimensionless 'friction factor' term , ψ , for the fluid.

The friction factor is calculated using the formula[6]:

$$\psi = 0.0396 \,\mathrm{Re}^{-0.25} \qquad \textbf{Equation 5.09}$$

The Reynolds number is a dimensionless term which describes the behavioural flow characteristics and is calculated by[7]:

$$\mathrm{Re} = \frac{\rho u d}{\mu} \qquad \textbf{Equation 5.10}$$

The friction head loss down cooling channels and through pipework is calculated by the formula[8]:

$$h_f = 8\psi \frac{L}{d} \frac{u^2}{2g} \qquad \textbf{Equation 5.11}$$

The length and diameter of the pipework is calculated to represent a realistic set-up for each system. The velocity was calculated by dividing the volumetric flowrate by the pipe cross-sectional area.

---

[5] 'Head' is a standard term in fluid dynamics, defined as energy per unit weight of fluid and measured in metres (Force x length/weight = length) and is represented by h.

[6] Where Re represents the Reynolds number of the flowing coolant

[7] Where ρ is the density of the fluid, u is the velocity, d is the diameter of pipe and μ is the viscosity of the fluid

[8] Where L is the equivalent length of pipe, d is the diameter, u is the velocity g is acceleration due to gravity - 9.81 m/s^2

For the stack coolant pump of the LC system, the fluid head friction losses into manifolds and down plate cooling channels have to be accounted for. The calculation of the Reynolds number (and hence head friction loss) down the stack plate cooling channels becomes more complicated due to the rectangular cross-sectional shape.

An equivalent hydraulic mean diameter was defined from:

$$d_m = \frac{2 \times width \times height}{width + height}$$ **Equation 5.12**

There are other head friction losses that must be accounted for including the losses through heat exchanger tubes etc., which were chosen from Coulson & Richardson, 1995.

Air pressurisation

The air compressor of the LC system and the centrifugal blower of the EC system represent the biggest parasitic loss in each model. The main calculation used is explained here.

Starting with fundamental energy conservation principles, Boyle' Law states that *a change in the absolute pressure of a gas results in an inverse change in the volume when held at a constant temperature.* Charles' Law states that *when the gas volume is held constant the absolute pressure will vary in proportion to the change in absolute temperature.* The influence of these relationships resulted in the ideal gas law, or perfect gas law, which introduces the concept of the universal gas constant, R.

$$\frac{P_1V_1}{T_1} = \frac{P_2V_2}{T_2} = R \qquad \textbf{Equation 5.13}$$

Boyles Law, as described above is expressed as:

$$P_1V_1 = P_2V_2 \qquad \textbf{Equation 5.14}$$

Such a relationship does not occur in nature and it has been established that when a gas is compressed or expanded the pressure will vary to an exponential power of the volume.

$$P_1V_1^{\gamma} = P_2V_2^{\gamma} \qquad \textbf{Equation 5.15}$$

This is equation is derived from first principles, Coulson & Richardson (1995). The expression γ represents the ratio of specific heats[9], C_p / C_v, and has a value of 1.4 for air.

Assuming that the air undergoing pressurisation obeys Equation 5.13, this relationship only describes an ideal change of state, wherein no heat loss or leakage occurs and friction is not accounted for, and is known as the adiabatic state. When such an adiabatic process is also reversible it is referred to as an isentropic process.

Rearranging Equation 5.15 as an expression for (V_1/V_2) and substituting into Equation 5.13 produces a ratio of post-compression air temperature, T_2, to the uncompressed temperature air T_1 for the adiabatic (isentropic) case, Dicks et al (2000).

$$\frac{T_2}{T_1} = \left(\frac{P_2}{P_1}\right)^{\frac{(\gamma-1)}{\gamma}} \qquad \textbf{Equation 5.16}$$

[9] Where C_p represents specific heat at constant pressure and C_v represents specific heat at constant volume

Rearranging, the 'ideal' gas discharge temperature can be defined as

$$T_2 = T_1\left(\frac{P_2}{P_1}\right)^{\frac{(\gamma-1)}{\gamma}} \qquad \textbf{Equation 5.17}$$

Therefore, by defining a desired pressure ratio and inlet temperature the outlet temperature can be calculated. This enables an energy balance upstream and downstream of the compressor to be calculated and a resultant value obtained for the energy obtained by the air, also referred to as discharge gas energy.

The desired calculation for the compressor or blower is the adiabatic power and to obtain this, a definition must be made of *isentropic efficiency* and applied to the measured discharge gas energy. This efficiency term is defined as the ratio of the work required for an ideal isentropic compression to the work actually expended in the compressor.

If sufficient heat is rejected to the environment the discharge temperature will be less than the calculation for an ideal adiabatic compressor, efficiency greater than 100%. If energy is added to the exhaust stream due to heating or mechanical inefficiencies the converse is true and the discharge stream will be hotter than that calculated for an ideal reversible compressor, i.e., efficiency less than 100%.

Assuming the term PR represents the pressure ratio, P_2/P_1, the formula for calculating isentropic (or adiabatic) efficiency becomes:

$$\varepsilon_{ad} = \frac{\dot{M}_{air}C_P T_1\left(PR^{\frac{(\gamma-1)}{\gamma}} - 1\right)}{\dot{M}_{air}C_P(T_2 - T_1)} \qquad \textbf{Equation 5.18}$$

Where $\dot{M}_{air}$ is the mass flow rate of the air and C_p is the air specific heat capacity.

Rearranging this to obtain an expression for the outlet temperature of the compressor:

$$T_2 = \frac{T_1}{\varepsilon_{ad}}\left(PR^{\frac{(\gamma-1)}{\gamma}} - 1\right) + T_1 \qquad \textbf{Equation 5.19}$$

This is similar to the turbine expander calculation which is expressed as:

$$T_{out} = T_{in} - \varepsilon_{ad}T_{in}\left[1 - \left(\frac{P_{out}}{P_{in}}\right)^{\left(\frac{\gamma-1}{\gamma}\right)}\right] \qquad \textbf{Equation 5.20}$$

Therefore, the final value of air compression power demand is calculated from an energy balance over the unit.

For the calculation of the power of the fan, which condensed the EC stack cathode exhaust flow, a figure for pressure drop over a heat exchanger tube bundle was obtained from Coulson & Richardson, 1995.

5.3 Model Results

5.3.1 System design power

Overview

The LC and EC fuel cell system characteristics at the 50 kW net power output design point are illustrated respectively in Figs. 5.09 and 5.10. The system flowcharts are shown, with figures for the associated energy generation, green text, and parasitic losses, blue text, adjacent to the relative component.

To obtain a 50 kW net system output, the LC system has to generate 57.95 kW stack power with an extra 5.09 kW from the turbine expander using the cathode exhaust gases, resulting in a total parasitic figure of 13.04 kW. In the EC system, a gross power output of 54.56 kW from the stack is required, equivalent to 4.56 kW parasitics.

The difference in both stack efficiencies represents the miniscule deviation in operating points required to calculate an exact 50 kW system output for an integer number of cells – 660.7 mV for each cell in the EC stack and 661.2 mV for each cell in the LC stack. The overall system efficiencies, at design load based on the 'lower heating value' of hydrogen are 45.4% for the LC system and 48.2% for the EC system.

Another point of note is the larger stack heat duty required with the LC system due to the much higher current generated in each fuel cell for the design potential.

Fig. 5.09 Liquid Cooled Fuel Cell System Supplying 50kW Net Power Operational Characteristics

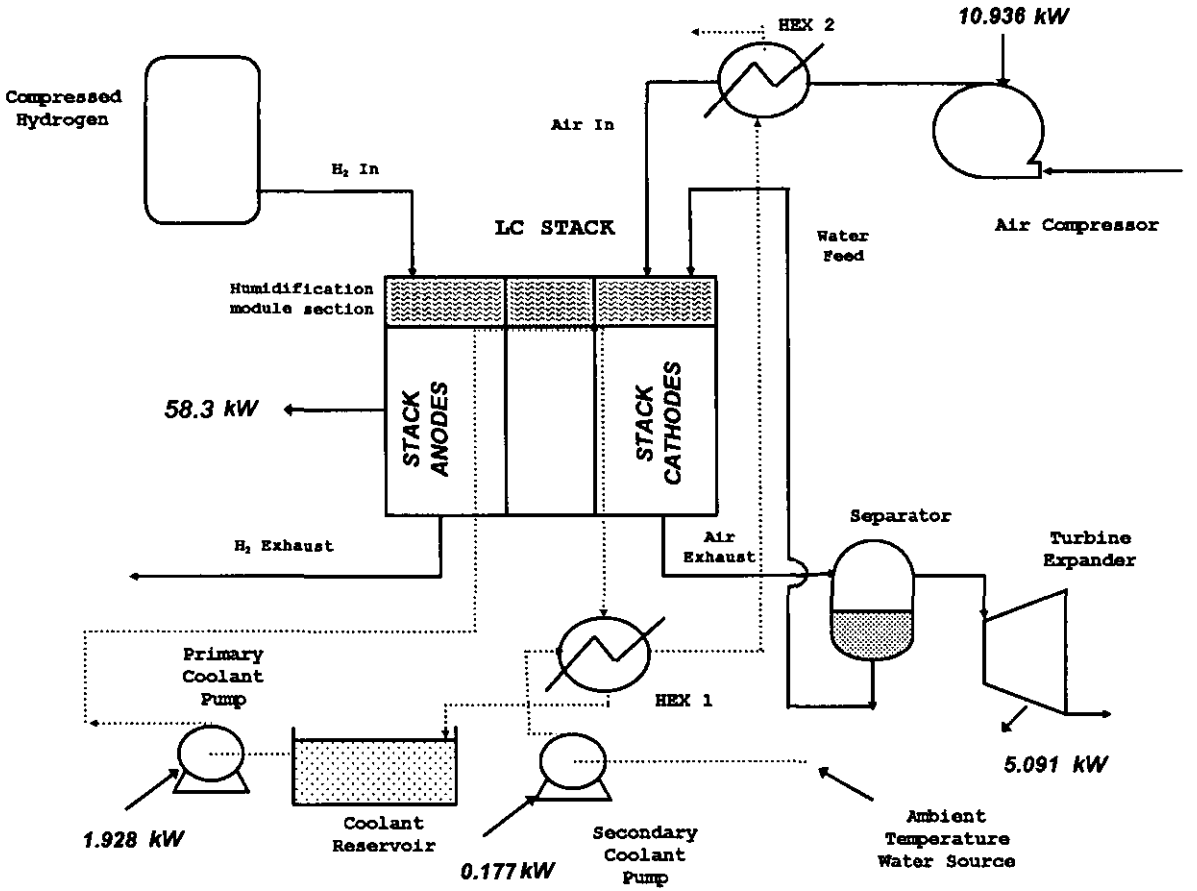

SYSTEM CHARACTERISTICS (AT DESIGN POWER)

Gross System Power (kW)	63.04
Net System Power (kW)	50.00
Stack Power (kW)	57.95
Turbine Power (kW)	5.09
Stack Heat Duty (kW)	67.85
Stack Efficiency	52.64%
Parasitic Losses (Kw)	13.04
Number Of Fuel Cells in Stack	111
Stack Volume (Litres)	60.33
Stack Volumetric Density (kW/L)	0.97
Stack Weight (Kg)	304.97
Stack Gravimetric density (kW/kg)	0.19
Stack Temperature °C	80
Stack Pressure (bar.g)	2
Hydrogen Stoichiometry	1.5
Air Stoichiometry	2
Hydrogen Flowrate Required (SLPM)	916.09
Air Flowrate Required (SLPM)	2908.22
System Efficiency	45.42%

Fig. 5.10 Evaporatively Cooled Fuel Cell System Supplying 50kW Net Power Operational Characteristics

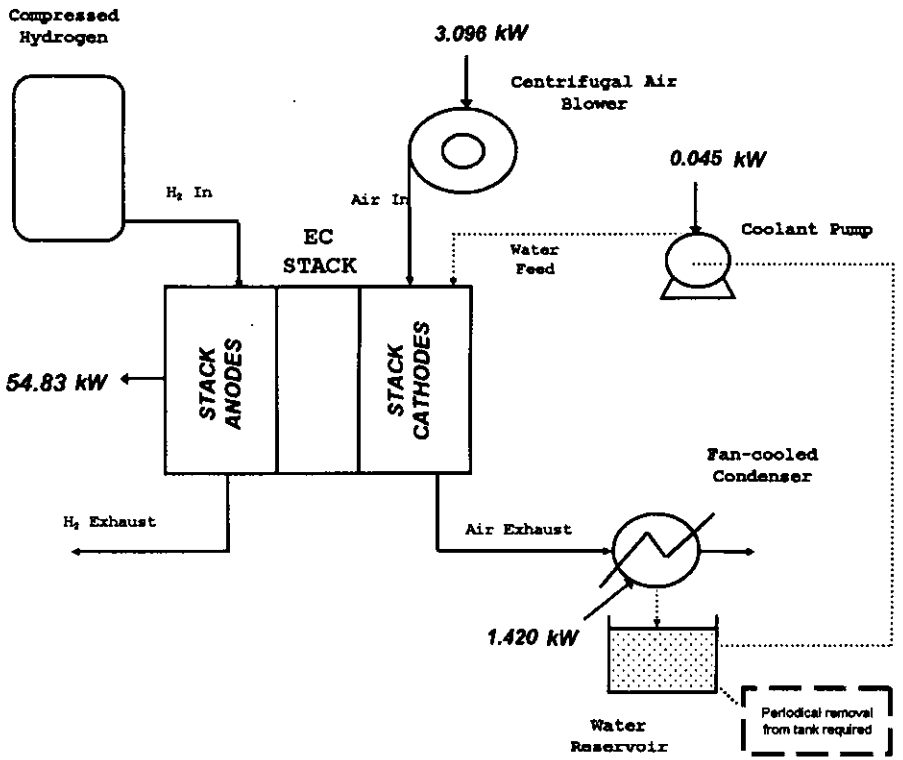

SYSTEM CHARACTERISTICS (AT DESIGN POWER)	
Gross System Power (Kw)	54.56
Net System Power (Kw)	50.00
Stack Power (kW)	54.56
Stack Heat Duty (kW)	44.86
Stack Efficiency	52.60%
Parasitic Losses (Kw)	4.56
Number Of Fuel Cells In Stack	190
Stack Volume (Litres)	56.02
Stack Volumetric Density (Kw/l)	0.98
Stack Weight (Kg)	262.39
Stack Gravimetric density (kW/kg)	0.21
Stack Temperature (average) °C	80
Stack Pressure (bar.g)	0.25
Hydrogen Stoichiometry	1.5
Air Stoichiometry	2.47
Hydrogen Flowrate Needed (SLPM)	863.09
Air Flowrate Needed (SLPM)	3385.81
System Efficiency	48.21%

5.3.1.1 Stack Characteristics

For the LC system, a total of 111 active fuel cells were required in the stack compared to 190 fuel cells in the EC system stack. However the LC stack required 5 humidification cells and 12 cooling plates, both of which were significantly bulkier than standard bipolar plates. As a direct result of this, the EC stack volume of 56 litres was less than the LC system stack volume of 60.3 litres. Similarly the LC stack weight was calculated to be approximately 305 kg but the EC system stack is 262 kg. Again, this is due to the weight of the in-situ humidification and cooling plates offsetting the difference of the extra cells in the EC stack. Both stack weight and volume figures do not account for end plates which would add equal amounts of bulk to both stacks. The relative stack sizes from a side view are illustrated in Fig. 5.11 below.

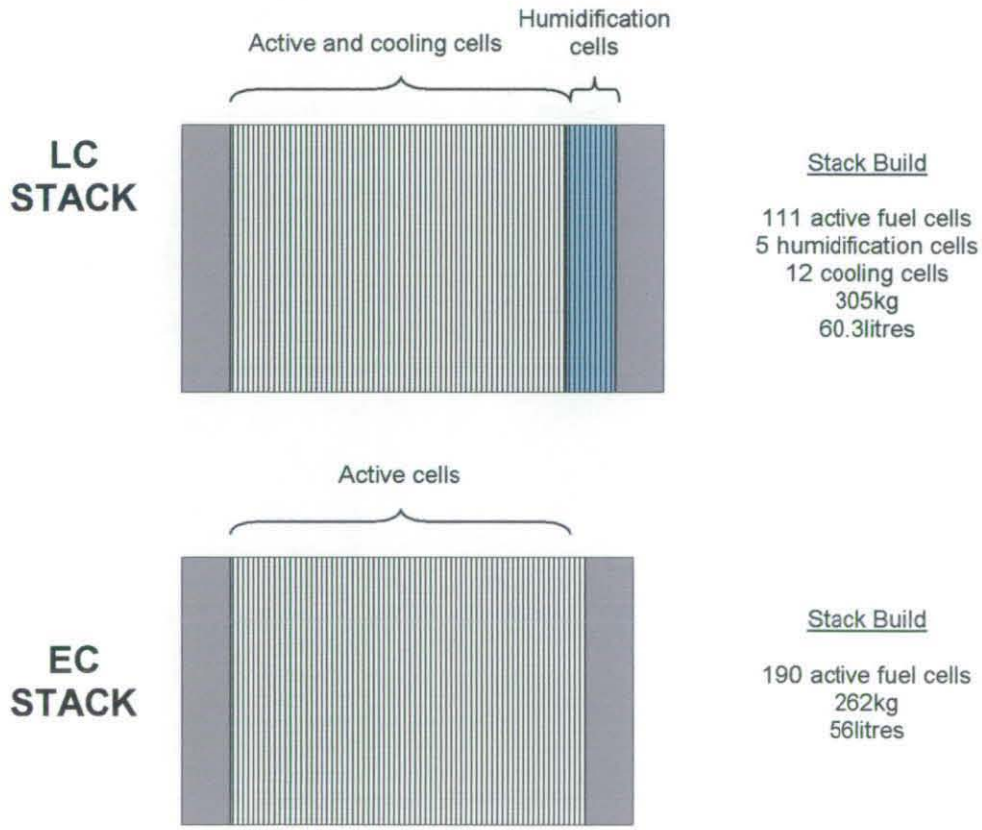

Fig. 5.11 Illustration of both stack builds

The stack volumetric densities are very similar, with the calculated figure, based on gross power output, for the EC stack being 0.98 kW/L and the LC stack being 0.97kW/L. The gravimetric densities are also similar - 0.19kW/kg for the LC stack and 0.21kW/kg for the EC stack.

5.3.1.2 Distribution of parasitic losses

The 13.04 kW of parasitic losses from the LC system are separated into the constituent parts in Fig. 5.12 to illustrate the distribution of power consumption between the components.

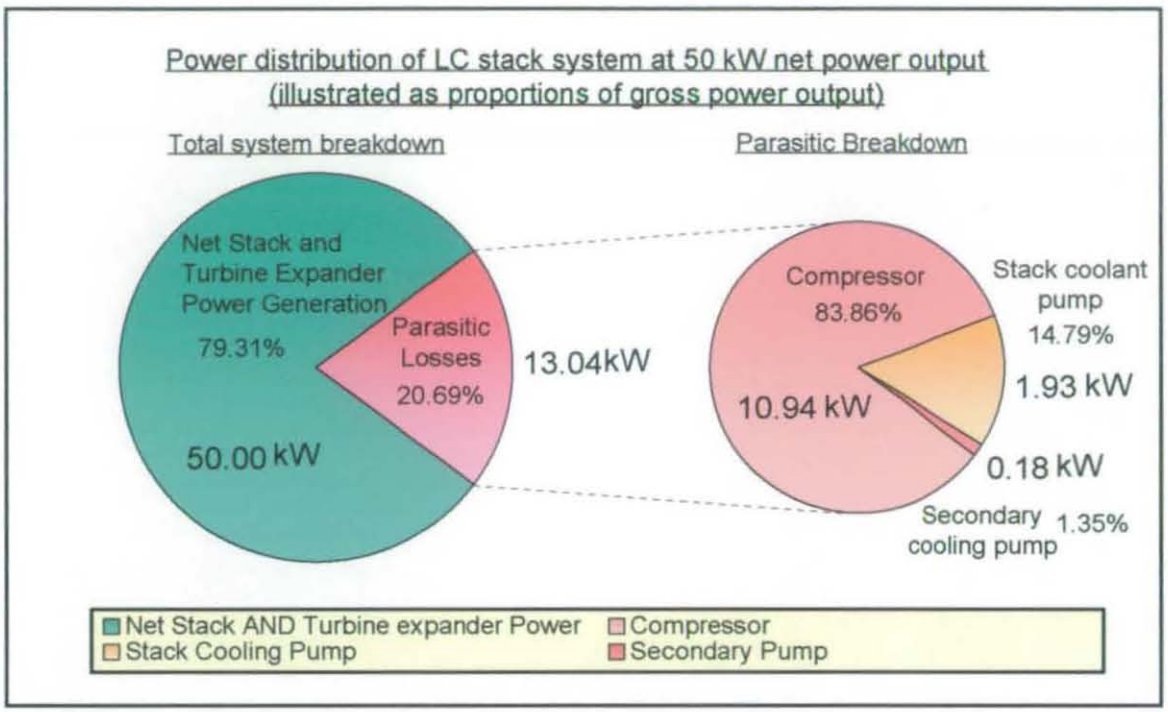

Fig. 5.12 Parasitic distribution for LC system

The left-hand pie chart shows that 20.7% of the gross LC system power, generated by the stack and turbine expander, is consumed by parasitics. In the right-hand pie chart it is seen how this parasitic loss is dominated by the energy requirement for air compression – a total of 10.94 kW, equivalent to 83.9% of the total. The remainder is distributed between the stack coolant pump (1.93 kW, equivalent to 14.8%) and the small secondary cooling pump (0.18 kW, equivalent to 1.4%). This confirms that the air compressor is by far the largest parasitic loss in the LC system

The 4.56 kW of parasitic losses of the EC system are separated into the constituent parts in Fig. 5.13 below.

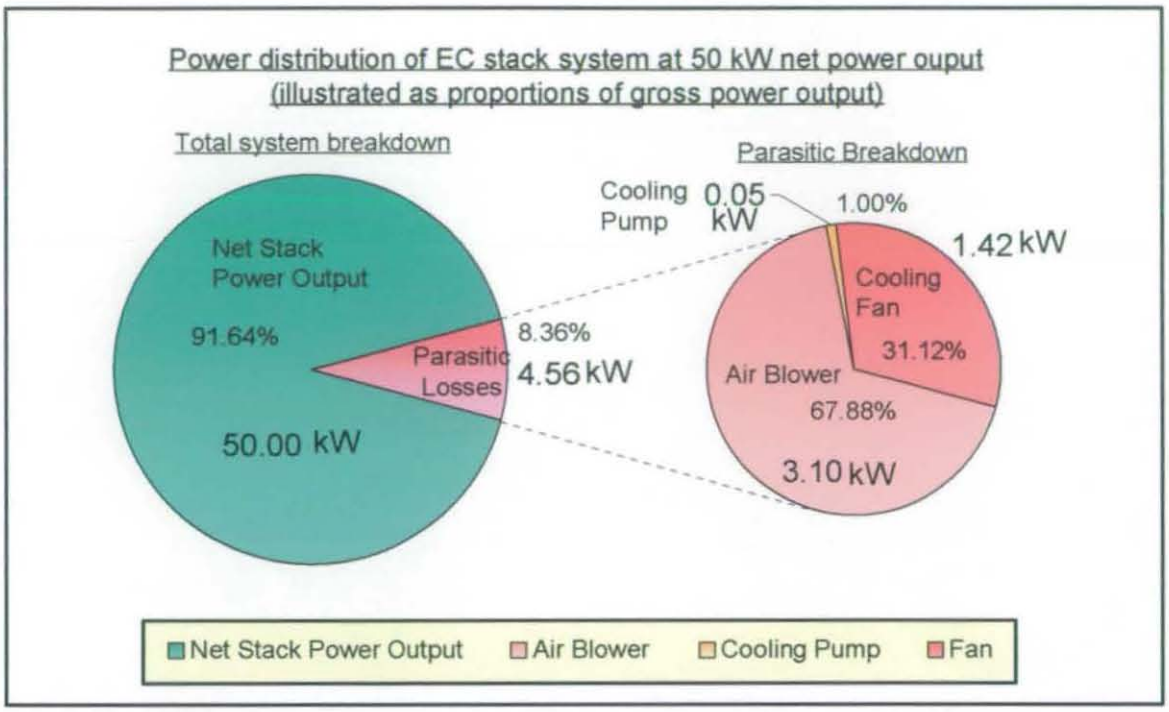

Fig. 5.13 Parasitic distribution for EC system

The left-hand pie chart shows that 91.6% of the gross stack power is delivered as net system power with only 8.4% parasitic loss in total - this is in comparison to the figure of 79.3% for the LC system. The right hand pie chart shows that, in a similar vein to the LC system, the highest parasitic component is caused by the air supply sub-system (the centrifugal blower) constituting 67.9% of the 4.56 kW system parasitics. The fan of the post-stack air condenser contributes 31.1% (1.42 kW) of the total parasitic drain and the EC pump the remaining 1% (0.05 kW). The latter figure is so small primarily due to the relatively low rates of water injection required for complete EC operation.

5.3.2 System load cycles

A full breakdown of the key operational data characteristics for both systems through the range of power outputs is illustrated separately in Fig. 5.14. From this, it is observed that the EC system was capable of delivering a peak power load of 98 kW, which represented 196% of the design power. The maximum power obtainable from the LC system was 76.9 kW, corresponding to 153% of the design power. With both systems the maximum output power does not correspond to the maximum stack operating power due to the influence of parasitics.

5.3.2.1 System efficiencies and parasitic losses

Comparative system efficiencies and parasitic data are illustrated in Figs. 5.15 - 5.17. In each of these plots the maximum system power output is illustrated as an enlarged white data marker.

The system efficiency plotted against the percentage of the 50kW system design power for both systems is illustrated in Fig. 5.15. It is seen how the EC system plot is approximately linear in nature, steadily decreasing from a value of 59.1% system efficiency, at 10% system load, to 31.7% at maximum system power. The LC system shows prominent dips in efficiency at low and high extremes of system power with a peak occurring between 50 and 75% of system power – both at 46.7% system efficiency - the nature of this plot is strongly influenced by the power demand of the compressor.

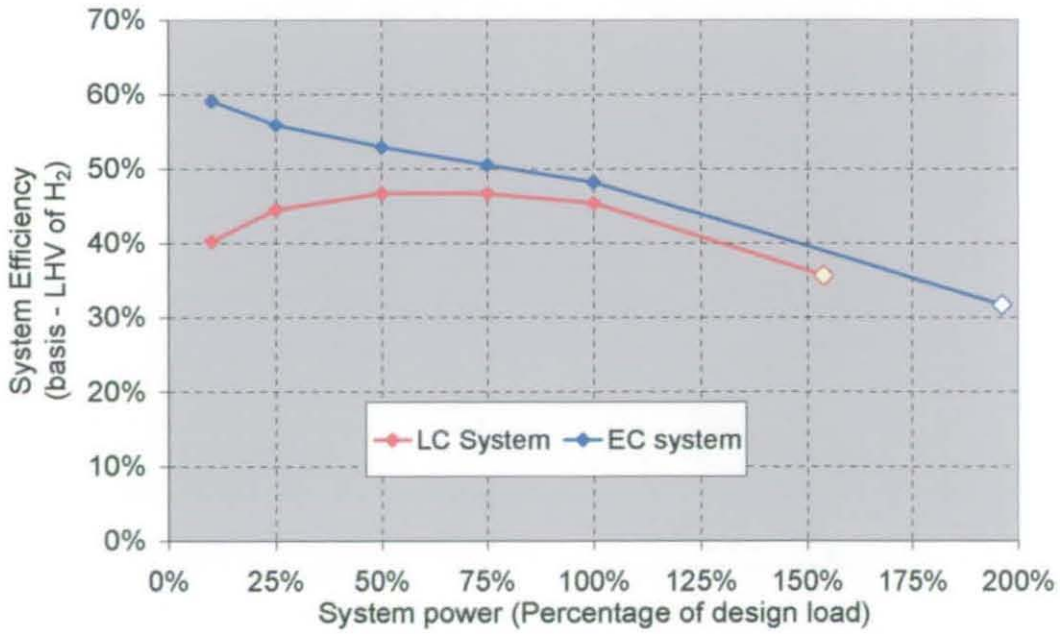

Fig. 5.15 System efficiency comparison – varying system power outputs

Fig. 5.14 Illustration of Operating Characteristics for both systems

SYSTEM 1 - EC STACK WITH WATER INJECTION EVAPORATIVE COOLING

Percentage of system design power	Stack Potential (V)	Stack Current /A	Stack Power / kW	Stack Efficiency (based on LHV)	Air Flow (SLPM)	H_2 Flow (SLPM)	Parasitic Losses (kW)	Stack Heat Duty kW	System Power / kW	System Efficiency % (LHV)
10%	161.61	35.46	5.73	67.7%	216.73	70.41	0.73	2.42	5.00	59.1%
25%	151.50	93.74	14.20	63.5%	617.10	186.17	1.70	7.32	12.50	55.9%
50%	140.90	197.99	27.90	59.0%	1400.98	393.19	2.90	17.49	25.00	52.9%
75%	132.79	310.94	41.29	55.6%	2317.59	617.51	3.79	29.91	37.50	50.5%
100%	125.55	434.59	54.56	52.6%	3385.81	863.09	4.56	44.86	50.00	48.2%
MAX. SYSTEM (196.2%)	83.61	1296.25	108.38	35.0%	12628.48	2574.31	10.29	186.50	98.08	31.7%
MAX. STACK (195.7%)	80.71	1345.93	108.62	33.8%	13294.12	2672.96	10.80	197.43	97.83	30.5%

SYSTEM 2 - LC STACK WITH CONVENTIONAL COOLING PLATES AND HUMIDIFICATION MODULE

Percentage of system design power	Stack Potential (V)	Current Drawn (A)	Stack Power (kW)	Stack Efficiency (based on LHV)	Air Flow (SLPM)	H_2 Flow (SLPM)	Parasitic Losses (kW)	Stack Heat Duty kW	System Power / kW	System Efficiency % (LHV)
10%	91.66	89.05	8.16	65.7%	327.98	103.31	3.39	6.45	5.00	40.3%
25%	87.05	201.52	17.54	62.4%	742.25	233.81	5.71	14.57	12.50	44.5%
50%	81.97	383.95	31.47	58.8%	1414.19	445.47	8.21	29.70	25.00	46.7%
75%	77.68	576.01	44.75	55.7%	2121.59	668.30	10.45	47.03	37.50	46.7%
100%	73.39	789.58	57.95	52.6%	2908.22	916.09	13.04	67.85	50.00	45.4%
MAX. SYSTEM (153.8%)	57.17	1546.95	88.44	41.0%	5697.80	1794.81	23.68	158.03	76.92	35.7%
MAX. STACK (150.9%)	53.27	1680.19	89.51	38.2%	6188.53	1949.39	27.35	178.95	75.45	32.2%

The plots of parasitic losses versus system load for both systems are shown in Fig. 5.16.

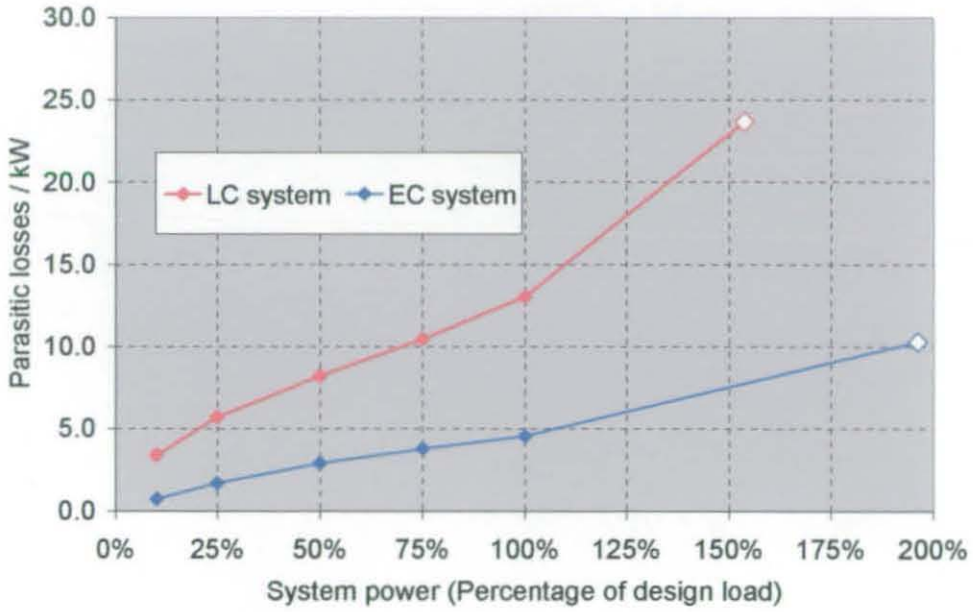

Fig. 5.16 Parasitic losses of both systems at varying system power outputs

The parasitic power of the LC system is seen to increase at a higher rate with system output than the EC system which, again, shows a more linear trend. At the maximum loads, the LC system parasitic approaches 25 kW - this is predominantly due to the increased power requirement of the air compressor, even though the throughput factor is close to unity for the calculation.

The parasitic losses of both systems expressed as a percentage of the gross power generated in each system is illustrated in Fig. 5.17.

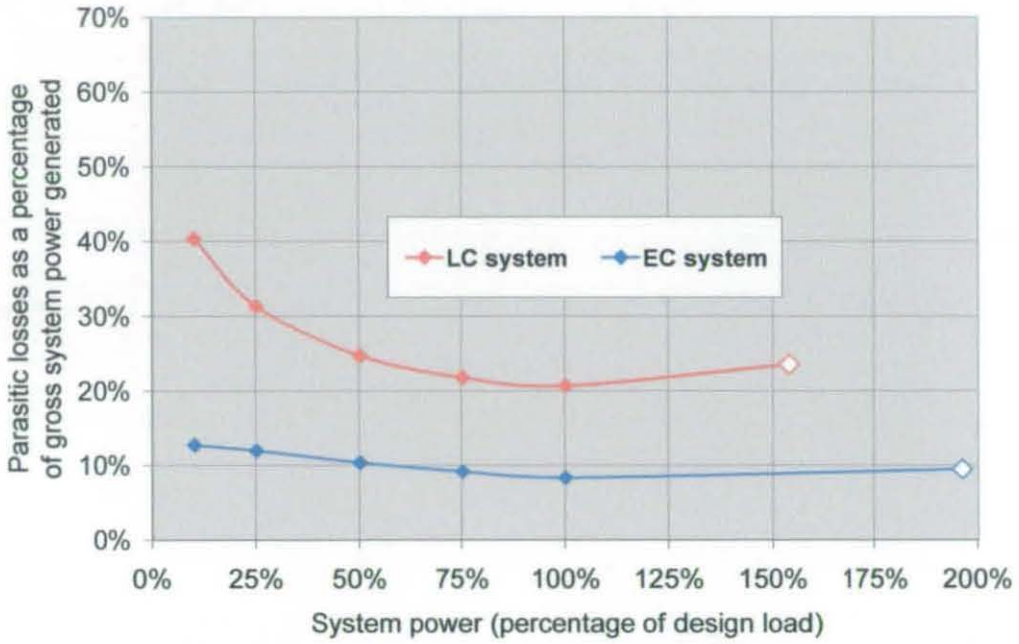

Fig. 5.17 Parasitic losses of both systems expressed as a percentage of gross system power - varying system power outputs

This clearly illustrates that, at the low and high extremes of LC system loading the efficiency is low. Here, the parasitic percentage is 40.4% at 10% system loading and 23.5% at maximum system output. For the EC system, at a 10% net system power loading, where all mechanical equipment will be operating at very low efficiencies the parasitic percentage value is 12.7%. At maximum system output the parasitic percentage loss is less than 10%.

5.4 Conclusions

The models developed in this chapter have illustrated that the EC stack can compete with a conventional high-pressure LC stack, primarily due to the reduction of parasitic losses associated with air compression but also because a higher stack packing density is achievable. These advantages are especially clear at partial power loads where the demands of the compressor penalise the LC system efficiency severely.

5.4.1 Limitations of models and comments

These steady-state models could not take into account aspects such as start-up from cold conditions and transient response to load changes. It could also be advantageous to cost the components of each system and it would then be possible to trade off capital cost and operating cost for each system.

One point to note is that the systems do not include a power conditioning subsystem, which would generally consist of a series of DC-DC converters, to alter the power supply to a more common voltage – e.g. 24 V

5.5 References

Amphlett J.C., Baumert R.M., Mann R.F., Peppley B.A., Roberge P.R., "**Performance modelling of the Ballard Mark IV Solid Polymer Electrolyte Fuel Cell 1: Empirical Model Development**" Journal of the Electrochemical Society, Vol. 142, pp 9-15, 1995

Amphlett J.C., de Oliveira E.H., Mann R.F., Roberge P.R., Rodrigues A, "**Dynamic interaction of a proton exchange membrane fuel cell and a lead-acid battery**", Journal of Power Sources, Vol. 65, pp173-178, 1997

Badrinarayanan, P., Ramaswamy, S., Eggert, A., Moore, R.M., "**Fuel Cell Stack Water and Thermal Management : Impact of Variable System Power Operation**", Fuel Cell Power for Transportation 2001, proc. of the SAE 2001 World Congress, pp 53-60, 2001

Bernardi Dawn M., Verbrugge Mark W., "**A Mathematical Model of the Solid Polymer Electrolyte Fuel Cell**", Journal of the Electrochemical Society, Vol. 139, No 9, pp 2477-2491, 1992

Bernardi Dawn M., "**Water Balance calculations for Solid Polymer Electrolyte Fuel Cells**", Journal of the Electrochemical Society, Vol. 137, No 11, pp3340-3350, 1990

Boettner, D.D., Paganelli, G., Guezennec, Y.G., Rizzoni, G., Moran, M.J., "**Proton exchange membrane (PEM) fuel cell system model for automotive vehicle simulation and control**", Proceedings of 2001 ASME International Mechanical Engineering Congress and Exposition, 2001

Coulson, J.M., Richardson, J.F., "**Coulson & Richardsons Chemical Engineering – Volume 1**", Fourth Edition, Pergamon Press, 1993

Cownden, R., Nahon, M., Rosen, M.A., "**Modelling and analysis of a solid polymer fuel cell system for transportation applications**", International Journal of Hydrogen Energy. Vol 26, pp615-623, 2001

Cunningham, J.M., Hoffman, M., Friedman, D., "**A Comparison of High Pressure and Low-Pressure Operation of PEM Fuel Cell Systems**", Fuel Cell Power for Transportatiion 2001, Proc. of the SAE 2001 World Congress, pp. 61-68, 2001

Dicks A., Larmanie J.E., *Fuel Cell Systems Explained*, John Wiley & Sons, Chichester , England, 2000

Friedman, D.J., Eggert, A., Badrinarayanan, P., Cunningham, J., "**Balancing stack, air supply and water/thermal management demands for an indirect methanol PEM fuel cell system**", Fuel Cell Power for Transportation 2001, Proc. of the SAE 2001 World Congress, pp37-46, 2001

Friedman, D.J., Moore, R.M., "**PEM Fuel Cell System Optimisation**", Proceedings of Second International Symposium on Proton Conducting Membrane Fuel Cells II, Edited by S. Gottesfeld et al, Electrochemical Society, Pennington, NJ, 1998.

Fronk, M.H., Wetter, D.L., Masten, D.A., Bosco, A., "**PEM Fuel Cell Systems solutions for Transportation**", Fuel Cell Power for Transportation 2000, Proc. of SAE 2000 World Congress, pp 101-108, 2000

Fuller, T.F., Newman, J.J., "**Water and thermal management in solid polymer electrolyte fuel cells**" Journal of the Electrochemical Society, Vol. 140, No. 5, pp 1218-1225, 1993

Guzzella, L., "**Control Oriented Modelling of Fuel Cell based vehicles**", Presentation in NSF Workshop on the Integration of Modelling and Control for Automotive Systems, 1999

Kim, J., Lee, S., Srinivasen, C., Chamberlin, J., "**Modelling of proton exchange membrane fuel cell performance with an empirical equation**", Journal of the Electrochemical Society, vol. 142, No. 8, pp2670-2674, 1995

Hamelin, J., Agbossou, K., Laperriere, A., Laurencelle, F., Bose, T.K., "**Dynamic behaviour of a PEM fuel cell stack for stationary applications**" International Journal of Hydrogen Energy, Vol.26, pp625-629, 2001

Lee, J.H., Lalk, T.R., Appleby, A.J., "**Modelling electrochemical performance in large scale proton exchange membrane fuel cell stacks**" Journal of Power Sources, Vol. 70, pp 258-268, 1998

Lee, J.H., Lalk, T.R, "**Modelling fuel cell stack systems**", Journal of Power Sources, Vol. 73, pp229-241, 1998

Nguyen, T.V., White, R.E., "**A Water and Heat management Model for Proton Exchange Membrane Fuel Cells**", Journal of the Electrochemical Society, Vol. 140, No. 8, pp 2178-2186, 1993

Pisani L., Murgia M., Valentini B., D'Aguanno B., "**A new semi-empirical equation approach to performance curves of polymer electrolyte fuel cells**" Journal of Power Sources, Vol. 108, pp192-203, 2002

Pukrushpan, J.T.; Stefanopoulou, A.G.; Peng, H.; "**Simulation and Analysis of Transient Fuel Cell System Performance based on a Dynamic Reactant Flow Model**", Proceedings of the International Mechanical Engineering Congress & Exhibition, pp1-11, 2002

Sena, D.R., Ticianelli, E.A., Paganin, V.A., Gonzalez, E.R., "**Effect of water transport in a PEFC at low temperatures operating with dry hydrogen**", Journal of Electroanalytical Chemistry, Vol 477, pp164-170, 1999

Springer T.E, Zawodzinski T.A., Gottesfeld S., "**Polymer Electrolyte Fuel Cell Model**", Journal of the Electrochemical Society, Vol. 138, No. 8, pp 2334-2342, 1991

Squadrito, G.,Maggio, G., Passalacqua, E., Lufrano, F., Patti, A., "**An empirical equation for polymer electrolyte fuel cell (PEFC) behaviour**" Journal of Applied Electrochemistry Vol 29, pp1449, 1999

Turner, W., Parten, M., Vines, D., Jones, J., Maxwell, T., "**Modeling a PEM fuel cell for use in a hybrid electric vehicle**", Proceedings of the 1999 IEEE 49th Vehicular Technology Conference, v.2, pp. 1385-1388, 1999

Virji, M.B.V., Adcock, P.L., Mitchell, P.J., Cooley, G., "**Effect of operating pressure on the system efficiency of a methane-fuelled solid polymer fuel cell power source**", Journal of Power Sources, Vol. 71, pp337-347, 1998

Yerramalla, S., Davari, A., Feliachi, A., Biswas, T., "**Modeling and Simulation of the dynamic behaviour of a polymer electrolyte membrane fuel cell**", Journal of Power Sources, Vol. 124, pp104-113, 2003

Yi, J.S., Nguyen, T.V., "**An along-the-channel model for proton exchange membrane fuel cells**", Journal of the Electrochemical Society, Vol. 145, No. 4, pp 1149-1159, 1998

Chapter 6:

Current mapping study of an EC fuel cell

6.1 Chapter Overview

In Chapter 4, it was observed that the temperature of the EC fuel cell varied, relative to the position along the straight gas tracks of the cathode flow field. In addition, the electrochemical performance, i.e. current density, will have varied across the electrode area during operation – although no clear assumptions could be made using the temperature data alone. The identification of areas of low current density would be a key step in optimising the design of components for the PEM fuel cell, particularly plate flow-field designs.

In this Chapter the concept of a fuel cell plate 'flow-field' is explained in more detail, with examples provided of the most common types. Following this, the concept of a segmenting a fuel cell electrode into separate areas for the purpose of obtaining current mapping plots is discussed, including a short literature review of the technique.

The main focus of the research in this Chapter is an investigation of the cathode flow-field for an EC fuel cell by using a segmented electrode tool. The study compares the performance obtained when utilising the parallel and interdigitated designs - illustrated in the form of current maps and polarisation plots.

6.1.1 Fuel cell flow-field arrangements

6.1.1.1 Overview

As stated in Chapter 2, the term "flow-field" refers to the arrangement of gas distribution channels fashioned into one side of a single cell flow plate or both sides of a stack bipolar plate. The main purpose of any plate flow-field arrangement is to achieve a complete and even distribution of reactant gas over the entire electrode, so that no areas become 'starved' during operation of the fuel cell. However, there are aspects of fuel cell assembly and operation that prevent such a uniform supply being possible:

1. To enable gas tight perimeter sealing and an acceptably low electrical contact resistance between the plate ribs and the diffuser material, a significant compaction pressure is applied to the fuel cell. As a result, areas of the diffuser directly below ribs undergo a degree of crushing such that gas transport to these areas becomes restricted due to much reduced permeability of the structure. This mechanism is illustrated for the cathode in Fig. 6.01

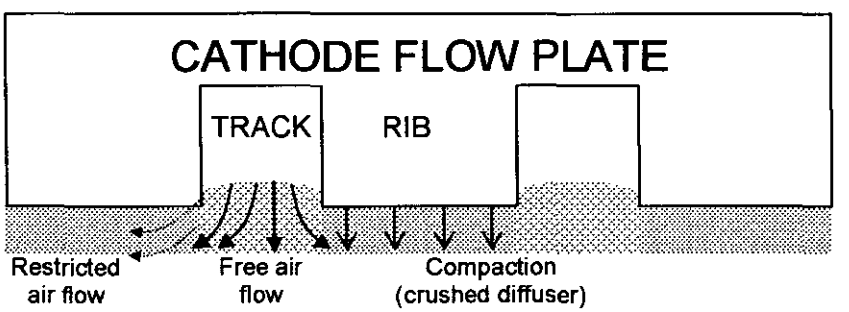

Fig 6.01: Illustration of the effects of diffuser crushing on gas transport

2. During fuel cell operation, product, and possibly humidification, water will accumulate in the pores of the diffuser material, particularly below ribs where, as stated above, gas transport is somewhat limited and there will be a lower rate of water evaporation. If not controlled, this water may shift from below the ribs, with droplets initially clinging to channel walls. These water droplets may tend to coalesce, forming larger droplets thus requiring a greater force to move them through the channel. Depending on the flow-field arrangement, the gas may then flow preferentially through the least obstructed channels with dead spots forming adjacent to the blocked channels throughout the fuel cell as illustrated in Fig 6.02. The degree of water accumulation may be controlled to a certain extent by using a diffusion material with a set amount of wet-proofing, see Chapter 7.

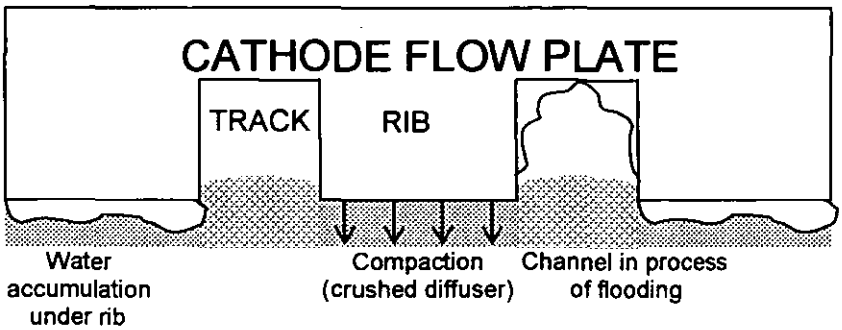

Fig 6.02: Illustration of the effects of cathode diffuser flooding

Therefore, all flow field designs - to some extent - represent a trade-off between flow channel area, for gaseous reactant distribution and reduced flooding, and rib area, for electrical contact paths and MEA support. Hence, the optimum flow field design for a PEM fuel cell application will be dependent on the fuel cell operating current, reactant gas stoichiometries, operating temperature and pressure, diffuser structure and compaction pressure, all of which influence the gas distribution and flooding behaviour.

As stated in Chapter 3, the controlling phenomena of fuel cell operational performance is the rate of the oxygen reduction reaction at the cathode. Thus, the statement can be made that *the choice of cathode flow-field geometry will have a strong influence on the performance characteristics of a PEM fuel cell.*

In the specification of a cathode flow-field, the following issues have to be considered:

- A flow-field must not present difficulties for a low-cost, high volume bipolar plate production process, although this is not an issue for small-scale laboratory-based research
- It must not unduly decrease the fuel cell stack power density by requiring thicker or reinforced plates - as would be the case with deep gas channels.
- It may be desirable to maximise the alignment of ribs of opposing anode and cathode flow field plate surfaces as this results in lower interfacial resistance due to an effective compression of the diffuser material between opposing plate ribs as described in Wynne et al (2001). Furthermore, channel-to-channel alignment increases the back diffusion of water across the membrane from cathode to anode.
- The choice of flow-field could also be restricted by the desire to use a 'corrugated' bipolar plate design, which requires thinner plate material than 'block plate'

designs as shown in Fig. 6.03. However, here the channel arrangement on one side of the plate is restricted by the presence of channels on the opposite side.

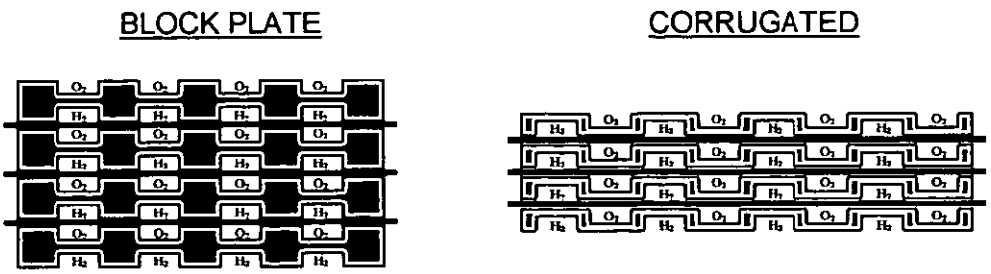

Fig 6.03: Illustration of necessary bipolar plate thickness with two different flow-field designs

- In applications such as the EC fuel cell, the pressure drop of the air caused by the flow field has to be low in order to reduce associated parasitics of air supply as much as possible.

6.1.1.2 Common Plate Flow-field Geometries

Many plate flow field designs are detailed in the literature, with all but the most novel categorised as one of the six types illustrated below in Fig. 6.04. These are briefly discussed with a view to suitability for use in the cathodes of an EC fuel cell.

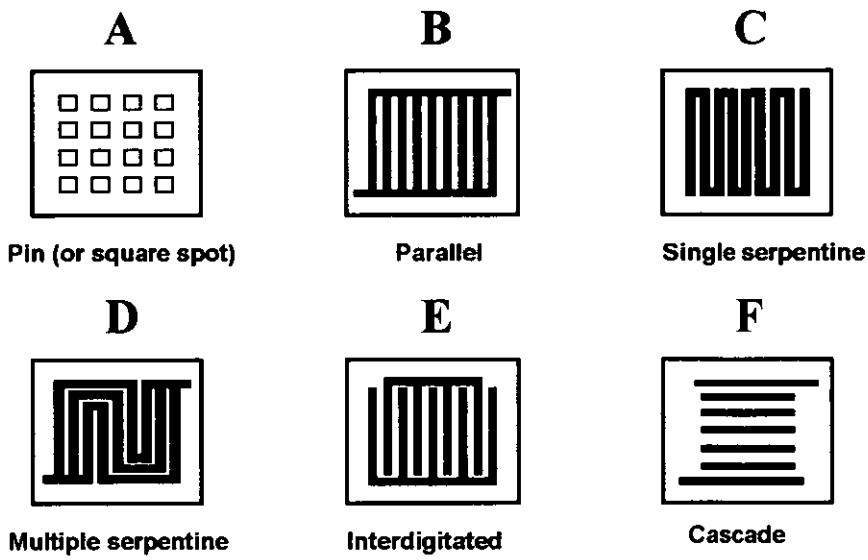

Fig 6.04: Illustration of different flow-field designs

The Pin, or square spot, flow field arrangement, design A, contains a series of interconnected flow channels, formed by a grid of raised plate contact areas, as detailed in Reiser et al (1988 and 1989). The particular nature of this arrangement will result in a low pressure drop of the air flow from the inlet manifold to the exit manifold. However, the gaseous reactants tend to follow preferential routes with the subsequent formation of stagnant areas. This design is rarely used in PEM fuel cells, and is usually only seen in very early examples of the technology. The significant presence of a two-phase flow in the cathode of an EC fuel cell eliminates the possibility of this flow-field being utilised.

With the single or multiple serpentine channel flow field, designs C and D, the reactant gas is obliged to follow a series of long paths over the entire electrode area, as described in Watkins et al (1991). These arrangements are advantageous in that they permit gas flow between adjacent legs of the same channel when a point of the flow channel is blocked, e.g. by a water droplet. In this regard, gas can flow from a portion of a channel, which is upstream of the blockage, through the diffuser material, to a portion of the channel downstream where the pressure is lower. However, the 180 degree bends of these flow paths can result in large pressure drops and introduce the possibility of undesired 'reactant-bypass' where the gaseous reactant does not traverse the entire length of the channel. This occurs when a high pressure inlet leg of a channel is located

close to a low pressure outlet leg of the adjacent channel, Epp et al, (1992), although this can be prevented to a certain extent by employing novel designs, Rock et al (2000). The high pressure drop generated by this flow field makes it unsuitable for an EC fuel cell.

A flow field with straight, parallel channels (design B) produces a lower pressure drop than a serpentine arrangement. However, as many low pressure-drop paths exist for the reactant gas flow, water droplets may not be removed effectively, resulting in preferential flow, although, not to the same degree as the square spot design. This design could be considered for an EC fuel cell

The interdigitated or 'forced-diffusion' configuration, design E, is similar in appearance to the parallel design except with only one entrance and exit port for each pair of tracks. This dead-ended feature forces all of the reactant gas into the diffuser material to reach the exit manifold. Here, the movement of reactant gas from the channel into the electrode resembles convection rather than diffusion and as a result, the rate of oxygen transport to the catalyst surface is increased and liquid water entrained in the diffusion material can be removed by the force of the gas flows. This flow field design was implemented in the cathode of the fuel cell utilised in the research described in Chapters 3 and 4. In the literature, it has been demonstrated that using the interdigitated design as the cathode flow-field of a PEM fuel cell improves performance, Nguyen (1996). Although there is likely to be a high pressure drop penalty this design could be considered for an EC stack due to the improved water management characteristics.

With the cascade structure, design F, the gas channels are isolated from the inlet and outlet manifolds and aligned perpendicular to the direction of the gas flow, Vanderleeden et al, (2002). The entire reactant gas flow passes from channel to channel by being forced through the small area of diffuser material located adjacent to each plate rib. The pressure drop, from entry manifold to exit manifold, in this arrangement will be very high. Furthermore, there may also be issues with maintaining the structural integrity of the diffuser over long periods of fuel cell operation due to a large amount of gas being forced through relatively small cross sectional areas. This flow-field would be unsuitable for the EC fuel cell as although cathode flooding would be minimised, the pressure drop would be very high and result in unacceptably large parasitic losses associated with the air delivery.

As a point of note there have been a few non-conventional attempts at creating flow-field designs for PEM fuel cells. These include:-

- Formation of gas channels in the diffuser, thereby attempting to eliminate the need for flow plates, with just a thin conducting separator required between cells, described by Wilkinson et al, (1993).

- Arrangements of metal wire, screens, Zawodzinski et al, (2001), and foils have also been investigated for flow-field purposes. However these particular techniques are beyond the scope of this thesis and were not considered in any detail.

6.1.1.3 Channel/Rib dimensions

Optimising individual channel and rib sizes for any given flow-field geometry is a complex task in which several considerations must be accounted for. Firstly, there has to be a careful balance between the rib contact areas and flow channel areas and any alteration to this ratio must not significantly reduce performance.

Decreasing the cross section area of the channels increases the velocity of a set gas flow, which should make the removal of liquid water more effective, but this would encourage a higher pressure drop. Increasing the cross sectional area, by increasing channel depth, lowers the pressure drop but would increase plate thickness and hence lower stack power density.

Examples in the literature of studies in flow plate track dimensions include West and Fuller (1996) and Nguyen et al (1995) who presented results indicating rib width has a strong influence on fuel cell performance.

6.1.2 Measurement of fuel cell current distribution

6.1.2.1 Overview

When a fuel cell is operational, the current density at any point of the active electrodes will be a function of many local parameters, i.e. - concentration of electrochemical species at both catalyst surfaces, membrane water content, temperature and compaction pressure. The difficulty in maintaining identical conditions at each point of the fuel cell is the primary reason for an irregular distribution of current obtained across the electrode area. Examples of this include the anticipation of a lower current density at the end of cathode gas tracks where there will be prevalent two-phase flow and lower concentrations of oxygen.

The ability to analyse the performance of individual regions of an electrode and thus obtain a 'mapped profile' of current distribution would be useful for the optimisation of a fuel cell design. There are several mathematical models in the literature which attempt to predict the distribution of current, usually by calculating parameters such as the transport of gaseous species or membrane water content. Some of these models provided data for a single gas track, Wang et al (2001) and Nguyen et al (1998). Other models focus on specific flow field geometries for the prediction of performance, Kazim et al, (1999) and Nguyen et al (1999). However, as explained earlier in Chapter 5, all analytical models have limitations and presently cannot account for all considerations of fuel cell operation to provide an accurate prediction of current distribution.

There are several examples of fuel cell performance analysis using current mapping in literature – these are detailed in the next section.

6.1.2.2 Current distribution study – literature review

Of the examples in the literature detailing current mapping techniques in electrolytic cells, most involve separating an electrode into segments with subsequent reassembly using electrical insulation between segments. One of the earliest examples demonstrated an electrode of a hypochlorite cell constructed from 20 separate electrically insulated blocks, each potentiostatically controlled, Czarnetzki et al (1989). Similar segmented arrangements were used in the investigation of mass transfer-current distribution relationships in electrochemical cells, Qi et al (1990) and Bisang (1993). Another technique in the measurement of current distribution in a PEMFC included an array of reference electrodes fabricated onto Nafion membrane using micro-lithographic techniques, Rieke et al, (1987).

Cleghorn et al (1997) used a copper printed circuit board (PCB) design to collect current distribution data from a fuel cell with a 100 cm^2 active area. The PCB contained a seven track parallel serpentine flow field spanning 18 gold plated segments. An interesting note of this particular study was the degree of segmentation that was achieved which eliminated any possibility of cross-plane conduction in the fuel cell. The catalyst layer was spliced with a scalpel when it was on the PTFE transfer block, prior to application to the PFSA membrane in the production of the MEA. The gas diffuser was also segmented, consisting of sections of ETEK carbon cloth in a silicone gasket frame. The major disadvantage with this arrangement was the necessity for two electronic load units. To measure the performance of a particular segment it had to be uncoupled from the main load unit, and then brought to the same potential as the remaining 17 segments, which took considerable time. The results showed the principal influence of fuel cell performance to be the water content of the Nafion 117 membrane.

Stumper et al (1998) presented work detailing three different techniques for the measurement of current distribution based on a 240 cm^2 active fuel cell area. In the first, referred to as the "partial MEA" method, three MEA's were manufactured with differing proportions of catalyst deposition: - one third, two thirds and complete catalyst coverage. By subtracting one set of polarisation data from another the performance could be obtained for any particular third of the electrode. The results showed an increased effect of flooding at higher current densities when the second and third portions were catalysed.

The second approach, the "sub-cell" method, used several electrically isolated 10 mm diameter sections in the anode and cathode gas diffusion electrodes, corresponding to pre-determined locations along the gas track. These were positioned opposite each other

on fuel cell assembly, thus forming several 'sub-cells', allowing a distinction between anode and cathode performance. The results indicated that at for a location far down the gas track, the anode overpotential was comparable to the cathode overpotential and electrode flooding was responsible for the low performance.

The third method reported in this paper, the "current mapping technique", demonstrated a spatial measurement of current mapping by using a passive resistor network distributed over the entire electrode area. This was done by constructing a block made up of 121 hexagonally arranged electrically isolated graphite elements, located between the rear of the flow plate and a separate current collector plate. By measuring the potential difference across each graphite element, the local current through the corresponding cross section of the cell could be calculated, and by scanning the entirety of the segments, the current distribution could be established. The results showed a large degree of scatter in the current distribution, with the main problem in the arrangement being the lack of segmentation of the flow field plate, therefore significant lateral currents could not be avoided.

Rajalaksmi et al (2002) developed a similar sub-cell current distribution method to that of Stumper, separating a 370 cm^2 active area into equal 12 parts. This was done by cutting sections in insulating acrylic anode and cathode flow plates and replacing them with graphite. The gas diffusion electrodes were also segmented by using a silicone gasket frame. However, to measure a sub cell current, each of the other segments had to be uncoupled from the load box. Noponen et al (2002) carried out a similar study using Stumpers third method, on a small air breathing fuel cell. It was illustrated that in this type of fuel cell the operating temperature had a significant effect on performance

Potter (1999) constructed a circular PEM fuel cell with a graphite current collector made up of 88 segments. This work showed the effect of using unhumidified gaseous reactants on the hydration levels (water content) on particular areas of the membrane and hence the performance obtained.

Bender et al (2003) detailed a study with an anode graphite block separated into ten pieces. The current lead wires of each segment were threaded through separate Hall sensor devices. This arrangement allowed monitoring of all segments as well as a measurement of high frequency resistance (HFR) distribution and spatial ac impedance spectroscopy. Natajaran et al (2003) described a small-scale segmented cell with graphite strips embedded into an acrylic block - this allowed a current distribution study of two parallel channels.

A technique developed by Wieser et al (2000) measured current distribution using a magnetic loop array. The advantage of this technique was the lack of requirement for any modification of the MEA, diffusers or flow plates. The principle behind this technique involved using Hall-sensors to determine the current by the measurement of magnetic induction. An array of 40 such sensors was built behind 38 x 38 mm^2 areas of a flow field plate covering a 578 cm^2 MEA area in total. The disadvantages of this technique were the restricted spatial resolution achievable and the inability to adapt the technique into fuel cell stacks.

6.2 Experimental Analysis with Segmented Fuel Cell

6.2.1 Overview

To study cathode flow-field design, it was decided to obtain measurements of current distribution from a fuel cell equipped with direct cathode liquid water injection to the cathode - the same technique as integrated into the fuel cell detailed in Chapters 3 and 4. A segmented fuel cell electrode tool was available that had been previously used in work by Potter (1999). This gave the ability to measure current distribution to a resolution of 0.5 mm in one dimension for a fuel cell with a 200 cm^2 active area.

The chosen area of study was a direct comparison of the fuel cell performance obtained with the parallel and interdigitated cathode flow field configurations. Studies by Nguyen et al, (1996) have illustrated that the interdigitated cathode flow field produces an elevated fuel cell performance over the parallel configuration, although, it is expected that the pressure drop from air inlet to exit will be higher due to the particular nature of the arrangement – see section 6.1.1.2. As illustrated in the models in Chapter 5, the air supply power requirements of a fuel cell system represent the largest proportion of the overall parasitic losses. Therefore, any enhancement in the fuel cell performance obtained from using the interdigitated flow field may be penalised by the inability to use a simple low pressure source to supply the stack with air.

A comparison of the distribution of current obtained with both parallel and interdigitated flow field configurations. would present the opportunity to identify reasons for variations in performance. Further characterisation of each flow-field would be possible by collecting data for variable operating pressures and air stoichiometries.

In the proceeding sections, firstly the equipment available is described along with the modifications that were necessary for its application to this particular research. Current maps, along with polarisation plots, are presented which illustrate the fuel cell performances using the two cathode flow-field configurations. Comparative measurements of the cathode pressure drop are also presented.

6.2.2 Equipment

This sub-section outlines the most critical functions of the equipment, however is not intended to be an exhaustive analysis; for a full detail of the build and choice of materials the reader is referred to Potter (1999)

The main component of the EC fuel cell was a segmented current collector piece, as illustrated in Fig. 6.05.

Fig 6.05 Segmented current collector piece

This had been constructed from 120 stainless steel shim pieces, 48 x 0.5 mm thickness shims in the centre region and 36 x 1.5 mm thickness shims either side, electrically isolated from each other with a 0.05 mm separator sheet of PTFE. The shims were arranged and clamped together between two machined end blocks by four clamping bolts, forming a flat plate face with a 200 cm^2 active area.

In each shim a resistive shunt feature had been formed, which allowed a value for the current flowing through the shim to be established by measuring the potential difference between two voltage pickup sockets, illustrated in Fig. 6.06, and then using a pre-measurement of resistance for the calculation of current.

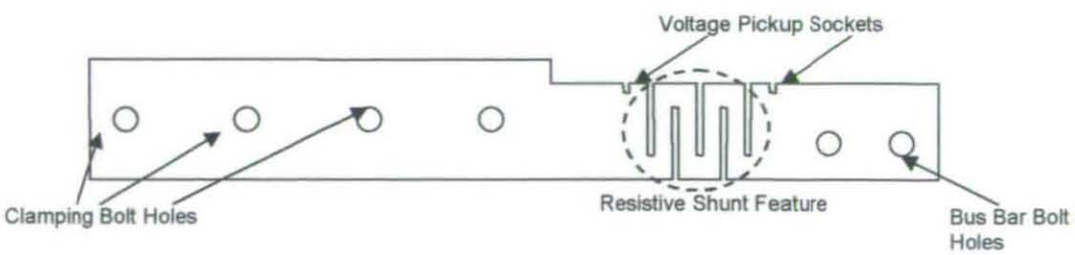

Fig 6.06 Single shim used in construction of segmented fuel cell

The potential difference across each shim was output as an analogue signal via pins in fitted 'D' sockets, built into the rear of the current collector piece, to a data acquisition device. The PVDF insulator sheets stopped after the shunt features and were replaced by a 50 micron stainless steel piece to the end of the shim length. Here, the shims and end blocks were clamped together via two further compaction bolts to a copper bus bar for current take-off. Straight channels, 138 mm in length and orientated perpendicular to the shims, had been previously formed in the plate face - these were supplied with gas via manifolding located in the end blocks.

With this design, the measurement of current distribution was similar to the third segmented fuel cell electrode method detailed by Stumper et al (1998), i.e. a passive resistor network. The crucial difference being that in this case, the flow plate was segmented which would yield data less skewed by cross plane conduction. In these tests the segmented face would be utilised as the anode so that the cathode flow-field could be designed as desired.

The segmented fuel cell assembly is shown in Fig. 6.07 below.

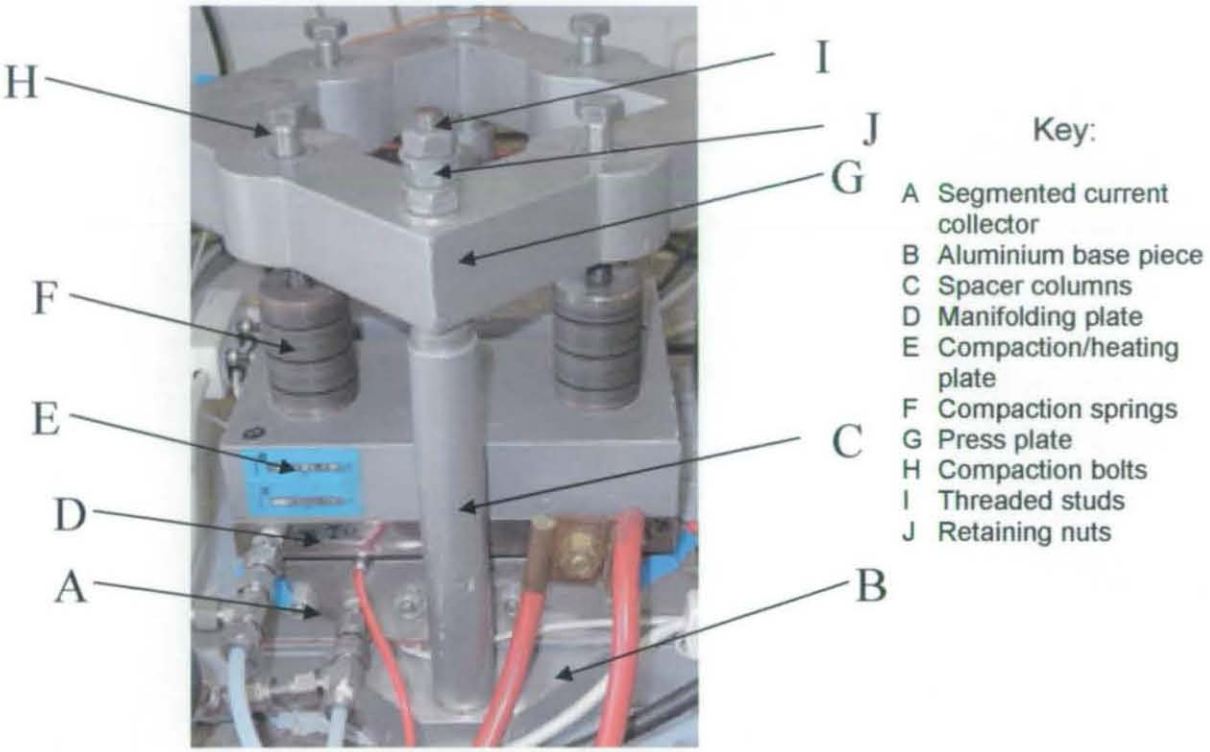

Fig. 6.07 Segmented rig arrangement

The segmented current collector plate (A) was mounted on an aluminium base piece (B), which is also shown in Fig. 6.05. This contained recesses on the underside for fixing spacer rods (C) via socket cap screws, which are not shown here. The single fuel cell was built on top of the segmented face, i.e. anode diffuser, MEA, cathode diffuser and cathode flow plate. Immediately on top of this was a 20 mm thick stainless steel cathode manifold plate (D) supplying air to the rear of the cathode flow plate via a side entry Swagelock fitting. It also contained a brass stud as the cathode current take-off point. Immediately on top of this there was a 40 mm thick compaction/heating plate (E) internally fitted with two cartridge heaters, and contained four circular recesses on the top face. These recesses accommodated four compaction springs (F) that consisted of a set of bevel washers around a steel stalk. These were used for measuring the force being exerted on the cell by the compaction bolts (H) that were threaded through a press plate (G), fixed to the top of the studs (I) by retaining nuts (J).

6.2.3 Modification of equipment

Several modifications had to be made in order to adapt the equipment to the operational simulation of an EC fuel cell – these are now discussed.

The previous work undertaken using this equipment, Potter (1999) focused on the current distribution over a single parallel cathode flow channel. This resulted in low currents passing through each shim and thus low measured shunt potentials that were subject to electrical noise. In addition, it had been reported that poor quality data had been obtained using the segmented current collector due to vastly differing contact resistances on the stainless steel shim faces. Subsequently, it had been necessary to establish a correction factor, to 'smooth out' the current maps, which may have eliminated some of the most crucial features of the data. In addition, small membrane humidifiers had been used to add moisture to the reactant gases that did not provide accurate control over the proportion of water added.

It was decided that this series of tests would use the full 200 cm^2 active area of the segmented current collector and thus produce more realistic current mapping data than had previously been obtained. To solve the problem of differing shim interfacial resistances, gold was sputtered onto the plate face[1] – scanned pictures of this process are shown separately in appendix D.

It was considered not feasible to run the rig thermally isolated, in a similar manner to the EC tests detailed in Chapter 4, due to the large heat sinks represented by the bulk of the anode current collector, aluminium base, cathode manifolding block and compression piece, parts A, B, D and E respectively. However, the results from Figs. 4.07 - 4.08 did not show a large deviation in performance between liquid water injection using EC and LC operating conditions. Therefore, the effects of liquid water injection with the two cathode flow fields would be illustrated using non-adiabatic conditions.

[1] This work carried out by Teer Coatings, Hartlebury

6.2.4 Choice of components

A sufficient number of Gore 6000 series MEA's from the original segmented rig testing were available to complete these tests. These contained an integrated expanded PTFE gasket surrounding the 200 cm^2 square active electrode area. The use of these MEA's meant that no other gasketing arrangement was necessary. Carbel CL was used as the diffuser material for both anode and cathode sides of the fuel cell.

6.2.4.1 Direct liquid water injection plate

A new cathode flow plate had to be designed, equipped with a direct liquid water injection mechanism, using a similar technique to that detailed in section 3.2.2.5. Due to the different dimensions of the segmented fuel cell components and the single fuel cell test stand in Chapter 3, the stainless steel flow plate could not be re-used. Therefore a new plate was constructed from a sheet of non-porous graphite, measuring 200 mm x 200 mm x 10 mm^2.

The water injection feature had to be designed, differently to the feature detailed in the cathode flow plate used in Chapter 3, due to the much more brittle nature of graphite in comparison to stainless steel. Linking a primary water gallery to an air manifold chamber, as shown in Fig. 3.10, would weaken the structure and risk breakage of the plate on the application of the compaction force to the fuel cell.

The novel approach taken is illustrated in Appendix E, which is an AutoCAD drawing of the graphite cathode plate design. The tappings drilled through the plate thickness linking the rear air manifold plenum to the flow field tracks were met by diagonal tappings from the water gallery on the FRONT face of the plate. The water gallery itself was packed with three layers of filter paper and a layer of silicon to create the pressure drop feature that ensured an even flow through each hole, a similar mechanism to that detailed in Chapter 3. The point of water injection was a small tapped hole on the side of the plate accommodating an M5 – 4 mm stainless steel push fitting. The flow field design consisted of forty six 1 mm wide by 1 mm deep by 140 mm long parallel gas tracks with a pitch spacing of 3 mm. The entry and exit points on the rear manifolds corresponded to the gas delivery and take-off ports in the stainless steel cathode manifold plate. The flow-field was to be converted from parallel to interdigitated configuration by blocking alternate feed and exit track holes with Araldite.

[2] Purchased from Erodex, UK

6.2.5 Data Acquisition and Software

The data acquisition system that had been used previously with this segmented electrode tool by Potter (1999) was available for use here. This was a high precision National instruments SCXI (Signal Conditioning eXtensions for Instrumentation) arrangement consisting of a SCXI 1000 chassis housing four SCXI – 1100 signal conditioning modules, each capable of multiplexing up to 32 analogue channels, in this case the potential differences over the shunt features of each shim, into a single differential analogue signal.

The connections on the segmented electrode tool were connected to the signal conditioning modules via SCXI-1300 terminal blocks. The chassis was connected, via a SCXI 1349- 5 metre long shielded cable assembly, to an At-MIO-16E-10 Multifunction DAQ card in a PC which had been pre-installed with the NI-DAQ driver software to communicate with the chassis and modules. A dedicated Labview software application had been previously written to simultaneously read, display and log the values of the current density from all 120 shims in real-time. The reader is referred to Potter (1999) for an in-depth description on this software.

6.2.6 Operational Control

For the accurate supply of reactant gases and injected water the Aera mass flow equipment and HPLC pump, detailed in Chapters 3 and 4, were used. For the accurate measurement of the pressure drop between cathode inlet and exit, two Keller digital manometers were purchased, which had a maximum range of 2 bar.g with a resolution of 1 mbar.

A 300 W heating mat had been previously installed into the base of the segmented current collector piece. This and the two 150 W cartridge heaters installed in the compression plate were powered from a 240 V ac power supply to maintain the fuel cell at the desired operating temperature. This was switched on and off by comparing a pre-set temperature with a value read from a reference 'K' type thermocouple inserted in the cathode plate. This was a similar method to the fuel cell temperature control used in the fuel cell rig detailed in Chapter 3. The large heat sinks meant there was no requirement for any external cooling mechanism except for the direct injection of liquid water to the cathode flow-field. The electronic load unit with the fitted resistive current shunt described in Chapter 3 was again utilised for the galvanostatically controlled delivery of current from the fuel cell.

6.2.7 Calibration of software and pre-testing of rig

Shim current calibration in software

The Labview software was re-calibrated by the author to accurately measure the current flowing through each shim channel. This was carried out by operating the DAQ hardware and Labview software while delivering a precise current of 1 Amp to each shim in turn from a high-precision, calibrated power supply. In the Labview software, each value of shim current density was calculated by dividing the potential difference between the voltage take off sockets by a variable value of resistance and the shim face area, the latter value differing between the 0.5 mm and the 1.5 mm thick shims. The shim resistance value for each channel was adjusted in the software accordingly so that 1 Amp equivalent current density was displayed on the real-time bar graph for that particular shim.

Compaction springs

A pre-calibration of the compaction springs, a measurement of spring height versus applied force, was carried out in an extensometer. Measuring the displacement of each spring with digital callipers and using this force/height calibration established the compaction pressure exerted on the segmented cell, during operation or assembly.

Initial testing

An initial series of tests was undertaken to check that the gold plating process had equalised the interfacial resistance of each shim. This was done by inserting two layers of Carbel diffusion material and setting up the fuel cell arrangement as normal and applying a 10 Amp current using the load unit set to 'active'. An even current distribution profile was obtained on the display software – also confirmed by manually logging potential measurements with a multimeter between the start of each shim and the bus bar.

6.2.8 Test design

Obtaining polarisation curves, similar to those detailed in Chapter 3 would illustrate the varying behaviour of the fuel cell using the two cathode flow fields at variable air stoichiometries and pressures. In addition, the polarisation plots were carried out with both a counterflow AND coflow arrangement of reactant gases to highlight any effects of varying water distribution around the fuel cell on the electrochemical performance. Water is injected to the cathode to obtain an equivalent relative humidity of 100%RH for the air.

The next stage of the investigation was to obtain current mapping plots with the same sets of operating conditions which will provide information on how the spatial performance over the fuel cell electrode is influenced by operational parameters. The current map data was recorded subsequent to the fuel cell having obtained complete steady state operation following at least 30 minutes of continuous operation, fixed at a potential of 500 mV, with the load unit operating galvanostatically. In doing this, instead of comparing maps of equal total current, the performances could be compared at equal operational efficiencies. All data presented are the average of the steady-state performance, logged by the software over a ten minute period.

The test matrix for the polarisation plots and current map tests was as follows:

Flow configuration of reactant gases	Temperature / °C	Pressure / bar.g	H_2 stoichiometry	Air stoichiometry	Air humidication / %RH
Coflow	60	0.5	1.5	2	100
Coflow	60	0.5	1.5	3	100
Coflow	60	0.5	1.5	4	100
Coflow	60	0.5	1.5	6	100
Counterflowflow	60	0.5	1.5	2	100
Counterflowflow	60	0.5	1.5	3	100
Counterflowflow	60	0.5	1.5	4	100
Counterflowflow	60	0.5	1.5	6	100
Coflow	60	Ambient	1.5	4	100
Coflow	60	0.5	1.5	4	100
Coflow	60	1	1.5	4	100
Coflow	60	1.5	1.5	4	100
Counterflowflow	60	Ambient	1.5	4	100
Counterflowflow	60	0.5	1.5	4	100
Counterflowflow	60	1	1.5	4	100
Counterflowflow	60	1.5	1.5	4	100

Fig. 6.08 Test matrix for segmented cell testing

6.2.9 Rig Assembly

There were two planned builds of the fuel cell, the first operating with the parallel cathode flow field and the second with the interdigitated flow field, however, any damage to the MEA would result in another build being necessary to complete the series of tests.

To begin a build, the single cell was constructed on top of the segmented face of the segmented current collector piece, which had been aligned correctly on the base piece. The stainless steel air manifolding plate was accurately positioned on top of the rear of the graphite cathode plate with an electrically conducting Grafoil gasket placed between to prevent damage to the plate.

An insulating sheet of glass reinforced silicone sheet was placed on top of the air manifold plate followed by the compaction/heater plate. The compaction springs were then placed in the recesses of the compaction plate and the press plate fixed in position at the top of the studs by the retaining nuts. The compaction bolts were then tightened to a sufficient degree so that gas, water and electrical fittings could be attached. Voltage probes were placed on the graphite flow plate and the copper bus bar and were connected to a multimeter. Air and hydrogen supply lines were attached to the fuel cell via Swagelock fittings and the reference thermocouple inserted into a recess in the graphite flow plate.

The same pre-test procedures as detailed in Appendix C were followed before each testing session. The gas and water flowrates used were supplied according to appendices A1 and B1.

6.2.10 Photographs of segmented fuel cell rig

Some photographs of the equipment set-up are shown below:

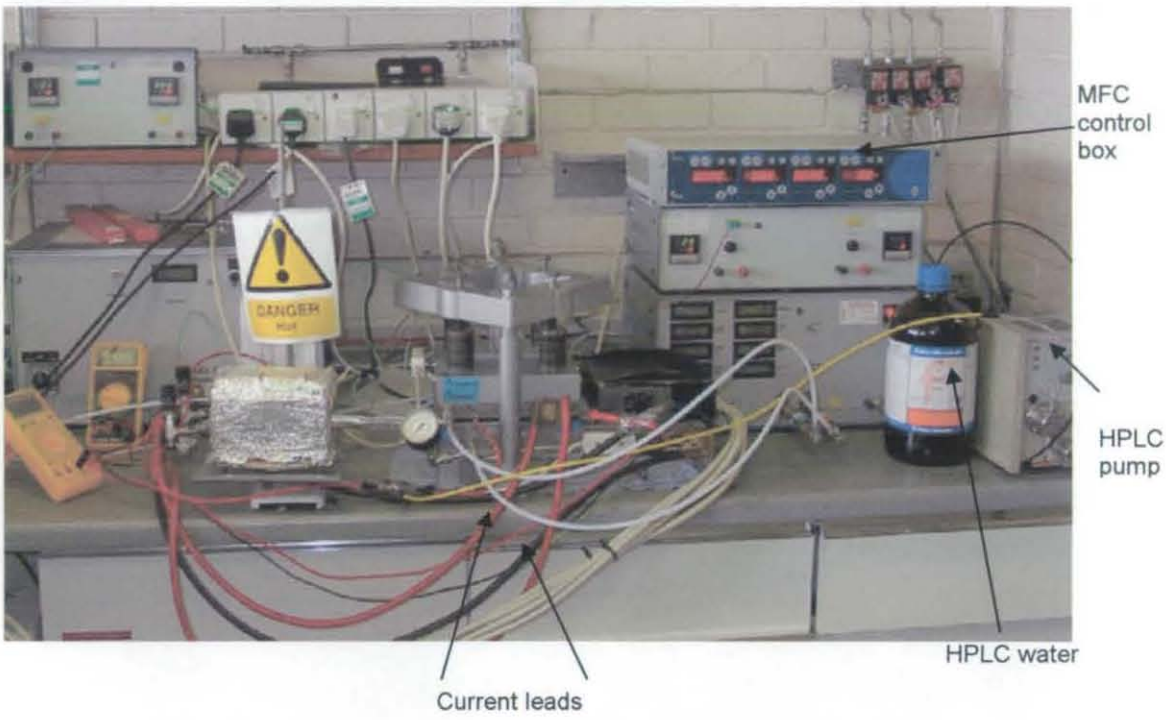

Fig. 6.09 Front view of segmented fuel cell rig assembly

Fig. 6.10 Data monitoring and acquisition for segmented fuel cell rig assembly

6.3 Results

6.3.1 Parallel vs. interdigitated cathode flow fields– polarisation plots

Variable air stoichiometry - Coflow

Polarisation curves obtained from the segmented fuel cell arrangement using both parallel and interdigitated cathode flow field configurations for different air supply stoichiometries are illustrated in Fig. 6.11. A coflow arrangement of hydrogen and air is used with the air humidified to as close to 100% RH as possible by direct water injection from the HPLC pump - the remaining operating conditions are detailed on the chart. The polarisation data have been collected on an increasing current basis.

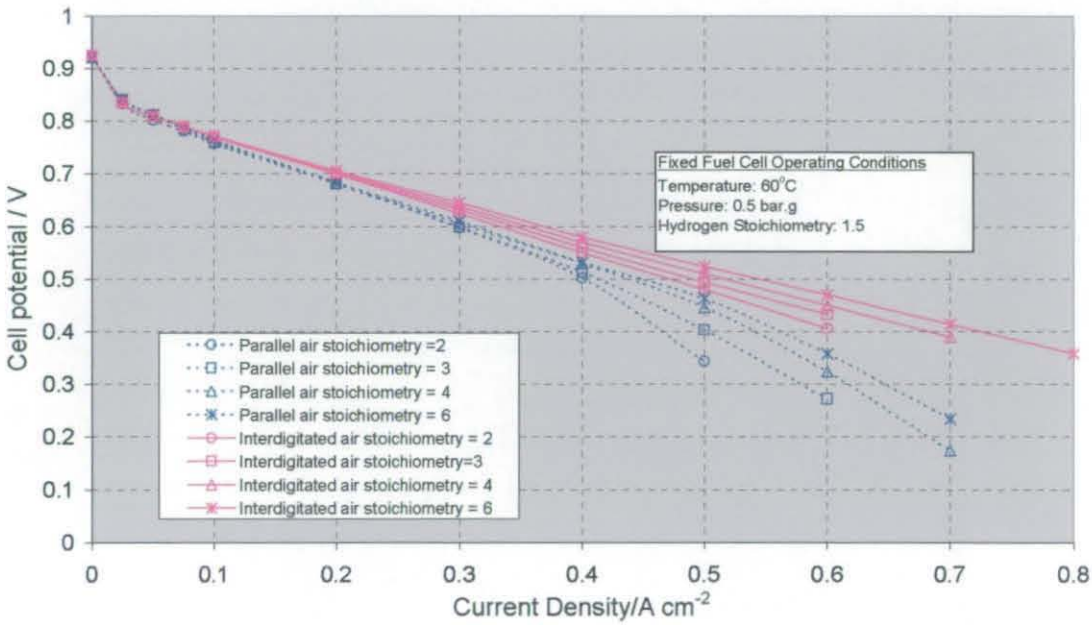

Fig. 6.11 Polarisation curves with parallel and interdigitated cathode flow fields using variable air stoichiometries – coflow configuration of reactant gases

It is observed that an elevated performance is obtained from the fuel cell by using the interdigitated cathode flow-field, here, the polarisation plots with different air stoichiometries show similar trends to those as seen in Fig. 3.17. With the parallel flow-field configuration there is clear evidence of mass transport overpotential dominating the ends of the plots, although the effect is lessened with increasing air stoichiometry.

At 0.6 Volts, all four parallel plots produce a performance of approximately 0.3 Amps/cm^2 and the interdigitated plots 0.34 - 0.37 Amps/cm^2. Hence, the polarisation plot obtained with an air stoichiometry of 2, using the interdigitated flow field, is superior to that obtained with an air stoichiometry of 6, using the parallel configuration. This appears to

confirm that the interdigitated configuration does indeed improve gas transport into the diffuser material, as reported by Nguyen et al (1996).

Variable air stoichiometry - Counterflow

The same set of polarisation tests performed in Fig. 6.11 were carried out for the counterflow arrangement of reactant gases, i.e. hydrogen inlet and exit lines switched around, these results are illustrated in Fig, 6.12.

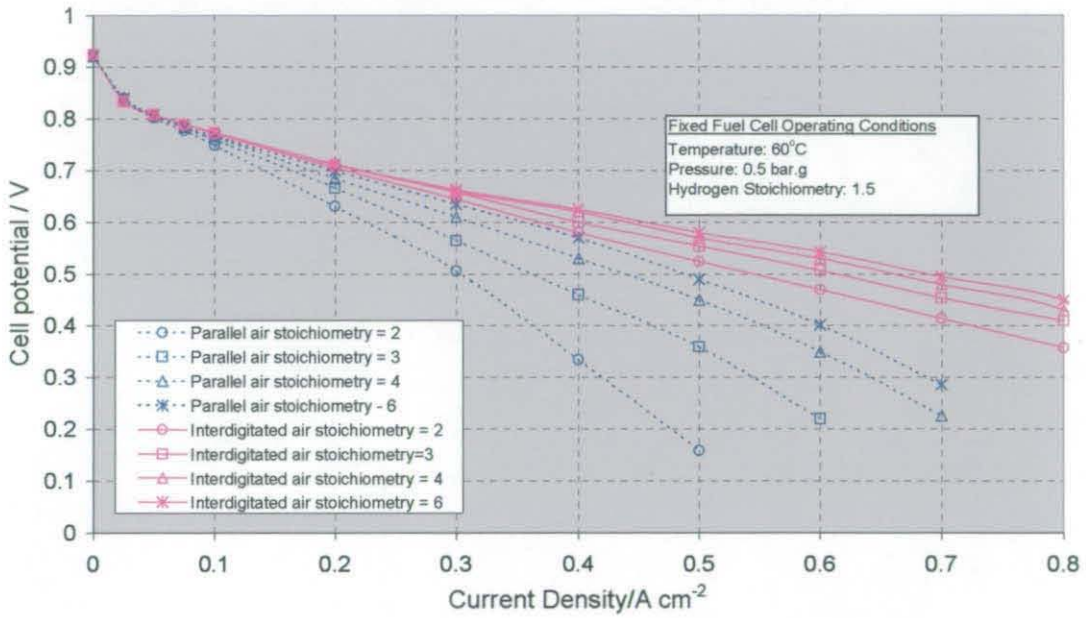

Fig. 6.12 Polarisation curves with parallel and interdigitated cathode flow fields using variable air stoichiometries – counterflow configuration of reactant gases

Again, the interdigitated cathode plots produce superior performance to the parallel plots and show similar behaviour to that seen in Fig. 6.11. The parallel counterflow performances are poorer than the coflow equivalents for low air stoichiometries (2 - 3) and are roughly equal with high air stoichiometries (4 - 6). This performance reduction with counterflow configuration and lower air flowrates is likely to be due to increased flooding in the cathode tracks due to a more even distribution of water around the fuel cell. Therefore, with the counterflow configuration there is two phase flow on the inner side of the electrode at the start of the cathode gas track due to electro-osmotic drag of water from anode to cathode. The large performance difference observed between the parallel polarisation plots with an air stoichiometry of 2 and 3 confirms this reduction in flooding. With the interdigitated cathode flow-field the performance is better for every counterflow polarisation plot over coflow. The difference is most prominent as a less steep linear region of the polarisation curve, indicating stronger differences in mass transport overpotential, i.e. transport of oxygen to catalyst sites but also lower resistance

of the membrane due to enhanced water distribution. At 0.6V, the performances with the parallel flow-field are 0.225-0.37A/cm^2 and with the interdigitated 0.36-0.46A/cm^2

Various Operating Pressure - Coflow

Polarisation curves obtained from the segmented cell arrangement with both cathode flow-field configurations, using a coflow arrangement of reactant gases and various operating pressures are illustrated in Fig 6.13.

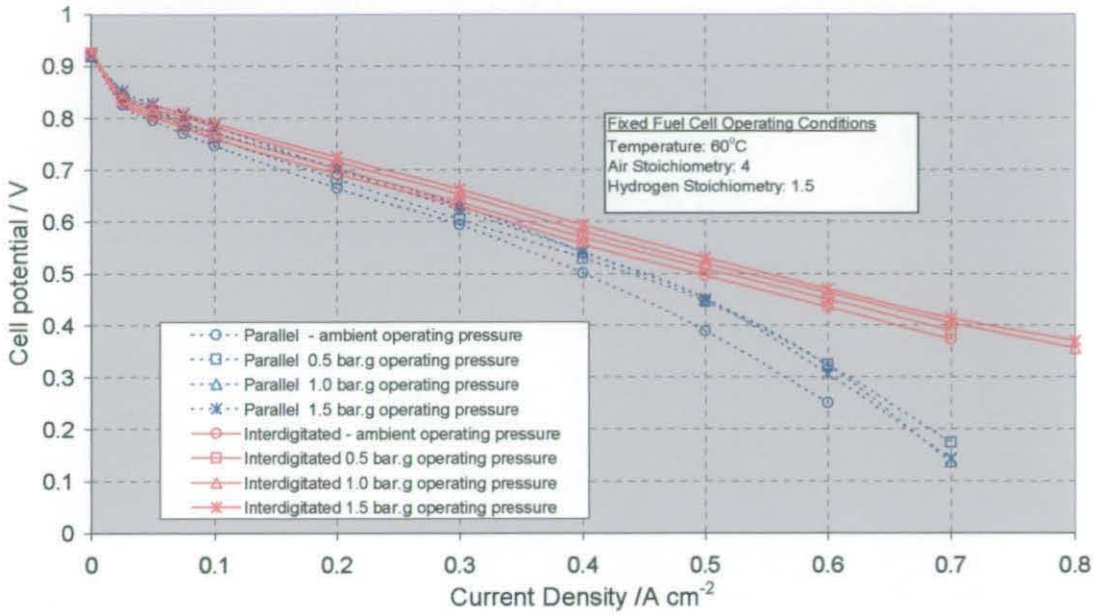

Fig. 6.13 Polarisation curves with parallel and interdigitated cathode flow fields with variable operating pressures – coflow configuration of reactant gases

Again, it is seen that the interdigitated cathode flow-field configuration produces superior results to the parallel arrangement. With the interdigitated flow field, the performance improves with increasing pressure in a similar manner to Fig 3.16, due to decreasing activation overpotential i.e. caused by a faster pace of the cathode reaction – refer to Chapter 2. In the parallel plots, although with increasing pressure the activation overpotential is lowered, the mass transport overpotential is increased due to the higher presence of liquid water – confirming Equation 3.07. This is observed at current densities in excess of 0.5 Amps/cm^2 where the parallel plots of 1.0 bar.g and 1.5 bar.g fall below the 0.5 bar.g plot.

For an operating potential of 0.6 Volts the parallel performances are 0.28 - 0.34 Amps/cm^2 and for interdigitated 0.34 - 0.39 Amps/cm^2.

Variable Operating Pressure - Counterflow

Polarisation plots obtained with variable operating pressures using both cathode flow-fields and a counterflow configuration of reactant gases are shown in Fig. 6.14.

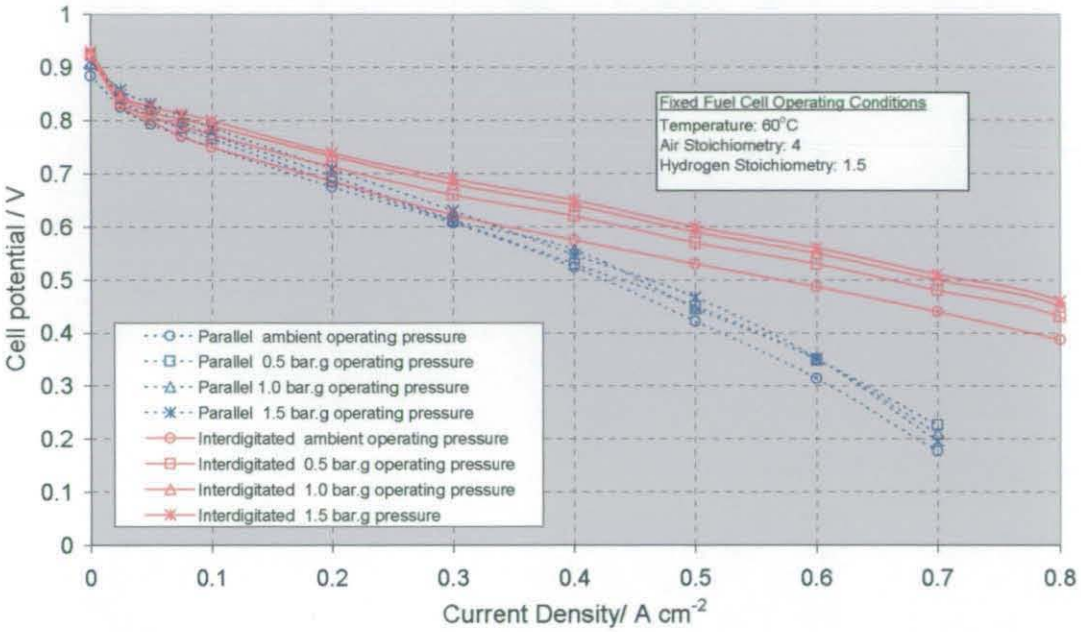

Fig 6.14 Polarisation curves with parallel and interdigitated cathode flow fields with variable operating pressures – counterflow configuration of reactant gases

Continuing the trend observed so far, the interdigitated cathode flow-field produces the superior fuel cell performance over the parallel configuration. There is a bigger elevation between the interdigitated plots as pressure increases compared to the coflow plots which is caused by greater reductions in activation overpotential – especially between ambient pressure and 0.5 bar.g - a result of the forced air flow mechanism. The same effect of increased mass transport overpotential with increasing pressure as observed in Fig. 6.13 is present in the parallel plots here.

At an operating point of 0.6 Volts the performance of the parallel plots is in the range 0.3 -0.34 Amps/cm^2 and the interdigitated plots in the range 0.34 - 0.5 Amps/cm^2.

Conclusions from Polarisation Plots

The observations from utilising parallel and interdigitated flow field configurations with both coflow and counterflow configurations of reactant gases are as follows:

- The parallel arrangement was seen to encourage electrode flooding with the effect of dominating mass transport overpotential clearly observed on every plot. This was not the case when using the interdigitated configuration.

- A counterflow arrangement of reactant gases was seen to further increase mass transport overpotential using the parallel cathode flow field. This was due to the enhanced distribution of water around the fuel cell which air is not able to remove when the parallel flow-field was used. However, the interdigitated plots show an enhanced performance using the counterflow configuration.

- A higher operating pressure encouraged the increased presence of liquid water in flow-field gas tracks, i.e. obeying the partial pressure gas law. When using the parallel flow field, this was observed to increase mass transport overpotential in the polarisation plot, however, this effect was absent in the polarisation plots with the interdigitated flow-field.

6.3.2 Current mapping plots

6.3.2.1 Coflow configuration of gases

Variable air stoichiometries

The first current mapping plot from the segmented cell arrangement is illustrated in Fig. 6.15 - these data have been obtained with the parallel flow-field on the cathode, using variable air stoichiometries and a coflow configuration of reactant gases while holding a potential of 500 mV. The distance along the cathode gas tracks from entry manifold to exit manifold is illustrated on the x-axis with the recorded current density flowing through each shim illustrated on the y-axis. Other operating conditions are shown on the plot.

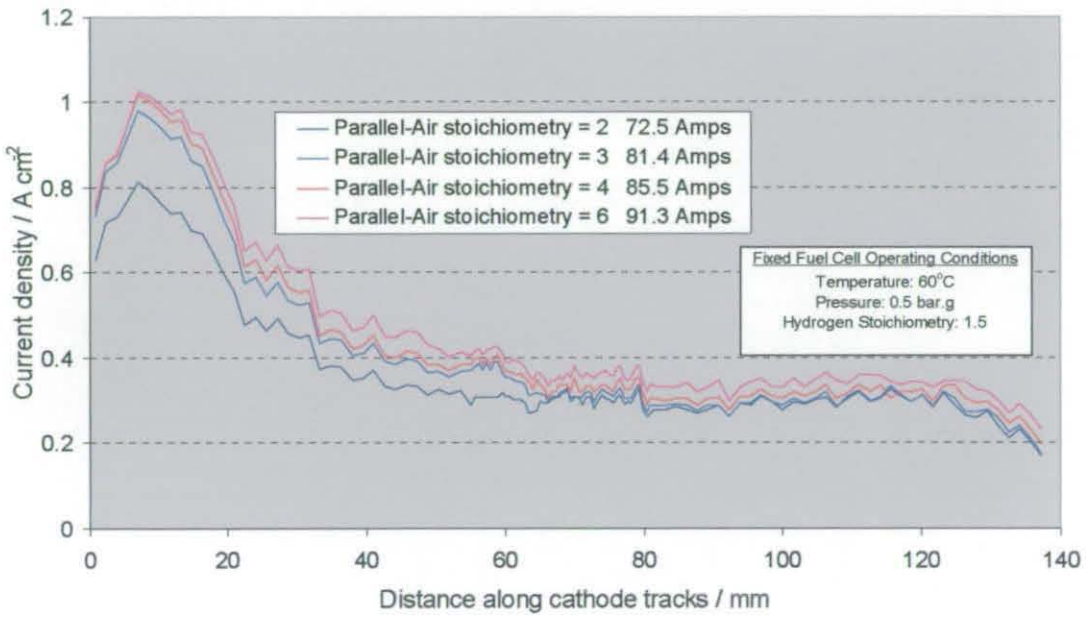

Fig 6.15 Current maps at fuel cell potential of 500 mV - parallel cathode flow field with variable air stoichiometries – coflow configuration

The general shape of each plot shows the current density initially having a high value with gradual deterioration towards the end of the cathode gas track. The total fuel cell current at a fixed potential increases with air stoichiometry, confirming the results from the previous polarisation plots.

For all four plots, the performance rises for the first 7 mm of the track, and then, immediately after drops rapidly before levelling off and then dropping further in the final 20 millimetres of track. The elevation in performance between plots, due to the higher air stoichiometry, is evenly distributed over the entire cathode gas track length.

It can be stated that the trend of a reduction in current density with distance along the cathode gas track is due to the depletion of the oxygen content in the air, and to a much lesser extent the hydrogen on the anode side. In addition to this the increasing presence of liquid water on catalyst sites and diffuser pores, i.e. electrode flooding, lowers performance with distance. This reflects the simple diffusion mechanism that the parallel flow-field encourages. The current peak at 7 mm is very likely to be caused by a low membrane water content adjacent to the gas track entrances. This is because water does not immediately penetrate the diffuser as the air is not hydrated, i.e. there is two phase flow, so water can be removed from the membrane by evaporation at this point.

The same current mapping plots for several air stoichiometries as obtained with the interdigitated cathode flow-field are illustrated below in Fig. 6.16.

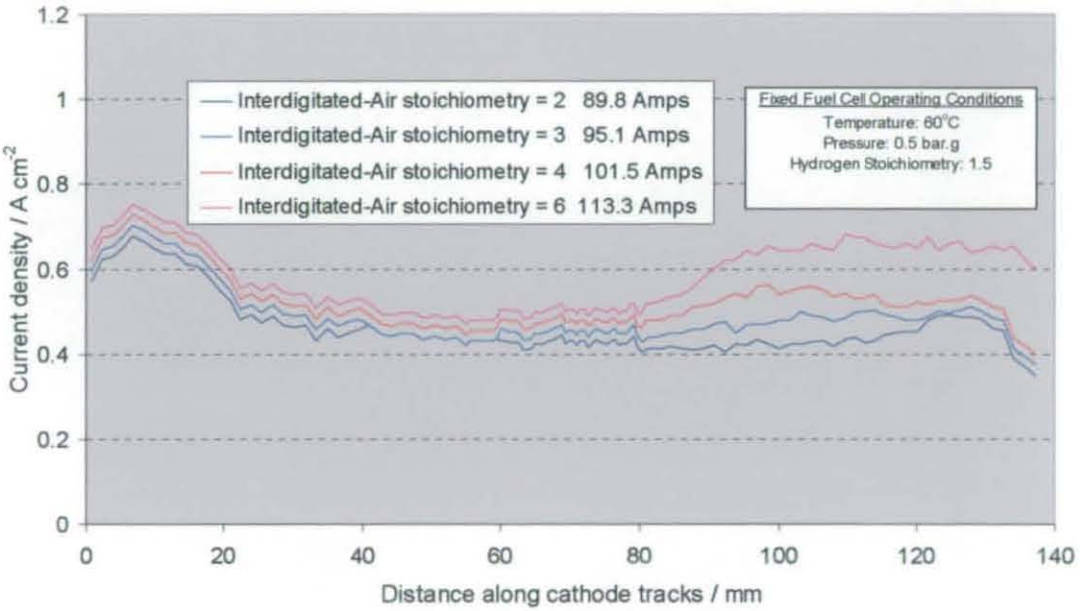

Fig. 6.16 Current maps at fuel cell potential of 500 mV - interdigitated cathode flow field with variable air stoichiometries – coflow configuration

These plots shows an increase in the current density in the final 50 mm of the cathode gas track which is in contrast to the continued deterioration of performance with track distance seen with the parallel flow field. This is likely to be due to the flow mechanism, instigated by the interdigitated flow field, where at the end of the gas tracks air is forced into the diffuser, increasing the concentration of oxygen at catalyst sites and reducing the effect of flooding. This effect is confirmed by the larger increase in performance at the latter portions of track with the higher air stoichiometries.

The contrast in the previous current maps obtained with the parallel and interdigitated cathode flow-fields is more clearly illustrated in Figs 6.17 and 6.18.

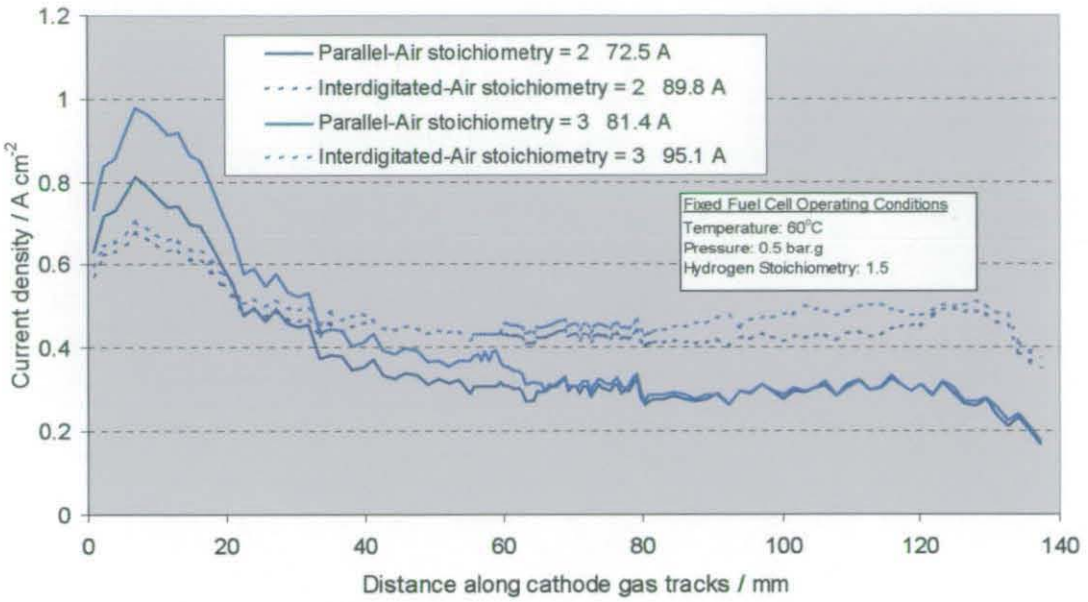

Fig 6.17 Current maps with both flow fields with low air stoichiometries
Data from Figs. 6.15 & 6.16 used - coflow configuration at 500 mV potential

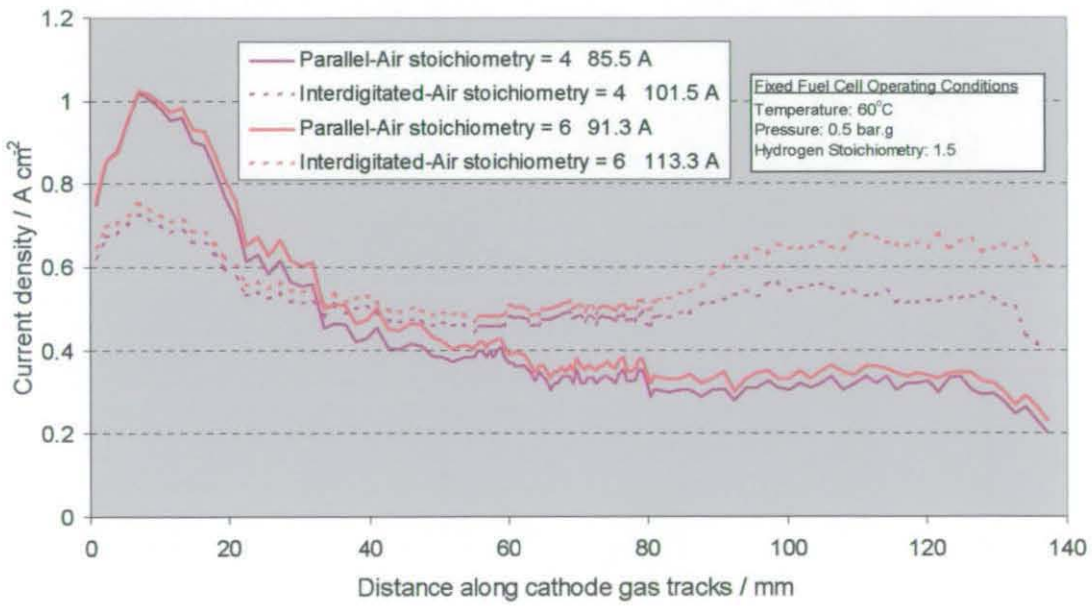

Fig 6.18 Current maps with both flow fields with high air stoichiometries
Data from Figs. 6.15 & 6.16 used - coflow configuration at 500 mV potential

Here, the effect of the interdigitated flow field mechanism on the fuel cell performance can be seen, particularly in the second half of the track.

Variable operating pressures

The current mapping plots obtained from the segmented fuel cell for a parallel cathode flow-field arrangement at various operating pressures with a coflow configuration of the reactant gases are shown in Fig. 6.19.

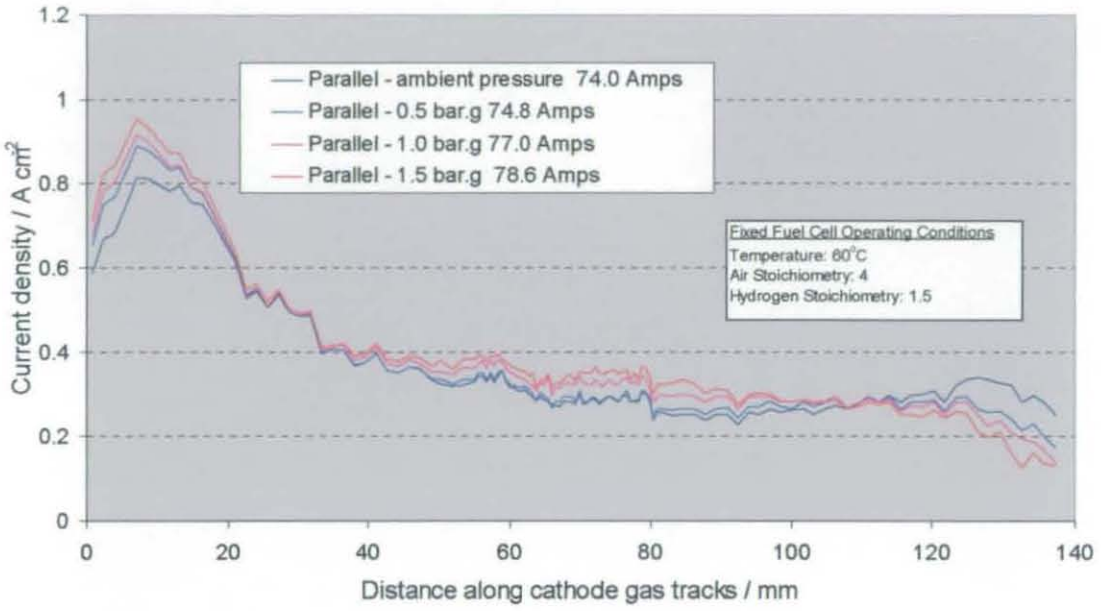

Fig 6.19 Current maps at fuel cell potential of 500 mV - parallel cathode flow field with variable operating pressures – coflow configuration

In a similar manner to the plots in Fig 6.15, there is a general degradation of performance from the entrance to the exit of the cathode gas track. It is observed that although the total current obtained from the fuel cell increases with operating pressure these improvements are mainly in the first 80 mm of the cathode track distance. The last 30mm of the cathode track shows an actual reduction in performance with increasing pressure. This is due to the increased presence of liquid water, due to the higher water partial pressure, hindering oxygen diffusion to catalyst sites in this region.

The same current mapping plots obtained with variable fuel cell operating pressures, now using the interdigitated cathode flow field are illustrated below in Fig. 6.20.

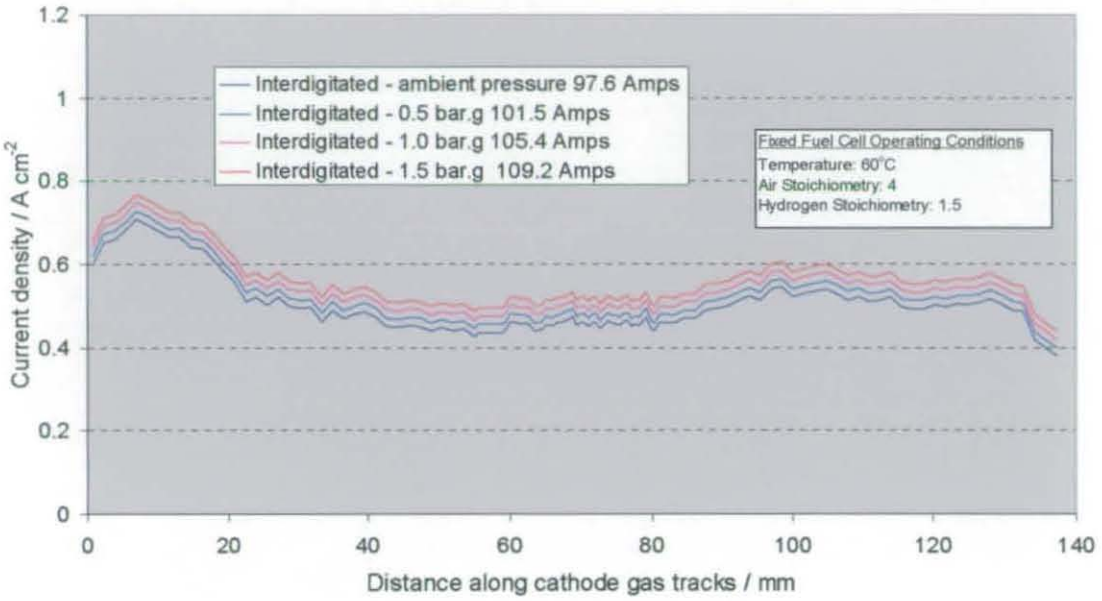

Fig 6.20 Current maps at fuel cell potential of 500 mV - interdigitated cathode flow field with variable operating pressures – coflow configuration

It is observed that in contrast to the parallel flow-field configuration, the elevation in total performances with higher operating pressure is spread evenly over the track length. There is no evidence of flooding caused by the higher operating pressure at the ends of the gas tracks.

Direct comparisons of the previous parallel and interdigitated current mapping plots for variable operating pressures are shown in Figs. 6.21 and 6.22.

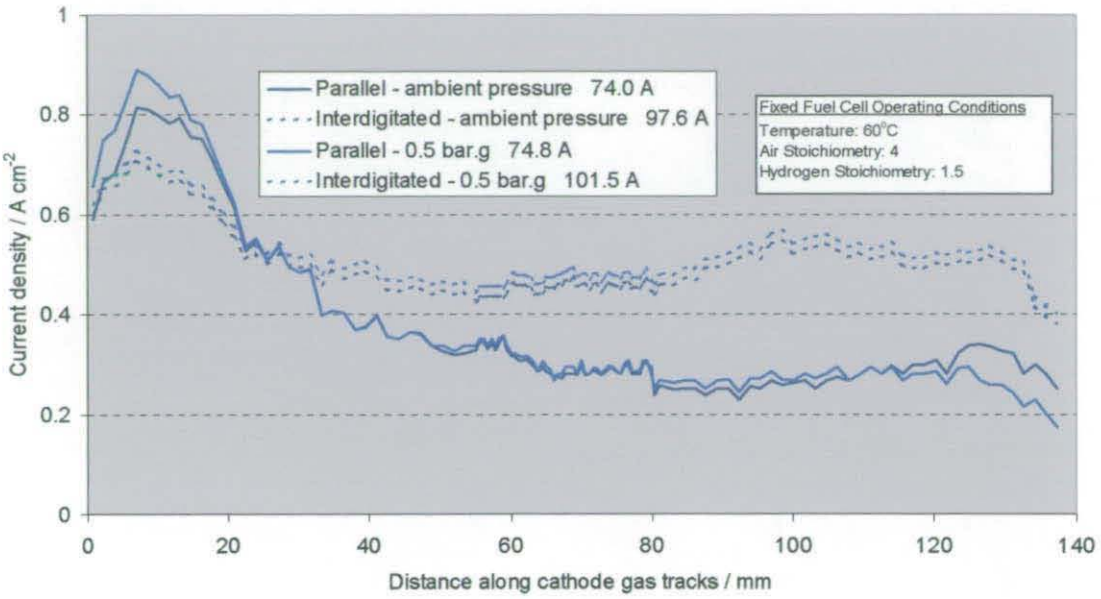

Fig 6.21 Current maps at fuel cell potential of 500 mV – both flow fields with low operating pressures – coflow configuration

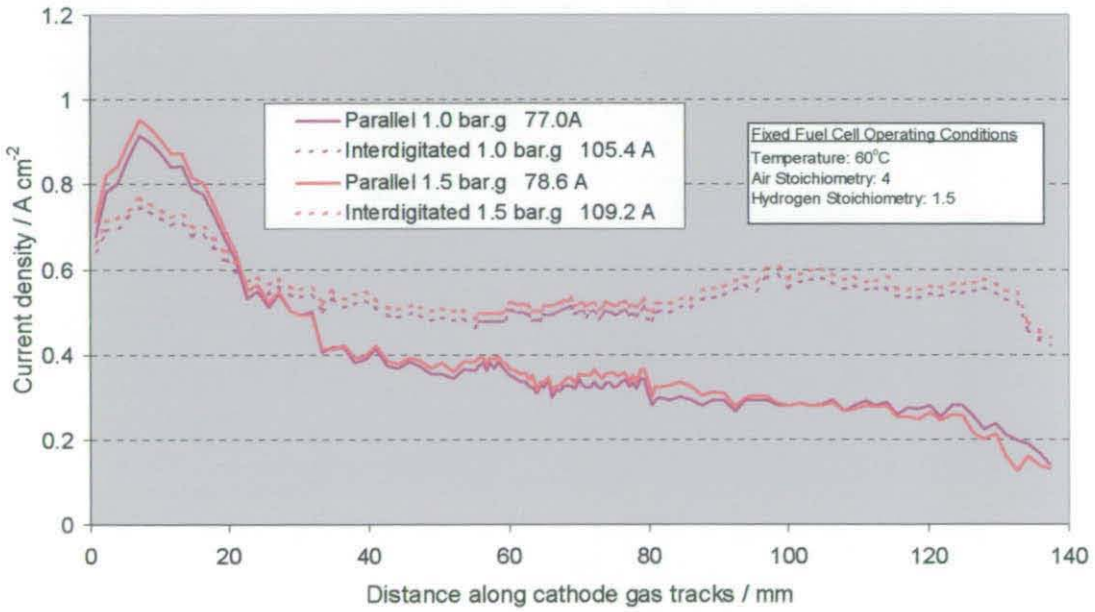

Fig 6.22 Current maps at fuel cell potential of 500 mV – both flow field with high operating pressures – coflow configuration

The effect of the interdigitated flow-field on performance is again clear, with a higher current density obtained in the latter sections of the cathode gas tracks

6.3.2.2 Counterflow configuration of gases

The following series of current mapping plots were obtained by a repeat of the previous tests, except carried out with the counterflow configuration of reactant gases. Any variation in the distribution of current compared to the previous tests will be due to the differing water distribution in the fuel cell. To display the plots in terms of distance down the cathode gas track, the current density values extracted from the raw data, have been reversed in order.

Variable air stoichiometry

The current mapping plots obtained at 500 mV, with variable air stoichiometries using the parallel cathode flow-field are shown below in Fig. 6.23. The same formatting for the charts used in the previous section is used.

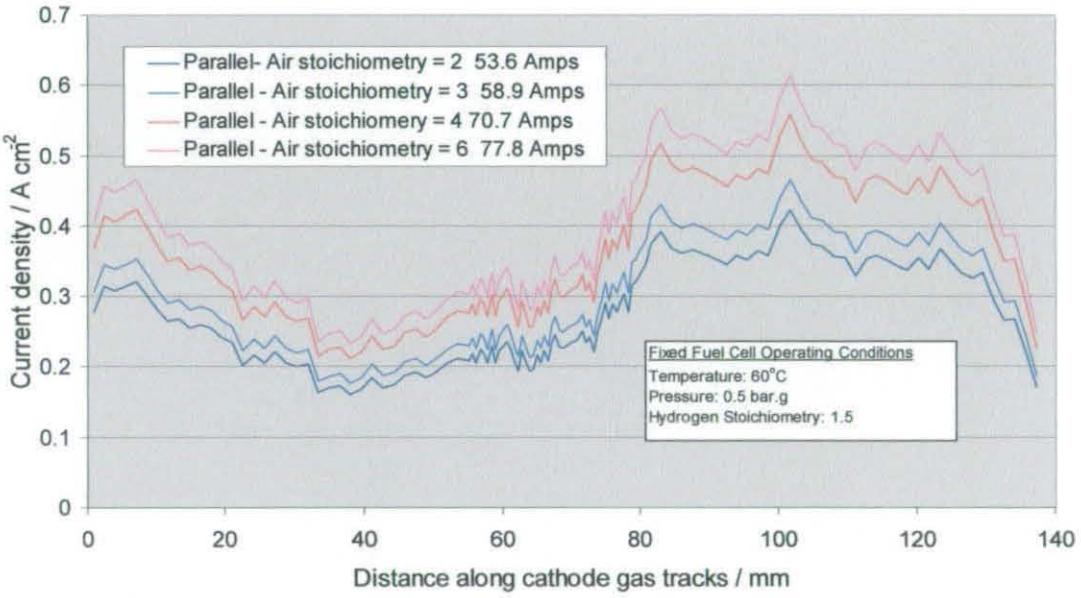

Fig 6.23 Current maps at fuel cell potential of 500 mV - parallel cathode flow field with variable air stoichiometries – counterflow configuration

In all four plots the current density initially deteriorates and reaches a minimum value approximately 40mm down the track. The values then rise to a maximum between 80-120 mm, before dropping off in the final 20 mm. These current plots exhibit different trends as seen with the parallel flow-field and a coflow configuration of gases. The minimum current density, observed around 40 mm from the track entrance, represents the location where the inner side of the electrodes were flooded due to saturated air and hydrogen, the latter which was obtained water from the air exhaust side through the back diffusion mechanism. Further down the track, water is able to be transferred to the anode

side where the hydrogen is drier and the performance is increased. The drop in current density in the final 20 mm of track is quite similar to that seen on the previous plots as oxygen is depleted from the air flow and the increased presence of liquid water .

The current mapping plots obtained with variable air stoichiometries using the interdigitated cathode flow-field are shown below in Fig. 6.24.

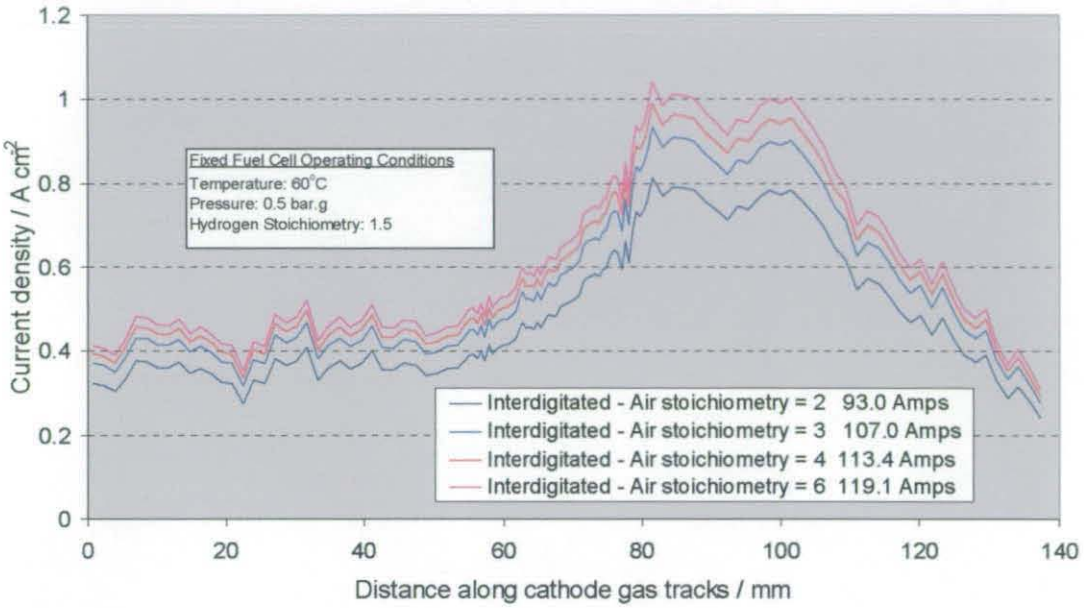

Fig 6.24 Current maps at a fuel cell potential of 500 mV - interdigitated cathode flow field with variable air stoichiometries – counterflow configuration

This shows an almost level performance of 0.4 Amp/cm^2 for the first half of the cathode track, which is in contrast to every current mapping plot observed so far. In the second half of the track, the peak area of performance of 1 Amp/cm^2 is between 80 – 120 mm, i.e. in a similar manner to Fig. 6.20. After 100 mm the performance steadily drops due to depletion of oxygen and increased two phase flow in the cathode.

Previously with the coflow configuration of gases and the interdigitated flow-field, Fig. 6.16, the highest performance was at the very end of the cathode gas track. Here there is dehydration of the anode side of the membrane due to the dry supply of hydrogen but the shear flow of air also removes water from the electrodes so the performance is further degraded by a dry membrane on the cathode side.

Direct comparisons of the current mapping plots between the two flow fields using the data from Figs. 6.23 and 6.24 are shown in Fig. 6.25 and Fig 6.26.

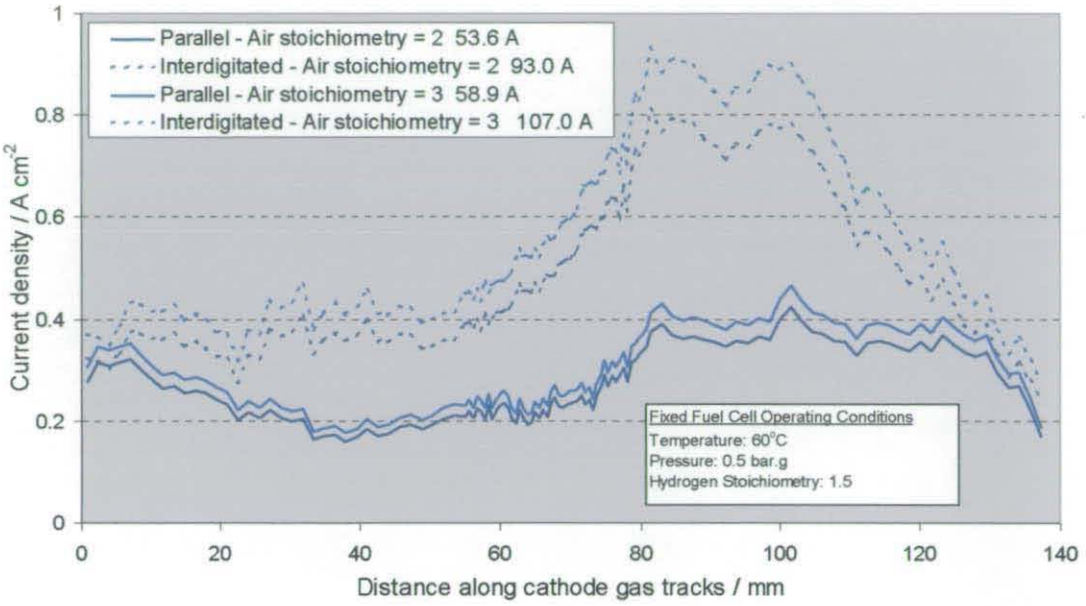

Fig. 6.25: Current maps with both flow fields with low air stoichiometries
Data from Figs. 6.23 & 6.24 used - counterflow configuration at 500 mV potential

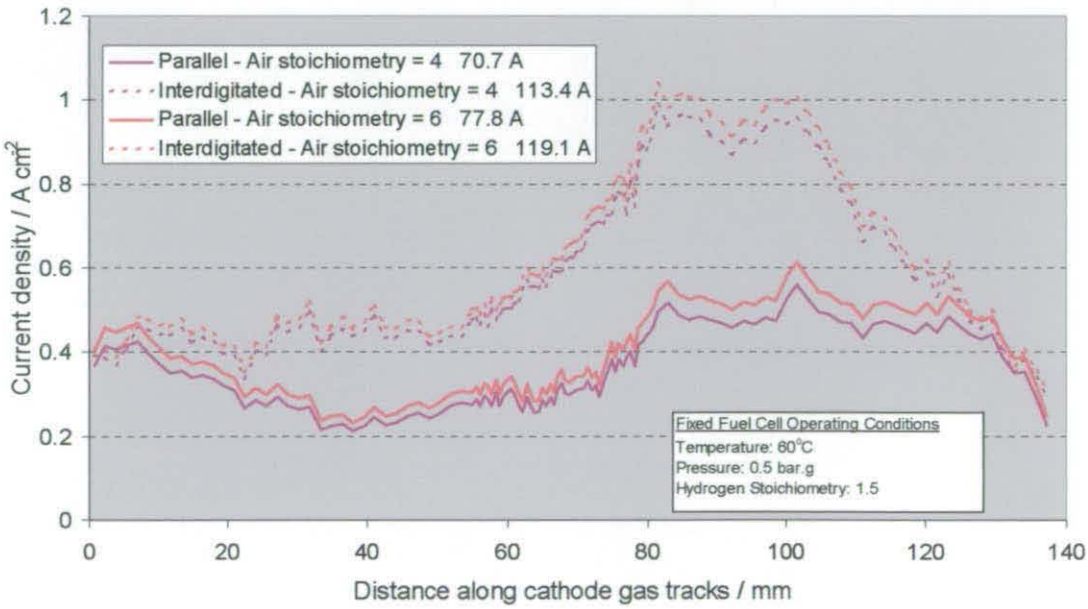

Fig. 6.26: Current maps with both flow fields with high air stoichiometries
Data from Figs. 6.23 & 6.24 used - counterflow configuration at 500 mV potential

It is observed that the flow mechanism encouraged by the interdigitated flow field causes a large peak, approximately two-thirds of the way down the cathode gas track, at a position 80 mm – 100 mm from the track entrance.

Variable operational pressures

The current mapping plots obtained from the segmented fuel cell with variable operating pressures are shown for the parallel cathode flow field in Fig. 6.27.

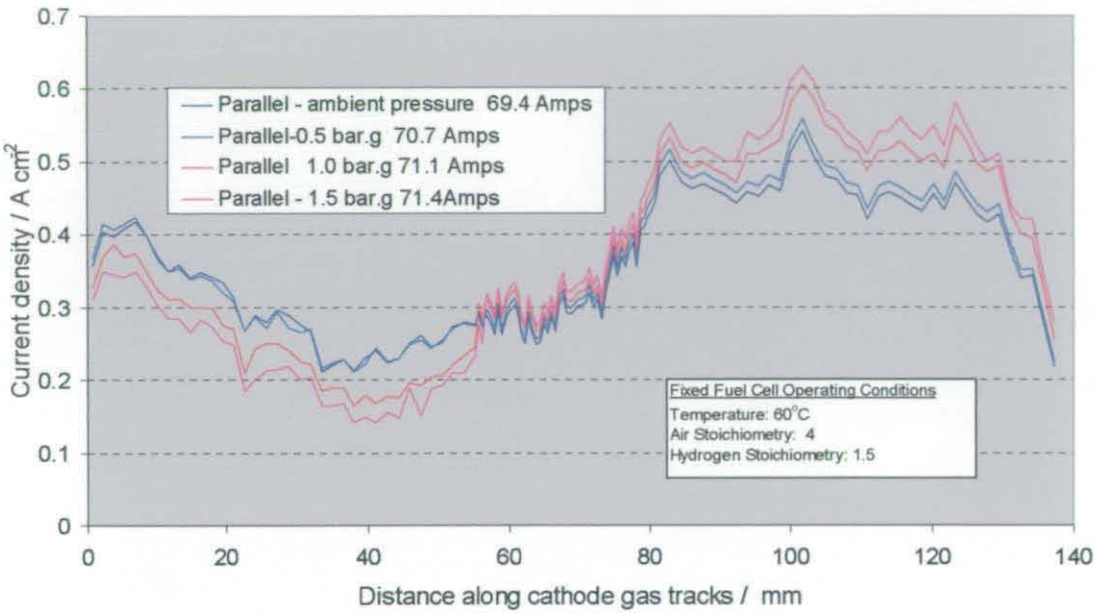

Fig. 6.27 Current maps at fuel cell potential of 500 mV - parallel cathode flow field with variable operating pressures – counterflow configuration

It is seen that with the plot of lowest operating pressure the performance is highest for the first half of the track but lowest in the second half. The previous current mapping plots, using a coflow arrangement of gases, Fig. 6.19, conversely showed a lower performance at the end of the cathode tracks, the higher pressure causing flooding in this region. Here, the dry hydrogen on the opposite side of the cell removes some of this water due to the back diffusion process across the membrane.

The current mapping plots obtained with the interdigitated cathode flow field for variable operational pressures is shown in Fig. 6.28.

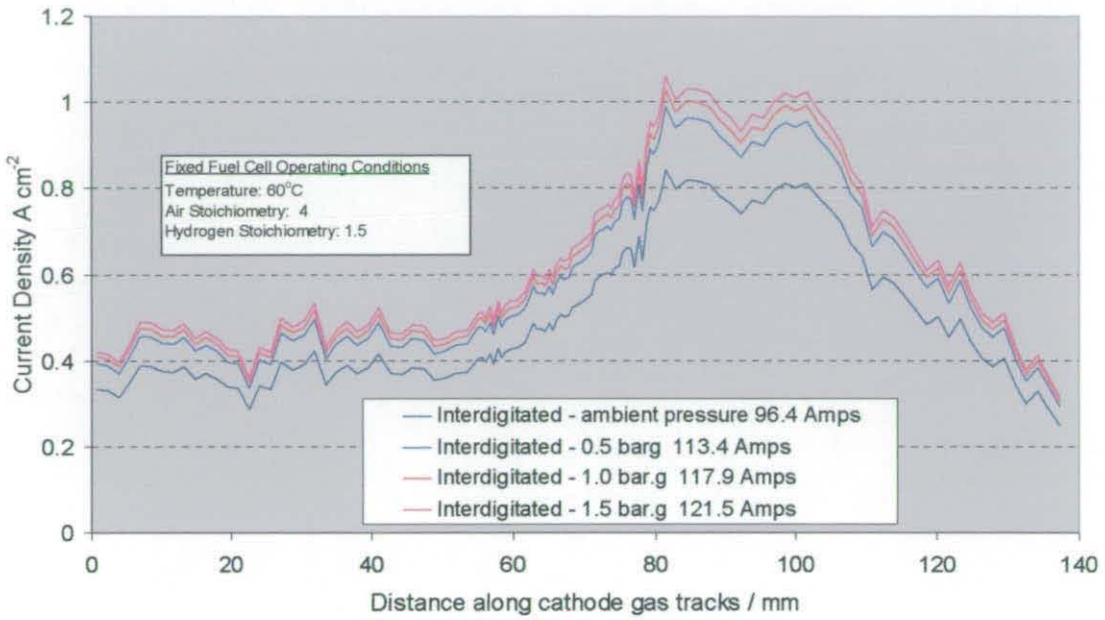

Fig. 6.28 Current maps at fuel cell potential of 500 mV – interdigitated cathode flow field with variable operating pressures – counterflow configuration

As the operating pressure is increased, the elevation in the performance between plots is observed to be approximately equal over all positions of the cathode gas tracks.

Performance comparisons of the variable pressure current mapping plots between the two flow field types are shown in Fig. 6.29 and Fig. 6.30.

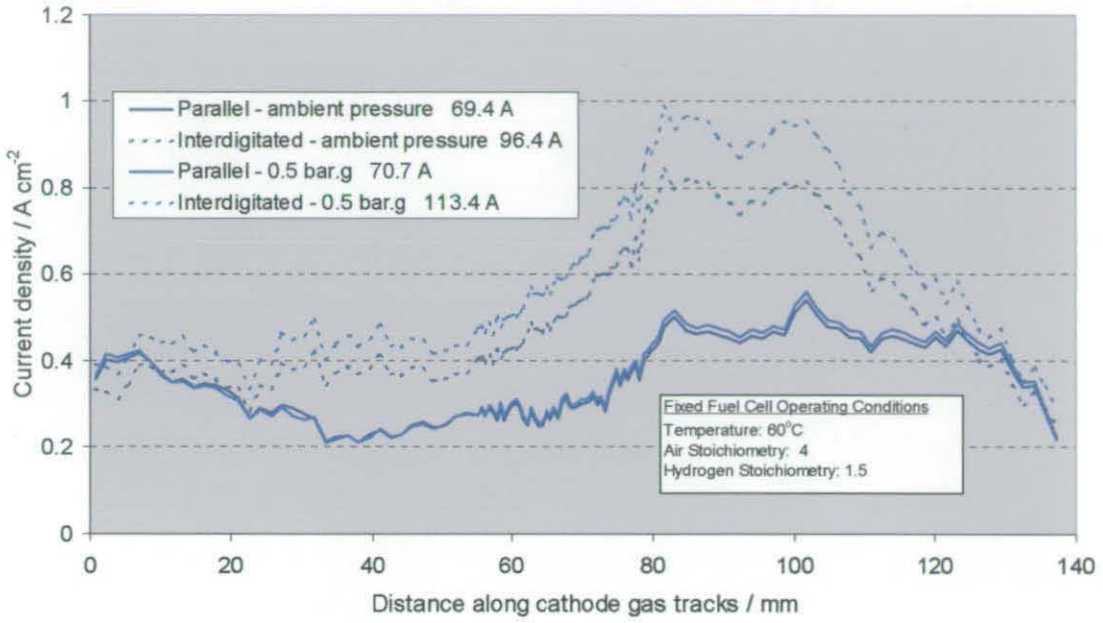

Fig 6.29: Current maps with both flow fields with low operating pressures
Data from Figs. 6.27 & 6.28 used - counterflow configuration at 500 mV potential

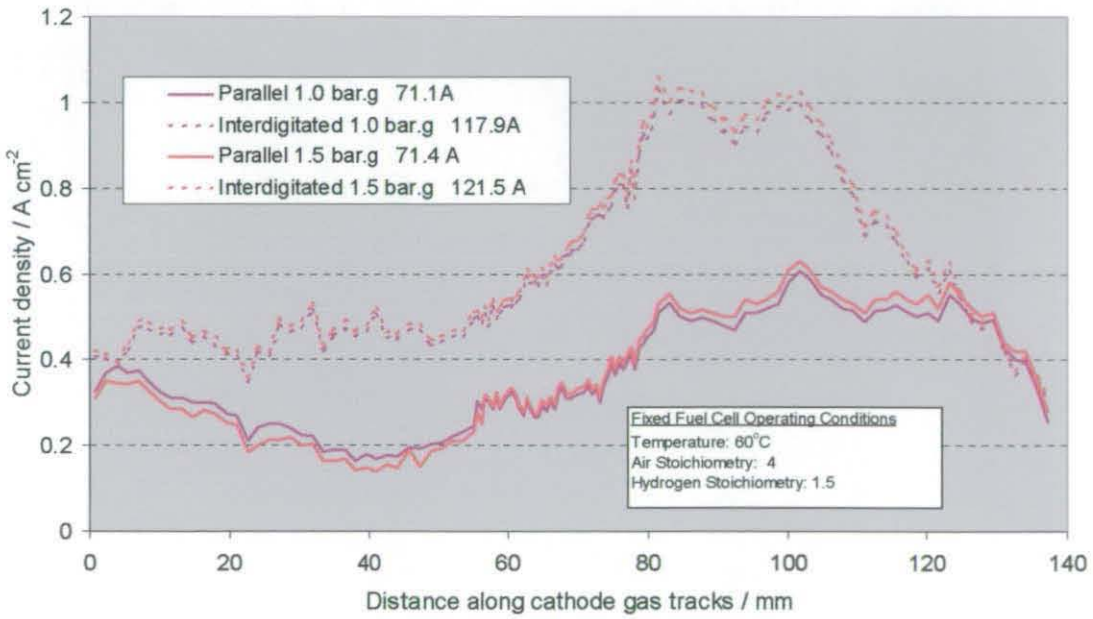

Fig 6.30: Current maps with both flow fields with high operating pressures
Data from Figs. 6.27 & 6.28 used - counterflow configuration at 500 mV potential

The elevation in performance due to the differing air flow mechanisms promoted by the two flow-fields and water contents is observed.

Summary of conclusions from current maps

From the current mapping plots presented, the following conclusions can be drawn:

- The interdigitated flow field promotes superior performance to the parallel flow field in all of the current map plots. The effect of the forced flow mechanism is clearly illustrated as the difference between parallel and interdigitated plots, with equivalent operating conditions. The elevated performance produced by the interdigitated flow field is shown as elevated current density in the final regions of the gas tracks.

- Significant differences in the current maps were seen when utilising a coflow and counterflow arrangement of the reactant gases. With the coflow configuration, a combination of reduced oxygen concentration and increased presence of liquid water lowered performance in the latter sections of tracks. With the counterflow configuration the ability to reduce the cathode water content at the end of the tracks by the process of back diffusion to the dry hydrogen resulted in superior performance in these locations as the entire thickness of the membrane was sufficiently hydrated.

- A summary of results for the current mapping tests are shown in Fig. 6.31 below:

			Total Current at 500 mV	
Flow configuration of reactant gases	Pressure / bar.g	Air stoichiometry	**Parallel**	**Interdigitated**
Coflow	0.5	2	72.5	89.8
Coflow	0.5	3	81.4	95.1
Coflow	0.5	4	85.5	101.5
Coflow	0.5	6	91.3	113.3
Counterflowflow	0.5	2	53.6	93.0
Counterflowflow	0.5	3	58.9	107.0
Counterflowflow	0.5	4	70.7	113.4
Counterflowflow	0.5	6	77.8	119.1
Coflow	Ambient	4	74.0	97.6
Coflow	0.5	4	74.8	101.5
Coflow	1	4	77.0	105.4
Coflow	1.5	4	78.6	109.2
Counterflowflow	Ambient	4	69.4	96.4
Counterflowflow	0.5	4	70.7	113.4
Counterflowflow	1	4	71.1	117.9
Counterflowflow	1.5	4	71.4	121.5

Fig 6.31 Summary of total current obtained from segmented fuel cell at various operating conditions holding a potential of 500mV

6.3.3 Flow-field pressure drop comparisons

The final series of data presented are a measurement of the pressure drop taken over the segmented fuel cell cathode. This was carried out by setting up the Keller digital manometers on the cathode inlet and outlet, taking both measurements and performing a simple subtraction. These measurements were taken during the polarisation tests detailed in Fig. 6.11, with the air stoichiometry equal to four, an operating pressure of 0.5 bar.g, a temperature of 60°C and water injection to 100%RH.

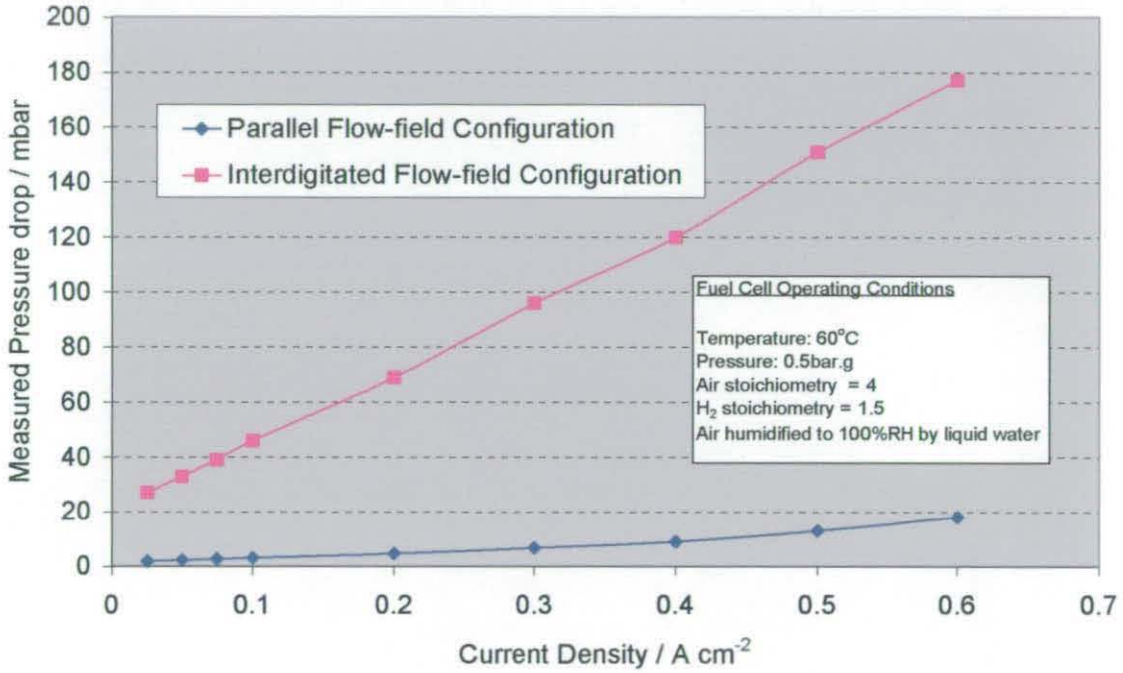

Fig 6.32 Cathode pressure drop measurements with both flow fields

It is observed how the pressure drop plot with the interdigitated flow-field has a substantially higher slope than the parallel flow field. For a drawn current density of 0.4 A/cm^2 the parallel pressure drop is around 9 mbar and the interdigitated is approximately 120 mbar. Clearly the effect of the flow mechanism significantly increases the pressure drop of the air due to the forcing of all air from each inlet leg to each exhaust leg. Also observed is how the pressure drop with the parallel flow field is slightly non-linear due to the increasingly turbulent flow mechanism of gas traversing channels at high flow rates.

6.4 Conclusions

A novel method of water injection to a fuel cell cathode was designed and implemented into a segmented fuel cell. Polarisation plots and operational current mapping plots were obtained from the fuel cell using two different cathode flow fields and different configurations of the directional air and hydrogen flows; from these the following statements can be made.

- The effect of mass transport overpotential on fuel cell performance is clearer using a parallel flow-field compared to the interdigitated flow-field. This is shown by a large potential drop at the end of the polarisation plot due to the difficulty in supplying oxygen to catalyst sites at a sufficient rate. This is due to the difference in the flow mechanisms that are readily encouraged by each design.
- In addition, the parallel flow field encourages greater degrees of mass transport overpotential with a higher operating pressure due to the extra presence of liquid water whereas the interdigitated configuration is unaffected.
- A counterflow arrangement of reactant gases is seen to promote a higher current density for an equivalent potential due to the better distribution of water around the fuel cell.
- The depletion of oxygen with distance along the cathode gas tracks is observed when using the parallel flow fields. With the interdigitated flow-field the increase in current density at the end of the tracks is representative of the forced flow in this region of diffuser material.
- Compared to the coflow arrangement, the counterflow configuration of reactant gases is shown to alter the position along the cathode gas tracks yielding the highest current density due to the differing water transport mechanisms across the membrane.

With regards to large cathode pressure drop recorded, an important consideration may be that the 3 mm pitch between tracks was too wide. To seriously study the interdigitated flow field for the EC fuel cell, ideally there should be several flow plates constructed with variable track pitches and dimensions. However, time and financial restrictions within the framework of this thesis meant this option was not possible. Future considerations in adapting the flow field to the EC fuel cell could include making the exhaust track of interdigitated pair wider to better accommodate liquid water. However, the next focus in reducing the pressure drop between the feed and exhaust track of the interdigitated pair is the diffuser material, detailed in Chapters 7 and 8.

6.5 References

Bender, G.; Wilson, M.S.; Zawodzinski, T.A., "**Further refinements in the segmented cell approach to diagnosing performance in polymer electrolyte fuel cells**", Journal of Power Sources, Vol. 123, pp163-171, 2003

Bender, G.; Ramsey, J., "**Flow-field design development using the segmented cell approach**", Proceedings of the third International symposium on proton conducting membrane fuel cells, 2003

Bisang, J.M., "**Effect of mass-transfer on the current distribution in monopolar and bipolar electrochemical reactors with a gas-evolving electrode**", Journal of applied electrochemistry , Vol 23 (10), pp966-974, 1993

Cleghorn, S.J.C., Derouin, C.R., Wilson, M.S., Gottesfeld, "**A printed circuit board approach to measuring current distribution in a fuel cell**", Journal of Applied electrochemistry, Vol 28, pp663-672, 1998

Czarnetzki, L.R.; Janssen, L.J.J., "**Electrode current distribution in a hypochlorite cell**", Journal of applied electrochemistry, Vol 19 (5), pp630-636, 1989

Epp, D. G.; Watkins, D.S.; Dircks, K. W., "**Novel fuel cell fluid flow plate**", US Patent No. 4,988,583, 21st Jan 1991

Epp, D. G.; Watkins, D.S.; Dircks, K. W., "**Fuel Cell Fluid Flow Plate**", US Patent No. 5,108,849, 28th April 1992

Kazim, A.; Liu, H.Y.; Forges, P., "**Modelling of Performance of PEM fuel cells with conventional and interdigitated flow fields**", Journal of Applied Electrochemistry, Vol. 29 (12) , pp1409-1416, 1999

Nguyen, T.V; Yi, J.S., "**The effect of the flow distributor on the performance of PEM fuel cells**", proceedings of the first international symposium on proton conducting membrane fuel cells, The electrochemical Society Inc., PV95-23, pp66-75, 1995

Nguyen, T.V.; Yi, J.S., "**An along the channel model for proton exchange membrane fuel cells**", Journal of the Electrochemical Society, Vol 145 (5), pp1149-1159, 1998

Nguyen, T.V.; Yi, J.S., "**Multicomponent transport in porous electrodes of proton exchange membrane fuel cells using the interdigitated gas distributors**", Journal of the Electrochemical Society, Vol 146 (1), pp38-45, 1999

Nguyen, T.V., "**A gas distributor design for proton exchange membrane fuel cells**", Journal of the electrochemical society, Vol 143, No. 5, L103-L106, 1996

Noponen, M.; Mennola, T.; Mikkola, M.; Hottinen, T.; Lund, P., "**Measurement of current distribution in a free-breathing PEMFC**", Journal of Power Sources, Vol 106, pp304-312, 2002

Potter, M.; "**Parametric Analysis of a Solid Polymer Fuel Cell using Current Distribution Mapping**", PhD thesis, Loughborough University, 1999

Qi, J.; Savinell, R.F., "**Mass-transfer in a laminar-flow parallel plate electrolytic cell with simultaneous development of velocity and concentration boundary layers**", Journal of Applied electrochemistry, Vol 20 (6), pp885-892, 1990

Rajalaksmi, N.; Raja, M.;Dhathathreyan, K.S., "**Evaluation of current distribution in a proton exchange membrane fuel cell by segmented cell approach**", Journal of Power Sources, Vol. 112, pp331-336, 2002

Reiser, C.A.; Sawyer, R.D. "**Solid Polymer Fuel Cell Stack Water management System**", US Patent No. 4,769,297, 6th September 1988

Reiser, C.A., "**Water and Heat Management in Solid Polymer Fuel Cell Stack**", US Patent No. 4,769,297, 2nd May 1989

Rieke, P.C.; Vanderbrough, N.E., "**Thin-film Electrode arrays for mapping the current-voltage distributions in proton-exchange membrane fuel cells**", Journal of the Electrochemical Society, Vol. 134 (5), pp1099-1104, 1987

Rock, J.A., "**Mirrored Serpentine Flow Channels for Fuel Cell**", US Patent No. 6,099,984, 8th August 2000

Stumper, J., Campbell, S.A., Wilkinson, D.P., Johnson, M.C., Davis, M., "**In-situ methods for the determination of current distribution in PEM fuel cells**", Electrochimica Acta, Vol. 43, No. 24, pp3773-3783, 1998

Vanderleeden, O.; Wilkinson, D.P.; Dudley, J.T., "**Fuel cell separator plate with discrete fluid distribution features**", US Patent No. 6,413,664, 2nd July 2002

Wang, C.Y.; Wang, Z.H.; Chen, K.S., "**Two phase flow and transport in the air cathode of proton exchange membrane fuel cells**", Journal of Power Sources, Vol. 94(1), pp40-50, 2001

West, A.C.; Fuller, T.F., "**Influence of Rib Spacing in proton-exchange membrane fuel cell assemblies**" , Journal of Applied Electrochemistry, Vol 26 (6), pp557-565, 1996

Wieser, C.; Helmbold, A.; Gulzow, E., "**A new technique for two-dimensional current distribution measurements in electrochemical cells**", Journal of Applied Electrochemistry, Vol. 30, pp803-807, 2000

Wilkinson, D.P.; Prater, K.B.; Voss, H.H., "**Lightweight membrane electrode fuel cell assembly with integral reactant flow passages**" , US Patent No. 5,252,410, 12th October 1993

Wynne, R.K.; Neutzler, J.K., Barbir, F.; Garau, V.; Pierce, W.E. "**Self Humidifiying Fuel Cell**", US Patent 6,207,312 27th March 2001

Zawodzinski ,C.; Wilson, M., "**Fuel Cell With Metal Screen Flow Field**", Us Patent No. 6,207,310, 27th March 2001

Chapter 7

Ex-situ Diffuser material testing for EC Fuel Cell

7.1 Chapter Overview

From the steady-state system models detailed in Chapter 5, it was established that the efficiency of the low-pressure EC fuel cell system was superior to the LC system, particularly at the upper and lower extremes of the power delivery ranges. The poorer electrochemical performance of the EC stack, a direct result of operating at low pressure, was offset by the ability to have a higher fuel cell packing density and considerably lower associated parasitic losses. The major reduction in parasitics was due to the much lower power consumption of a centrifugal blower compared to the compressor used in the LC system.

In the EC model, during periods of high power delivery, a high stoichiometric ratio of air was required to control stack temperature, and the assumption was made that the pressure drop of air flow over the stack, i.e. differential pressure from inlet to exit, was consistently 250 mbar. However, as shown in section 6.3.3, in practice the pressure drop of the air was actually proportional to the volumetric flowrate supplied to each fuel cell, and hence to the stack. It is therefore conceivable that in a poorly designed EC stack, the situation may arise where the flowrate of air required for sufficient temperature control is greater than a low power centrifugal blower is able to supply due to excessive pressure drop.

Therefore, elimination of excessive cathode pressure drop is a critical consideration in the design of EC fuel cell stacks. In an actual FC system there would be pressure drop over components external to the stack, such as the exhaust gas condenser, but these will not be investigated here. The individual pressure drop characteristics of several common flow-field configurations were discussed previously, in section 6.1.1.2.

In this Chapter it is shown that the characteristics of the cathode gas diffuser material are a critical influence on the measured pressure drop over a fuel cell cathode, particularly when using the interdigitated flow field. Ex-situ and in-situ tests were undertaken in an attempt to find a suitable alternative to Carbel CL, with the study providing groundwork for later in-situ tests.

7.1.1 Pressure drop of air flow over stack

The pressure drop of air across a fuel cell stack contributes significantly to the power consumption of the air delivery subsystem. The pressure drop of hydrogen is not usually an important issue due to the characteristic low density, high diffusion rates and the fact it is usually supplied from a high pressure source, such as a compressed cylinder or a reformer. The stages of air pressure drop through a typical stack manifolding arrangement and cathode plate design are illustrated in Fig. 7.01.

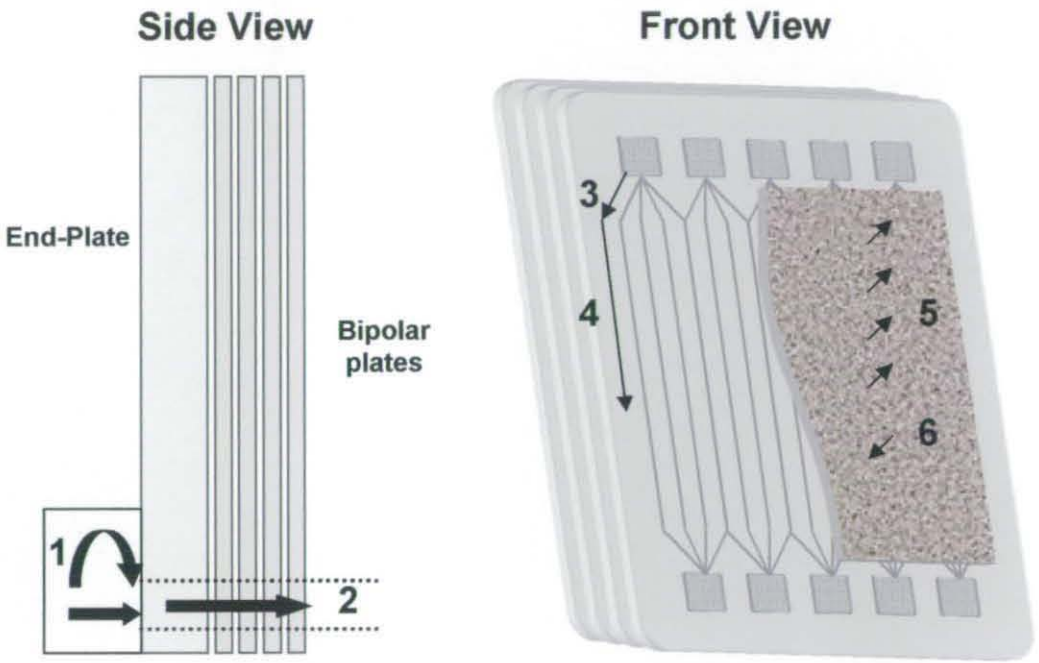

Fig. 7.01: Air pressure drops in a typical fuel cell stack

During the supply of air to the fuel cell stack, pressure drop occurs firstly in the entry plenum chamber, (1), as it is forced into the manifold cross-sections and then as it flows along manifolding, (2). A further drop occurs as it separates into many small flows when entering ports to individual cathode plates, (3), and then the narrow channels of the plate flow-field (4) and finally through the porous diffusion media to reach the catalyst sites (5). In all but specialised applications, air is used as the oxidant for the fuel cells meaning the cathode cannot be dead-ended so there is a further pressure drop (6) required to force nitrogen, liquid and vapour water and excess oxygen to exit the stack. The flow of air through the entry plenum and manifolding represents a significantly smaller pressure drop than the flow mechanisms internal to the fuel cells and will not be considered any further.

7.1.1.1 Pressure drop of interdigitated cathode flow-field

Previously in section 6.3.2, the interdigitated flow-field was observed to promote superior fuel cell performance over a parallel design with identical track spacing and dimensions. From these current-mapping plots, it was demonstrated how the effects of cathode flooding were reduced, particularly towards the end of the gas tracks. However, in section 6.3.3, it was shown that the pressure drop of air was much higher with the interdigitated flow field.

The reduced electrode flooding characteristic of the interdigitated flow field should be particularly suited to the fuel cells of an EC stack, but the high pressure drop associated with the design would be problematic for compatibility with a low pressure air supply. The major source of the high pressure drop is the forced flow of air traversing the volume of diffuser media from the inlet track to the exit track of each pair of tracks. This pressure drop will increase with the power output from the fuel cell stack due to higher stoichiometric flows of air required and the increasing presence of product water in diffuser pores.

As mentioned in the conclusions of Chapter 6, to reduce this pressure drop it would be possible to make alterations to the interdigitated design, such as narrowing the track pitch and thus increasing the overall number of tracks. However, there would be restrictions on the possible extent of this, as small pitches would be likely to lower performance due to a reduced electrical contact area between plate ribs and diffuser.

7.1.1.2 Pressure drop across the diffuser material

To recap, in a PEM fuel cell the main function of the diffuser media is to allow the distribution of reactant gas to electrode areas that are not directly exposed to flow channels, i.e. under plate ribs, resulting in almost complete utilisation of the active electrode area. The diffuser also provides drainage of product and humidification water back to the flow channels. For the interdigitated flow field the entire gas flow must pass through the diffuser, therefore a solution for lowering the pressure drop without altering the flow-field design is to increase the *permeability* of the gas diffuser material. This can be achieved by reducing the compaction pressure exerted on the fuel cell but this will result in an increased contact resistance and excessively lower fuel cell performance if not using flow plates with very low surface resistance, e.g. graphite. Hence, the solution may lie in investigating the properties of alterative gas diffusers. Carbel CL has, so far, been the only diffuser material used in the fuel cell builds in the research detailed in this thesis.

The pressure drop for a specified set flow of gas, in any direction through a cross sectional area of fuel cell diffuser media will be a function of the material permeability. An expression referred to as the *Gurley number* is often quoted for a measurement of diffuser permeability, although this only refers to through-the-plane direction. In the case of an interdigitated flow field, there is more interest in the permeability in the *cross-plane* direction.

Diffuser permeability is a function of *structure composition*, *working thickness* and also *water content* in an operating fuel cell. The former two characteristics are discussed in more detail in the following sections

Diffuser Permeability – material structure

Fuel cell diffuser media is comprised of a carbonaceous substrate structure usually containing one, or more, performance enhancing *post-treatments*. The two main classifications of diffuser substrate are carbon cloth and carbon paper, both highly conductive, semi-permeable structural arrangements of carbon fibres. The former is a relatively stiff planar arrangement of fixed fibres and the latter a flexible woven arrangement. Processes for the manufacture of different grades of carbon paper and carbon cloth are detailed in appendix F. The structures for two selected grades of diffuser material are shown in Fig 7.02. With carbon cloth there is different permeability in the x and y directions due to the weave but this can also be true to a lesser extent for carbon paper structures, Vielstich et al (2003).

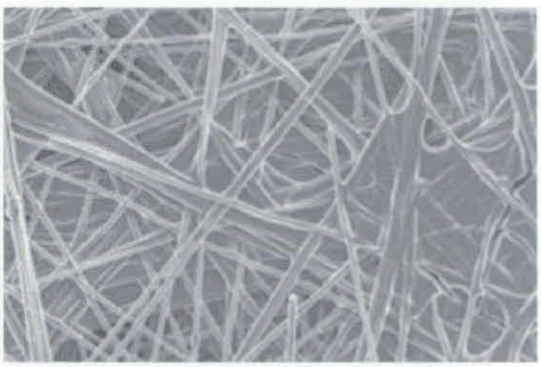

Carbon fibre paper – Spectracorp 2050A

Carbon cloth – Textron Avcarb 1071 HCB

Fig. 7.02 – Structures of carbon paper and cloth

The most common post-treatment of a diffuser substrate is *wet proofing* where the entire structure is impregnated with PTFE to a specified percentage by weight. Although this decreases permeability and electrical conductivity, studies have illustrated how a wet-proofed diffuser substrate improves fuel cell performance by controlling the extent of water accumulation in the pores, Dhathathreyan et al (1999).

A second treatment is the deposition of a mixture of PTFE and a very fine carbon powder through a proportion of the substrate thickness to form two distinct layers within the structure, the *macrodiffuser* (unfilled pores) and the *microdiffuser* (pores filled with mixture). In the literature the microdiffuser layer has been referred to as the microporous *sub-layer*, *diffusion layer*, or *gas diffusion layer;* however, care must be taken as the latter two definitions are sometimes used to describe the actual diffuser media. The purpose of the microdiffuser layer is to reduce the presence of liquid water immediately

adjacent to the catalyst layer and promote a more intimate electrical contact between the catalyst and the diffuser fibres, as described by Qi et al (2002), Jordan et al (2000) and Uchida et al (1996). The thickness of the microdiffuser layer has a significant effect on diffuser media permeability and hence also pressure drop, especially in the through-plane direction, although not all of the reactant gas has to pass through the microdiffuser during fuel cell operation.

In terms of lowering pressure drop the microdiffuser should be kept as thin as possible, but the thickness that produces the optimum fuel cell performance is influenced by many factors including PTFE content and the grade of carbon powder, as described by Antolini et al (1998 and 2002), Lufrano et al (1999), Passalacqua et al (2001) and Moreira et al (2003). In addition, if gas diffusion electrodes are used to manufacture the MEA, see Chapter 2, the microdiffuser provides the physical support for the catalyst, and a thick layer will be required. A thicker microdiffuser may also be necessary with a carbon cloth substrate due to the pliancy of the plain carbon fibre weave producing unstable electrical contact with the catalyst. Pore forming-additives may be applied to the microdiffuser layer to reduce through-plane pressure drop, as described by Fischer et al, (1998) Kong et al, (2002) and Gamburzev et al, (2002).

A thin microdiffuser layer can be used if the MEA has been manufactured by a direct application of catalyst to either side of a polymer membrane, as with most commercially produced MEA's. As the microdiffuser does not have to be a rigid and planar surface, here a trade-off can be made between low contact resistance and through plane permeability.

Diffuser Permeability –Working Thickness

In an assembled PEM fuel cell, both anode and cathode diffusers are crushed to certain *working thicknesses,* due to the compression forces exerted by the end plates. The working thickness of each represents a pre-determined trade-off between the interfacial electrical resistance of the MEA/diffuser/flow plate ribs and the pressure drop. These characteristics and their relationship to applied compaction force are shown in Fig. 7.03. The general shape of a pressure drop / compaction pressure plot is similar to an exponential function plot and an electrical resistance/compaction plot is similar in appearance to the plot of a negative logarithmic function.

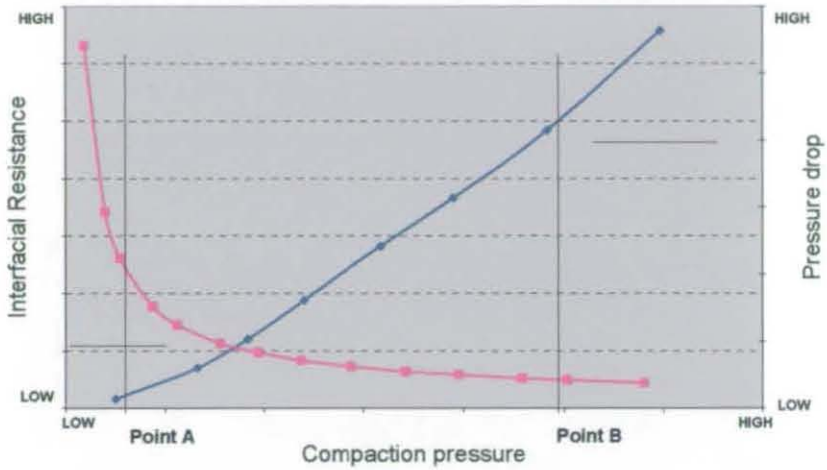

Fig 7.03 Generalised resistance/P drop behaviour of a fuel cell diffuser with applied compaction force

Point 'A' on Fig. 7.03 represents a point of low-pressure drop - high interfacial resistance while point 'B' represents a point of high-pressure drop but with low resistance properties. The diffuser working thickness, or applied compaction pressure, chosen can also be influenced by the components used in the stack build; e.g., if graphite flow plates are used, the compaction pressure can be lower as the interfacial resistance will not be as high as that obtained with stainless steel flow plates.

The control over the diffuser working thickness is achieved by the thickness of the sealing gaskets and/or force exerted by the compaction bolts via fuel cell end plates. However, due to the flexible nature of the thin polymer membrane structure it is not possible to control the diffuser working thickness on only one side of the MEA, therefore the controlled dimension is actually the *diffuser combination thickness* of both anode and cathode diffuser materials.

When fuel cell sealing gaskets are made from a rigid material, i.e. with a low degree of crushing, such as glass reinforced silicone, the minimum diffuser combination thickness is solely controlled by the gasket thickness, refer to stages A and B of Fig. 7.04. On administering sufficient compaction force to achieve a gas-tight seal the diffuser combination thickness is equal to the combined thickness of both gaskets (plus the difference between the membrane and surrounding sub-gasket) and any excess compaction force created by a further tightening of the compaction bolts will be taken up by the gaskets. Hence, rigid gaskets offer excellent control of a selected minimum diffuser thickness, but a prior knowledge of the optimum crushing dimension is required, Lee et al (1999),

When deformable gaskets are used, such as exfoliated graphite, Grafoil, they can be crushed past the point of gas sealing to a pre-determined target dimension. refer to stages C and D of Fig. 7.04. However, caution must be exercised, as a diffuser material excessively crushed will significantly lower the permeability and some weaker carbon paper structures risk breakage at high compaction pressures. Additionally, over-crushed deformable gaskets can 'flow' resulting in partial, or complete blockage of gas manifolding. Conversely, insufficient crushing results in a high contact resistance between diffuser and plate ribs and risks integrity of the gas seal.

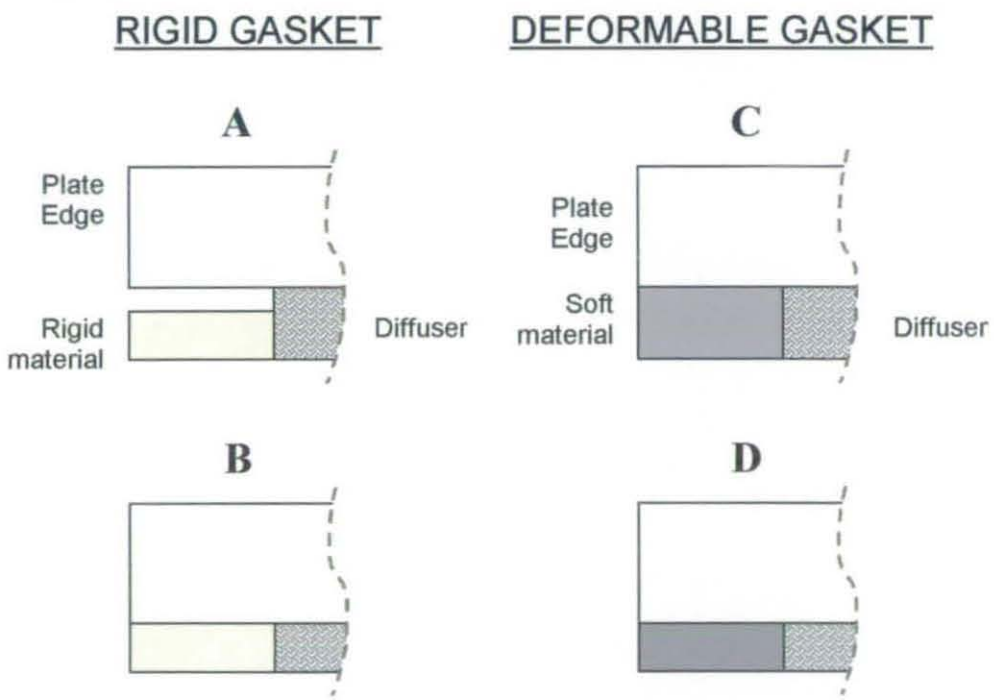

Fig. 7.04 - Rigid and deformable gaskets – stages of compression

7.1.2 Focus of study

It was decided to undertake a program of research on gas diffusion media for PEM fuel cells with the emphasis placed on finding a material suitable for use in an EC fuel cell cathode, i.e. high cross-plane permeability under compaction load and an adequate electrochemical performance in the presence of two phase flow in the air. All research detailed so far in this thesis has used Carbel CL, a carbon cloth based diffuser material, in the fuel cell builds. Therefore, quantities of other commercial diffuser grades were obtained, these are detailed in section 7.2.2.

The research was structured in two phases with firstly a large range of materials evaluated by several ex-situ tests, which are detailed in section 7.2. The data from these individual tests established useful correlations between pressure drop, electrical resistance and the degree of crushing to the diffuser structure and any existing post treatments. This established the most suitable materials for the second phase - testing of selected diffusers into a full size EC fuel cell, as detailed in Chapter 8.

7.2 Ex-situ analysis of diffusers

7.2.1 Overview

A series of simple tests were designed and undertaken in order to evaluate the characteristics of a range of gas diffuser materials and thus assess their suitability for integration into an EC fuel cell.

One crucial parameter to consider was the interfacial resistance of the diffuser against a flow-field plate. It was also considered favourable to separately evaluate cross-plane and through-plane permeability, as both individually contribute to the overall pressure drop of the air using an interdigitated cathode flow field. To make a calculation of permeability it was also necessary to measure the thickness of the material at the same compaction load. At the time of writing, to the author's knowledge, there have been no published studies of air pressure drop through a diffuser in more than one direction and very little work detailing the importance of working thickness and related permeability in the selection of diffuser materials for fuel cells

As stated previously, a critical factor in evaluating a diffuser material is establishing a thickness where interfacial contact resistance is sufficiently low but the pressure drop not excessive. Therefore, each material had to be tested at several thicknesses. To do this, a precisely controlled range of compaction loads had to be applied to each sample for each test. The extensometer used in Chapter 6 for the calibration of the compaction springs was available for use. This was able to exert a compaction force of up to a maximum of 5000 N, with the physical configuration providing a circular compaction area approximately 58 mm in diameter. As a guide, the compaction pressure used in fuel cells at Loughborough University had been measured at approximately 200 N/cm^2 based on the active electrode area. Therefore the diffuser samples for all tests were designed to be an appropriate size so that at least this level of compaction pressure could be applied.

Special plate configurations were used, allowing the tests to be carried out in-situ under the crushing load of the extensometer - these are described in detail in the individual sub-sections.

7.2.2 Diffuser materials

The materials that were available for testing are listed below in Fig. 7.05.

Manufacturer	Diffuser grade	Material/manufacturing technique (refer to appendix F)	Manufacturers guide thickness / microns	PTFE content of substrate	Notes
W.L. Gore	Carbel CL	Weaved carbon cloth	400	unknown	microdiffuser of undisclosed composition
SGL Technologies	SGL 10BB SGL 10BA SGL 30BC SGL 31BC	Dry-laid carbon filled paper	420 380 320 330	5% 5% 5% 5%	23% PTFE content in microdiffuser no microdiffuser 23% PTFE content in microdiffuser 23% PTFE content in microdiffuser
ETEK	Spectracorp plain Spectracorp wet proofed Spectracorp macroporous plain Spectracorp macroporous wet-proofed	Carbon composite fibre paper	510 380 510 510	0% unknown 0% unknown	
	Carbon A cloth ELAT NC ELAT HL/SS/V2	Weaved Carbon Cloth Carbon cloth based electrode Carbon cloth based electrode	350 unknown unknown	35% unknown unknown	
Toray Industries	Toray 060 35% Toray 090 10% Toray 090 35% Toray 120	Carbon composite fibre paper	190 280 280 370	35% 10% 35% 0%	
Technical Fibre Products	Optimat 203 Optimat 203 Optimat 203	Carbon fibre substrate via papermaking stage	unspecified unspecified unspecified	0% 0% 0%	weight basis 20g/m^2 weight basis 30g/m^2 weight basis 34g/m^2
Lydall Filtration Products	c332 c352 c484-4 c484 c494 c484-3	Wet laid filled carbon papers	333 268 328 417 300 351	3.1% 6.2% 10.0% 3.1% 6.2% 10.0%	

Fig. 7.05 Table of diffuser materials

Descriptions of the different methods for manufacturing fuel cell diffuser materials are given in appendix F.

7.2.3 Compaction pressure / Diffuser thickness

Description

The purpose of this series of tests was to obtain data on the degree of crushing for each grade of diffuser material with applied compaction pressure.

Procedure

A sample piece for the particular diffuser was cut as a concentric circle shape - outer diameter 41mm, inner diameter 20 mm. The apparatus used to measure the diffuser thickness consisted of a DTI (Dial Test Indicator) mounted in a 50 mm diameter stainless steel plate with the stem spring protruding. The vertical position of the DTI in the mounting plate could be adjusted after loosening a holding screw in the side with a small Allen key. For each test an arrangement, as shown in Fig 7.06, was built on the extensometer mounting plate. A stainless steel bevelled plate was used to ensure alignment of the arrangement under compaction.

1 Extensometer compression plate
2 Extensometer mounting plate
3 Bevelled alignment plate
4 DTI mounting plate
5 Stainless steel compression plate
6 Mercer DTI gauge

Fig. 7.06: Arrangement on the extensometer for the compaction-thickness tests

The diffuser piece was centrally positioned on the bevelled stainless steel plate (3) followed by the DIT in the mounting plate (4 and 6). The DTI had been previously zeroed by placing on a pure flat surface and adjusting the small screw in the side of the plate to allow correct positioning. This was followed by the compression plate, which had a bevelled top feature, for alignment, and a machined recess to allow reading of the DTI display.

The extensometer was then carefully adjusted so that the compression plate eased slowly towards the top of the arrangement. Once it was established that the bevel of the stainless steel top plate was aligned with the hole in the extensometer top plate the extensometer was further adjusted until the LCD display showed a small force starting to be exerted (approximately 30 N). The arrangement was then compressed in stages, with the exerted force and diffuser thickness being manually logged.

Results

The results are plotted with 'percentage of original thickness' on the y-axis of each chart instead of the actual measured thickness as this more clearly illustrated the characteristic crushing of separate materials. The graphs are grouped as selections from the same manufacturer, with Carbel CL, by W.L. Gore, shown as a reference plot on each chart.

The crushing characteristics of Carbel CL and the SGL range of carbon paper based diffusers are illustrated below in Fig. 7.07. All of the information for these materials is provided in section 7.2.2.

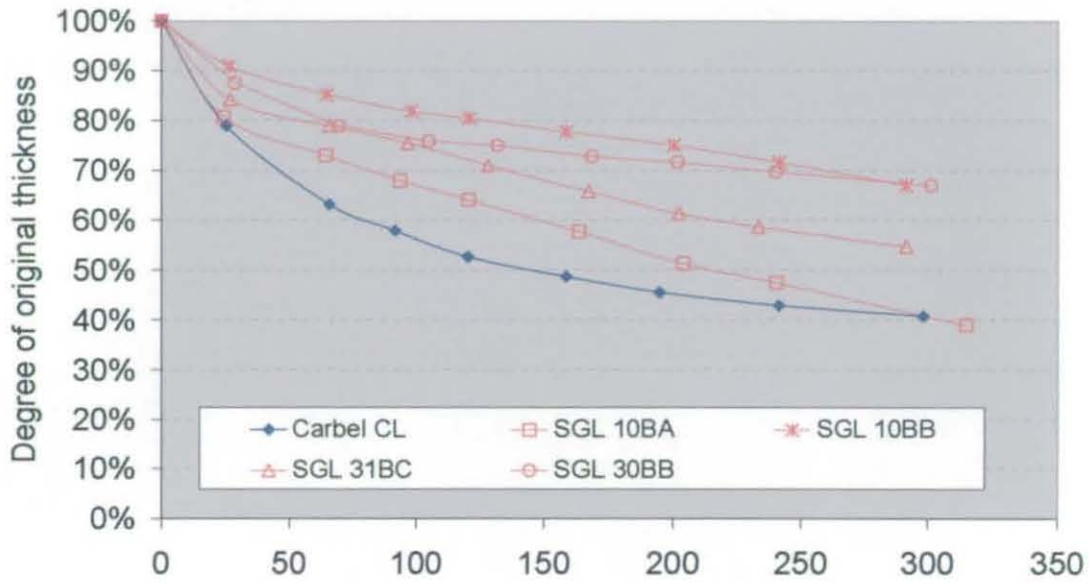

Fig. 7.07: Compaction – crushing plots for SGL diffusers

It is observed that the flexible woven carbon fibre structure of Carbel CL crushes much more readily than the more rigid 'dry-laid' carbon paper structures of the SGL materials. The SGL 10BB is the least readily deformed material, with a 76% degree of crushing at a compaction pressure of 200 N/cm^2. Although having the same substrate base structure, the 10BA grade deforms most readily out of all the carbon paper structures, with a 53% degree of crushing at 200 N/cm^2. This indicates that the deposition of a microdiffuser layer reinforces the diffuser substrate structure, with filled pores collapsing less readily under pressure than unfilled pores. It is also illustrated how the low permeability 30BB material deforms less readily than the 'high-permeability' 31BC due to the increased strength of the formers' high-density substrate structure.

The crushing characteristics of the Spectracorp range of carbon composite fibre paper diffusers, again with Carbel CL used as the reference, is shown in Fig. 7.08. There are two different grades of these materials tested here, a standard grade and a '*macroporous flow field*' grade. The latter has a much more permeable structure and was designed to be used in a fuel cell without the need for any discernible flow field, just a flat plate with an entrance and exit port. The density of this paper is approximately half of the ordinary Spectracorp carbon paper grade.

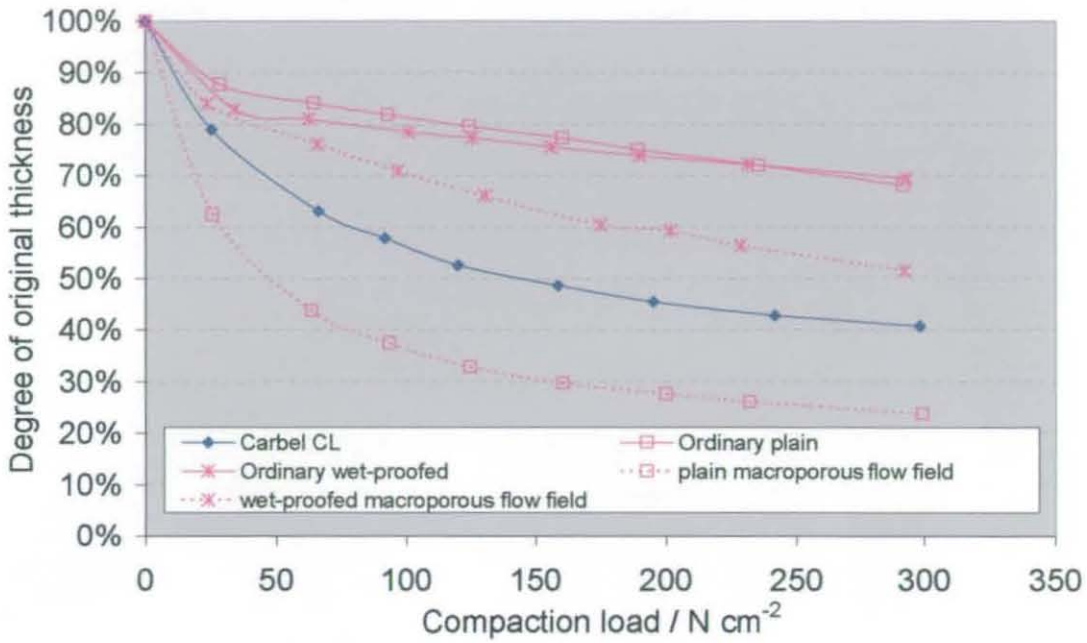

Fig. 7.08: Compaction – crushing plots for Spectracorp diffusers

The difference in the strength of the substrate structures is illustrated in the graph, with the macroporous flow field grade crushing more readily than the grades with a regular substrate, almost in a similar manner to the crushing characteristic of Carbel CL. In addition it is observed how a degree of wet proofing reinforces the substrate structures– with the treated macroporous material being much more resilient to crushing than the plain equivalent. This is not so obvious between the ordinary substrates as the wet-proofed material is thinner (375 micron) than the plain (500 micron) but a difference in the linear slope of the plots is observed and above 250 N/cm^2 the degree of crushing of the former is lower. As a point of note, the macroporous Spectracorp grades were very brittle and fell apart on removal from the extensometer arrangement after crushing. It is therefore doubtful if they would have the endurance requirements for use in a fuel cell utilising a forced liquid water flow mechanism such as for evaporative cooling.

The crushing characteristics of the various grades of Toray carbon composite fibre paper diffusers are shown in Fig. 7.09 – the degree of PTFE is indicated as a percentage by weight).

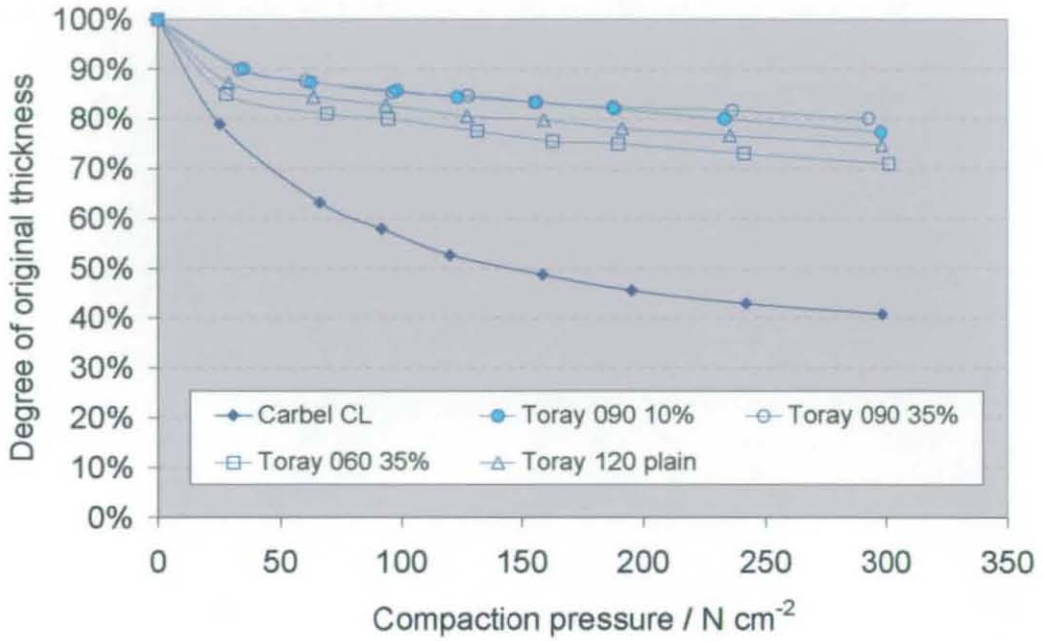

Fig. 7.09: Compaction – crushing plots for Toray diffusers

Here it is observed that the Toray 060 grade, the thinnest material at 150 micron, is deformed most readily, even with a relatively high PTFE content. The Toray 120 has no wet proofing at all and this is deformed less readily that the Toray 060. The least readily deformed materials are the two grades of Toray 090 – where it is illustrated how the extra PTFE content makes the structure more rigid than the plain grade of thicker Toray 120. The Toray 090 with 35% wet-proofing has a less steep linear slope indicating the extra strength exhibited in the structure.

The characteristic crushing of the Optimat diffuser materials is shown in Fig. 7.10.

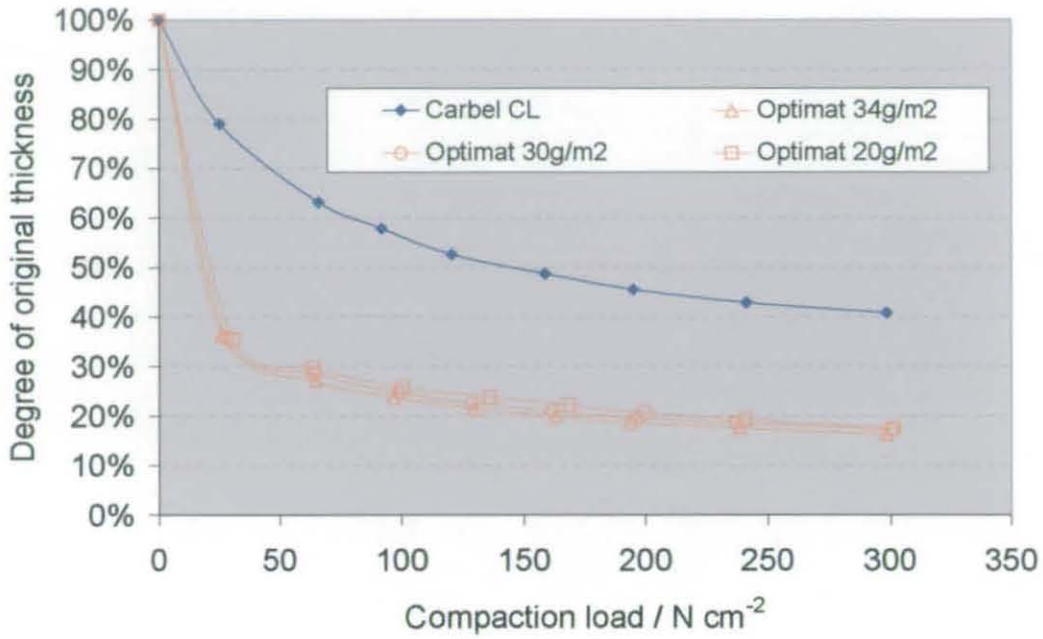

Fig. 7.10: Compaction – crushing plots for Optimat diffusers

It is observed that the Optimat materials have very low mechanical strength and crush much more readily than Carbel CL. All the grades are approximately 20% of the original thickness at a compaction pressure of 200 N/cm^2. These very permeable structures, the product of the papermaking technique detailed in appendix F, are usually given further treatments.

The crushing characteristics of the Lydall wet-laid filled carbon paper diffusers are shown in Fig. 7.11.

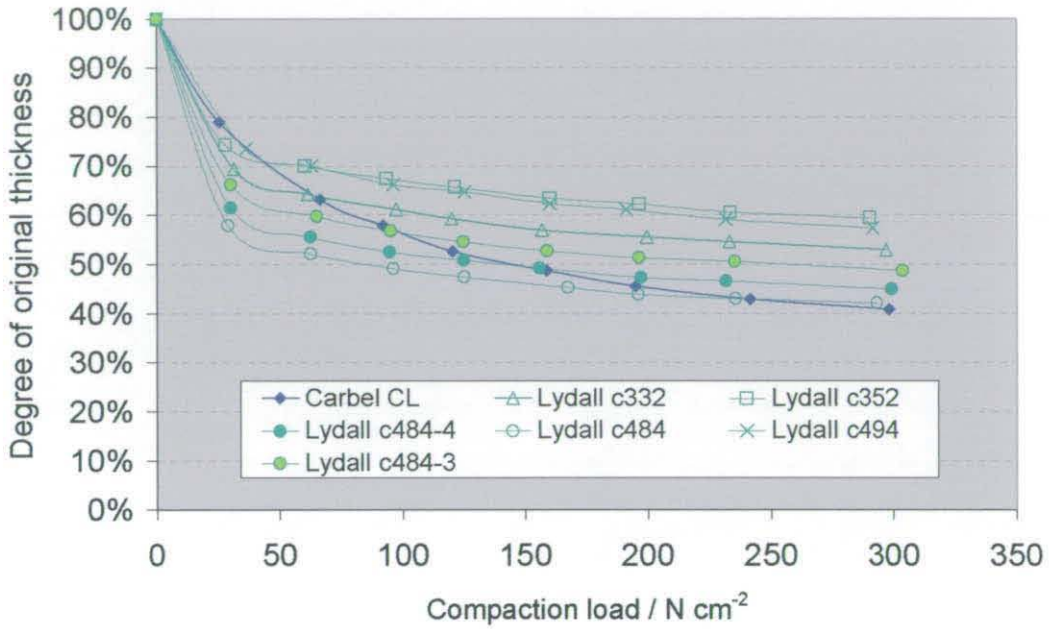

Fig. 7.11 Compaction – crushing plots for Lydall diffusers

The Lydall materials have a non-woven base substrate similar to the Optimat materials, with a complete impregnation of a PTFE and carbon powder mixture, similar in composition to a microdiffuser layer, through the entire thickness. With comparison to the Optimat plots of Fig. 7.10, it is observed how extra strength is given to the structure by this impregnation.

The crushing characteristics of the ETEK carbon-cloth based diffusers are shown in Fig. 7.12.

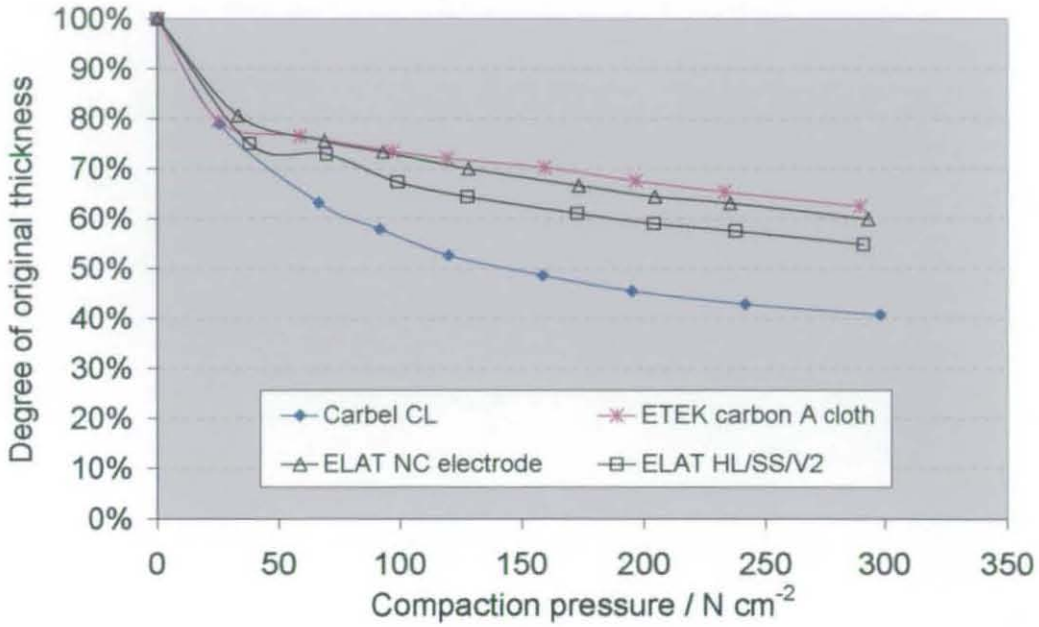

Fig. 7.12: Compaction – crushing plots for ETEK diffusers

These materials are the most similar in composition to Carbel CL of the diffusers available for testing. The ETEK carbon 'A' cloth is the base material of the two electrodes – however the plain material here has a 35% PTFE content, which is seen to significantly reinforce the structure of the substrate so it has a higher strength than Carbel CL.

The ELAT HL/SS/V2 material has a microdiffuser layer on one side and the NC material is a non-catalysed electrode with microdiffuser deposited throughout the entire thickness. The level of PTFE in both these materials is proprietary. It is seen how the electrode with a microdiffuser layer on one side deforms more readily than the material with both sides treated.

Conclusions from compaction - thickness plots

The crushing characteristics for all diffuser materials tested at a compaction pressure of 200 N/cm^2 is shown below in Fig. 7.13.

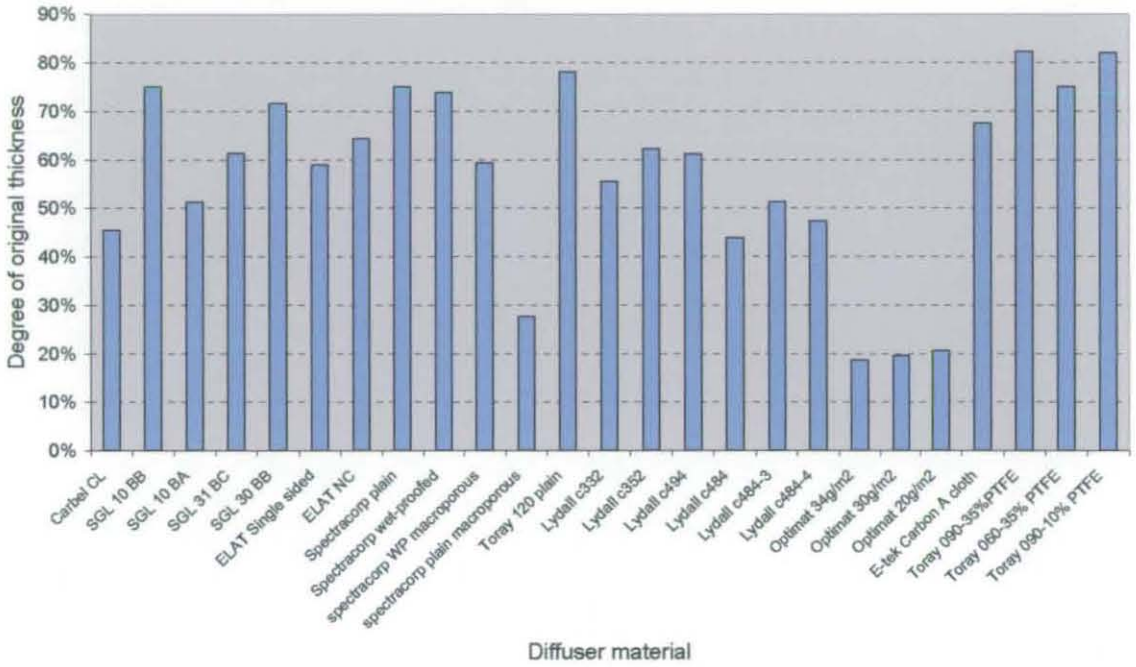

Fig. 7.13: Degree of crushing for all diffusers at 200 N/cm^2

From this chart, the following observations can be made:

- The carbon cloth based material, Carbel CL, was observed to deform quite readily in comparison to the carbon composite fibre and dry-laid filled papers.
- The Optimat materials exhibited very low strength, however the impregnated versions of these materials, the Lydall grades, showed superior mechanical strength. Similarly, the same improvement was seen with the addition of a microdiffuser layer to the SGL dry-laid diffuser materials.
- The carbon composite fibre papers were the most resistive to crushing but were the most brittle materials with a low flexural strength.
- By adding PTFE to the substrate structure, the diffuser material is reinfored , i.e. becomes more resistive to the effects of compaction force thus behaving as if it is of a thicker grade.

7.2.4 Compaction/ Resistance testing

Description

The aim of these tests was to obtain data on the electrical resistance for each diffuser material with the application of compaction pressure, and hence varying thickness. The basic premise was the supply of a precisely controlled level of electrical current through the diffuser via flow field plates, and a measurement taken of the potential difference between the plates to calculate a value for combined bulk and surface resistance. This resistance is sometimes referred to as the 'through plane sheet resistance' with the technique referred to as the 'four point probe' method. This value of resistance includes contributions from the bulk diffuser material and the two contact resistances between diffuser and plates.

Procedure

In each test, two circular pieces of the particular diffuser material were cut, diameter 38 mm, and placed between two 50 mm diameter POCO graphite flow-field plates, containing a single serpentine track design. The alignment of diffusers and plates was identical to the in-situ fuel cell arrangement, with microdiffuser layers (if any) touching, and the flow fields touching the rear side of the diffuser. An arrangement as shown in Fig 7.14 was then built on the mounting plate of the extensometer, again with a bevelled base plate used for alignment.

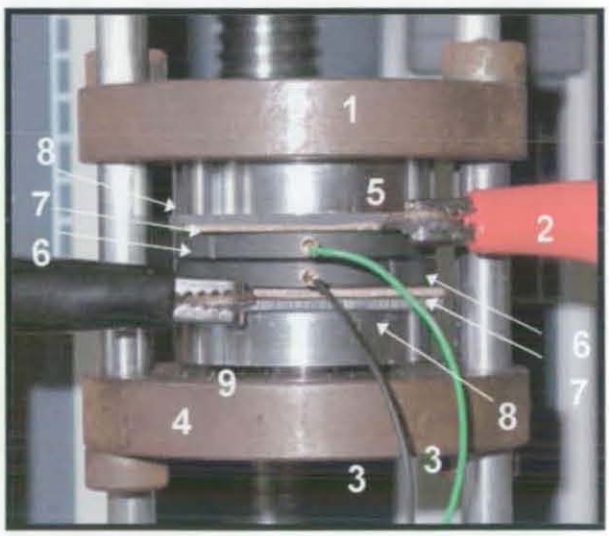

1. Extensometer compression plate
2. Current delivery/ takeoff leads
3. Voltage probe leads
4. Extensometer compression mounting
5. Stainless steel spacer plate
6. POCO graphite flow plates
7. Copper current plates
8. Perspex insulator sheets
9. Stainless steel mounting plate

Fig. 7.14: Arrangement on the extensometer for compaction-resistance tests

Immediately adjacent to the flow plates were copper current collector plates with a protruding feature for current delivery/takeoff, these were surrounded by Perspex sheets to electrically insulate the extensometer plates from the current supply.

The same initial alignment and compression procedure as described in the previous section was carried out. A dc power supply was connected to the copper current plates using crocodile clips, and set to deliver 5 Amps, equivalent to current density of 0.45 A/cm^2, relative to the diffuser areas. Needle probes, connected to potential leads, were inserted into the recesses in the graphite plates.

The arrangement was then compressed in stages with the exerted force indicated on the extensometer display, and the potential reading across the needle probes read from a calibrated multimeter, with both manually logged. A simple calculation using Ohm's Law, Equation 7.01, produced a figure for the combined bulk and surface resistances (measured in mOhm cm^2) for the diffuser material through a range of compaction loads.

$$R = \frac{V}{I \cdot A} \qquad \textbf{Equation 7.01}$$

Results

The results are plotted with the calculated figure for through-plane resistance on the y-axis of each chart, and the compaction force on the x-axis. As before, the graphs are grouped into material selections from the same manufacturer with Carbel CL shown as the reference plot on each chart.

The first chart, Fig. 7.15, shows the resistance of the Optimat diffuser materials.

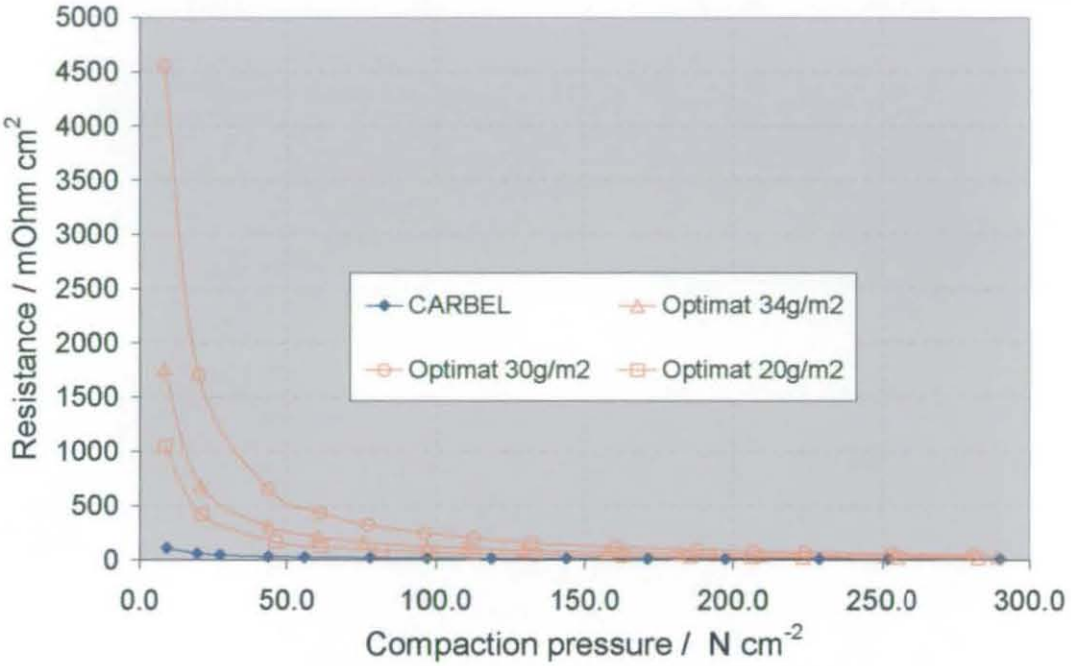

Fig. 7.15: Compaction – resistance plots for Optimat diffusers

These are seen to have very poor electrical resistance properties relative to Carbel CL– These particular samples have not all been manufactured using the same technique. The Optimat 30 g/m^2 material, which shows the highest resistance of the three, has been manufactured with a PVOH (polyvinyl alcohol) structural binder to a 10% by weight ratio. The other two samples (20 g/m^2 and 34 g/m^2) use an 'emulsion' polyester based treatment to approximately 8-12% by weight.

However, it is clear that all of the Optimat materials would produce unacceptable interfacial resistance levels in a fuel cell using anything but graphite flow plates and a high compaction pressure.

The resistance characteristics of the Spectracorp range of carbon composite fibre paper diffusers are shown in Fig. 7.16.

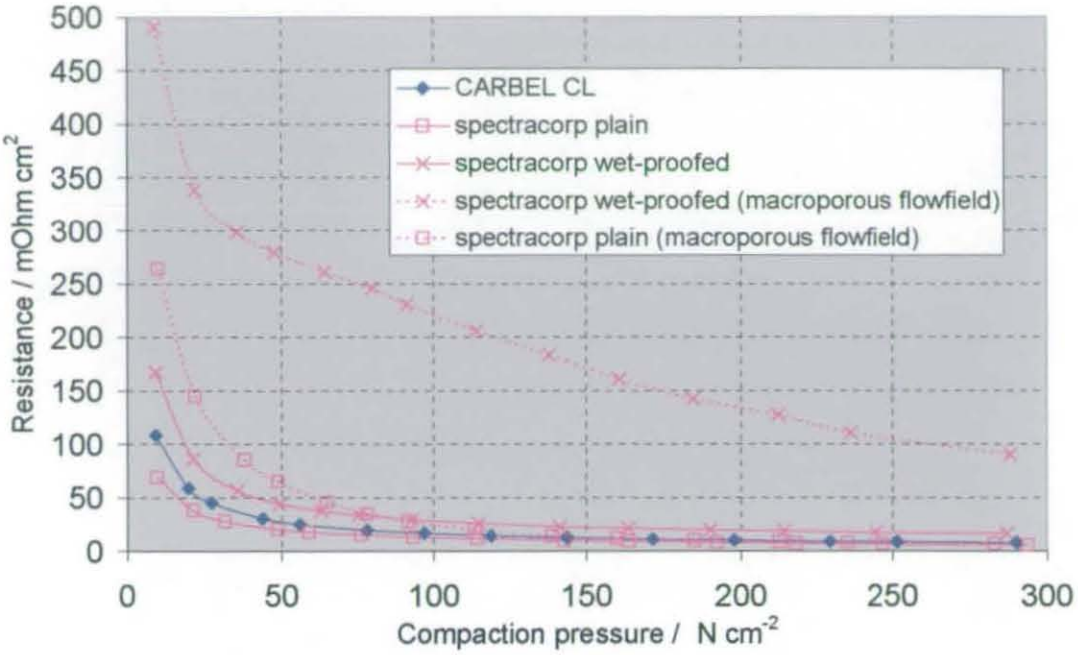

Fig. 7.16: Compaction – resistance plots for Spectracorp diffusers

The wet-proofed 'standard' Spectracorp grade has a higher resistance than the plain material, which indicates that the dispersion of PTFE in a diffuser structure increases bulk and contact resistances. The plain macroporous grade produces a higher resistance to that of the wet proofed standard grade at compaction pressures below 80 N/cm^2 but above this its resistance decreases below the latter. This can be attributed to an initial higher interfacial resistance due to a reduced 'contact area' between the fibres and the graphite flow plates. However as higher compaction pressure was applied the weaker macroporous structure began to collapse, readily increasing the contact area and lowering the resistance. The highest resistance is displayed by the wet-proofed macroporous grade.

The compaction resistance plots for the wet laid filled Lydall grades are shown in Fig. 7.17.

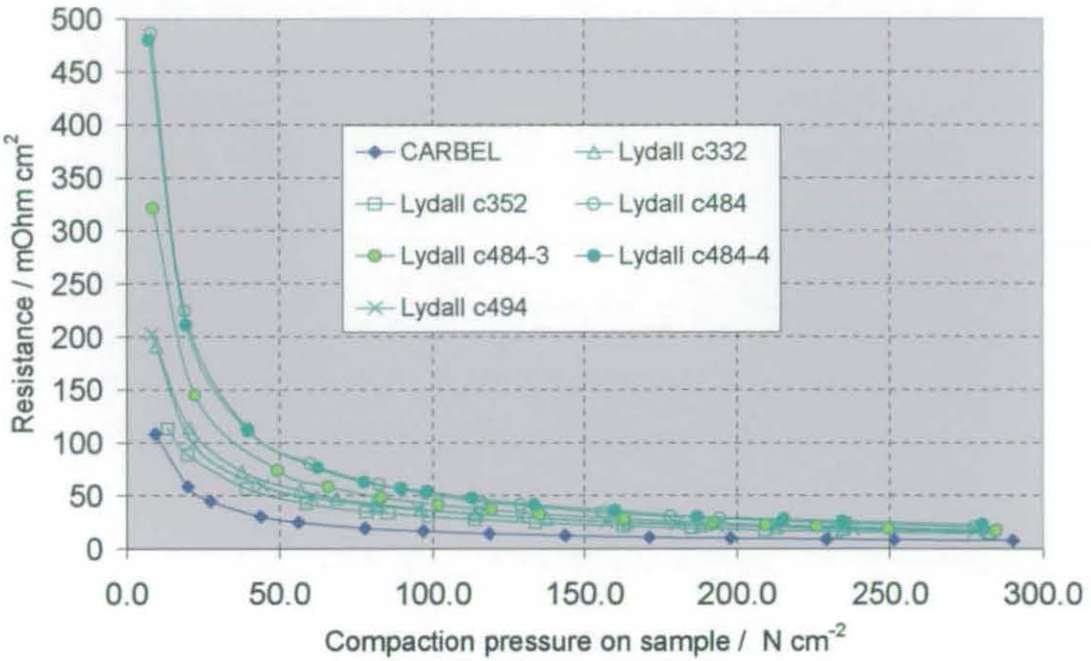

Fig. 7.17: Compaction – resistance plots for Lydall diffusers

At medium-range compaction pressures (150-200 N/cm^2) the resistances of the Lydall materials are all very similar, around 20 milliohm cm^2, and approximately twice the value calculated for Carbel CL. There are however, large variations in resistance at low compaction pressures illustrating the differences between grades. The plots appear to follow a trend of the lowest density material having the highest resistance- (c352 has the highest density and c484 the lowest). These materials show much improved resistance properties to the Optimat range of materials, indicating the enhanced conductivity provided by the dispersed carbon powder mixture.

Compaction-pressure resistance plots for the Toray carbon composite fibre papers are illustrated in Fig. 7.18.

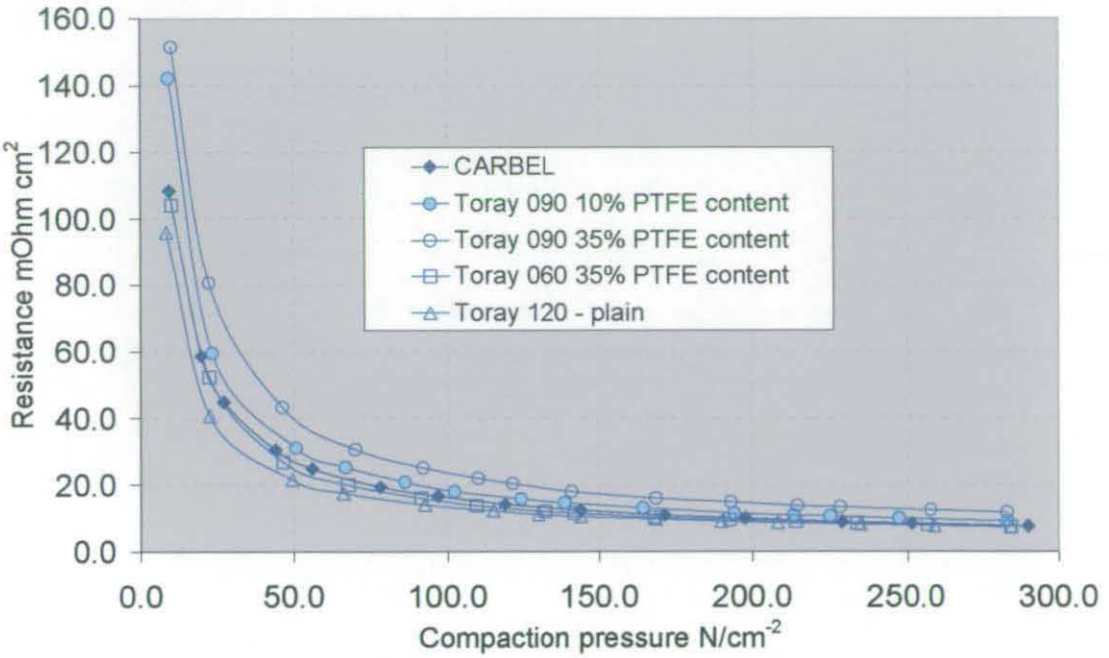

Fig. 7.18: Compaction – resistance plots for Toray diffusers

The plain Toray 120 grade produces the lowest resistance profile due to the purest carbon content. The highest resistance was obtained using Toray 090 with 35% PTFE content. The effect of differing degrees of PTFE content on the material resistance is illustrated by comparing the plots of the two Toray 090 materials.

The next chart shows compaction - resistance plots of Carbel CL along with the miscellaneous cloth-based diffuser materials from ETEK, Fig. 7.19.

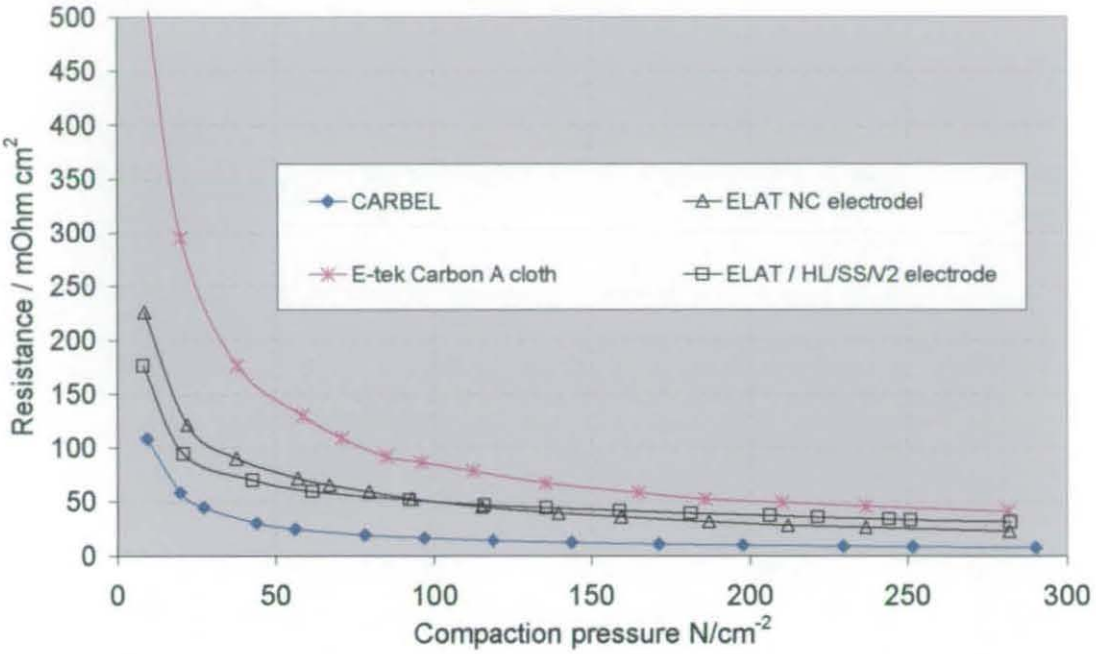

Fig. 7.19: Compaction – resistance plots for ETEK diffusers

The resistance profile of the E-TEK carbon 'A' cloth illustrates the poor surface contact that is achieved using a carbon cloth without a microdiffuser layer. In addition there is also a very high bulk resistance due to the high loading of PTFE. With this material, the resistance is not lowered to acceptable levels until significant compaction pressure is applied.

The remaining two electrode materials show higher resistance properties than Carbel CL. From the shape of the plots it is clear there is a higher PTFE content, either in the substrate or the microdiffuser. The single side electrode, which contains platinum catalyst and is a complete gas diffusion electrode, has a lower resistance at low compaction pressures than the other, which is packed with microdiffuser through the whole thickness. However, above a compaction pressure of 150 N/cm^2 the converse is true.

The compaction/resistance plots the dry laid SGL diffuser materials are shown in Fig. 7.20.

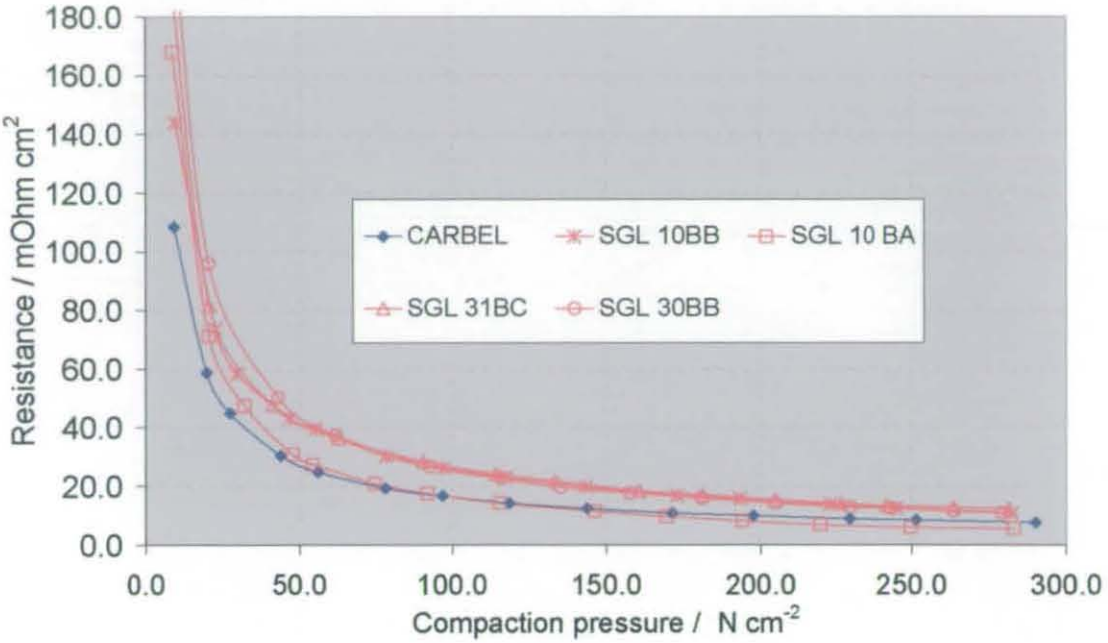

Fig. 7.20: Compaction – resistance plots for SGL diffusers

It is observed that the Carbel and SGL 10BA produce a resistance approximately 10 mOhms cm^2 lower over the medium-high range of compaction pressures than the other materials, SGL 10BB, 31BC and 30BB. The latter diffusers have a similar PTFE substrate content and a microdiffuser layer and hence produce approximately the same resistance over the full range of compaction pressures.

Conclusions from compaction-resistance plots

The calculated through plane resistance values for each diffuser grade at a compaction pressure of 200N/cm^2 is shown in Fig. 7.21.

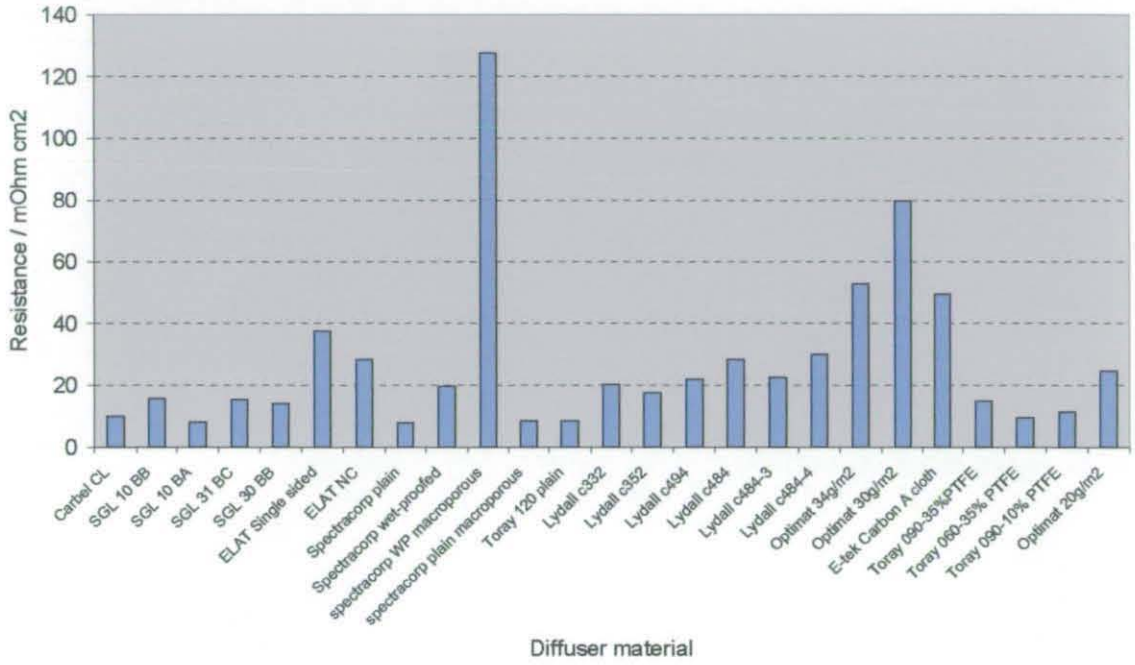

Fig. 7.21: Electrical resistance for all diffusers at 200 N/cm^2

The conclusions from this series of tests are as follows:

- The dispersion of PTFE in a diffuser substrate increases the electrical resistance
- The Optimat substrates, manufactured via the paper making technique detailed in appendix F, have a very high resistance due to the high binder contents. The powder filled versions, i.e. the Lydall grades, of these are still not as conductive as Carbel CL
- For a woven carbon cloth substrate, the microdiffuser decreases surface resistance but not for the carbon fibre structures.

7.2.5 Compaction/ Cross-plane pressure drop

Description

The aim of this series of tests was to obtain data on the air pressure drop in a 'cross-plane' direction for each diffuser material at stages of applied compaction pressure, and hence, a range of material thickness. This was to be carried out by supplying a fixed flow of air to the centre of a ring-shaped piece of diffuser material and measuring the pressure difference between the feed point and atmospheric conditions. The use of a ring shape piece of material effectively nullified pressure drop influences in the x and y directions due to large variations in the structural characteristics associated with the cloth weave. This made a general comparison between carbon paper diffusers and Carbel CL possible and also eliminated potential discrepancies between 'machine' and 'cross' directions for some grades of carbon papers, particularly the SGL dry laid materials.

Procedure

In each test, a concentric circular shape of the particular diffuser material is cut with 39 mm inner diameter and 50 mm outer diameter. An arrangement as shown in Fig. 7.22 was then built on the extensometer mounting plate. This consisted of the bevelled stainless steel alignment plate (6), followed by the diffuser piece and then a stainless steel top disc (7). This top-plate, the design of which is detailed in appendix G, enabled the delivery of air to the centre of the sample from a top feed fitting and allowed a pressure measurement from a machined tapping. The top compression plate (5) followed this.

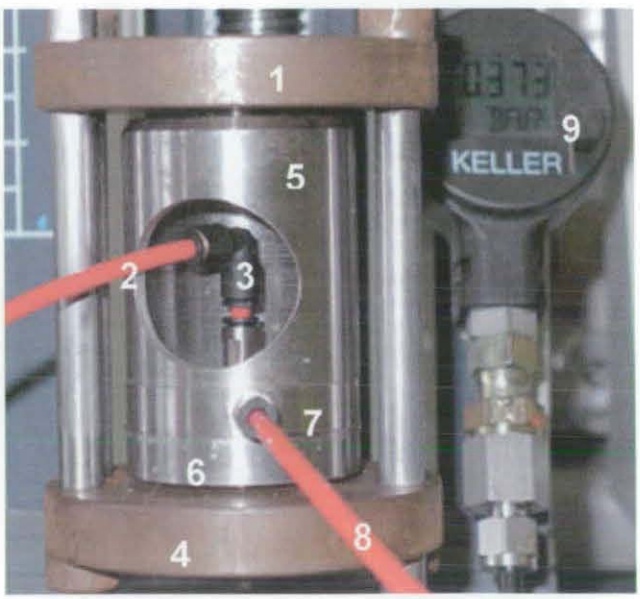

1 Extensometer compression plate
2 Air delivery tube – 4 mm nylon
3 90 degree Legris elbow fitting
4 Extensometer compression mounting
5 Stainless steel compression plate
6 Bevelled alignment plate
7 Stainless steel radial flow plate
8 Pressure tapping tube
9 Keller digital manometer

Fig. 7.22: Arrangement on the extensometer for the compaction-cross plane pressure drop tests

A carefully controlled flow of air was supplied via the top plate to the centre of the diffuser sample piece and transport through the material to atmosphere; this is shown in Fig. 7.23.

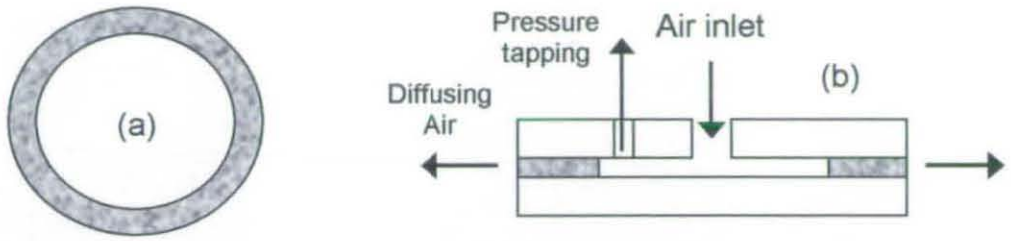

Fig. 7.23: Diffuser piece (a) and mechanism (b) for the compaction-cross plane pressure drop tests

The Aera mass flow control equipment, used in Chapters 3 and 4, was used to deliver an accurate air flow to the sample with the pressure measurement taken from the tapping in the top disc, connected by a 4 mm nylon tube to one of the Keller digital manometers described in Chapter 6.

For the pressure drop analysis, it was necessary to calculate a delivery flow rate of air that, relative to the ring area of diffuser material, represented realistic cross plane gas flows in an EC fuel cell using the interdigitated cathode flow field. By using such a representative air flow rate, then, theoretically a realistic pressure drop figure for the transport of air between the entry and exit channels of an interdigitated pair would be obtained. However, this test could not take into account the effects of operating temperature or water content on the air pressure drop.

The flow rate was to be calculated to represent a high stack power output and the associated high air stoichiometry needed for the removal of waste heat as required in an EC fuel cell. Basing the calculation on the 200 cm^2 active electrode area used so far in this thesis, a maximum current of 240 Amps, equivalent to a current density of 1.2 A/cm^2, was chosen, close to the maximum power point in Fig 5.02 of Chapter 5.

The required flowrate of oxygen in moles/second:

= 240 Coulombs / sec / (4 electrons/mole*96500 Coulombs/mole)

= 6.218 moles / sec

Converted into standard litres per minute of air:

= 6.218 moles /sec * 100/21 moles air / moles O_2 * 22.4 litres/mol * 60 secs / min

= 3.979 SLPM

Assuming an air stoichiometry of 3 to enable complete evaporative cooling:

= 3.979 SLPM * 3

= 11.938 SLPM

It is necessary to correlate this flowrate with the area of diffuser it will travel through, i.e. for the interdigitated flow field all of the gas flow is forced between the inlet and exit track. The calculated flow area was based on the total rib area of the graphite cathode plate as used in the segmented cell in Chapter 6, illustrated in appendix E.

The track area is given by the number of gas tracks on segmented cell cathode plate:

= Forty six, 1mm wide, 140mm long tracks - Interdigitated configuration – pitch 3mm.

Area for cross-plane diffusion (area under ribs): = Total area – track area

$=200cm^2 - (46 * 0.1\ cm * 14c\ m) = 135.6\ cm^2$

Dividing to get the flow rate per unit area gives:

$=11.938\ SLPM / 135.6\ cm^2$

$= 0.088\ SLPM / cm^2$

So, the air flowrate required to feed to the circular test arrangement:

$=0.088 * 6.433\ cm^2 = 0.566\ SLPM$

Therefore this flow of air was to be delivered to the diffuser sample at varying compaction pressures.

The same initial alignment and compression procedure as described in the previous section was carried out. The arrangement was then compressed in stages with the pressure drop on the Keller manometer manually logged for the delivery of a flow of 0.566 SLPM of air.

Results

The results are plotted with the pressure drop reading from the Keller manometer on the y-axis and compaction pressure applied to the diffuser sample on the x-axis.

The cross plane pressure drop of Carbel CL and the Spectracorp range of carbon composite fibre diffuser materials is illustrated in Fig. 7.24.

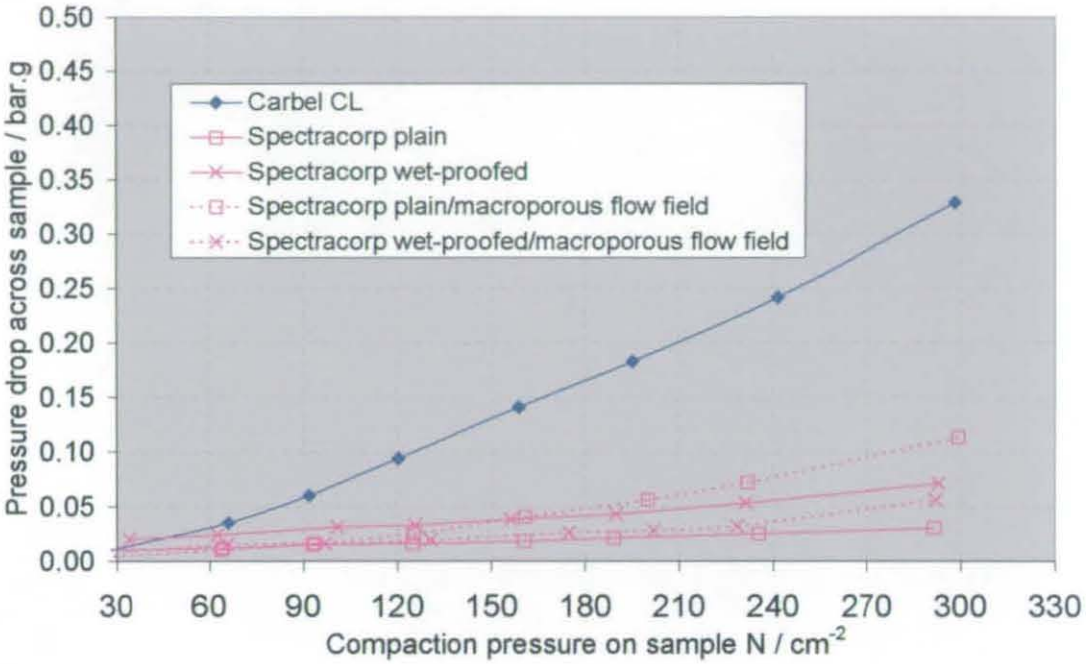

Fig. 7.24: Compaction – cross plane pressure-drop plots for Spectracorp diffusers

The main observation is that the Carbel CL material produces a much higher pressure drop compared to the Spectracorp diffusers. As Carbel CL has been impregnated with a microdiffuser layer to an unspecified thickness, it is expected that in this region the pressure drop would be very high. In addition, the physical configuration of the woven carbon cloth substrate means there are only a few large areas for cross-plane gas diffusion.

Focusing on the Spectracorp materials, the wet-proofed standard material has the higher pressure drop at lower compaction pressures due to the PTFE treatment partially blocking pores, producing a higher pressure drop than the plain equivalent material. The pressure drop plots of both standard material grades are very linear in nature. The macroporous grades are very permeable at low compaction pressures, however, it is seen that at the higher compaction loads the pressure drop rises in a non-linear manner. This is due to the effect observed in section 7.2.3 where the macroporous structures began to collapse at low-to-medium compaction pressures. As a result the untreated

macroporous grade becomes the least permeable in a cross-plane direction at compaction pressures above 150 N/cm^2. This non linear behaviour was also observed using the wet proofed macroporous grade although the wet-proofing treatment adds a degree of strength to the macroporous structure and thus it has a higher permeability than its untreated equivalent at high compaction pressures.

Fig. 7.25 shows the cross plane pressure drop plots for the range of Optimat diffuser materials.

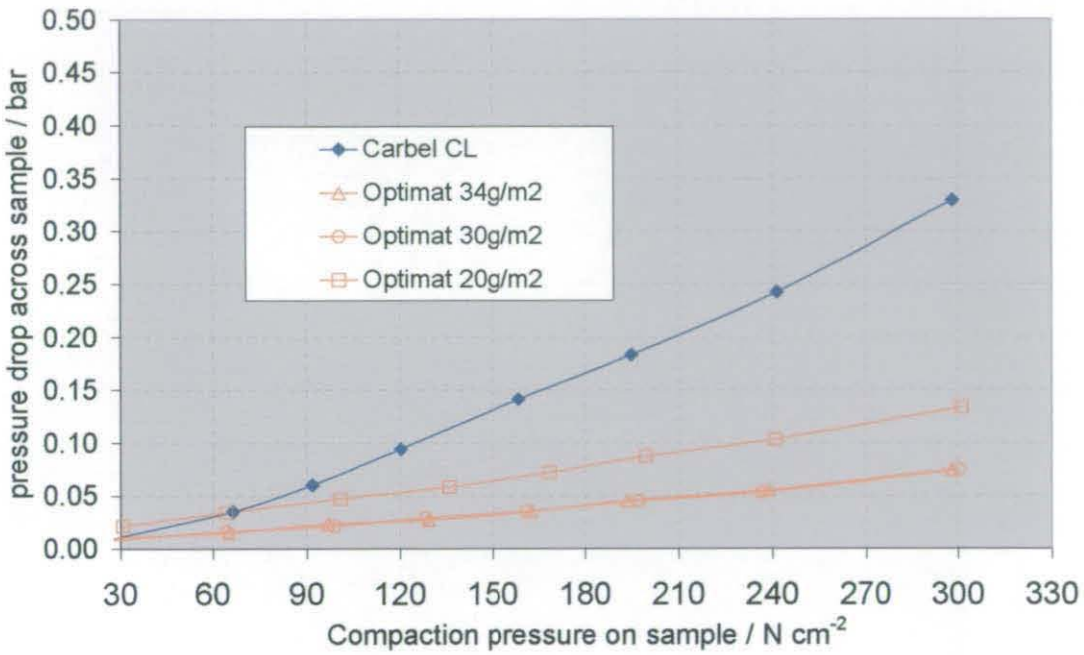

Fig. 7.25: Compaction – cross plane pressure-drop plots for Optimat diffusers

The Optimat materials show a linear increase with pressure drop over the range of compaction pressures with the highest pressure drop produced by the 20 g/m^2 grade. The emulsion treatment was to a fixed depth on each side of the diffuser, therefore with the thinnest grade of diffuser material, the highest pressure drop was achieved.

The cross plane pressure drop plots for the range of Toray carbon composite fibre papers are illustrated in Fig. 7.26.

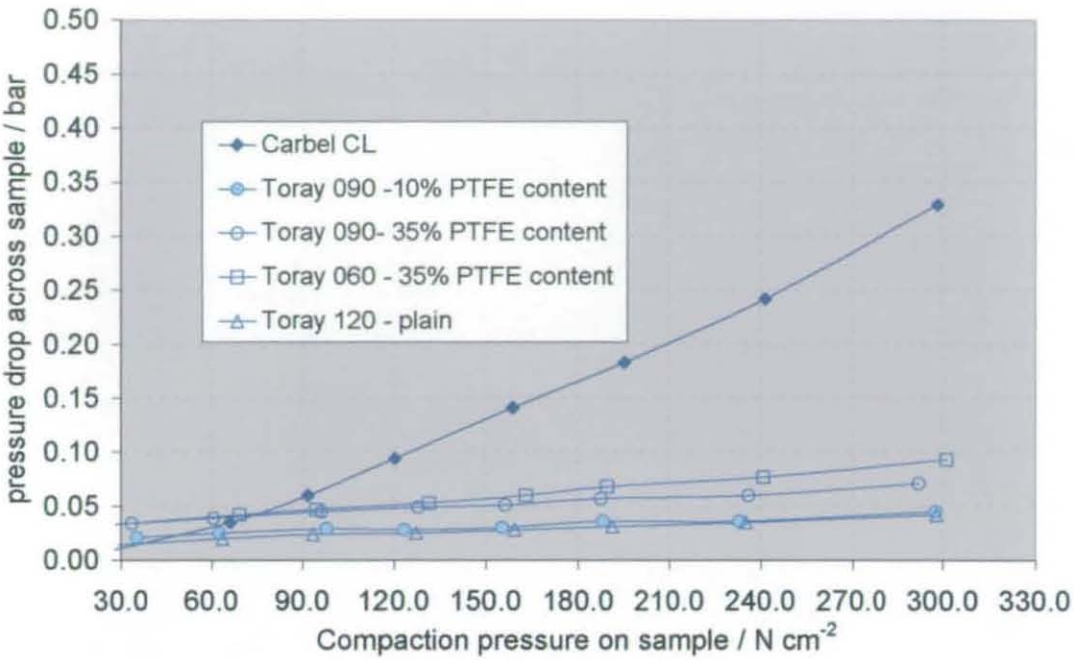

Fig. 7.26: Compaction – cross-plane pressure drop plots for Toray diffusers

All of the Toray pressure drop plots are linear reflecting the high mechanical strength and stiffness of the structures. The lowest pressure drop is produced by Toray 120 which, as it is the thickest grade, has the highest cross sectional area for cross-plane gas diffusion.

The effect of differing degrees of wet-proofing on pressure drop is observed when comparing both Toray 090 plots - Toray 090 with 35% PTFE content has its cross-sectional area reduced significantly in comparison with Toray 090 with 10% PTFE. Similarly, the plain Toray 120 and 10% PTFE Toray 090 plots are very similar which indicates that the cross-plane permeability of both materials are similar. The Toray 060 with 35% PTFE content has the highest pressure drop due to the smallest cross sectional area.

The cross plane pressure drop data for the SGL 'dry-laid' carbon paper diffusers is illustrated in Fig. 7.27.

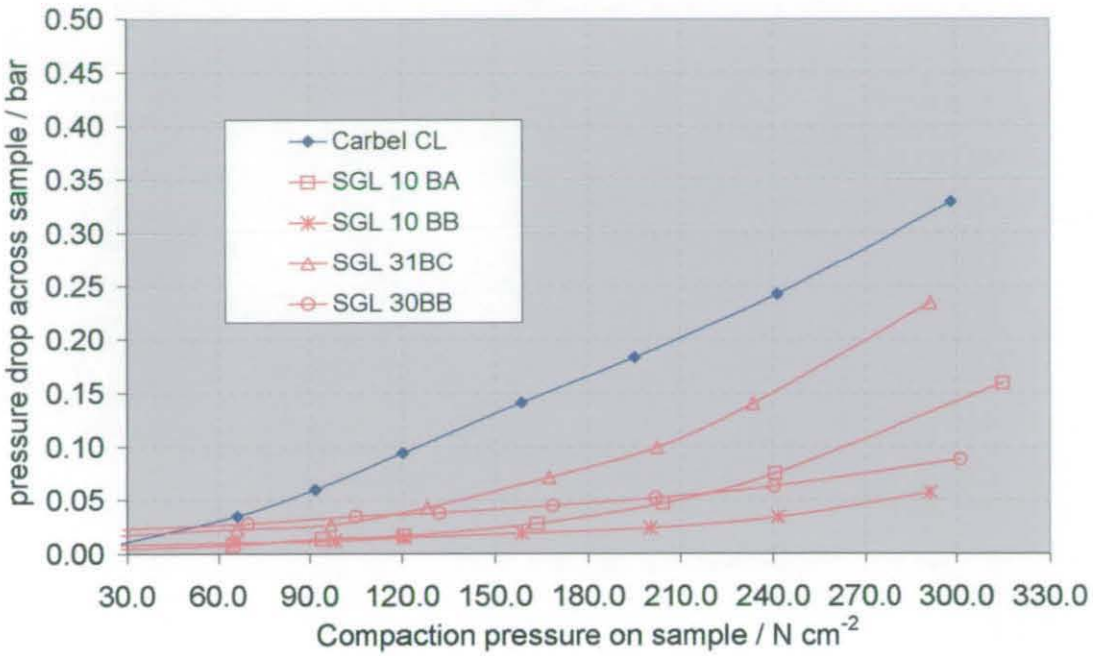

Fig. 7.27: Compaction – cross plane pressure drop plots for SGL diffusers

It is observed that the plots for the SGL diffusers are non-linear, indicating a structural collapse at the higher compaction pressures.

The effect on pressure drop of the deposition of a microdiffuser into the substrate is illustrated by comparing the plots of the 10BA and 10BB materials. Below 60 N/cm^2 the 10BA material shows a lower pressure drop over the range than the 10BB material which contains a microdiffuser. However, above this compaction load, the pressure drop of the plain material is greater with an increasingly collapsing structure, evident by the less linear plot. As both materials have the same substrate PTFE content of 5% by weight, it can be concluded that the microdiffuser layer serves to reinforce the substrate structure. In the compaction-thickness testing, section 7.2.3, it was seen how the microdiffuser hindered the degree of crushing which confirms these observations.

The 30BB grade has the most linear plot as this is the lowest permeability grade and has the strongest structure. Similarly, the 'high permeability' 31BC grade has the least linear plot as it has the weakest structure and hence the lowest permeability at high compactions.

The cross plane pressure drop data for the Lydall and ELAT range of gas diffusion materials are shown in Fig. 7.28.

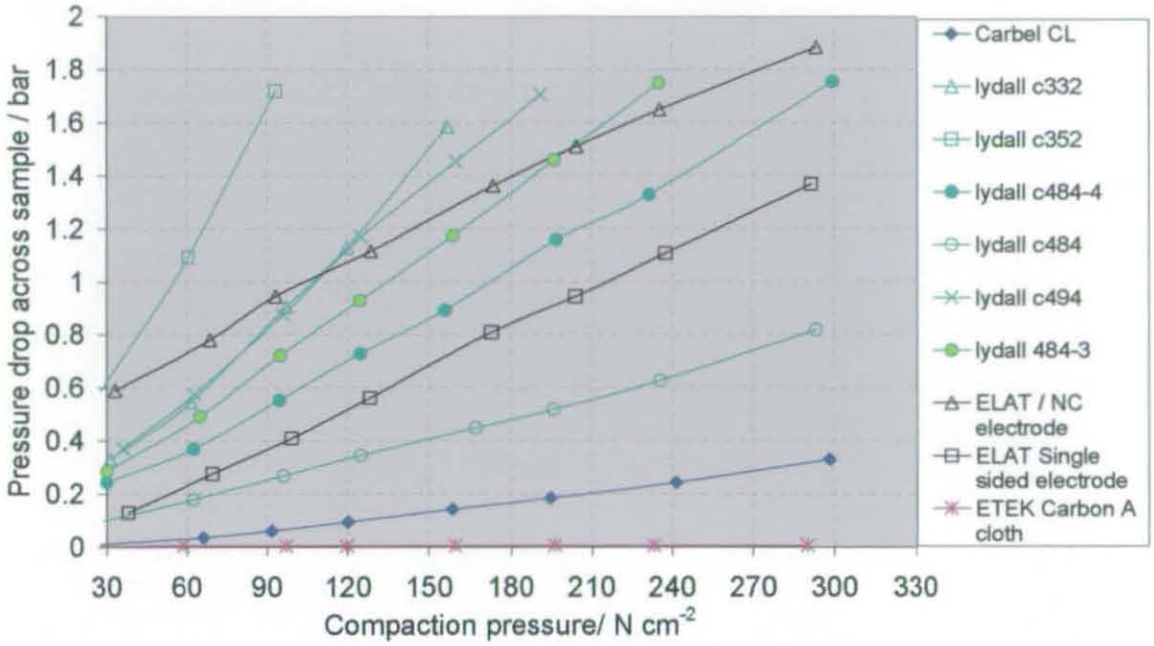

Fig. 7.28: Compaction – cross plane pressure drop plots for ETEK & Lydall diffusers

All of these materials, with the exception of the plain ETEK carbon 'A' cloth, produce a much higher pressure drop than Carbel CL. Clearly, the deposition of carbon powder mixtures into the diffuser substrates dramatically lowers the cross plane permeability. These pressure drops are clearly too high to be considered for use in an EC fuel cell.

Conclusions from compaction-cross plane pressure drop plots

The crushing characteristics for all diffuser materials tested at a compaction pressure of 200 N/cm^2 is shown below in Fig. 7.29.

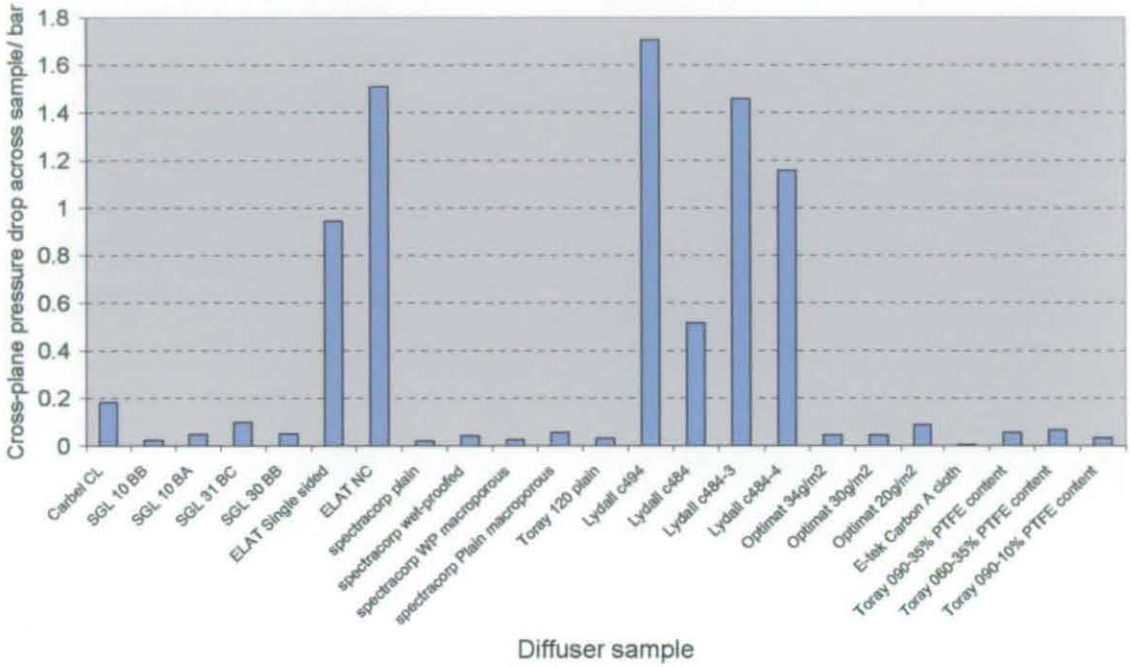

Fig. 7.29: Cross plane pressure drop plots for all diffusers at 200 N/cm^2 with an air flow of 0.566 SLPM

The following observations can be made:

- The Carbel CL showed a high cross-plane pressure drop, relative to most of the carbon fibre paper structures.
- The largest cross-plane pressure drops were obtained from materials with filled pores, namely the grades of Lydall and the ETEK diffusers.
- With some of the carbon paper structures the degree of cross plane pressure drop increased in a non-linear manner due to the collapsing of the structure

7.2.6 Through-plane pressure drop

Description

The aim of this series of tests was to obtain data on air pressure drop in the 'through-plane' direction for each of the diffuser material grades. This was performed by feeding a set flow of gas *through* a sample piece of diffuser and measuring the pressure difference between the feed point and ambient conditions. To eliminate the possibility of any cross-plane gas diffusion to the edges of the sample the largest possible sample piece, 50 mm diameter, was used and the maximum compaction force applied to it by the extensometer – 5000 N. In addition, a thin bead of sealant was applied to seal the edges of the plate arrangement

1 Extensometer compression plate
2 Air delivery tube – 4 mm
3 90 degree elbow fitting
4 Extensometer compression mounting
5 Stainless steel compression plate
6 Bevelled stainless steel alignment plate
7 Stainless steel radial flow plate
8 Pressure tapping tube
9 Bead of Silcoset151 sealant

Fig. 7.30: Arrangement on the extensometer for the compaction-through plane pressure drop tests

Procedure

Custom stainless steel discs were designed and manufactured for these tests – these are detailed in appendix H. These consisted of a holed and bevelled alignment plate and a top plate with a pressure tapping taken off from the air delivery channel. The sample area of interest, the 5 mm hole, is not crushed on compaction of the arrangement.

The arrangement, as shown in Fig. 7.30, was built on the extensometer. This was done by positioning the holed and bevelled plate on a flat surface and aligning the 50 mm diameter diffuser sample on top. The flow delivery plate was then placed on top and the

whole arrangement was held in place by a pair of grip locking pliers. A bead of Silcoset 151 was then deposited around the rims of the two plates, so that the gap was completely covered, and allowed to cure for 60 minutes. Silcoset 151, a high performance aerospace sealant, was chosen as the seal had to be flexible in nature and yet relatively easy to remove after the test.

The arrangement was then placed on the extensometer mounting plate followed by the compaction plate and the maximum force of 5000 N applied. The same initial alignment and compression procedure, as described in the previous section, was carried out. The fittings and tubes for gas delivery and pressure measurement were then attached to the stainless steel flow plate. A carefully controlled flow of air was to be fed via the top plate to the sample piece and the pressure measured, this is shown in Fig 7.31.

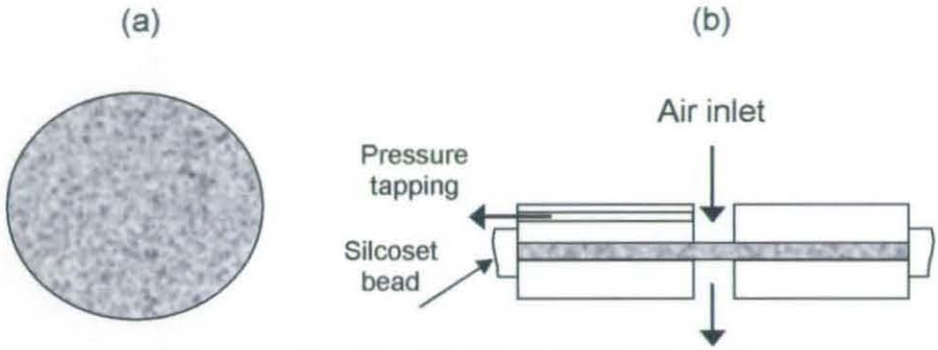

Fig. 7.31: Diffuser piece (a) and mechanism (b) for compaction-through plane pressure drop tests

The Aera mass flow control equipment, used in the previous section, would again be used to deliver an accurate air flow to the sample. It was necessary again to calculate a delivery rate of air that, relative to the 5 mm diameter through-plane area of diffuser material, represented realistic through plane gas flows for an EC fuel cell using the interdigitated flow field.

From earlier, it was calculated that a large air flowrate representing maximum power output in a 200 cm^2 active area EC fuel cell was 11.938 SLPM (An air stoichiometry of 3 and a current density of 1.2 A/cm^2)

The area for transverse flow (gas track area):

$$= (46 \text{ tracks} * 0.1 \text{ cm} * 14 \text{ cm}) = 64.4 cm^2$$

Calculating the flow of air per unit area:

$$= 11.938 \text{ SLPM} / 64.4 \text{ cm}^2 = 0.185 \text{ SLPM} / \text{cm}^2$$

With 0.5cm^2 hole the area is:

$= \pi * (0.25\ cm)^2 = 0.196\ cm^2$

Flowrate of air required:

$= 0.185\ SLPM / cm^2 * 0.196\ cm^2 = 0.036\ SLPM$

The arrangement was then compressed in stages with the pressure drop on the Keller manometer manually noted for the delivery of a flow of 0.036 SLPM of air.

Results

The pressure drop measurements for all the diffuser materials are shown below in Fig. 7.32.

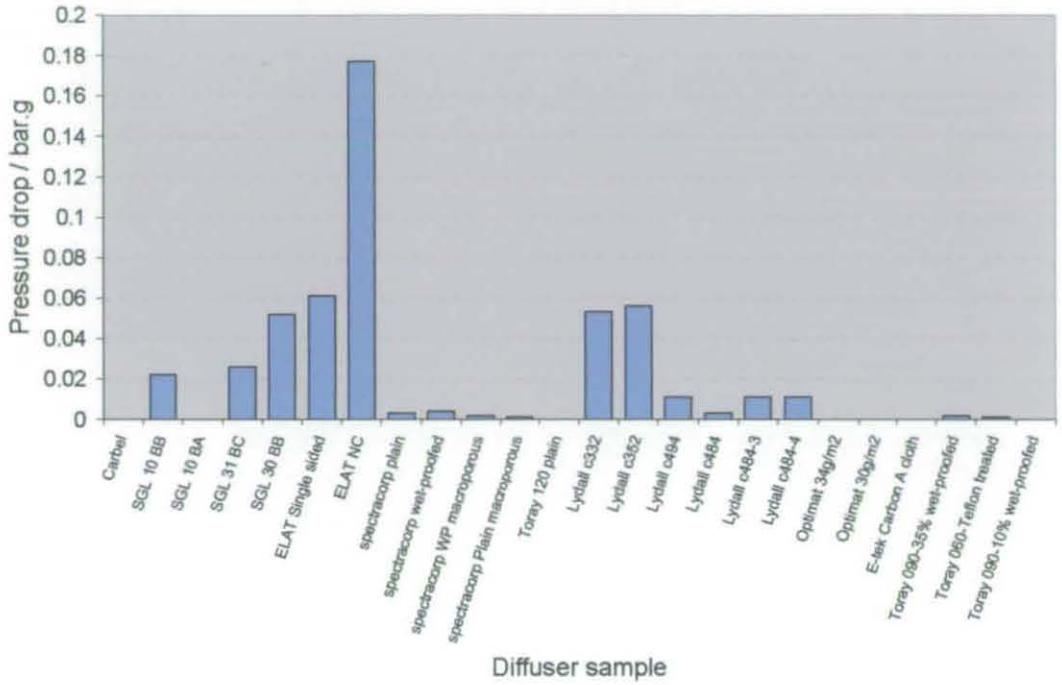

Fig. 7.32: Through-plane pressure drop plots for all diffusers – 0.036 SLPM air

It is seen that the ELAT double sided electrode clearly produces the highest measured through-plane pressure drop of around 180 mbar. The microdiffuser layer here is completely packed through the entire thickness of the carbon cloth fibre weave. The next largest through plane pressure drop of 60mbar is produced by the single sided ELAT gas diffusion electrode.

Looking at the separate graphs with Lydall grades and Carbel it is seen that the grades of Lydall material with the highest pressure drop are c332 and c352, with the rest being significantly lower. The Optimat materials all have zero through plane pressure drop.

The Spectracorp diffusers confirm the earlier results in the testing for cross-plane pressure drop. The least permeable material is the wet-proofed standard grade, this is followed in order by the plain standard then the wet-proofed macroporous grade and finally the macroporous plain grade.

The through-plane pressure drop of Carbel is virtually zero as the microdiffuser does not penetrate more than half the structure thickness and thus does not block the large pores of the weave structure.

The SGL 10BA, which contains no microdiffuser layer, also has virtually zero through plane pressure drop. The largest pressure drop experienced using the SGL materials is 50 mbar, produced by the 30BB material which, being the low permeability grade, confirms earlier testing. However, the pressure drop through the high permeability grade 31BC, 26 mbar, is slightly larger than with the 10BB, 22 mbar, which may be due to the microdiffuser layer. The C grade is supposed to have the same composition as the B grade but has a different method of application, which ensures less 'cracking'.

Conclusions from through plane pressure drop tests

The deposition of PTFE in the substrate structure and the deposition of a microdiffuser layer increases through plane pressure drop of a diffuser material, however the latter has by far the largest effect.

7.2.7 Permeability Calculations

The data obtained for diffuser thickness and cross-plane pressure drop allows a calculation of the intrinsic permeability for each material at a compaction pressure of 200N/cm^2. The calculations used for obtaining these permeability figures are provided in appendix J.

Diffuser Material	Calculated Permeability / m^2
Carbel CL	-2.178E-10
SGL 10BA	-7.423E+08
SGL 10BB	-2.272E+08
SGL 30BB	-6.382E+08
SGL 31BC	-1.376E+09
Toray 120 plain	-3.458E+08
Toray 090 10%	-4.598E+08
Toray 090 35%	-7.179E+08
Toray 060 35%	-1.446E+09
Spectracorp Plain	-1.780E+08
Spectracorp WP	-4.474E+08
Spectracorp MP plain	-1.004E+09
Spectracorp MP WP	-2.381E+08
Optimat 20g/m2	-4.377E+09
Optimat 30g/m2	-1.365E+09
Optimat 34g/m2	-1.246E+09
Lydall c484-4	-2.809E+10
Lydall c484	-8.032E+09
Lydall c494	-4.660E+10
Lydall c484-3	-4.073E+10
ETEK Carbon A cloth	-4.675E+07
ELAT NC	-2.358E+10
ELAT HL/SS/V2	-1.509E+10

Fig 7.33: Calculated cross plane intrinsic permeability for the diffuser materials tested

7.3 Conclusions

From the ex-situ testing of gas diffusion media for PEM fuel cells detailed in this Chapter, the main conclusions are as follows.

- Several materials were shown to exhibit superior cross-plane pressure drop characteristics to Carbel CL – the standard diffuser material used in the research of this thesis. The carbon cloth substrate was observed to deform quite readily, particularly, in comparison to the carbon composite fibre and dry-laid filled papers. This significantly increased the cross-plane pressure drop of Carbel CL
- The dispersion of PTFE in a diffuser substrate increases the electrical resistance; however, the structural strength is improved such that with the application of medium-high compaction force, the cross-plane pressure drop was lower than with the untreated equivalent material. A similar behaviour was observed with thicker grades of the same untreated diffuser.
- A similar improvement in mechanical strength, and thus permeability, was seen with the addition of a microdiffuser layer to the SGL dry-laid diffuser materials
- The Optimat diffuser substrates, manufactured via the paper making technique detailed in appendix F, have very high resistances, particularly at low compaction pressures, due to the high binder contents. The wet-laid filled versions of these materials are not suitable for an EC fuel cell due to the high pressure drop caused by the filled resin which exerts conductivity to the structure.
- For a diffuser with a woven carbon cloth substrate such as Carbel CL, the microdiffuser decreases surface resistance however this is not the case for the carbon paper fibre structures.
- The highest cross-plane and through-plane pressure drops are obtained from materials with filled pores, either from the dispersion of a microdiffuser or the wet-laid filled carbon papers.
- The carbon composite fibre papers, Toray and Spectracorp grades, were the most resistant to crushing and therefore the most brittle materials with low flexural strength.

7.4 References

Antolini, E.; Passos, R.R.; Ticianelli, E.A., "**Effects of the cathode gas diffusion layer characteristics on the performance of polymer electrolyte fuel cells**", Journal of Applied Electrochemistry, Vol. 32, pp 383-388, 2002

Antolini, E.; Passos, R.R.; Ticianelli, E.A., "**Effects of the carbon powder characteristics in the cathode gas diffusion layer on the performance of polymer electrolyte fuel cells**", Journal of Power Sources, Vol. 109, pp 477-482, 2002

Antolini, E.; Giorgi, L.; Pozio, A., "**Development of Gas Diffusion Electrodes for Polymer Electrolyte Fuel Cells**", Materials Technology, Vol. 13.2, pp65-68, 1998

Dhathathreyan, K.S.; Sridhar, P.; Sasikumar, G.; Ghosh, K.K.; Velayutham, G.; Rajalakshmi, N.; Subramaniam, C.K.; Raja, K.; Ramya, K., "**Development of polymer electrolyte membrane fuel cell stack**", International Journal of Hydrogen Energy, Vol.24, pp1107-1115, 1999

Fischer, A.; Jindra, J.; Wendt, H., "**Porosity and catalyst utilisation of thin layer cathodes in air operated PEM-fuel cells**", Journal of Applied Electrochemistry, Vol.28, pp277-282, 1998

Gambururzev, S.; Appleby, A.., "**Recent progress in performance improvement of the proton exchange membrane fuel cell (PEMFC)**", Journal of Power Sources, Vol. 107, pp5-12, 2002

Handbook of Fuel Cells – Fundamentals, technology & Applications, Volume 3: Fuel Cell Technology & Applications, Chapter 46: Diffuser media materials and characterisation, John Wiley & Sons, Edited by Vielstich et al, Gasteiger, H.A., Lamm, A., 2003

Jordan, L.R.; Shukla, A.K.; Behrsing, T.; Avery, N.R.; Muddle, B.C.; Forsyth, M., "**Diffusion Layer Parameters influencing optimal fuel cell performance**", Journal of Power Sources, Vol.86, pp250-254, 2000

Kong, C.S.; Kim, D.Y.; Lee, H.K.; Shul, Y.G.; Lee, T.H., "**Influence of pore-size distribution of diffusion layer on mass transport problems of proton exchange membrane fuel cells**", Journal of Power Sources, Vol 108, pp185-191, 2002

Lee, W.; Ho, C.H.; Van Zee, J.W.; Murthy, M., **"The effects of compression and gas diffusion layers on the performance of a PEM fuel cell"**, Journal of Power Sources, Vol. 84, pp45-51, 1999

Lufrano, F.; Passalacqua, E.; Squadrito, G.; Patti, A.; Giorgi, L., **"Improvement in the diffusion characteristics of low Pt-loaded electrodes for PEFCs"**, Journal of Applied Electrochemistry, Vol. 29, pp445-448, 1999

Moreira, J.; Ocampo, A.L.; Sebastian, P.J., Smit, M.A.; Salazar, M.D.; del Angel, P.; Montoya, J.A.; Perez, R.; Martinez, L., **"Influence of the hydrophobic material content in the gas diffusion electrodes on the performance of a PEM fuel cell"**, International Journal of Hydrogen Energy, Vol. 28, pp625-627, 2003

Passalacqua, E.; Squadrito, G.; Lufrano, F.; Patti, A.; Giorgi, L. **"Effects of the diffusion layer characteristics on the performance of polymer electrolyte fuel cell electrodes"**, Journal of Applied Electrochemistry, Vol. 31, pp449-454, 2001

Qi, Z.; Kaufman, A., **"Improvement of water management by a microporous sublayer for PEM fuel cells"**, Journal of Power Sources, Vol 109, pp38-46, 2002

Uchida, M.; Fukuoaka, Y.; Sugawara, Y.; Eda, N.; Ohta, A., **"Effects of Microstructure of Carbon support on the Performance of Polymer-Electrolyte Fuel Cells"** , Journal of the Electrochemical Society, Vol.143, No.7, pp2245-2252, 1996

Chapter 8:

In-situ testing of diffuser combinations

8.1 Chapter Overview

From the extensometer testing of diffusers in the previous Chapter, it was observed that many materials produced high-cross plane pressure drop at compaction pressures, and hence thicknesses, where contact resistance with the flow plates was acceptably low. Therefore only a few diffusers were considered suitable for in-situ EC fuel cell testing.

This Chapter describes the evaluation of a selection of diffuser materials in a study of the cathode pressure drop caused by water accumulation under the ribs of an interdigitated flow field plate, occurring during fuel cell operation. It was investigated how the extent of this phenomenon was related to diffuser material structure and compaction pressure. It was also determined if any other diffuser material, of those tested in-situ, was more suitable than Carbel CL for utilisation in the cathode of an EC fuel cell.

A fuel cell rig was constructed, equipped with compressible sealing gaskets and direct liquid water injection to simulate the two-phase flow characteristics of an EC fuel cell. The data from the extensometer testing was used to define the most suitable ranges of cathode diffuser working dimensions using a selected combination of Carbel and SGL carbon paper materials. The main tests take the form of current 'shifts', from open circuit to a medium range current, with a measurement of the differential cathode pressure drop.

Background

During operation of an EC fuel cell, water accumulation occurs, resulting from the electrochemical reaction and liquid water injection, mainly in cathode diffuser areas located under the ribs of the flow-field plate. The presence of this water will increase the pressure drop between cathode inlet and exit for a set flow rate of air. As explained in Chapter 7, for an EC stack a low pressure drop of air is critical for effective temperature control, thus diffuser water content is an important parameter.

As observed in Chapter 6, by using the interdigitated flow field, compared to a parallel flow field, results in greatly reduced levels of water settling in the pores of the diffuser during fuel cell operation,. However, this does not mean that all excessive water is removed, if an interdigitated cathode flow-field is utilised. After a certain time period, with the fuel cell held at steady operating conditions, an equilibrium will be reached between water supply/generation and water removal via the evaporation effect of air, hence a 'fixed' level of water will be established in the cathode diffuser pores, and hence also the polymer membrane structure. This was very well illustrated in the thermal mapping endurance charts of Chapter 4, where, after a change in operating conditions, the fuel cell potential, after an initial large change, eventually 'settled' on a perceptible steady-state value. Here elevated levels of cathode flooding, i.e., diffuser water content, were illustrated by an oscillating value of the cell potential, representing the continually changing rates of oxygen transport to catalyst sites in the presence of large volumes of liquid water. Therefore, there was scope for lowering the diffuser substrate water content and thus lowering the pressure drop of air through the cathode.

The equilibrated level of water content in the cathode diffuser of an operating EC fuel cell will be determined by a variety of operational conditions such as:- current density, rate of water injection, temperature, pressure and air stoichiometry and also diffuser material parameters such as substrate permeability, hydrophobicity and the composition of any micro-diffuser layer. Some of the diffuser materials tested in Chapter 7 may have the ability to retain less water than Carbel CL, and this will be the main focus of the chapter.

Looped Polarisation curves

As detailed in Chapter 3, polarisation curves provide information on the irreversible losses of fuel cell operation but the performance stability over long durational periods cannot be predicted. However, the phenomena of 'looped' polarisation curves can provide some indication to the flooding behaviour and possible long-term cathode flooding issues.

When polarisation data are obtained from a fuel cell shifting from open circuit conditions to maximum current density then back to open circuit, the recorded potential values will be the same at each point during the upward and downward sweep *only* if equilibrated conditions, i.e. membrane water content and oxygen diffusion rates, are established at each current density. However, due to the slow rates of the various mass transfer phenomena, changes in current density place the fuel cell in a transitional state for a period until all the overpotentials again reach an equilibrated value. It is usually impractical to allow such long periods between current shifts when obtaining polarisation curves and usually the potential values are only recorded in one direction, which is, acceptable as long as the comparisons in any series of fuel cell testing are consistent in this manner, refer to Chapters 3 and 6.

When carrying out a 2-way polarisation with a quick scan rate, looped polarisation curves are obtained, which indicate that the overpotential contributions have changed during the measurement in each direction, this is illustrated in the following polarisation plots.

Improved potential values on the backwards sweep, as shown in Fig. 8.01, can be caused by increased water content in the membrane, which, due to the slowness of water removal is temporarily higher than it would be with continuous steady state conditions. This shape indicates there is no excessive water content in the diffuser pores and cathode flooding is unlikely.

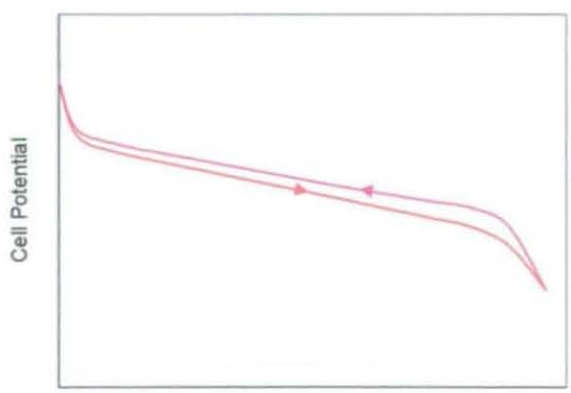

Fig. 8.01: Looped Polarisation plot with improved potential values on backwards sweep

Lower values on the reverse potential sweep, as shown in Fig. 8.02, possibly indicates flooding of the diffuser pores at the higher current densities due to the increased levels of product water. This shape can also occur when the anode side of the MEA is dehydrated, due to increased rates of electro-osmotic drag, but this is only likely with PFSA membrane structures thicker than the Gore reinforced materials, i.e. Nafion.

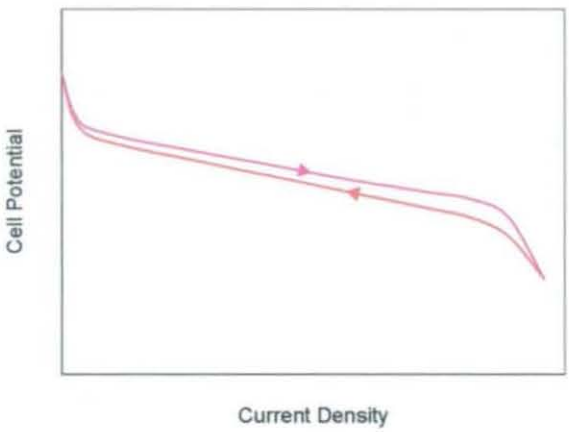

Fig. 8.02: Looped Polarisation plot with lower potential values on backwards sweep

Looped polarisation curves could be used to evaluate the flooding behaviour of diffuser materials for an EC fuel cell. In addition, a measurement of the pressure drop over the fuel cell cathode, moving from open circuit conditions to equilibrated conditions when drawing a medium range current, would be an effective method for diagnosing the extent of cathode flooding. By carrying out this test for a selection of diffusers and also logging the fuel cell performance, each material's suitability to the EC fuel cell can be assessed. Ideally an operational cathode pressure drop of less than 150 mbar will be obtained with a good performance delivered by the fuel cell.

With this measurement of cathode pressure differential, it is possible to distinguish between pressure drop caused by water accumulation from, (a) the direct injection of liquid water and (b) the electrochemical reaction. In the case of the former, water accumulation will tend to occur in the outer substrate layers and will influence the pressure drop obtained at open circuit potential. In the case of the latter, water accumulation will occur in the inner layers and microdiffuser. This will be shown as the difference between cathode pressure drop at open circuit potential and the chosen operating point - an example of this was shown previously, refer to Fig 4.05 in chapter 4.

Focus of study

It was decided to undertake both of the previously described tests in a study of alternative cathode diffuser materials, for an EC fuel cell utilising the interdigitated flow-field. A crucial consideration was the testing of each diffuser at several working thicknesses, as any material will have a certain optimum dimension for the EC application and the particular flow-field configuration used, with respect to cathode pressure drop and fuel cell performance.

In the literature, particularly in the few articles including an assessment of diffusion materials, there is very little priority given to the importance of the cathode diffuser working dimension. To the author's knowledge, this is the first diffuser study of this kind for internally cooled PEM fuel cells.

8.2 Fuel cell Rig design

8.2.1 Selection of diffusion media for in-situ tests

From the extensometer tests the permeability and electrical resistance characteristics of the SGL 'dry-laid' carbon paper diffusers made them a strong candidate for an in-situ comparison with Carbel CL. In order to undertake a fair comparison with Carbel CL, which contained a microdiffuser layer, the SGL diffusers selected would require a microdiffuser layer, eliminating the 10BA grade as a candidate.

The main challenge in designing the rig and the tests was operating the fuel cell with a range of cathode diffuser thicknesses. Using rigid gaskets of a precise thickness would be costly and extremely impractical due to the continual requirement of disassembly and reassembly of the rig to switch between gaskets. The diffusion media and MEA would also have to be scrapped after each test, introducing further costs. Therefore, it was decided to use a deformable 0.35 mm Grafoil sealing gasket on both anode and cathode sides that could be crushed to all necessary dimensions by varying the level of applied compaction force, see Fig. 7.04.

Usually, out of convenience more than any other factor, it is common practice to equip the anode and cathode sides of a PEM fuel cell with the same grade of diffuser material. This was observed in Chapters 3, 4 and 6 where Carbel CL was used on both sides of every fuel cell build. However, in the operation of an EC fuel cell, the cathode pressure drop is as an important a parameter as the electrochemical performance. From the results of the extensometer testing, there was only a certain range of material thicknesses where the permeability of any one diffuser, and hence pressure drop obtained, was suitable for the EC fuel cell cathode when using the interdigitated flow field. There will also be a restriction in the thickness that the Grafoil can be crushed to, probably no more than approximately 60% of the original thickness, i.e. 0.21 mm. Therefore, to obtain the appropriate range of permeabilities for the cathode diffuser at the limited range of thicknesses, a 'mixed' diffuser combination may have to be utilised.

Mixed diffuser combinations

Generally, there may be some advantage in using a mixed diffuser combination in an EC fuel cell, e.g. by choosing so the anode diffuser permeability is higher and PTFE content is lower than the cathode diffuser, the back diffusion mechanism will be encouraged thus removing extra water from the cathode. Conversely, for a stack design employing a dead-ended anode with a pure hydrogen source, a lower permeability or higher PTFE content of the anode diffuser would lessen the frequency of 'purges' required to clear flooding. Further influences on the degree of net electro-osmotic drag across the membrane could also be achieved by altering the PTFE content of the microdiffuser layer. These possibilities will not be studied any further in this thesis but would provide a valuable body of research in the future.

The 10BB, 30BB and 31BC grades of SGL diffusers were to be used, therefore to calculate the number of potential diffuser combinations, taking into account the fact a material can be used on both sides, a factorial expression was defined[1]:

$$\text{Number of diffuser combinations} = \frac{(n+1)!}{r!(n-r)!} \qquad \textbf{Equation 8.01}$$

To select the potentially optimum performing combinations and hence reduce the number of tests to be carried out, it was possible to calculate relative cross-plane pressure drops and through plane resistance for each material in the combination, using the data obtained for the cross-plane pressure drop and electrical resistance from the extensometer testing in Chapter 7. To do this, a 5th degree polynomial approximation is calculated for each of the dimension-compaction force plots for Carbel CL and the three SGL diffuser materials, as illustrated in appendix J1. The cross-plane pressure drop, relative to 0.088 SLPM/cm^2 – see section 7.25, and through-plane resistance plots for these materials can be revised with dimension instead of compaction pressure plotted on the x-axis, these are illustrated in appendix J2 and J3 and are also fitted with 5th order polynomial approximations.

Using these formulae, relative values for cross plane pressure drop and through plane resistance for each material at a selected thickness can be calculated for a combined dimension of 0.60 mm - this is illustrated in Fig 8.03 and includes the through-plane pressure drop values, based on 0.185 SLPM/cm^2, previously illustrated in section 7.2.6.

[1] Where n is the number of materials and r is the number of material in a diffuser combination. For n = 4 and r = 2 this equates to ten possible combinations.

A point of note is that these figures in the table are all relative and will not reflect actual measured parameters in a fuel cell.

	Diffuser A Type	Diffuser B Type	This column is solved: Compaction force for 0.6mm total - N/cm2	Formula used in appendix J1: Diffuser A thickness	Diffuser B thickness	Total Thickness	Formula used in appendix J2: Diffuser A Cross-plane pressure drop / bar	Diffuser B Cross-plane pressure drop / bar	Formula used in appendix J3: Diffuser A Resistance / mOhms cm2	Diffuser B Resistance / mOhms cm2
PAIRED COMBINATIONS	10BB	10BB	277	0.300	0.300	0.600	0.050	0.050	11	11
	30BB	30BB	45	0.300	0.300	0.600	0.022	0.022	46	46
	31BC	31BC	59	0.300	0.300	0.600	0.020	0.020	36	36
	Carbel	Carbel	28	0.300	0.300	0.600	0.008	0.008	48	48
MIXED COMBINATIONS	10BB	30BB	179	0.338	0.262	0.600	0.020	0.045	18	17
	10BB	31BC	162	0.343	0.257	0.600	0.018	0.057	20	19
	10BB	Carbel	73	0.369	0.231	0.600	0.011	0.045	30	20
	30BB	31BC	52	0.295	0.305	0.600	0.023	0.017	41	41
	30BB	Carbel	33	0.311	0.289	0.600	0.022	0.010	59	41
	31BC	Carbel	37	0.318	0.282	0.600	0.017	0.012	58	37

Through-plane pressure drop / bar

Carbel	0
SGL 10BB	0.023
SGL 31BC	0.026
SGL 30BB	0.052

Fig. 8.03: Table of relative diffuser characteristics for a combination thickness of 0.60mm

It was decided that the higher through plane pressure drop of SGL 30BB eliminated this material from consideration as a cathode diffuser in the EC fuel cell build.

The two combinations chosen for testing were SSL 30BB on anode, SGL 10BB on cathode and SGL 30BB on anode, SGL 31BC on cathode in addition to a paired combination of Carbel CL.

8.2.2 Equipment design

8.2.2.1 Rig Components

It was necessary to construct an EC fuel cell rig, set up for cathode water injection and differential pressure measurement, using Grafoil sealing gaskets in order to compress to various working dimensions. Time and budget constraints meant a new rig could not be designed and manufactured from scratch.

The SGL and Carbel diffuser materials were in plentiful supply which meant readily available MEA's with a 200 cm^2 active electrode areas could be used. Furthermore, this meant that the base plate, press plate, compression/heater plate, compaction springs and top manifold plate from the segmented cell arrangement in Chapter 6 could be re-used. The segmented current collector itself was deemed unsuitable for these tests; therefore a new manifold block was manufactured[2]. This was designed to be 40 mm thick to compensate for the missing height of the segmented electrode base in the arrangement. As this block was to be utilised for the *cathode* air manifolding, it was not designed to include a heating element as the assumption was made that the cathode would generate enough heat from the electrochemical reaction during operation to keep this side of the fuel cell warm. External heating of the anode side was undertaken by the heating/compression plate. Although the rig was set up to simulate two-phase flow conditions, true adiabatic operation was not going to be possible due to the bulky metallic components forming large heat sinks, as previously described in Chapter 6.

As explained in section 8.2.1, 0.35 mm Grafoil, exfoliated graphite, was used as the fuel cell sealing gasket material, as it was one of the few materials available that was able to yield the required degree of crushing without a significant level of 'flowing' that would be experienced with a material such as silicone. Gore prototype 5620 series MEA's, with an active electrode area of 200 cm^2 and no features cut in the sub-gasket area were available. The graphite flow plate detailed in appendix E, previously used in the segmented cell testing, was already set-up with an integrated water injection feature and was used again. A second plate graphite flow plate, identical in design except minus the water injection feature was manufactured[3].

A method had to be established for measuring the diffuser combination working thicknesses. Compressing the fuel cell to a force indicated by the compaction springs and using diffuser compaction/dimension data would be unsuitable as the distribution of load between the diffusers and Grafoil sealing gasket could not be measured. Instead,

[2] This work carried out by M.E. Cooper & Sons, Sileby

following compression of the fuel cell, the diffuser combination thickness was established by measuring the displacement between the inner edges of the anode and cathode graphite flow plates, using high accuracy verniers with an LCD display. A second measurement was also taken using a set of precision feeler gauges (from 0.05 mm to 1.0 mm in 0.05 mm stages). Neither of these measurements could be taken during operation, as there would be a risk of electrical shorting and subsequent damage to the fuel cell.

With the displacement measured between the flow plates the diffuser combination thickness was established by subtracting the thickness of the MEA, in this case 35 micron, from this figure. The formulas in appendix J1 were then used to establish the cathode diffuser material thickness.

[3] This work carried out by Erodex, UK

8.2.2.2 Rig Development

Several modifications had to be made to some rig components to produce a safe and fully operational fuel cell for the analysis, these alterations are now detailed.

A concern was that due to the use of deformable sealing gaskets, high compaction forces would be required to crush to small combined diffuser dimensions, exceeding what the compression elements of the rig were initially designed for. Therefore, the following alterations were made.

- The original studs, part I in Fig. 6.07, which fixed the press plate to the columns had been manufactured from regular stainless steel, and now represented potential structural failure points. To minimise this risk these, along with the bolts fixing the spacer columns to the base piece, were replaced with 12.9 grade Unbrako tensile bolts at both ends of the columns.

- The bevel washers, which comprised the compaction springs, parts F in Fig. 6.07, had the same orientation to reduce the level of elastic force displacement experienced with compaction. This could be potentially hazardous upon any structural failure of the compaction elements within the rig.

Another important issue was the fact that the graphite flow-field plates and MEA's were of different sizes, although both designed for a 200 cm^2 active area. The graphite plates measured 200 mm by 200m m and the MEA size, including sub-gasket area was, 197 mm by 150 mm. This introduced the risk of severe plate deflection and/or breakage at the unsupported edges on compaction of the cell, see Fig. 8.04 below.

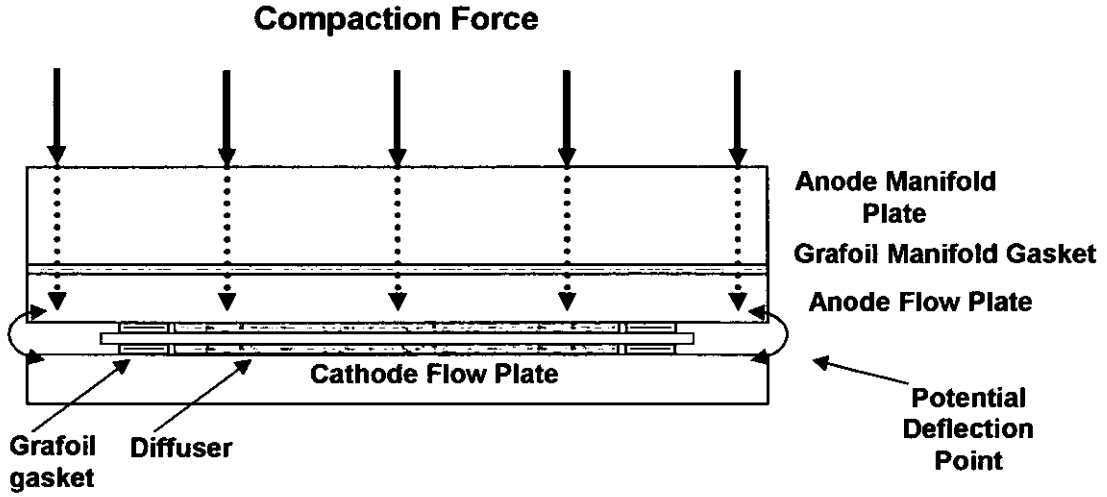

Fig 8.04 : Potential deflection points on cathode flow plate

This could not be corrected by allowing the Grafoil sealing gaskets to protrude from the side of the MEA to provide support as this would cause an electrical short between anode and cathode. Instead, the deflection risk was minimised by design of the 0.5 mm thick Grafoil manifolding gaskets located between rear of the graphite plates and the stainless steel manifold blocks so that there was minimal compaction pressure on unsupported plate areas.

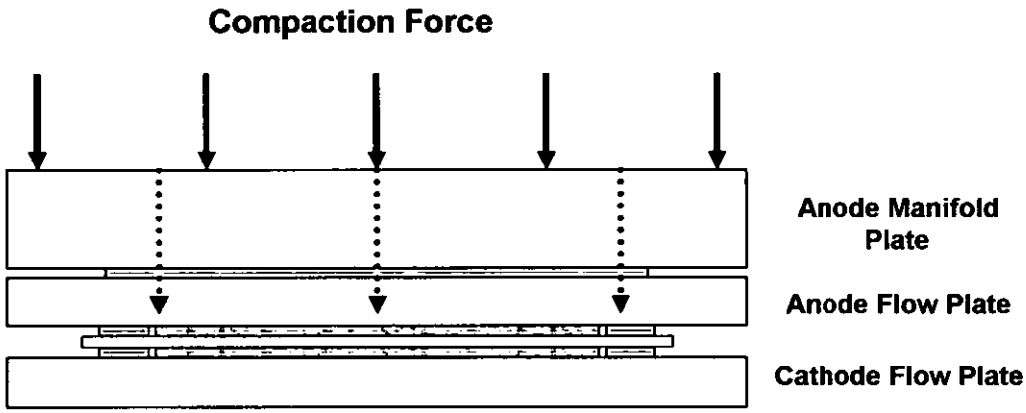

Fig 8.05 : Minimisation of deflection points on cathode flow plate by alteration of manifold

As the porting holes in the manifold blocks and the graphite plates were located outside a supported area, there were small winged features to cover these, and maintain the sealing integrity, see Fig. 8.06 below.

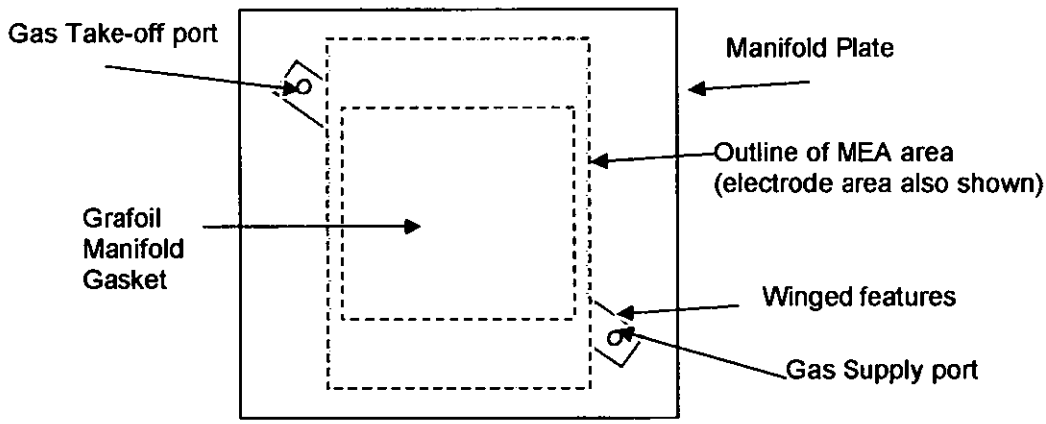

Fig. 8.06: Winged features on Grafoil sealing gaskets

At the smaller diffuser working dimensions, calliper measurement on the inner edge of the flow plates would be difficult, therefore, edge features were machined in the anode and cathode manifold blocks so that the callipers could measure around the outer edge of the flow plates instead.

The Grafoil sealing gasket area had to be reduced as much as possible as this would reduce the total force needed to crush the diffusers to the required thicknesses. At all times, however, the water injection features located in the front face at the periphery of the cathode graphite flow plate active area, refer to appendix E, had to be under compressive load in order for the water injection mechanism to distribute water evenly to each track. Therefore the Grafoil sealing gasket had to cover this area on both sides of the fuel cell. It was also critical that the Grafoil gaskets on either side of the MEA did not come into contact, causing an electrical short

The small cartridge heaters in the compression/heating block were replaced as they were occasionally causing an earth fault, tripping the RCD of the lab electrical ring circuit on being supplied with power. Therefore, new units were purchased and installed which eliminated the problem.

The components of the active fuel cell were isolated from the other rig components using an electrically insulating heat conducting mat between the anode current collector/flow plate and heater plate and a sheet of glass reinforced silicone between the base piece and the cathode current collector/ flow plate.

8.2.2.3 Operational control, Data acquisition & software

It was necessary to record data from the fuel cell over considerable operational periods, with the important parameters being potential, current, temperature and cathode pressure drop.

For the acquisition of data, a DaqPad was available (MIO-16XE-50) capable of processing 8 differential analogue inputs and also supplying a digital 5-volt output. The analogue inputs to the DaqPad were as follows:

- The potential of the cell as read from 2 mm probes fitted into recesses in the side of the anode and cathode graphite flow-field plates.
- The current was measured by probing the potential difference over a current shunt connected between the load unit and the cell.
- The fuel cell temperature, measured using a K type thermocouple inserted into a recess in the anode graphite plate. A reference LM-35 temperature sensor was used for cold junction compensation
- The pressure of the cathode inlet and exhaust lines were measured by two small Druck pressure transducers, rated for a maximum operating pressure of 400 mbar.g and were powered by a 12 Volt dc power supply.

The temperature of the fuel cell was controlled using a mains ac power supply with an in-built switching mechanism which compared a temperature set-point, input via a digital LED interface, with a reading from a second K type thermocouple in the anode plate. If required, a fan, directed onto the large cathode manifold block, could reduce the fuel cell temperature.

To drop out the 'active' load and prevent the fuel cell from electrolysing, a 24 V rated contactor was fitted between the anode current lead and the load unit. This would be tripped if the potential of the fuel cell dropped below a pre-determined set-point. A small solenoid saver circuit was used so that the 24 V potential initially used for closing the contactor was scaled down, after a few seconds to 12 V, sufficient to hold the switch in position. This prevented the contactor becoming hot during long periods of fuel cell operation. The supply of power to the contactor via the saver circuit was switched by the 5 Volt digital output signal from the DaqPad.

The hydrogen and air flowrates to the fuel cell were manually controlled using the Aera mass flow control equipment and the current drawn controlled by the galvanostatic load

unit, both of which were previously utilised in Chapters 3, 4 and 6. The supply of water for direct injection to the fuel cell cathode was again from a pure HPLC bottled source.

The display and control software was written using the Testpoint graphical programming language - a screenshot of the main operational display screen is illustrated in Fig 8.07.

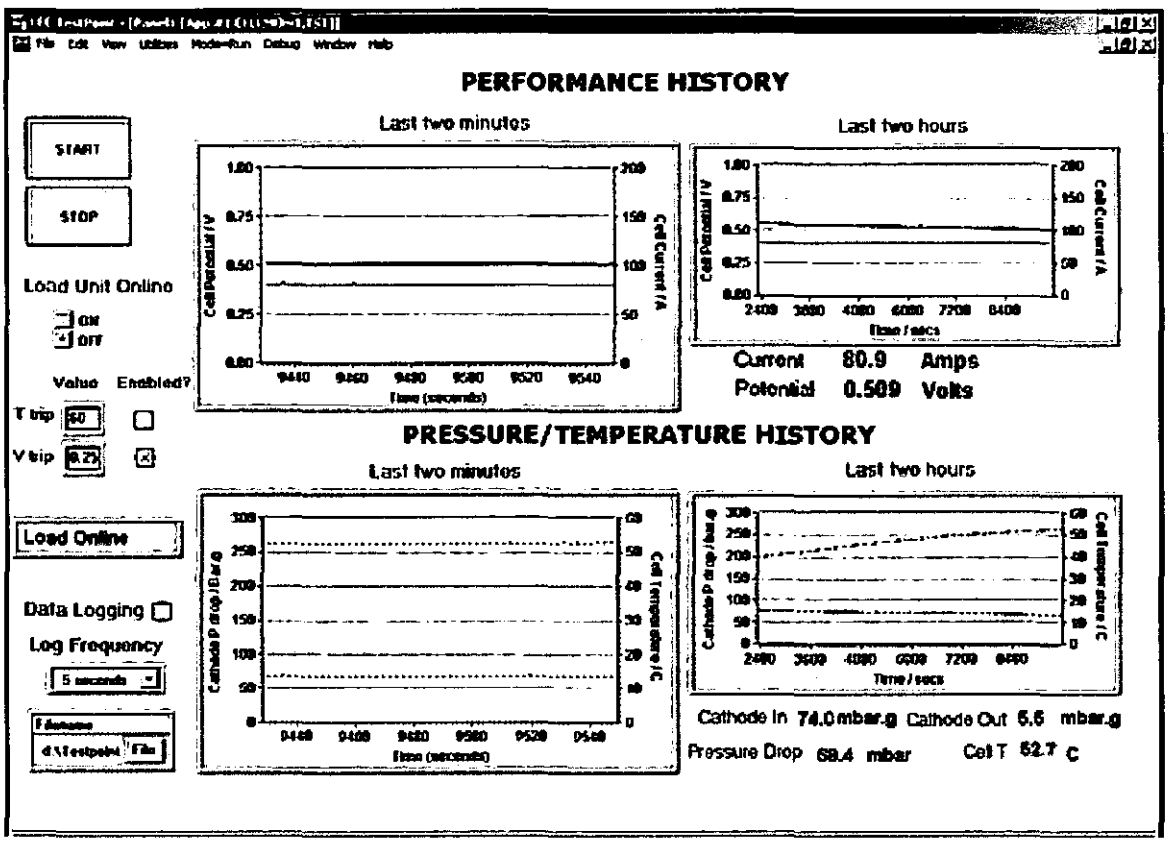

Fig. 8.07 Screenshot of Testpoint program for fuel cell monitoring

This displayed the present fuel cell operational parameters in the form of alphanumerical digital displays and historical data, for both the previous two minutes and two hours on constantly updated strip charts. A load-tripping feature, triggered by either high temperature or low voltage, allowed the fuel cell to operate unattended. On the left-hand side of the screen, the temperature and potential trip values could be altered while the program was running. When the fuel cell current dropped, or cell temperature rose, below or above the respective set-points the contactor on the load unit was opened. The contactor could be manually opened and closed by the 'Load Unit Online' button selection. The small message screen displayed the current status of the fuel cell in red text. The software also allowed a data logging frequency to be selected which could be altered without interruption to the data logging process.

Logic diagram for Testpoint program

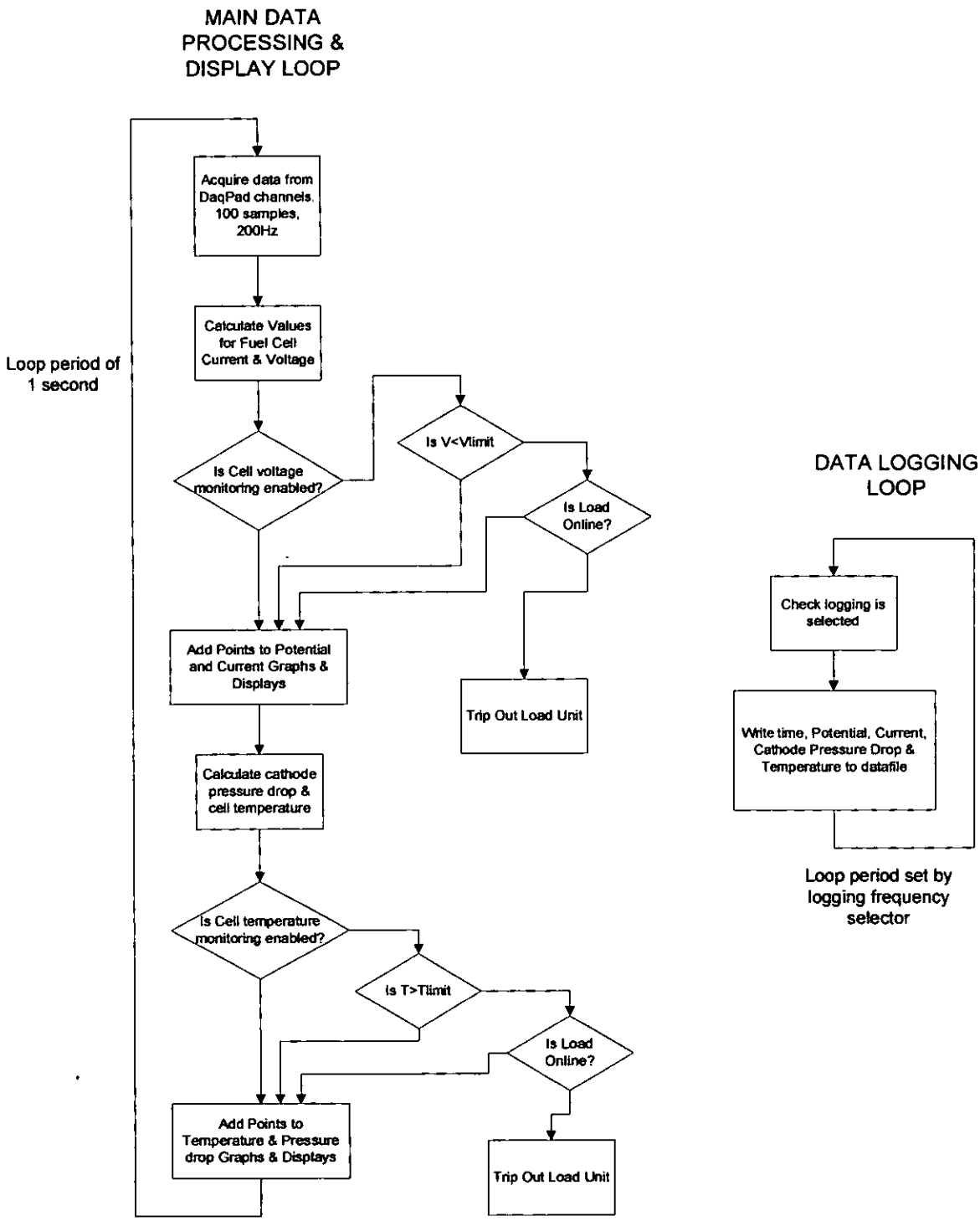

Fig. 8.08 Logic for Testpoint program

8.2.2.4 Procedure for cell assembly

The first step in the assembly of the fuel cell was preparation of the electrically conducting Grafoil manifold gaskets, which were to be positioned between the rear of the graphite flow plates and the current collector / manifold blocks. The current collector face of both manifold blocks were cleaned using an IPA based solvent cleaner. A Perspex template and scalpel were used to cut the manifold gasket shape, containing the winged features, from a sheet of 0.5 mm Grafoil. The gasket was treated with a light application of spray mount and positioned in place on the manifold blocks, using the gas port holes to obtain the correct alignment.

The next requirement was to assemble an integrated MEA containing the diffuser pieces and the 0.35 mm Grafoil sealing gasket. This was done due to the size difference between the graphite plates and MEA, which made the accurate positioning and adjustment of individual components very difficult. A perspex template was used to cut the sealing gasket shapes from a roll of 0.35 mm Grafoil. The sealing gaskets were spray mounted and precisely positioned on the sub-gasket area of the MEA, relative to the active electrode. The diffuser pieces were then cut with a small amount of spray mount applied to the corners and positioned on to both electrode areas of the MEA. The fuel cell was then built up on top of the cathode manifold block, i.e. cathode flow plate, MEA, anode flow plate, anode manifold block, compaction block, springs and press plate.

On disassembly of the fuel cell to test another diffuser combination, both the Grafoil manifold and sealing gaskets had to be re-cut and the MEA replaced. Although time consuming this was absolutely necessary as due to the nature of Grafoil, it would not return to its original dimension and risked poor sealing integrity if re-used. More importantly, it tended to adhere to the respective surfaces and break on any attempt of fuel cell disassembly, thus it had to be completely scraped off the current collector side of the manifold blocks and the flow-field side of the graphite plates.

Flow diagram of equipment

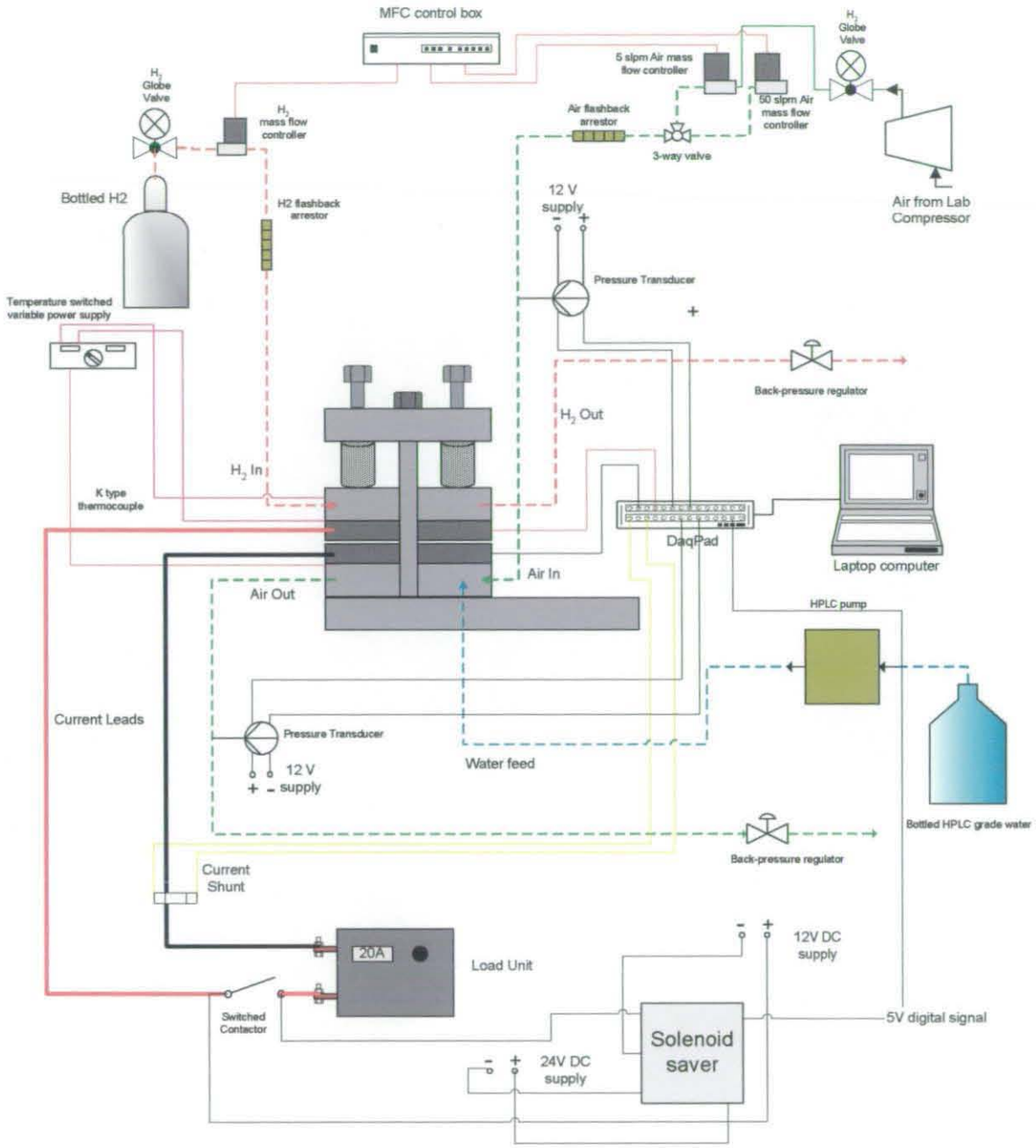

Fig. 8.09 Flowchart of equipment

8.2.2.5 Photographs of rig

Some photographs of the assembled rig are shown below:

Side view

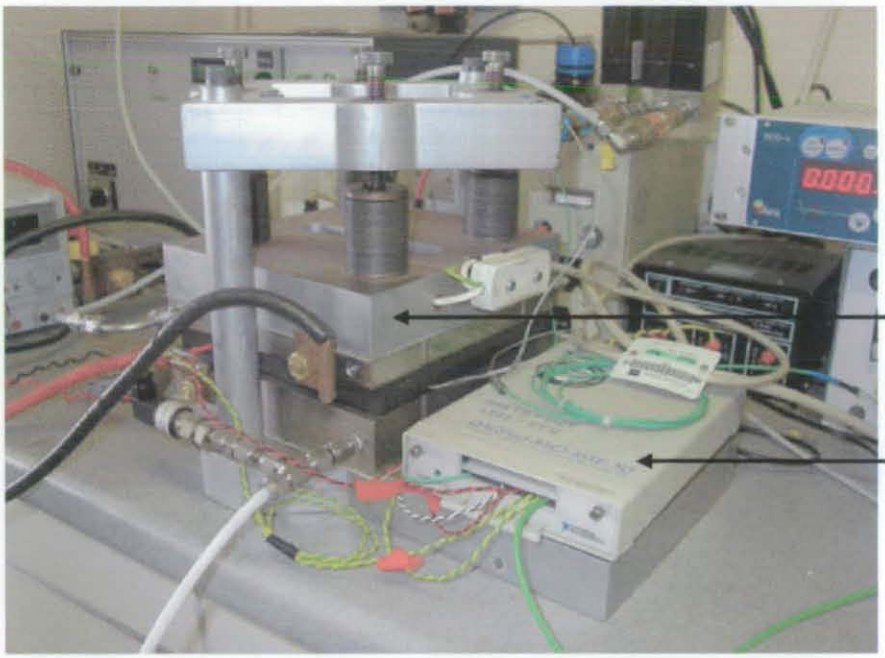

Fig 8.10 Side view of fuel cell rig

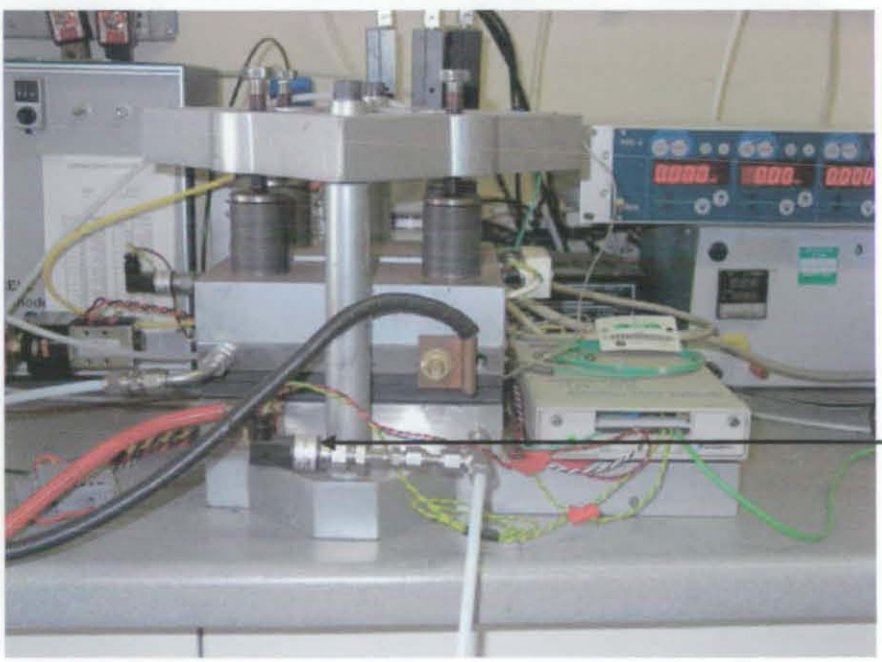

Fig. 8.11 Front view of fuel cell rig

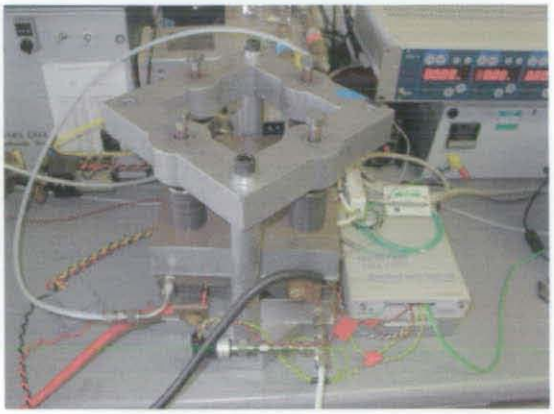

Fig. 8.12 Top view of rig

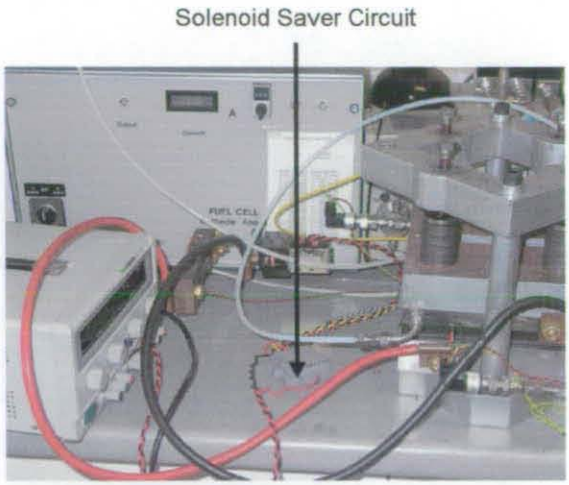

Fig. 8.13 Shifted view

Fig. 8.14 Overall view of rig

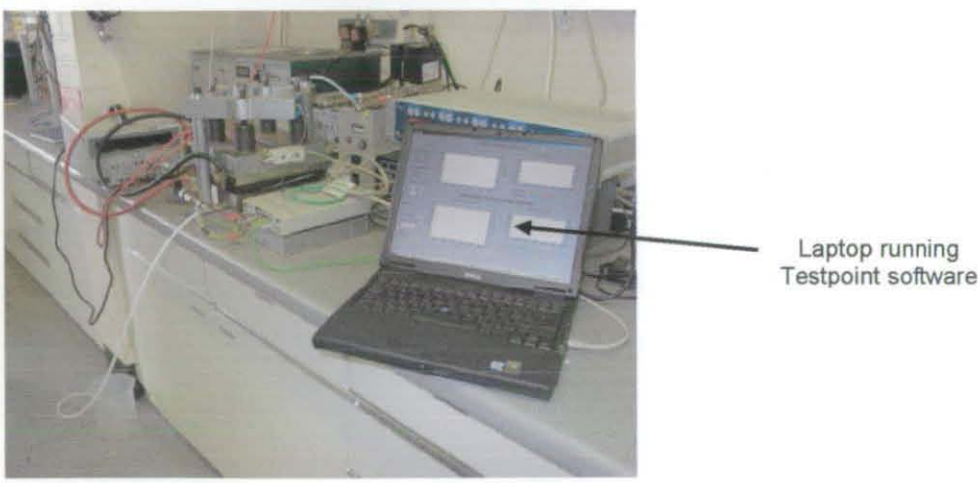

Fig. 8.15 View including Display software

8.3 Results

8.3.1 Test description

In each current shift test the fuel cell current was shifted from open circuit conditions, zero Amps, to a middle-range load of 80 Amps, equivalent to a current density of 0.4 Amp/cm^2, and fixed at this point for at least two hours. Open circuit conditions were maintained for approximately 15 minutes to obtain equilibrated conditions.

It was important that the rise in the cathode pressure drop could not be attributed to any change in the fuel cell operating conditions (i.e. temperature, reactant flow rates, water injection rates) after the shift in current to 80 Amps. Therefore at open circuit, the water and gaseous reactants were delivered to the fuel cell in the correct proportions for 80 Amps and this did not change for the duration of the test. As the fuel cell was maintained at 50°C by the compression/heater block at open circuit, water was injected to 100%RH so that the MEA did not become dehydrated due to dry gas flow and result in damage.

Looped polarisation curves are also obtained to characterise the fuel cell performance with the cathode diffusers at the particular working dimensions. The pre-testing procedures as detailed in appendix C are used to check for leaks or MEA damage before each period of operation. At all points in the testing, the air stoichiometry is fixed at 3 and the hydrogen stoichiometry at 1.5 with a counterflow configuration of hydrogen and air gases used.

8.3.2 Carbel CL – Carbel CL combination

Current shifts

The first fuel cell build utilised the reference diffuser combination of Carbel CL on both sides of the MEA. The following chart, Fig. 8.16, shows the data from the current shift test with the thickness of Carbel calculated to be 0.34 mm on the cathode - equivalent to 89% of its uncrushed dimension. The current drawn by the load unit is displayed by the red dashed plot and the cathode pressure differential, measured in mbar, as a blue plot, both of these scales read off the left-hand y-axis. The potential from the fuel cell is displayed as a black plot, and the scale read from the right-hand y axis.

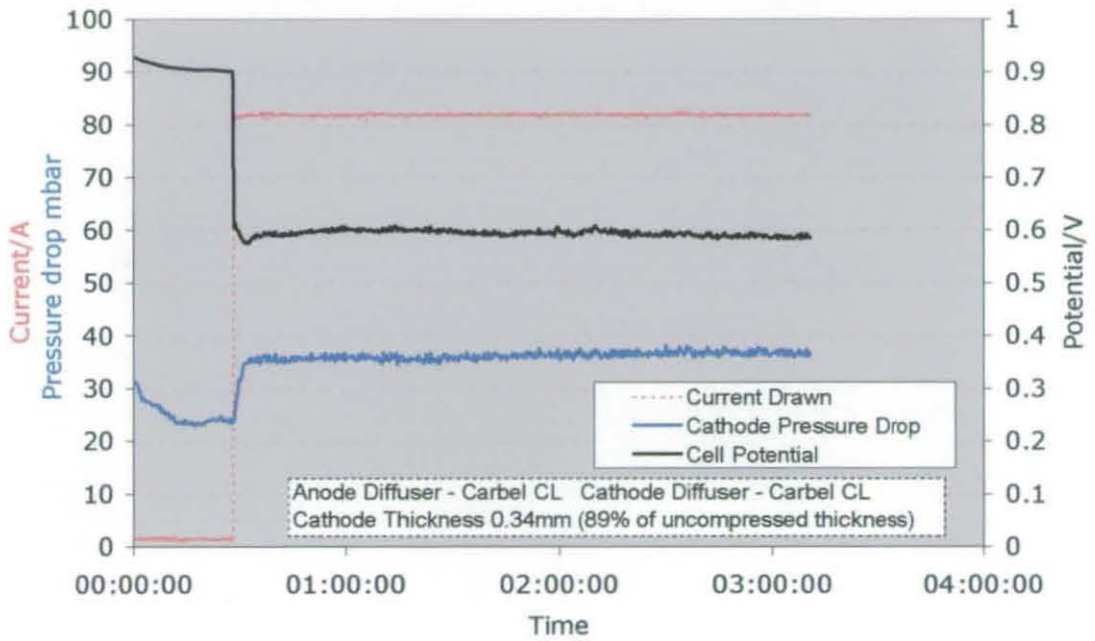

Fig. 8.16: Fuel cell potential and cathode pressure drop data from current shift test with Carbel CL at a thickness of 0.34 mm

At the beginning of the test, the fuel cell reaches equilibrated conditions at open circuit with a potential of approximately 0.90 V with the cathode pressure drop at 24 mbar. Approximately 30 minutes following the start of the test, a current of 80 Amps was drawn, the potential dropped immediately and the pressure drop rose sharply for 5 minutes as product water began to fill the inner pores of the diffuser. The value of the pressure drop then oscillated at approximately 36 mbar for the remainder of the test. These oscillations reflect the liquid water being continually flushed out of pores and then re-accumulating, i.e. the same effect observed in the endurance thermal mapping plots in Chapter 4. The potential value is observed to hold a steady value of 0.6 V for the remainder of the test, with very small oscillations.

In the next chart, Fig.8.17, further compaction force has been administered to the fuel cell by an increased tightening of the compaction bolts and the Carbel has been crushed to a dimension of 0.3 mm on the cathode, equivalent to 79% of the original thickness.

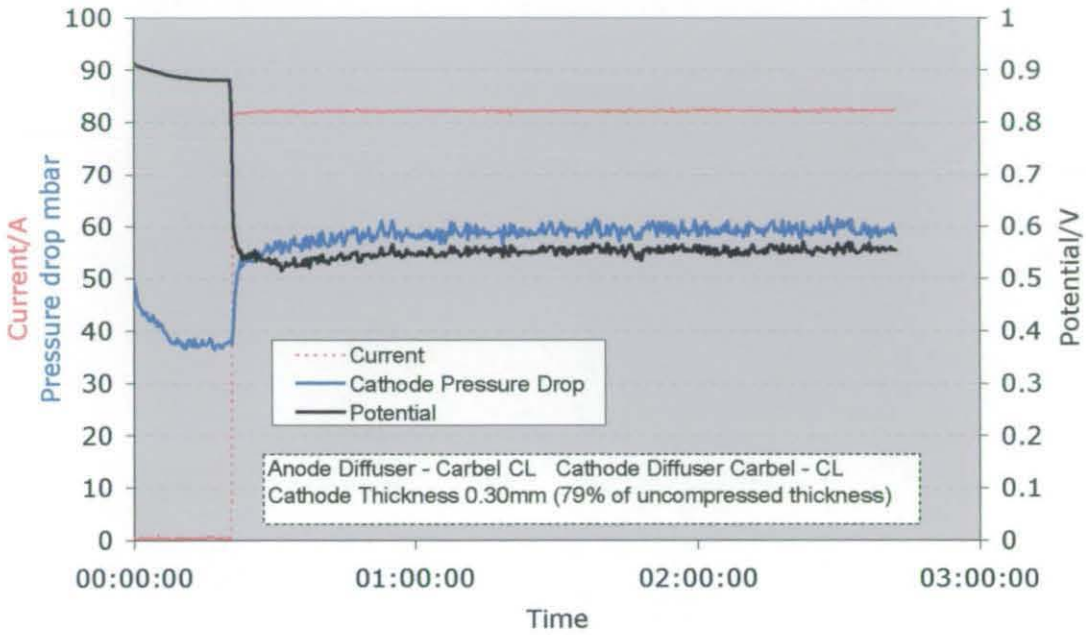

Fig. 8.17: Fuel cell potential and cathode pressure drop data from current shift test with Carbel CL at a thickness of 0.30 mm

With equilibrated open circuit conditions, the pressure drop is seen to be higher than that observed in Fig 8.16, at approximately 37 mbar with the potential lower, now at 0.88 V. On drawing 80 A current, again a sharp rise in pressure drop is observed as product water fills the pores. However, here it takes approximately 30 minutes for the cathode pressure drop to settle around 59 mbar. It is observed that the oscillations of pressure drop value are larger than in Fig. 8.16, which is also reflected in the behaviour of the cell potential, which has a lower average value than Fig. 8.16, at around 0.56 V. This shows a strong link between the oscillations of the pressure drop and the potential value, confirming increasing variations in the transport rates of oxygen to catalyst sites with a lower permeability of the diffuser material.

The final current shift test using Carbel CL on the cathode is illustrated in Fig. 8.18. Further compaction force has been exerted so that the calculated cathode diffuser working dimension is 0.275 mm, equivalent to 72% of the original thickness.

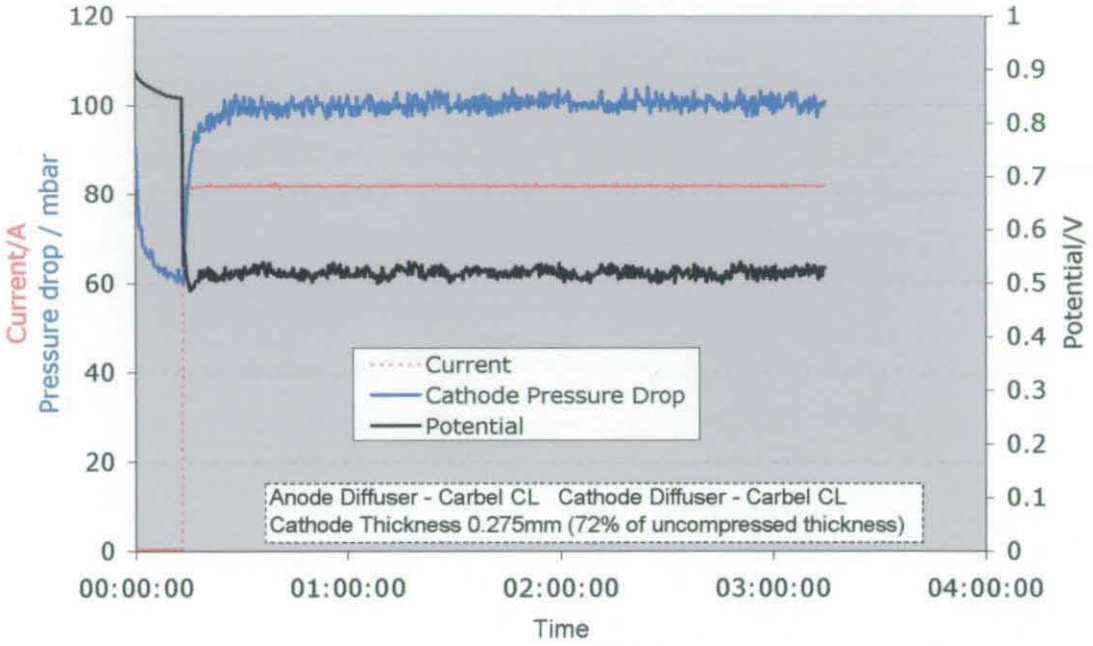

Fig. 8.18: Fuel cell potential and cathode pressure drop data from current shift test with Carbel CL at a thickness of 0.275 mm

With equilibrated open circuit conditions, the pressure drop is again higher, at approximately 61 mbar, with the potential lower, now at 0.85 V. On drawing current there is again a sharp rise in pressure drop as product water fills the pores, taking 15 minutes for the value to settle at approximately 100 mbar, with the oscillations again larger.

The oscillations in potential are larger than previous but now show another previously unseen behaviour, displaying large sinusoidal waves. This was due to the slow response of the fuel cell temperature control system which cycled between 48°C and 55°C over twenty minute periods. The appearance of this sinusoidal shape at this Carbel dimension suggests the fuel cell is less able to regulate its temperature than at lower compaction loads i.e. water cannot be evaporated so readily at this diffuser dimension. Over the whole test period drawing 80 Amps, the approximate value of the potential was 0.52 V.

Polarisation plots

The following polarisation plots were obtained from the fuel cell using varying Carbel CL diffuser dimensions, as shown in Figs. 8.19 - 8.21.

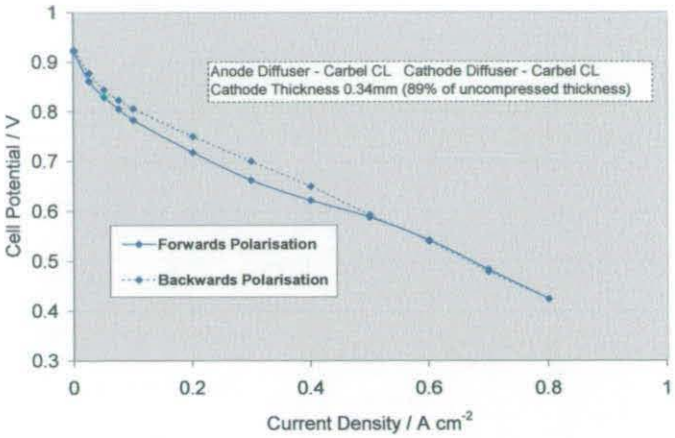

The potential values are similar at higher current densities for the forwards and reverse sweeps. However at lower current densities the backwards sweep produces higher potential values.

Fig. 8.19 Polarisation plot with Carbel CL at 0.34 mm

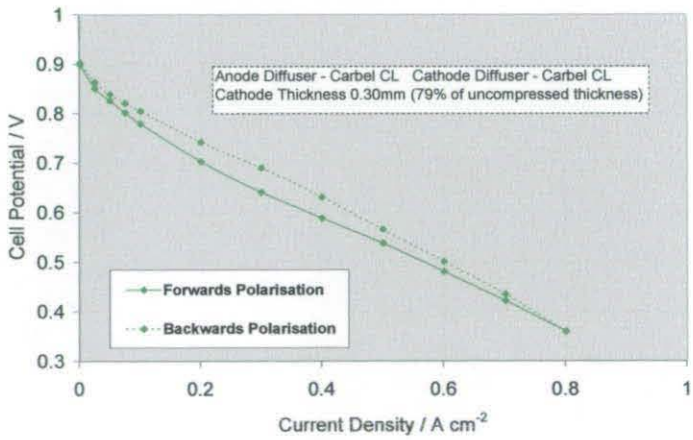

The open circuit potential has dropped and all reverse sweep potential values are greater. The overall performance is slightly lower.

Fig. 8.20 Polarisation plot with Carbel CL at 0.30 mm

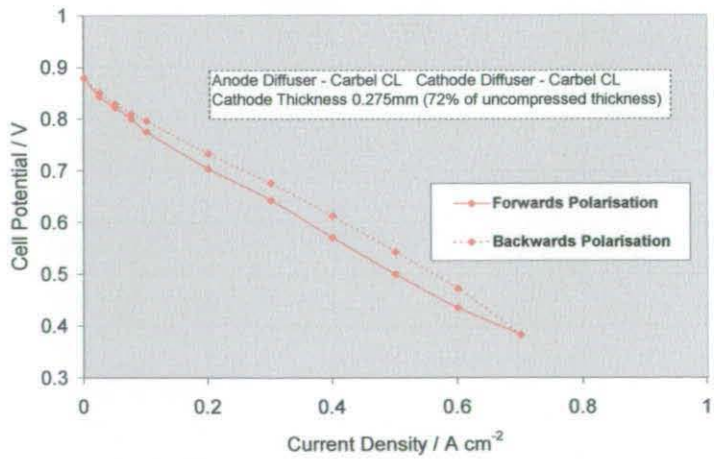

This shows similar behaviour except all potential values have fallen further.

Fig. 8.21 Polarisation plot with Carbel CL at 0.275 mm

8.3.3 SGL 30BB - SGL 10BB combination

Current Shifts

The next series of current shift tests were done using a diffuser combination of SGL 30BB on the anode and SGL 10BB on the cathode side. The following chart, Fig. 8.22 shows results using SGL 10BB at a calculated thickness of 0.41 mm on the cathode of the fuel cell, equivalent to 93% of the original dimension. The same format for the graphs detailed as in the Carbel CL tests is used.

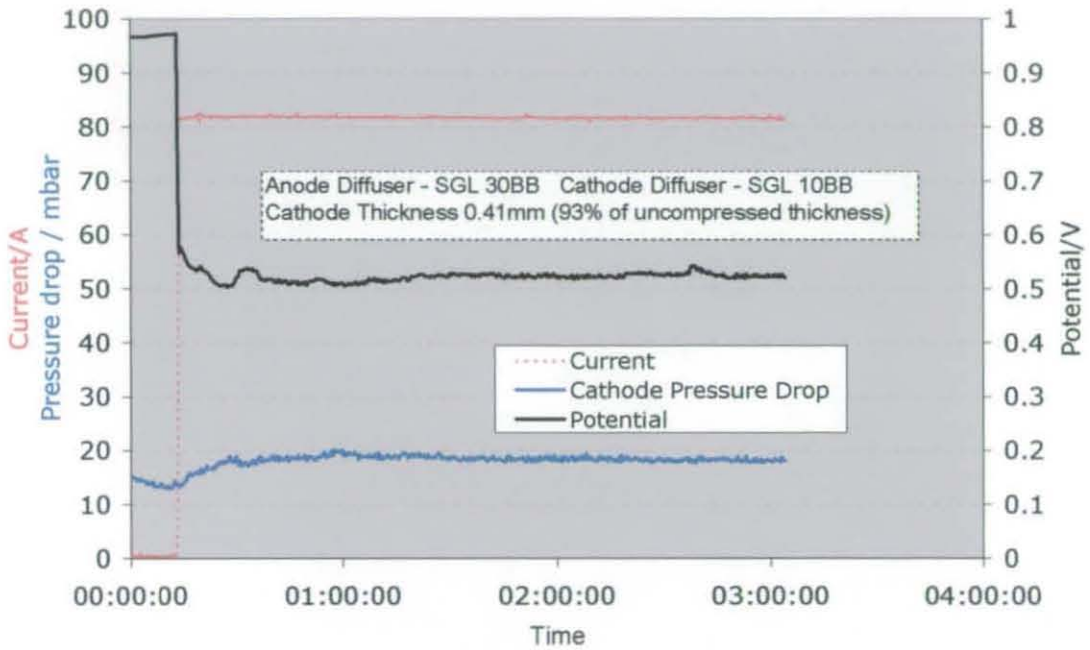

Fig. 8.22: Fuel cell potential and cathode pressure drop data from current shift test with SGL 10BB at a thickness of 0.41 mm

The fuel cell reaches equilibrated open circuit conditions with the potential at 0.97 V and the cathode differential pressure drop measured at 13 mbar. On drawing current there is an immediate drop in potential accompanied by a small and gradual rise in the cathode pressure drop value, taking 30 minutes to settle at approximately 18 mbar. The oscillations in both potential and pressure drop are very small indicating fixed rates of oxygen transport. The fuel cell potential is approximately 0.53 V and the cathode pressure drop is approximately 18 mbar.

The next chart, Fig. 8.23, shows results from the current shift test after the fuel cell has been further compressed, with an SGL 10BB cathode diffuser thickness of 0.39 mm, equivalent to 88% of original thickness.

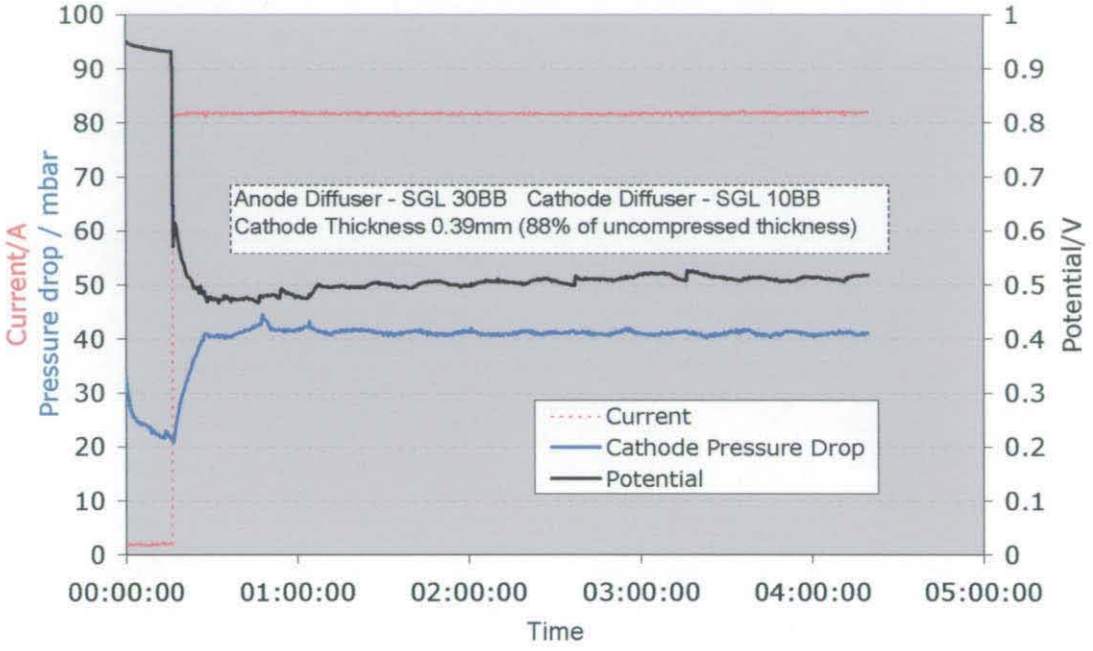

Fig. 8.23: Fuel cell potential and cathode pressure drop data from current shift test with SGL 10BB at a thickness of 0.39 mm

The equilibrated open circuit value of potential is 0.93V and the cathode pressure drop is 22 mbar. After the current shift, the cathode pressure drop settles, on a value of 41mbar and the potential on a value of 0.52 V. It is noticed that the sinusoidal waves, caused by the fuel cell temperature control, are inversely related in the potential and pressure drop plots. This is due to a greater level of water being able to be evaporated at the higher temperature, thus reducing the pressure drop.

The fuel cell was then further compressed to a SGL 10BB cathode diffuser thickness of 0.37mm with the data from the current shift test shown in Fig. 8.24.

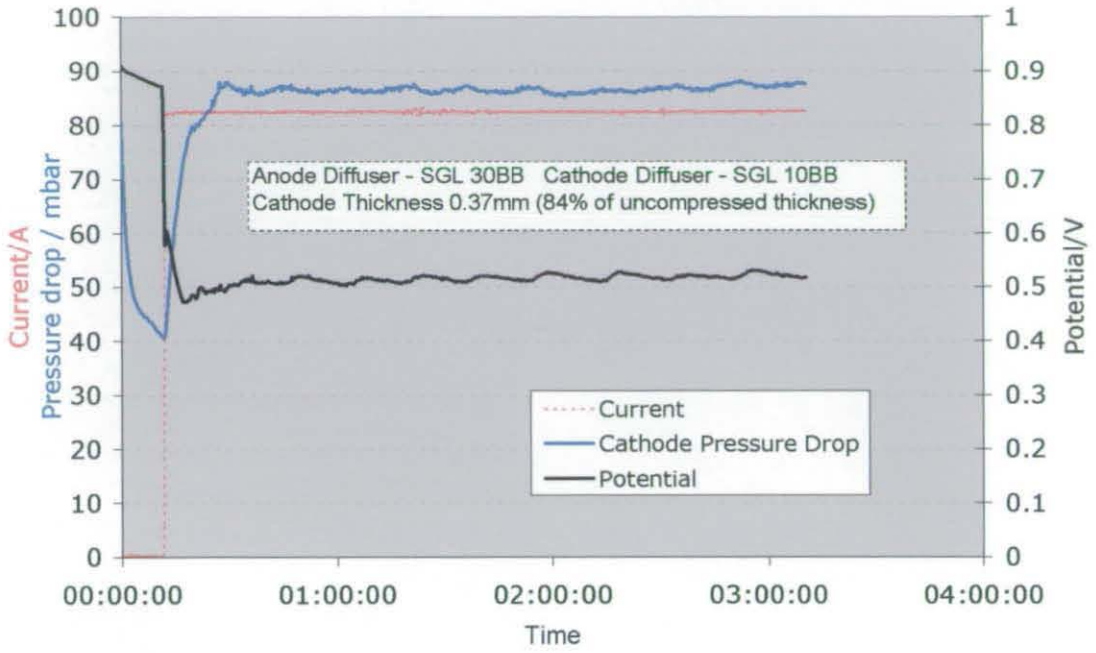

Fig. 8.24: Fuel cell potential and cathode pressure drop data from current shift test with SGL 10BB at a thickness of 0.37 mm

The equilibrated value of open-circuit potential has fallen to 0.87 V and the cathode pressure drop is now 41 mbar. On drawing 80 Amps current there is a much more rapid jump in pressure drop, which settles at 85 mbar, however, the equilibrated potential has a similar value to Fig. 8.23, at 0.52 V. The sinusoidal waves are more obvious here than in the previous plot.

The fuel cell was then compressed for a final time to produce a SGL 10BB cathode diffuser dimension of 0.35 mm; the current shift test data is shown in Fig. 8.25

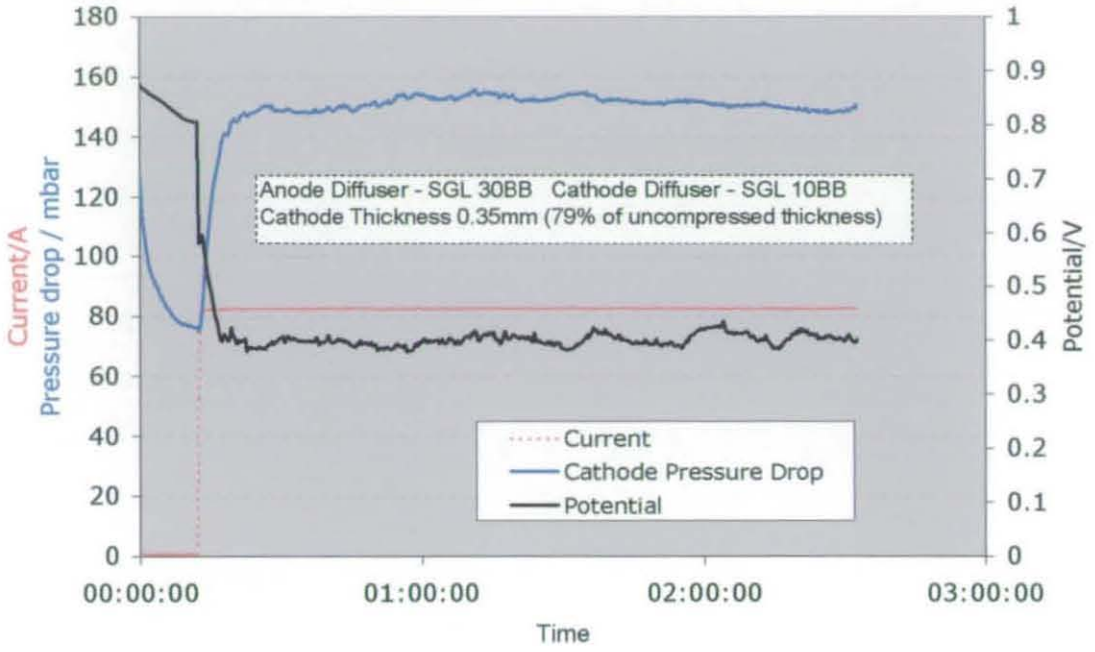

Fig. 8.25: Fuel cell potential and cathode pressure drop data from current shift test with SGL 10BB at a thickness of 0.35mm

The open circuit potential is 0.806 V and the equilibrated cathode pressure drop is approximately 76 mbar. On drawing current from the fuel cell the cathode pressure drop rises to around 150 mbar and the potential drops to an approximate value of 0.4 V. However, the performance of the fuel cell is clearly unstable, as reflected in the small oscillations in the value of potential; however, these are not as large as those observed when using Carbel CL, Figs. 8.16 – 8.18.

Polarisation Curves

The following polarisation plots were obtained from the fuel cell with the various SGL 10BB cathode dimensions, as shown in Fig. 8.26 - 8.29

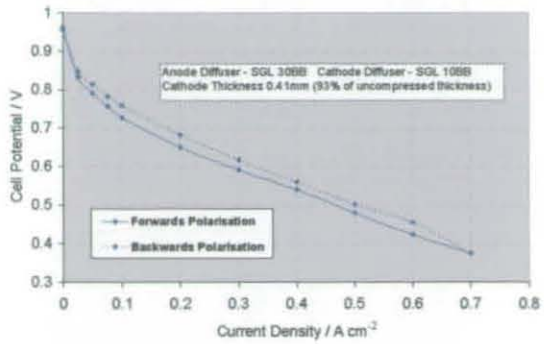

Fig. 8.26 Polarisation plot - SGL 10BB at 0.41 mm

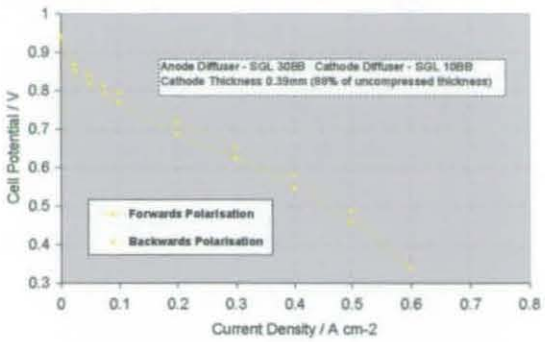

Fig. 8.27 Polarisation plot - SGL 10BB at 0.39 mm

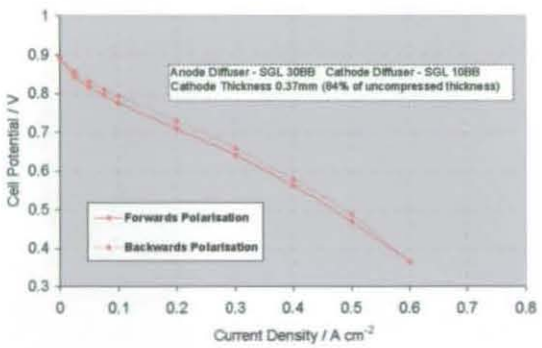

Fig. 8.28 Polarisation plot - SGL 10BB at 0.37 mm

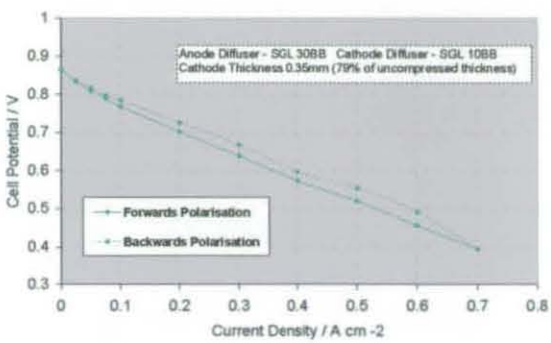

Fig. 8.29 Polarisation plot SGL 10BB at 0.35 mm

The polarisation plots do not show a lot of variation but the reverse current sweep always produces higher values of potential than for the forwards sweep. It is observed that none of the performances are as high as those that were obtained using Carbel CL.

8.3.4 SGL 30BB - SGL 31BC combination

The next series of results were obtained with a diffuser combination of SGL 30BB on the anode and SGL 31BC on the cathode side.

The following chart, Fig. 8.30, shows the current shift test for SGL 31BC at a cathode dimension calculated to be 0.35 mm on the cathode of the cell – 92% of the original thickness. The same format for the data presentation shown previously is again used.

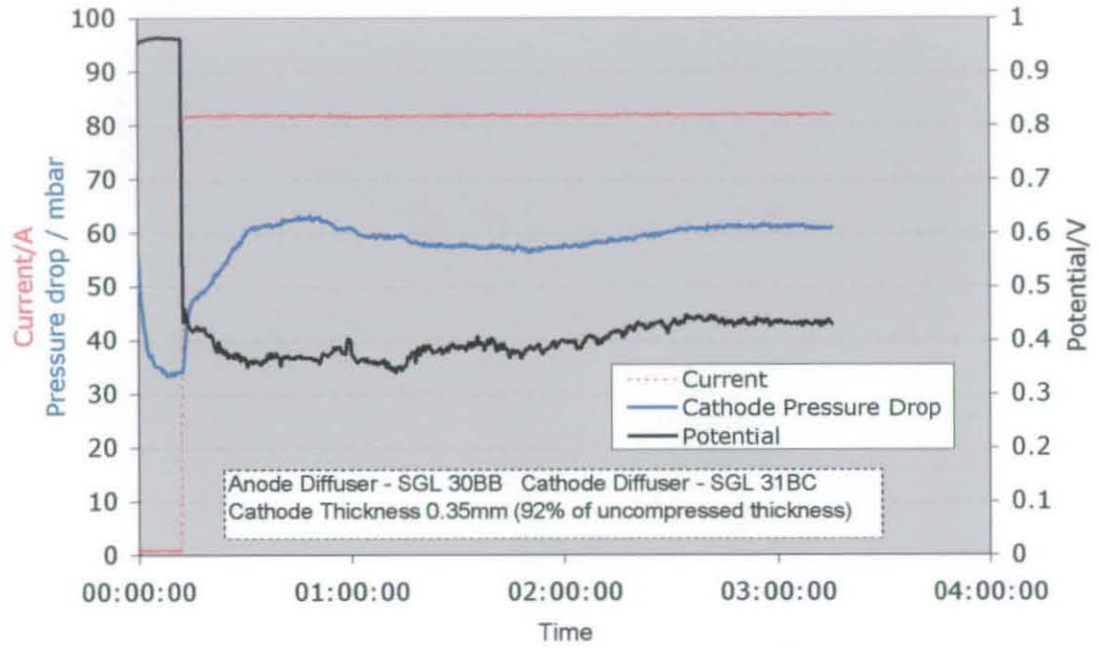

Fig. 8.30: Fuel cell potential and cathode pressure drop data from current shift test with SGL 31BC at a thickness of 0.35 mm

The fuel cell reaches equilibrated open circuit with the potential at 0.96 V and the cathode differential pressure drop measured at 34 mbar. On drawing current there is an immediate drop in potential accompanied by an initial sharp rise in pressure drop followed by a more gradual rise to around 60 mbar. The potential irregularly shifts around a value of 0.4 V over the following three hours

The next chart, Fig. 8.31, shows data from the current shift test with the fuel cell having been compressed to obtain a calculated cathode diffuser dimension of 0.33 mm - equivalent to 87% of original thickness.

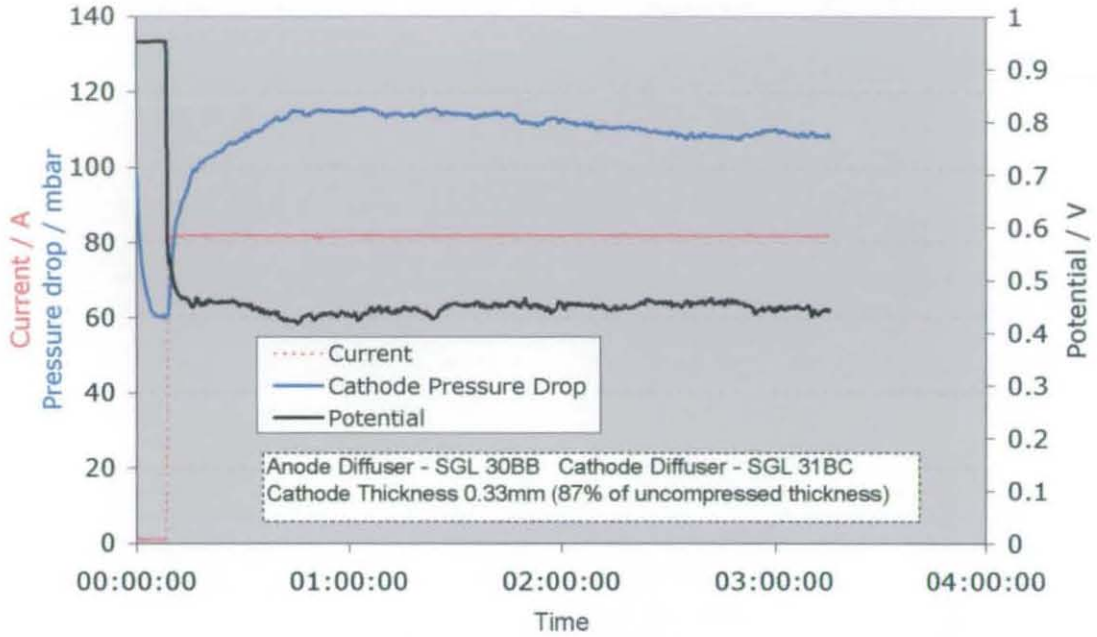

Fig. 8.31: Fuel cell potential and cathode pressure drop data from current shift test with SGL 31BC at a thickness of 0.33mm

The equilibrated cathode pressure drop has risen to approximately 60 mbar, but the open circuit potential has not changed, which is not been observed so far with the other cathode diffuser materials. After the current shift the pressure drop rises to 108 - 115 mbar with the potential around 0.45 V. This performance and its degree of oscillation have improved from Fig. 8.30.

The final chart was obtained with the fuel cell having been crushed a final time to obtain a cathode diffuser dimension of 0.31mm, 81% of original thickness.

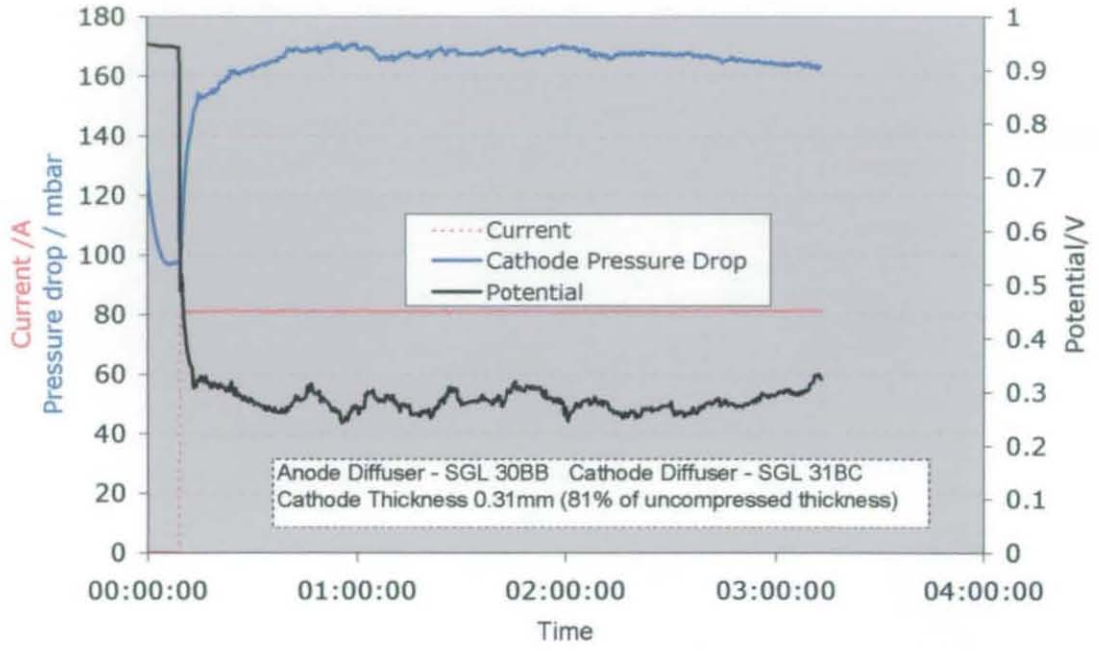

Fig. 8.32: Fuel cell potential and cathode pressure drop data from current shift test with SGL 31BC at a thickness of 0.31 mm

Again the open circuit potential has not shifted after the administering of further compaction pressure, however, the equilibrated pressure drop is now approximately 97 mbar. After the current shift the pressure drop is approximately 170 mbar and the potential has dropped in value and oscillating wildly at an approximate value of 0.25 V.

Polarisation curves

The following polarisation plots were obtained from the fuel cell with the SGL 31BC diffuser at varying cathode dimensions as shown in Figs. 8.33 - 8.35.

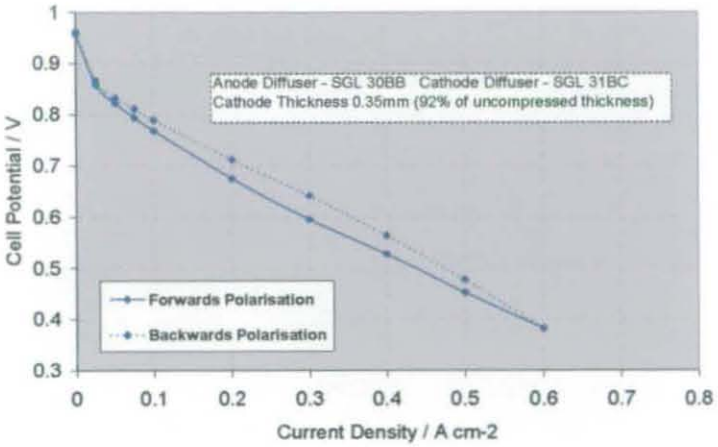

All backwards potential sweep potential values are greater.

Fig. 8.33 Polarisation plot with SGL 31BC at 0.35 mm

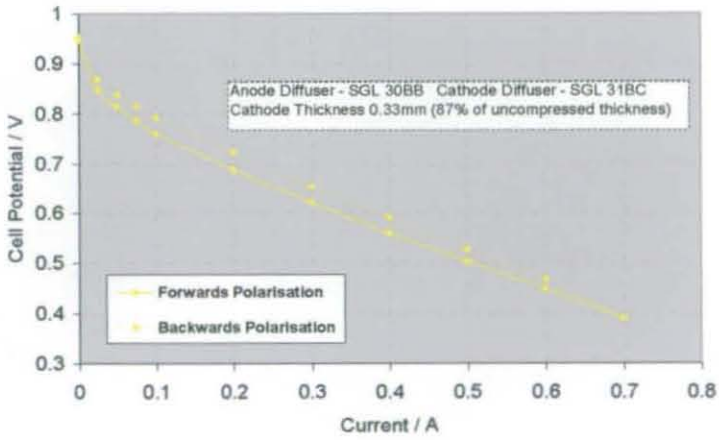

This polarisation curve shows an increased in performance from the previous plot.

Fig. 8.34 Polarisation plot with SGL 31BC at 0.33 mm

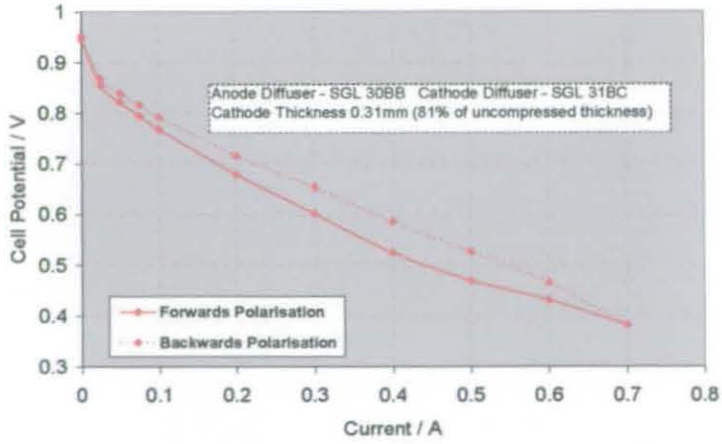

However, this plot shows a lower performance and a bigger difference between forwards and backwards sweeps. It is possible that, here, the lower permeability is allowing less injected water to reach the membrane.

Fig. 8.35 Polarisation plot with SGL 31BC at 0.31 mm

8.3.5 Final comparisons

The fuel cell potentials obtained at 80 Amps for the different cathode diffusers at different dimensions is shown in Fig. 8.36. These data have been averaged from the final two-hour period from the current shift testing and are accompanied by a trendline.

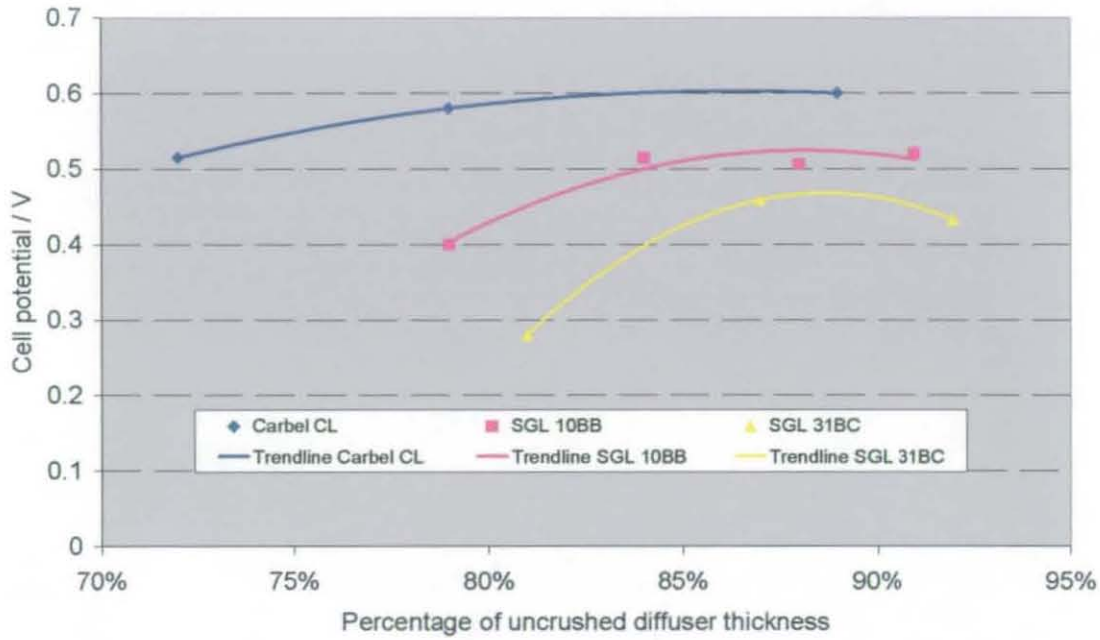

Fig. 8.36 Potential values at a drawn current of 80 Amps with different diffuser combinations

Each diffuser material plot displays a distinctive peak potential for steady-state performance at 80 Amps. The poorest performing cathode diffuser material is SGL 31BC, which in Chapter 7 was shown to exhibit low permeability on compaction due to the weak structure. It is likely this low permeability is responsible for the low performance seen here. The best performing diffuser is Carbel CL which has a peak performance around 85% of the original thickness.

The differential cathode pressures obtained at open circuit conditions and 80 Amps with the different cathode diffusers at various dimensions is shown below in Fig. 8.37 – again these data are the average over the final two-hour period from the current shift tests.

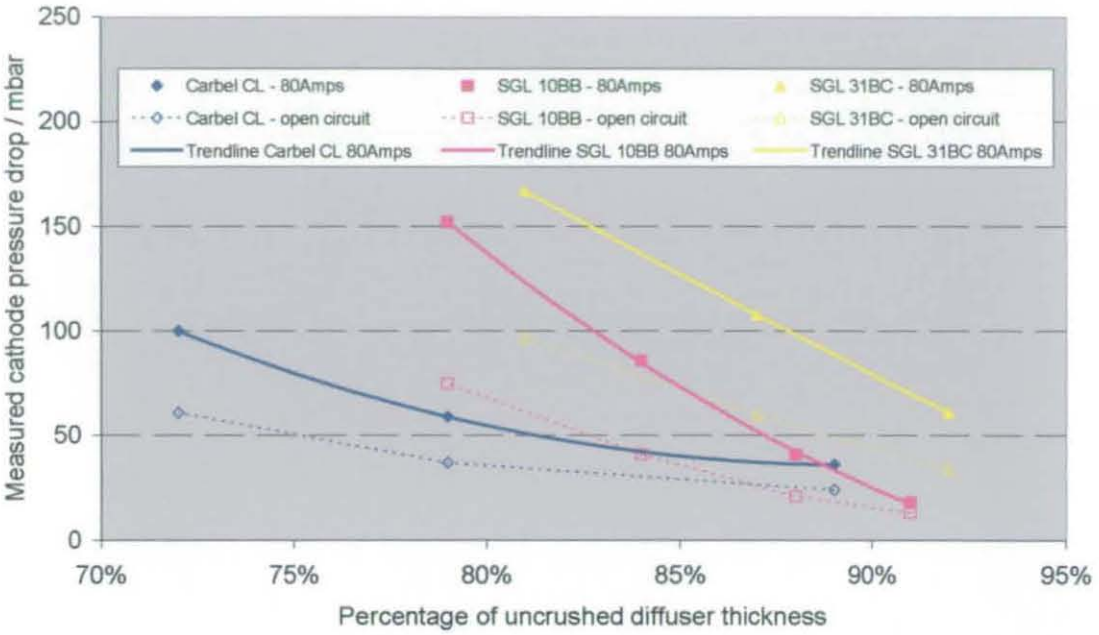

Fig. 8.37 Cathode pressure drop over the fuel cell at 80Amps for all diffuser combinations

It is observed here how the Carbel CL produces the lowest pressure drop out of the three cathode diffusers tested. The SGL 31BC produces a higher pressure drop than the SGL 10BB which confirms the results presented in Chapter 7. However, the Carbel CL produces a lower 'operational', i.e. at 80 Amps, pressure drop than expected. Of all the diffusers, it has the smallest difference between the pressure drops open circuit and at 80 Amps. This indicates a lesser degree of water accumulation in the diffuser pores than experienced with the two SGL materials.

The substrate and microdiffuser PTFE content of Carbel CL is proprietary so it is difficult to make conclusions from these results; however, both SGL materials have 5% PTFE in the substrate structure and 23% in the microdiffuser layer. If the Carbel CL contains a higher level of PTFE in either, this could explain the superior water management characteristics.

8.4 Conclusions

Several cathode diffuser materials were tested in an EC fuel cell with the interdigitated flow field at a temperature of 50°C. The main conclusions are summarised as follows:

- For the limited range of materials and working dimensions tested, none of the alternative SGL diffuser materials performed as well as Carbel CL, either, in terms of a lower cathode pressure drop, or, a higher electrochemical performance.

- The ex-situ testing had predicted that lower cross-plane pressure drops would be obtained by using the SGL materials. Therefore, the large in-situ pressure drops measured at open circuit conditions when using the SGL cathode diffuser materials can be attributed to the influence of through-plane pressure drop on the overall measurement.

- Referring to Fig. 8.37, differing degrees of water management of each diffuser, was confirmed by the difference in cathode pressure under open circuit conditions and drawing a current of 80 Amps. This difference was also shown in the degree of the oscillations experienced in the pressure drop value in the few hours after the current shift.

- The large oscillations exhibited by Carbel CL were reflective of the carbon cloth weave structure, with the large pores being continually filled and then flushed out with liquid water

- In all polarisation curves, the backwards sweep showed superior performance indicating that the membrane did not achieve optimum water content under the steady-state fuel cell operating conditions.

- In the majority of the polarisation curves, the performance was lowered with additional compaction pressure applied to the fuel cell. If an alternative material to graphite had been used for the flow plates, e.g. stainless steel, the lowering of surface resistance with compaction would have influenced this result

Further work

Further study would be advantageous as the work here represented a limited range of materials and conditions for the study of cathode pressure drop in an EC fuel cell. In particular, it would be interesting to carry out the same tests using SGL diffuser materials containing a higher PTFE content to discourage the presence of water underneath plate ribs. It is anticipated that this would increase the electrochemical performance and lower cathode pressure drop due to the superior water management characteristics and the extra PTFE content also reinforcing the structure for a set compaction load, thus increasing material permeability.

The observation of cathode pressure drop slowly rising as water accumulated in the diffuser pores gave possible scope for the development of techniques to keep this pressure drop low by occasionally 'pulsing' large amounts of air through an EC fuel cell cathode. If this was effective in removing the presence of water from the outer diffuser layers, it may even be possible to use the low-pressure drop parallel flow-field without the penalty of electrode flooding.

Chapter 9:

Conclusions

9.1 Conclusions

This thesis investigated the concept of a PEM fuel cell which utilised a combined humidification and cooling mechanism based on the direct injection of liquid water to the cathode flow-field. This 'EC – evaporatively cooled' design would eliminate the weight and volume penalties of conventional plate-based thermal control and water management sub-systems in PEM fuel cell stacks. From the work detailed, the following conclusions can be made

- Prior to an initial humidification study, it had been proposed that a PEM fuel cell utilising an MEA containing an ultra-thin reinforced membrane may have been sufficiently humidified by product water from the fuel cell reaction, thus allow 'dry' operation. However the results from this study indicated that the fuel cell performance was severely affected by dehydration of the membrane structure due to the evaporation effect of the reactant gases, with the extent of the membrane dehydration shown to obey the law of gas partial pressures.

- Following this, a liquid water injection mechanism was designed and built into the cathode of a PEM fuel cell. This was found to give slightly poorer performance than pre-saturation of the air by steam and was due to the hydrophobic diffuser preventing a large proportion of the injected liquid water reaching the membrane structure, and hence a low membrane hydration state was achieved. However, the fuel cell coped with large excesses of injected water which was partially due to the use of an interdigitated flow-field on the cathode.

- This cathode water injection mechanism was then utilised as a combined cooling and humidification system and was shown to perform very well. A thermal mapping profile across a cathode gas track showed a general increase in temperature from air inlet to exit. It was illustrated how the rate of injected water and the flowrate of air were both major influences on this thermal profile. Operating with a constant drawn current, the value of the fuel cell potential was observed to oscillate due to restrictions on the rate of oxygen transport to catalyst sites, occurring with low air supply stoichiometries or a high rate of injected water. The endurance test showed the formation of equilibrated membrane water contents with water injection rates much higher than the amount calculated for 100% RH of the air. This again confirmed that injected water, although evaporating and controlling the fuel cell temperature, was not reaching the membrane.

Several studies relating EC fuel cell development were then undertaken:

- Two steady state models were developed of fuel cell systems, one using the more 'conventional' stack operating at an elevated pressure and with plate-based humidification and cooling subsystems (referred to as LC operation) and the other based on the direct injection of liquid water for humidity and thermal control (referred to as EC operation). The EC system was shown to be able to compete with a conventional high-pressure LC stack, primarily due to the reduction of parasitic losses associated with air compression but also a higher stack packing density was achievable. The differences in system performance, i.e. efficiencies based on energy value of hydrogen fuel, were emphasised at partial power loads where the demands of the compressor penalised the LC system severely.

- A measurement of current distribution across a fuel cell was undertaken in a fuel cell set up for direct cathode liquid water injection utilising the parallel and interdigitated flow fields with identical gas track pitch and dimensions. Polarisation plots showed the dominating effect of mass transport overpotential at high current densities when using the parallel configuration. In the current mapping study, data from the fuel cell was obtained at identical potentials with different operating conditions. The interdigitated flow-field was shown to increase the current density obtained, particularly in the latter sections of the cathode gas tracks. The performance obtained with the parallel flow field was greatly reduced by the presence of liquid water in the diffuser adjacent to the latter sections of cathode gas track. A counterflow configuration of gases was observed to increase the performance when using the interdigitated flow field.

- Ex-situ tests were carried out as part of a study into lowering cathode pressure drop - one of the crucial issues for successful EC fuel cell operation. In Chapter 7, several diffuser materials were tested ex-situ in addition to Carbel CL, which had been the diffuser material used in all fuel cell builds. The crucial characteristics for utilisation in EC fuel cell utilisation (permeability, resistance) were explained in relation to the diffuser substrate structure and treatments. In particular, the addition of PTFE or dispersal of a microdiffuser layer was shown to increase the mechanical strength of a diffuser. Carbel CL was shown to have a low cross-plane permeability due to the low mechanical strength of the carbon fibre weave which crushed relatively easily on compaction in comparison to the carbon fibre paper based materials.

- In-situ testing in a fuel cell utilising cathode water injection was undertaken for selected SGL diffusers, which had indicated good electrical resistance and permeability characteristics in the ex-situ testing. The cathode pressure drop was measured over the fuel cell at open circuit conditions and also at 80 Amps where water was generated by the fuel cell reaction. The results illustrated that the fuel cell produced superior performance with Carbel CL, both in terms of cathode pressure drop and potential.

9.2 Future work

The EC fuel cell operating mechanism has been proved in the work detailed in this thesis. However, the significant issue of a reduction in cathode pressure drop could be investigated further.

Time and cost restrictions prevented a full study of variable interdigitated flow field dimensions. Such an investigation, particularly including the effects of different widths of the track pitch would be invaluable

Testing carbon fibre paper diffusers, similar to the SGL materials, with a higher PTFE content would reduce the water accumulation during fuel cell operation and increase the strength of the substrate material. Both of these characteristics would result in a lower cathode pressure drop for an equal fuel cell performance.

There should also be an investigation of liquid water delivery methods with a view to improving the hydration level of the polymer membrane during EC fuel cell operation.

Appendices

Appendix A1 - Definition of stoichiometry and flow calculations

It is common practice to supply the reactant gases to a fuel cell in excess amounts to what is exactly calculated to be required. The amount of gas supplied is usually expressed as a figure called the stoichiometric constant or ratio and expressed as λ (a value for λ of 1 means exactly the right amount is being supplied).

A formula for calculating the required volumetric flowrate of *hydrogen* in standard litres per minute (SLPM) is[1]:

$$\dot{V}_{H_2} = \frac{I}{2.F} \times 22.4 \times 60 \times \lambda_{H_2} \qquad \textbf{Equation A.01}$$

Simplifying in order to express purely as a function of current and stoichiometry:

$$\dot{V}_{H_2} = 6.9637 \times 10^{-3} \times I \times \lambda_{H_2} \qquad \textbf{Equation A.02}$$

The amount of *air* required in standard litres per minute is expressed as[2]:

$$\dot{V}_{air} = \frac{I}{4.F} \times 22.4 \times 60 \times \frac{100}{21} \times \lambda_{air} \qquad \textbf{Equation A.03}$$

Simplifying this to express purely as function of current and stoichiometry:

$$\dot{V}_{air} = 1.6580 \times 10^{-2} \times I \times \lambda_{air} \qquad \textbf{Equation A.04}$$

Appendix A2 shows some calculated gas supply rates that have been used in the tests in this thesis.

---

[1] Where I is the fuel cell current (Amps = Coulombs (units of electrical charge per second) 2 = number of electrons transferred per molecule of hydrogen, F – faraday constant = 96500 Coulombs of charge per mole) The figure of 22.4 converts from moles per second to standard litres per second and the figure of 60 converts from per second to per minute. The symbol λ represents the stoichiometric constant. In all tests in this thesis a hydrogen stoichiometry of 1.5 is used.

[2] This is similar to the expression for hydrogen flowrate except 4 = number of electrons transferred per molecule of oxygen. There is an air to oxygen conversion ratio of 100/21 to include the 79 percentile nitrogen content of air.

Appendix A2: Calculated gas flow requirements for fuel cell - varying operating stoichiometries (standard litres/minute)

Current Drawn	Hydrogen stoichiometry			Air stoichiometry						
	1	**1.5**	**2**	**1**	**2**	**3**	**4**	**6**	**8**	**10**
5	0.03	0.05	0.07	0.08	0.17	0.25	0.33	0.50	0.66	0.83
10	0.07	0.10	0.14	0.17	0.33	0.50	0.66	1.00	1.33	1.66
15	0.10	0.16	0.21	0.25	0.50	0.75	1.00	1.49	1.99	2.49
20	0.14	0.21	0.28	0.33	0.66	1.00	1.33	1.99	2.65	3.32
40	0.28	0.42	0.56	0.66	1.33	1.99	2.65	3.98	5.31	6.64
50	0.35	0.52	0.70	0.83	1.66	2.49	3.32	4.98	6.64	8.30
60	0.42	0.63	0.84	1.00	1.99	2.99	3.98	5.97	7.96	9.96
80	0.56	0.84	1.11	1.33	2.65	3.98	5.31	7.96	10.62	13.27
100	0.70	1.05	1.39	1.66	3.32	4.98	6.64	9.96	13.27	16.59
120	0.84	1.25	1.67	1.99	3.98	5.97	7.96	11.95	15.93	19.91
140	0.98	1.46	1.95	2.32	4.65	6.97	9.29	13.94	18.58	23.23
150	1.05	1.57	2.09	2.49	4.98	7.47	9.96	14.93	19.91	24.89
160	1.11	1.67	2.23	2.65	5.31	7.96	10.62	15.93	21.24	26.55
180	1.25	1.88	2.51	2.99	5.97	8.96	11.95	17.92	23.89	29.87
200	1.39	2.09	2.79	3.32	6.64	9.96	13.27	19.91	26.55	33.18
220	1.53	2.30	3.07	3.65	7.30	10.95	14.60	21.90	29.20	36.50
240	1.67	2.51	3.34	3.98	7.96	11.95	15.93	23.89	31.86	39.82
260	1.81	2.72	3.62	4.31	8.63	12.94	17.26	25.88	34.51	43.14
280	1.95	2.93	3.90	4.65	9.29	13.94	18.58	27.87	37.17	46.46
300	2.09	3.14	4.18	4.98	9.96	14.93	19.91	29.87	39.82	49.78
320	2.23	3.34	4.46	5.31	10.62	15.93	21.24	31.86	42.48	53.09
340	2.37	3.55	4.74	5.64	11.28	16.92	22.57	33.85	45.13	56.41
360	2.51	3.76	5.02	5.97	11.95	17.92	23.89	35.84	47.78	59.73
380	2.65	3.97	5.30	6.30	12.61	18.91	25.22	37.83	50.44	63.05
400	2.79	4.18	5.57	6.64	13.27	19.91	26.55	39.82	53.09	66.37

Appendix B1 - Water supply calculations

Throughout the research detailed in this thesis the water is supplied at set relative humidity levels of the cathode air supply. Therefore there is a requirement to derive a formula for the level of water required to saturate a gas stream, expressed in cc/min in order to directly set the correct water delivery flowrate on the HPLC pump.

Slightly altering equation A.03 obtains a formula for calculating the molar flowrate of air per second:

$$\dot{n}_{air} = \frac{I}{4.F} \times \frac{100}{21} \times \lambda_{air} \qquad \textbf{Equation B.01}$$

From equation 3.03, for a gas flow with 100% RH the partial pressure of water is equivalent to its saturation pressure at that temperature. Hence the molar ratio of water to air in a saturated gas stream can be expressed as[1]:

$$\frac{\dot{n}_{H_2O}}{\dot{n}_{air}} = \frac{P_{sat}}{P_{tot} - P_{sat}} \qquad \textbf{Equation B.02}$$

Substituting equation B.01 into B.02 will result in an expression for the molar flowrate of water. By including a molar volume factor of 18cc/mole (molar weight of water is 18g/mole and the density 1g/cc) and a conversion of 60seconds/minute, this gives an expression for the volumetric flowrate of water:

$$\dot{V}_{H_2O} = \frac{I}{4.F} \times \frac{100}{21} \times \lambda_{air} \times \frac{P_{sat}}{P_{tot} - P_{sat}} \times 18 \times 60 \qquad \textbf{Equation B.03}$$

To calculate the water required for different levels of gas saturation substitute P_{sat} with the partial pressure of water in the air flow. This amount can be calculated relative to P_{sat} e.g. for a ϕ value of 50% $P_{H_2O} = 0.5P_{sat}$

The amount of water required to be added to the air flow to obtain a predetermined level of ϕ will change if the fuel cell temperature, pressure or air stoichiometry changes. Appendix B2 illustrates the water injection rates that have been used for the tests in this thesis.

[1] Where $\dot{n}_{H_2O}$ is the molar flowrate of water. P_{tot} is the total pressure. P_{sat} is the water saturation pressure.

Appendix B2: Calculations of water requirement for 100% RH air

Current Drawn	Fuel Cell Operating Conditions								Water produced (moles/sec)	Water produced (cc/min)
	60C 0.5bar.g air stoi=2	**60C 0.5bar.g air stoi=4**	**60C 1.5bar.g air stoi=2**	**60C 1.5bar.g air stoi=4**	**80C 0.5bar.g air stoi=2**	**80C 0.5bar.g air stoi=4**	**80C 1.5bar.g air stoi=2**	**80C 1.5bar.g air stoi=4**		
5	0.02	0.04	0.01	0.02	0.05	0.10	0.03	0.05	2.5912E-05	0.03
10	0.04	0.08	0.02	0.05	0.10	0.19	0.05	0.11	5.1824E-05	0.06
15	0.06	0.12	0.03	0.07	0.15	0.29	0.08	0.16	7.7736E-05	0.08
20	0.08	0.16	0.05	0.09	0.19	0.39	0.11	0.22	1.0365E-04	0.11
40	0.16	0.33	0.09	0.18	0.39	0.78	0.22	0.44	2.0730E-04	0.22
60	0.24	0.49	0.14	0.28	0.58	1.16	0.33	0.66	3.1095E-04	0.34
80	0.33	0.65	0.18	0.37	0.78	1.55	0.44	0.88	4.1459E-04	0.45
100	0.41	0.82	0.23	0.46	0.97	1.94	0.55	1.10	5.1824E-04	0.56
120	0.49	0.98	0.28	0.55	1.16	2.33	0.66	1.32	6.2189E-04	0.67
140	0.57	1.14	0.32	0.65	1.36	2.72	0.77	1.54	7.2554E-04	0.79
160	0.65	1.31	0.37	0.74	1.55	3.10	0.88	1.76	8.2919E-04	0.90
180	0.73	1.47	0.42	0.83	1.75	3.49	0.99	1.97	9.3284E-04	1.01
200	0.82	1.63	0.46	0.92	1.94	3.88	1.10	2.19	1.0365E-03	1.12
220	0.90	1.80	0.51	1.02	2.13	4.27	1.21	2.41	1.1401E-03	1.24
240	0.98	1.96	0.55	1.11	2.33	4.66	1.32	2.63	1.2438E-03	1.35
260	1.06	2.12	0.60	1.20	2.52	5.04	1.43	2.85	1.3474E-03	1.46
280	1.14	2.29	0.65	1.29	2.72	5.43	1.54	3.07	1.4511E-03	1.57
300	1.22	2.45	0.69	1.38	2.91	5.82	1.65	3.29	1.5547E-03	1.68
320	1.31	2.61	0.74	1.48	3.10	6.21	1.76	3.51	1.6584E-03	1.80
340	1.39	2.77	0.78	1.57	3.30	6.60	1.86	3.73	1.7620E-03	1.91
360	1.47	2.94	0.83	1.66	3.49	6.99	1.97	3.95	1.8657E-03	2.02
380	1.55	3.10	0.88	1.75	3.69	7.37	2.08	4.17	1.9693E-03	2.13
400	1.63	3.26	0.92	1.85	3.88	7.76	2.19	4.39	2.0730E-03	2.25

Appendix C – Pre-test and Shutdown Procedures for FC rigs

Pre-test procedures

Leak testing

Before any period of fuel cell operation the pipework, equipment and fuel cell gasketing had to be checked for leaks:

The anode leak testing was carried out by the following procedure:

1. Fully closing the anode back-pressure regulator
2. Adjusting the hydrogen supply regulator to obtain a pressure of 0.5bar.g., as displayed on the anode pressure gauge
3. Backing off the hydrogen supply regulator
4. Noting the pressure loss on the gauge after sixty seconds to obtain a leakage rate per minute

The same procedure was also carried out for the cathode using air. Acceptable pressure losses were 0.1bar/minute for the anode and 0.3 bar/minute for the cathode. The latter figure could be significantly higher as an air leak did not present any significant hazard.

Crossover testing

The fuel cell MEA had to be checked for any possible damage that could have occurred from long periods of operation with a slight pressure differential between anode and cathode or insufficient humidification. This was essential to carry out due to the risk of an explosive gas mixture of hydrogen and air in the presence of a catalyst.

A damaged MEA was checked by recording the gas 'crossover' rate; using the following procedure:

1. Adjusting the gas supply to deliver nitrogen instead of hydrogen
2. Closing the anode back pressure regulator and adjusting the nitrogen supply regulator to pressurise the anode to 0.5 bar.g
3. Releasing the *cathode* exhaust pipe from the air back pressure regulator
4. Filling a measuring cylinder with water and inverting this in a beaker filled with water
5. Positioning the cathode exhaust pipe in the measuring cylinder
6. Logging the rate of water displacement from the cylinder markings by the bubbles of N_2 in one minute to obtain a figure for gas crossover rate.

An acceptable crossover rate was below 5 sccm

MEA conditioning

Following a new cell build, the MEA required a period of 'conditioning' - in this case 5 hours of operation, cycling through a full range of current densities. In addition, before any testing session the fuel cell was run for approximately 30 minutes at a medium range current. Both these procedures endured the conditioning level of the membrane was equivalent and therefore, did not have any effect on the results obtained.

Electrical short check

Electrical shorts can occur from any erroneous connections between the anode and cathode sides of the cell such as touching probing tabs, protruding Grafoil gaskets, potential probes or indeed, a holed MEA.

A check for such 'shorts' was to use a digital multimeter with probes, and after ensuring no hydrogen was present on the anode side (by flushing out with nitrogen for a few minutes) checking if the MEA charges up in a similar manner to a capacitor, with the multimeter set to the lowest resistance (ohms) setting.

Shutdown procedures

Emergency shutdown procedure

The electronic load unit was set to an active setting with a power supply in series, to overcome the voltage drop in the current leads, meaning the fuel cell would be electrolysed if it could not supply the set delivery current. If there was no automatic trip to drop out the load unit, hitting the red trip button closed the wall mounted hydrogen solenoid downstream of the supply regulator and switched to the nitrogen supply - the load unit was also shut off.

Normal shutdown procedure

The load unit was backed off to zero amps, the hydrogen and air regulators were completely backed off and the mass flow displays set to zero on the control box. The HPLC pump was turned off and the steam generation unit and cell heaters disengaged.

Appendix D – Sputtering of gold onto segmented cell face

COATING OF SEGMENTED FUEL CELL CURRENT COLLECTOR FOR LOUGHBOROUGH UNIVERSITY

UNCOATED COMPLETE PART

UNCOATED FACE TO BE COATED

MASKED PART BEFORE COATING

MASKED FACE TO BE COATED

FACE COATED WITH GOLD

COMPLETED JIG AFTER COATING

Scanned images provided by Teer Coatings, Hartlebury

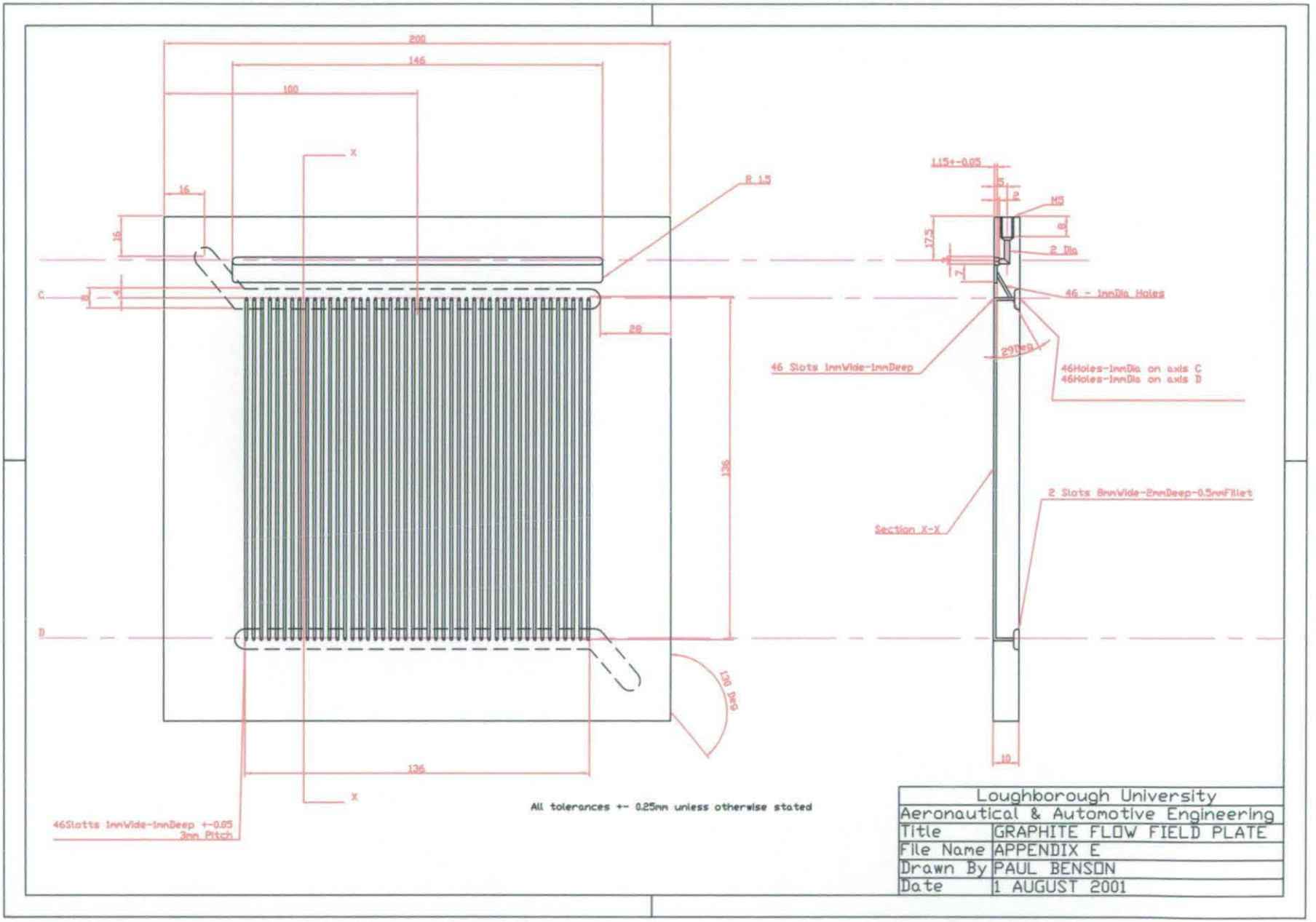
200
146
100
X
16
16
R 1.5
C
8
4
28
136
D
130 Deg
136
X
46Slotts 1mmWide-1mmDeep +-0.05
3mm Pitch
All tolerances +- 0.25mm unless otherwise stated
1.15+-0.05
5
2
M3
8
17.5
2 Dia
7
46 - 1mmDia Holes
29Deg
46 Slots 1mmWide-1mmDeep
46Holes-1mmDia on axis C
46Holes-1mmDia on axis D
2 Slots 8mmWide-2mmDeep-0.5mmFillet
Section X-X
10
Loughborough University
Aeronautical & Automotive Engineering
Title GRAPHITE FLOW FIELD PLATE
File Name APPENDIX E
Drawn By PAUL BENSON
Date 1 AUGUST 2001

Appendix F – Manufacturing processes for gas diffusion media

In the production of carbon fibre based gas diffusion media, an organic precursor material is used which is usually a copolymer comprising greater than 90% polyacrylonitrile (PAN) although other materials such as cellulose (e.g. Rayon) and phenolic (e.g. Kynol) have been used.

There are four main methods of manufacturing carbon based diffuser media, three of which can be defined as non-woven 'carbon paper' structures as illustrated below in Fig. F.01

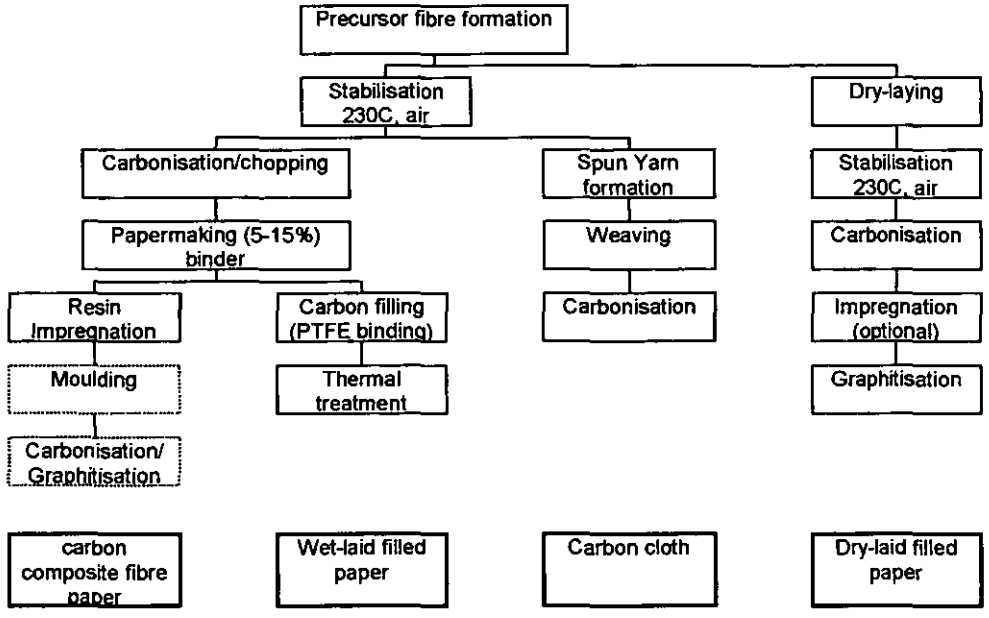

Fig. F.01 Processing routes for producing PEFC diffusion media used PAN-based precursor
Boxes with dashed surrounds indicate batch processes - all others are continuous

Papermaking

In two of the processes, one of the intermediate steps is 'papermaking', where continuous rolls of carbon fibre paper are manufactured using a wet-laid process using conventional papermaking equipment. In this process, the chopped carbon fibre is dispersed in water with binders, typically polyvinyl alcohol. The binder content after papermaking is typically 5-15% by weight. These materials exhibit a preponderance of fibres laid out in the machine direction due to the manufacturing process in which fibres are drawn in the machine direction as they are deposited into the fibre mat.

Carbon composite fibre

The non-woven substrates used most often in fuel cells as gas diffusion media are wet-laid carbon fibre papers indicated by the leftmost production path although traditionally this material is referred to as 'carbon paper'. However this material is best described as a carbon-carbon composite since after the graphitisation step it consists of carbon fibres held together by a carbon matrix.

Wet-laid filled paper

Another approach in Fig F.01 is what is referred to "wet-laid filled paper". In this approach a carbon or graphite is added to the wet-laid carbon paper and bound, e.g. with PTFE. The powder provides conductivity rather than relying on a final carbonisation or graphitisation step. The binder can also impart hydrophobic properties to the material

Carbon fibre cloth

The fabrics used as gas diffusion media are woven from spun PAN yarns and are subsequently carbonised or graphitised using continuous batch or a combination of both processes. Rather than being held together by a resin, their woven structure provides the mechanical integrity needed, the process shown by the third column in Fig F.01. The details for the manufacture of carbon cloth are outlined in the US Patent 3541582

Dry-laid materials

The other approach to gas-diffusion media production is shown in the far right process in Fig. F.01. Here PAN fibres usually in the pre-stabilised form are dry laid into a thin fibre fleece mat through a carding-combing process. In the process some fibres orient in the through plane direction and creates a mechanically bonded non –woven fabric. The PAN woven mat is then oxidatively stabilised, followed by carbonisation. The material can be optionally filled with carbon or graphite powder and a resin binder followed by graphitisation to yield a gas diffusion media product.

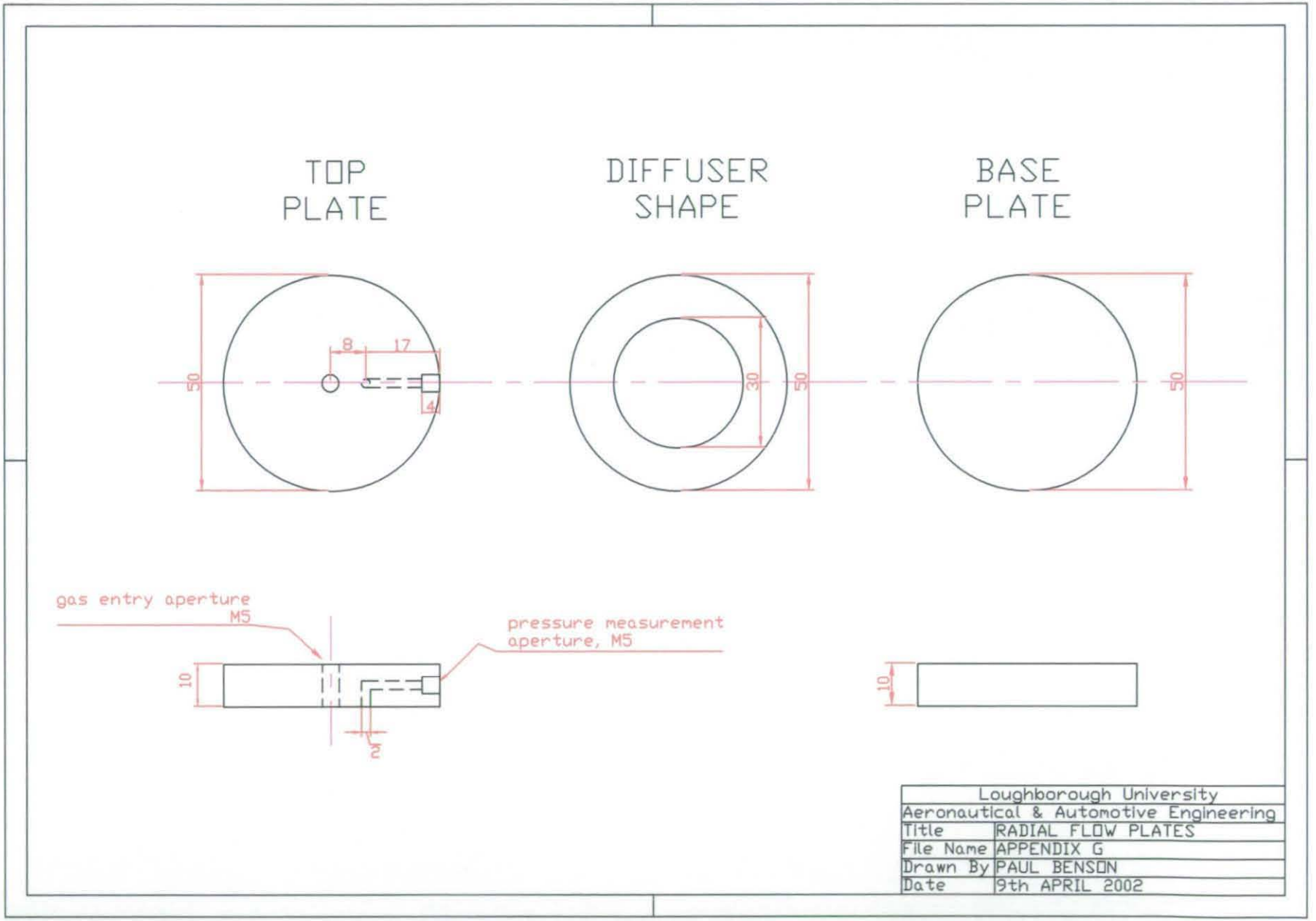
TOP
PLATE
DIFFUSER
SHAPE
BASE
PLATE
8
17
4
50
30
50
50
gas entry aperture
M5
pressure measurement
aperture, M5
10
2
10
Loughborough University
Aeronautical & Automotive Engineering
Title
RADIAL FLOW PLATES
File Name
APPENDIX G
Drawn By
PAUL BENSON
Date
9th APRIL 2002

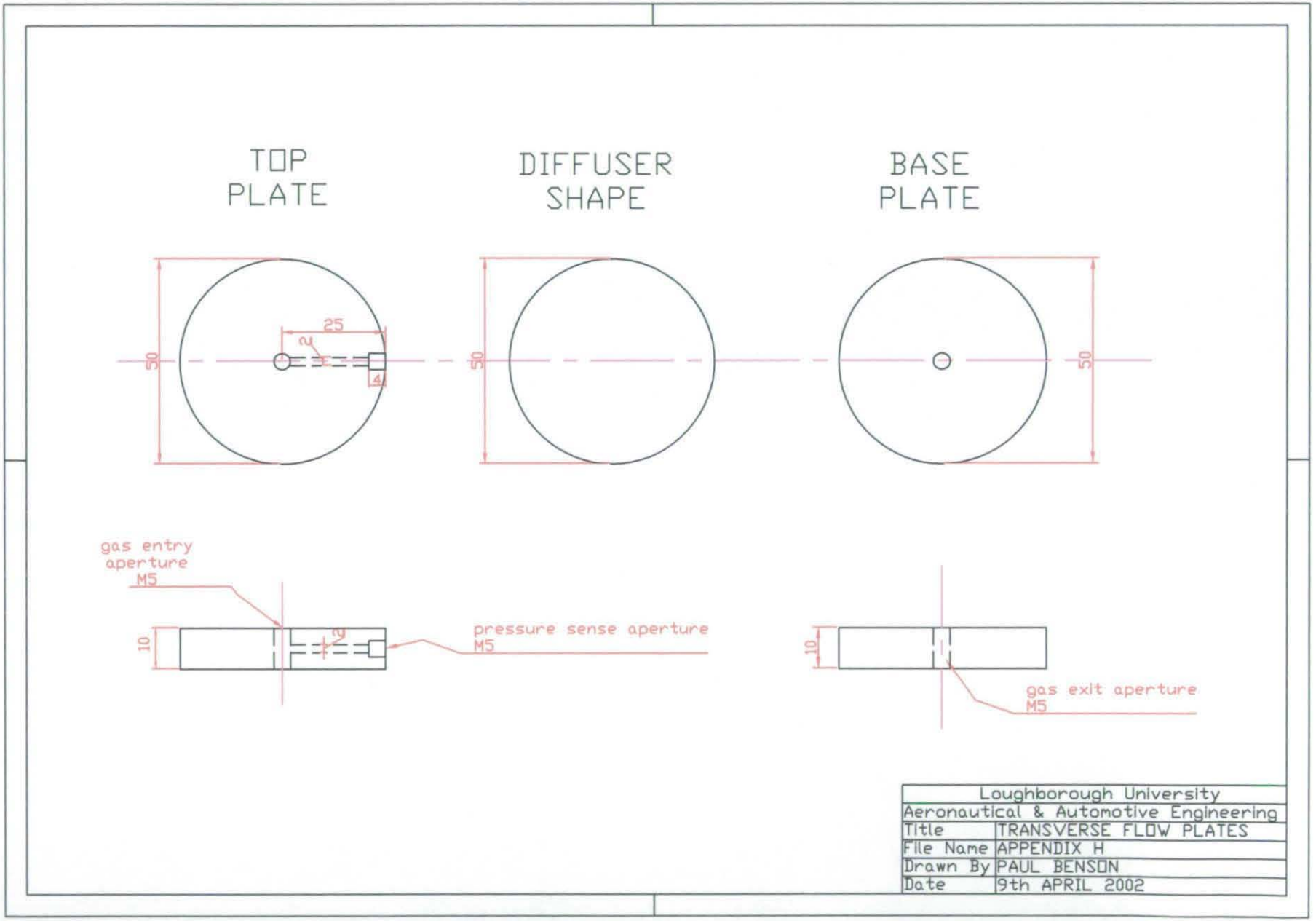
TOP PLATE
DIFFUSER SHAPE
BASE PLATE
50
25
2
4
50
50
gas entry aperture M5
10
2
pressure sense aperture M5
10
gas exit aperture M5
Loughborough University
Aeronautical & Automotive Engineering
Title
TRANSVERSE FLOW PLATES
File Name
APPENDIX H
Drawn By
PAUL BENSON
Date
9th APRIL 2002

Appendix I – Calculation of cross plane permeability

Fluid flow in porous media is described by Darcy's equation which states that the volumetric flowrate $\dot{V}$ of liquid through a specimen of porous material is proportional to the hydrostatic pressure difference ΔP across the specimen, inversely proportional to the length L of the specimen, and proportional to the cross sectional area A.

$$\dot{V} = \frac{kA\Delta P}{L} \qquad \textbf{Equation I.01}$$

The constant of proportionality, k, as defined by Darcy's law is the Darcy permeability of the material and as defined in this equation has dimensions $kg^{-1}m^3$ s

However it is common to express hydrostatic pressures in terms of the pressure potential $p = \frac{P}{\rho g}$ - where ρ is liquid density and g is the standard acceleration. This value has dimension length and is entirely equivalent to the hydrostatic head. Darcy's law can then be expressed as:

$$\dot{V} = \frac{K_s A\Delta p}{L} \qquad \textbf{Equation I.02}$$

The quantity K_s is the conventional saturated permeability of the material with the dimensions length/time $K_s = k\rho g$ - this law is often written $\dot{V} = K_s iA$, where i is the hydraulic gradient

However these constants depend on both the fluid and the material - an intrinsic permeability k' can be defined which is independent of the fluid used to measure it and has dimensions m^2. Intrinsic permeability is defined as $k' = k\mu$ where μ is the fluid viscosity. (Hence $k' = \frac{K_s \mu}{\rho g}$)

Both definitions of permeability are used in materials literature although K_s more widely than k'. The conversion between the two depends not only on the viscosity but also on the density of the fluid at the temperature of measurement.

Here, we want to obtain an expression for calculating the intrinsic permeability of the samples in the cross plane flow directions using the pressure drop data from the extensometer testing.

$$\dot{V} = \frac{k' A \Delta P}{L \mu}$$ **Equation I.03**

Changing equation J.03 to vector velocity gives

$$\bar{v} = \frac{k'}{\mu} \nabla P$$ **Equation I.04**

It is necessary to model the radial flow in the diffuser sample as a cylinder where all the flow is radial and the gas source is from the center. In cylindrical geometry where all flow is radial with a center source

$$v_r = \frac{k'}{\mu} \frac{\partial P}{\partial r} \Leftrightarrow \frac{\partial P}{\partial r} = \frac{\mu}{k'} v_r$$ **Equation I.05**

It is necessary to obtain an expression relating pressure drop to radius so we can integrate and solve for k'. The fluid flow velocity at any radius r can be derived from the conservation of mass

$$\dot{V}_{in} = \dot{V}_{out}$$ **Equation I.06**

The ideal gas law states $P\dot{V} = \dot{n}RT$, where $\dot{n}$ is the molar flowrate, R is the universal gas constant, T is the temperature in Kelvin, $\dot{V}$ is the volumetric flow rate

The volumetric flow rate can also be defined as $2\pi r z v_r$ where z is the thickness of the diffusion material at the particular compaction pressure

The fluid flow velocity at the radius r can be defined as:

$$v_r = \frac{RT\dot{n}}{2\pi r P h} = \frac{RT\dot{V}}{2\pi r P h v^O}$$ **Equation I.07**

where v^O is the standard molar volume.

Substituting this expression into Equation I.05 gives

$$\frac{\partial P}{\partial r} = \frac{RT\dot{V}\mu}{2\pi r P z v^O k'} \Leftrightarrow P\partial P = \frac{RT\dot{V}\mu}{2\pi z v^O k'} \frac{\partial r}{r}$$ **Equation I.08**

By integrating we get

$$\int_{P_1}^{P_2} P\partial P = \frac{RT\dot{V}\mu}{2\pi z v^{O} k'} \int_{r_1}^{r_2} \frac{\partial r}{r} \Leftrightarrow \frac{P_2^2 - P_1^2}{2} = \frac{RT\dot{V}\mu}{2\pi z v^{O} k'} \ln\left(\frac{r_2}{r_1}\right) \quad \textbf{Equation I.09}$$

$$P_2^2 - P_1^2 = \frac{C_1 \dot{V}}{z k'} \quad \textbf{Equation I.10}$$

Where C_1 is a constant with a value of $\frac{RT\mu}{\pi v^{O}} \ln\left(\frac{r_2}{r_1}\right)$

Therefore, the equation for calculating intrinsic permeability is:

$$k' = -\frac{C_1 \dot{V}}{z(P_2^2 - P_1^2)} \quad \textbf{Equation I.11}$$

Appendix J1: Approximation formulae for dimension / compaction pressure plots - SGL materials and Carbel CL

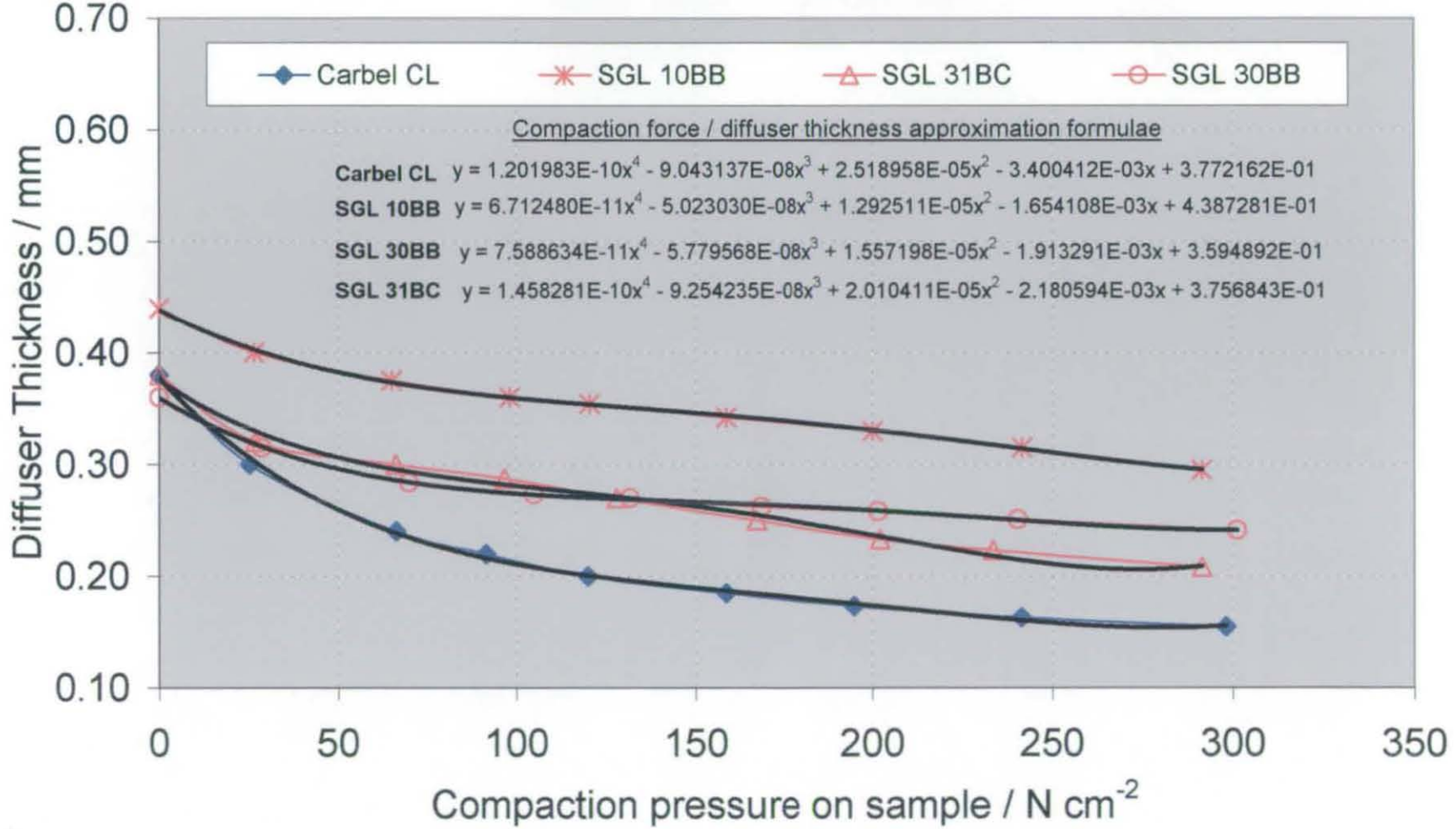

Appendix J2: Approximation formulae for dimension / cross-plane pressure drop - SGL materials and Carbel CL

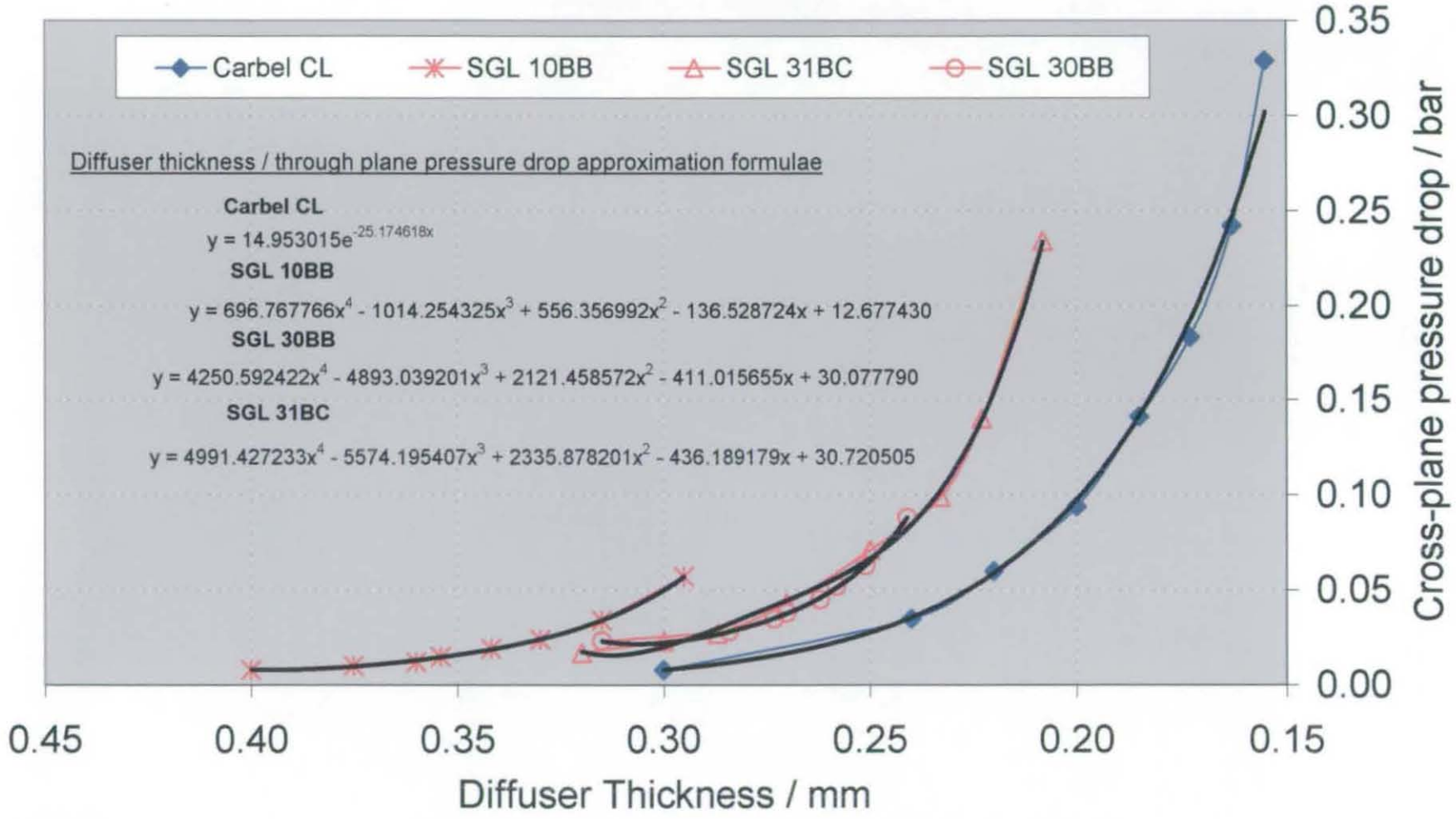

Appendix J3: Approximation formulae for dimension/ electrical resistance - SGL materials and Carbel CL